Diss. ETH No. 18053 and
ETHZ-IPP Internal Report 2008-16

ETH Institute for Particle Physics

Measurement of Charm in Charged Current at HERA

A dissertation submitted to the

Swiss Federal Institute of Technology Zurich

for the degree of

Doctor of Sciences

presented by

Tobias Zimmermann

Dipl. Phys. ETH
born on July 17, 1979
citizen of Zürich (ZH)
and Ebikon (LU)

accepted on the recommendation of
Prof. Dr. Ralph Eichler, examiner and
Prof. Dr. Urs Langenegger, co-examiner

2008

Abstract

A measurement of charm production in charged current (CC) polarized electron-proton deep inelastic scattering processes with data from the H1 detector at the HERA collider is presented. This process in principle allows access to the strange quark density in the proton.

In total 5460 CC candidate events in e^+p and 6253 in e^-p data are selected in the kinematic range $Q^2 > 223$ GeV^2 and $0.03 < y < 0.85$. The measured CC cross sections are

$$\sigma_{CC} = (28.9 \pm 1.4) + P_e \cdot (28.6 \pm 4.7) \text{ pb} \qquad \text{for } e^+p \text{ and}$$
$$\sigma_{CC} = (49.2 \pm 2.3) - P_e \cdot (42.5 \pm 6.8) \text{ pb} \qquad \text{for } e^-p,$$

where P_e is the lepton beam polarization. While the measured cross section for e^+p data is in agreement with the theoretical prediction, the cross section for e^-p data shows a weaker dependence on P_e than predicted.

The charm fractions in the selected CC candidate event samples are extracted using the muon charge asymmetry. Muons originating from charmed hadron decays in CC events at HERA always have the same charge as the beam lepton. The extracted charm fractions in the selected CC candidate event samples are

$$\mathrm{F}_c = 9.5 \pm 8.9 \pm 3.0\ \% \qquad \text{for } e^+p \text{ and}$$
$$\mathrm{F}_c = 4.4 \pm 6.9 \pm 2.6\ \% \qquad \text{for } e^-p.$$

Due to the large statistical errors of the measured charm fractions, the strange quark density in the proton has not been extracted.

Zusammenfassung

Es wird eine Messung von Charm-Produktion in Ereignissen des geladenen Stromes (Charged Current, CC) in polarisierter, tief inelastischer Elektron-Proton-Streuung mit den Daten des Detektors H1 am Speicherring HERA vorgestellt. Dieser Prozess ermöglicht prinzipiell die Messung des Strange-Quark-Anteils im Proton.

Total wurden 5460 Kandidaten für CC-Ereignisse in e^+p und 6253 in e^-p-Daten selektiert im kinematischen Bereich $Q^2 > 223$ GeV^2 und $0.03 < y < 0.85$. Die gemessenen CC-Wirkungsquerschnitte sind

$$\sigma_{CC} = (28.9 \pm 1.4) + P_e \cdot (28.6 \pm 4.7) \text{ pb} \qquad \text{für } e^+p \text{ und}$$
$$\sigma_{CC} = (49.2 \pm 2.3) - P_e \cdot (42.5 \pm 6.8) \text{ pb} \qquad \text{für } e^-p,$$

wobei P_e die Leptonstrahl-Polarisation bezeichnet. Während der gemessene Wirkungsquerschnitt in e^+p-Daten mit der theoretischen Vorhersage übereinstimmt, zeigt der Wirkungsquerschnitt in e^-p-Daten eine schwächere Polarisationsabhängigkeit als erwartet.

Die Charm-Anteile in den selektierten CC-Kandidatsereignissen werden mit Hilfe der Muon-Ladungsasymmetrie bestimmt. Muonen aus Zerfällen von Charm-Hadronen in CC-Ereignissen bei HERA haben immer die gleiche Ladung wie das Strahllepton. Die extrahierten Charm-Anteile in den selektierten CC-Kandidatsereignissen sind

$$\mathrm{F}_c = 9.5 \pm 8.9 \pm 3.0\ \% \qquad \text{für } e^+p \text{ und}$$
$$\mathrm{F}_c = 4.4 \pm 6.9 \pm 2.6\ \% \qquad \text{für } e^-p.$$

Aufgrund der grossen statistischen Fehler der gemessenen Charm-Anteile wurde die Dichte der Strange-Quarks im Proton nicht bestimmt.

Contents

1 Introduction **9**

2 Theory **11**
2.1 Electron-Proton Scattering . . . 11
2.1.1 Introduction to ep Scattering . . . 11
2.1.2 Kinematics in ep Scattering . . . 11
2.1.3 Elastic Scattering . . . 13
2.1.4 Deep Inelastic Scattering . . . 14
2.2 DIS in the Quark Parton Model and QCD . . . 14
2.2.1 Quark Parton Model . . . 14
2.2.2 Quantum Chromodynamics (QCD) . . . 15
2.3 Electroweak Processes: NC and CC Interactions . . . 17
2.3.1 NC and CC Cross Sections . . . 17
2.3.2 Parity Violation . . . 19
2.3.3 Electron-Proton vs. Positron-Proton Scattering . . . 20
2.3.4 The CKM-Matrix . . . 21

3 The Strange Content of the Proton **23**
3.1 Introduction . . . 23
3.2 Elastic Scattering . . . 23
3.2.1 Formalism and Measured Quantities . . . 23
3.2.2 HAPPEX . . . 24
3.2.3 G0 . . . 25
3.2.4 A4 and SAMPLE . . . 25
3.3 Neutrino-Nucleon Deep Inelastic Scattering . . . 27
3.3.1 Formalism . . . 27
3.3.2 Dimuon Events . . . 27
3.3.3 CHARM II . . . 28
3.3.4 NuTeV and CCFR . . . 28
3.3.5 CHORUS and NOMAD . . . 29
3.4 Measurements at HERA . . . 29
3.4.1 HERMES . . . 29
3.4.2 ZEUS . . . 31
3.4.3 H1 . . . 32
3.5 Putting the Picture Together . . . 32

4 The H1 Experiment at HERA **35**
4.1 The HERA Accelerator . . . 35
4.2 Overview of the H1 Detector . . . 39
4.3 Tracking System . . . 39

4.3.1 Tracking Chambers . . . 41
4.3.2 Silicon Vertex Detectors . . . 43
4.3.3 Track Reconstruction . . . 43
4.4 Calorimeters . . . 44
4.4.1 Liquid Argon Calorimeter . . . 45
4.4.2 Spaghetti Calorimeter . . . 45
4.5 Muon System . . . 46
4.5.1 Central Muon Detector . . . 46
4.5.2 Forward Muon Detector . . . 46
4.6 Luminosity Measurement . . . 47
4.7 Trigger and Data Acquisition . . . 48

5 Simulation of Electron-Proton Collision Events 51
5.1 Simulation of Events . . . 51
5.2 Simulated Event Samples . . . 52
5.2.1 Charged Current . . . 52
5.2.2 Background Processes . . . 53
5.3 Event Reweighting and Pseudo Charged Current . . . 56
5.3.1 Reweighting of Simulated Events . . . 56
5.3.2 Pseudo Charged Current . . . 57

6 Charged Current Measurement 59
6.1 Trigger . . . 59
6.1.1 CC Trigger Definitions . . . 59
6.1.2 Trigger Efficiency . . . 60
6.2 Data Selection . . . 61
6.3 Rejection of Non-ep Background . . . 62
6.3.1 Event Timing . . . 64
6.3.2 Background Finder . . . 64
6.3.3 Vertex . . . 65
6.3.4 LAr Calorimeter Noise . . . 65
6.4 CC Event Selection . . . 65
6.4.1 Event Kinematics Criteria . . . 65
6.4.2 Rejection of Remaining Photoproduction Events . . . 66
6.4.3 Rejection of Remaining Neutral Current DIS Events . . . 68
6.4.4 Polarization . . . 69
6.4.5 Visual Scanning . . . 69
6.5 Summary of the CC Event Selection . . . 70
6.6 Selected Event Samples . . . 71
6.7 Systematic Uncertainties . . . 74
6.8 Charged Current Cross Sections . . . 76
6.8.1 Calculation of the Cross Section . . . 76
6.8.2 Measured Charged Current Cross Sections . . . 77

7 Charm in Charged Current and the Strange Content of the Proton 81
7.1 Measuring the Strange Sea in the Proton . . . 81
7.2 Charm Production in Charged Current . . . 81
7.2.1 Production Processes . . . 82
7.2.2 Theoretical Expectation for the Charm Fraction in Charged Current . . . 84
7.3 Properties of Charm Events in Charged Current . . . 84
7.3.1 Kinematics of Charm and Uds Events . . . 84
7.3.2 Selection Efficiency of Charm and Non-Charm Events . . . 87

7.4 Methods for Charm Tagging . . . 87

8 Charm Fraction Extraction using Lifetime Information 89
8.1 Introduction . . . 89
8.2 Tracks and Jets . . . 90
8.2.1 Track Reconstruction Efficiency . . . 90
8.2.2 CST Linking . . . 91
8.2.3 Track Selection . . . 91
8.2.4 Jets . . . 93
8.2.5 Assignment of Tracks to Jets . . . 93
8.2.6 Identification of Tracks Originating from Charm Decays . . . 94
8.3 Secondary Vertex Reconstruction . . . 95
8.3.1 Deterministic Annealing Algorithm . . . 95
8.3.2 Track Weights and Vertex Multiplicity . . . 97
8.3.3 Decay Length . . . 98
8.3.4 Performance of the Secondary Vertex Finding in Simulation . . . 99
8.4 Statistical Analysis of Track Impact Parameters . . . 101
8.4.1 Analysis Method . . . 101
8.4.2 Performance of the Impact Parameter Analysis in CC Simulation . . . 102

9 Charm Fraction Extraction using Muons 103
9.1 Introduction . . . 103
9.2 Muon Selection . . . 104
9.2.1 Preselection of Muon Candidates . . . 105
9.2.2 Polar Angle . . . 107
9.2.3 Momentum . . . 108
9.2.4 Linking . . . 108
9.2.5 Track Length . . . 109
9.2.6 Complete Muon Selection . . . 110
9.3 Studies of Other Potential Muon Selection Quantities . . . 110
9.3.1 Isolation Criteria . . . 111
9.3.2 Calorimeter Information . . . 112
9.3.3 Distance of the Muon Track to the Event Vertex . . . 113
9.4 Remaining Background from Charged Pions and Kaons . . . 115
9.5 Background Muons from Non-CC Events . . . 116
9.5.1 Expectation for Muons from Non-CC Events . . . 116
9.5.2 Rejection of Muons from Non-CC Events . . . 117
9.6 Selected Muon Data Samples . . . 118
9.7 Charm Fraction Extraction using the Muon Charge Asymmetry . . . 120
9.7.1 Combined Positron Sample . . . 123
9.7.2 Combined Electron/Positron Sample . . . 123
9.8 Charm Fraction Extraction using a Charge-p_T Likelihood . . . 124
9.9 Systematic Errors of the Charm Fraction Extraction . . . 125
9.9.1 Muon Charge Reconstruction . . . 125
9.9.2 Muon Selection Efficiency and Branching Ratio . . . 126
9.9.3 Charge Asymmetries in the Simulation . . . 126
9.9.4 Background Subtraction of Muons from Non-CC Events . . . 127
9.9.5 Total Systematic Errors on the Charm Fractions . . . 127
9.10 Results . . . 128
9.10.1 Charm Fractions . . . 128
9.10.2 Cross Sections . . . 129

10 Conclusions **131**
10.1 Summary of the Results 131
10.2 Outlook 132

A Non-ep Background Finder Flags **135**

B Selected Muon Events **137**

List of Figures **143**

List of Tables **147**

Bibliography **149**

Danksagung **155**

Curriculum Vitae **157**

Chapter 1

Introduction

The understanding of the basic building blocks of matter and the interactions between them is one of the most fundamental questions addressed by philosophers and scientists for thousands of years. Ancient philosophers in Greece and in east Asia described all matter as being combinations of fundamental elements. Most of these theories featured as elements earth (solid states), water (liquid), air (gas), fire (plasma) and a fifth element sometimes called idea, void, quintessence or aether. The term "quintessence" (meaning the fifth element) is still used today for the essential point of an idea or a theory. Also the idea of atoms as basic building blocks of matter originates in ancient Greece. Around 400 BC the philosophers *Democritus* and *Leucippus* proposed indivisible particles called atoms (from the Greek "atomos", indivisible) as the fundamental building blocks of matter [1]. These atoms always existed and could not be created or destroyed, but they could be rearranged to form new types of matter. The macroscopic properties of matter were then determined by the types of atoms involved and the interactions between them. Since it was not possible at that time to test these ideas experimentally they did not get much attention for more than 2000 years.

The ideas of Democritus came to new life in the very beginning of the 19th century, when *John Dalton* tried to explain the so called *law of multiple proportions* (also called Dalton's Law) [2]. This law states that if two elements can combine with each other to form more than one compound, the weights of one element that combines with a fixed weight of the other are in a ratio of small whole numbers [3]. For example carbon (C) and oxygen (O) can form carbon monoxide (CO) or carbon dioxide (CO_2), where for a fixed amount of carbon the second process will take exactly twice as much oxygen as the first one. This can be seen as the first experimental evidence for atoms as building blocks of matter.

In 1909 *Ernest Rutherford* concluded from scattering experiments that atoms have a structure: A small, massive and positively charged nucleus orbited by negatively charged electrons [4]. With this experiment, physicists took over the study of the fundamental structure of matter from philosophers and chemists and the era of nuclear physics began. In the following decades big advances were made both in the experimental and theoretical understanding of atoms and their nuclei. It was found that atomic nuclei themselves have a structure and are made up of smaller particles, the positively charged protons and the neutral neutrons [5]. At the same time the theory of quantum mechanics was developed [6, 7], leading to a much better understanding of atoms and their constituents.

The transition from nuclear physics to particle physics in the quest for the fundamental constituents of matter occurred in the 1960s, when it was discovered that protons and neutrons themselves are built of even smaller particles, called *quarks* [8]. A few years later this substructure was confirmed by experiments [9, 10]. These discoveries together with further advances in experimental techniques and the formulation of quantum field theories led to the still valid *Standard Model of Particle Physics* [11].

According to the Standard Model, all matter is made from three groups of particles, called *families* or *generations*. Each of these families consists of two quarks, one charged lepton (electron-like particles) and one neutral lepton, called neutrino. While all these particles are fermions (particles

with half-integer spin), the interactions between them are mediated by bosons (particles with integer spin). The *electromagnetic interaction* is mediated by the neutral and massless photons. The *weak interaction* is mediated by the massive W and Z bosons, where the W boson carries electric charge and the Z boson is neutral. Therefore the exchange of photons and Z bosons is called *Neutral Current (NC)* and the exchange of W bosons is called *Charged Current (CC)*. The third fundamental interaction, the *strong interaction*, is mediated by gluons. Unlike the other force-mediating bosons the gluons can also interact among themselves. These different properties of the associated bosons lead to completely different properties of the electromagnetic, weak and strong interactions, even though they can all be described in the framework of quantum field theory.

Unfortunately the Standard Model does not contain all fundamental interactions. The fourth, *gravitation*, could not yet be formulated as a quantum field theory and is therefore missing in the Standard Model. For small masses gravitation is however much weaker than the other three interactions and can therefore be neglected for the study of fundamental particles.

While one can tell exactly how many protons, neutrons and electrons build a given atom, for the substructure of protons and neutrons this is not so clear. Due to the complicated properties of the strong interaction, protons are not static constructs with a fixed number of constituents, but rather dynamic systems where quarks and gluons are created and annihilated permanently[1]. To study these processes and the structure of protons, the HERA accelerator [12] and the experiments H1 [13, 14], ZEUS [15] and HERMES [16] have been built (see chapter 4).

In the work summarized in this thesis, the data of the H1 experiment has been used to study a specific contribution to the proton structure: The so called *strange quarks*. Understanding this contribution to the proton structure would mean another small step in the big quest for understanding what matter is made of, a quest started by ancient philosophers millennia ago.

This thesis is structured as follows: In the next chapter, a short introduction to the theoretical framework on which this study is based is given. The formalism and kinematics of electron-proton scattering are also introduced.

The current experimental understanding of the strange quark contribution to the proton is reviewed in chapter 3. Drawing on the example of neutrino-proton scattering, the use of charm production in charged current processes for the measurement of strange quarks in the proton, the subject of this thesis, is introduced.

In chapter 4, the experimental setup for the presented measurement is explained. The HERA accelerator and the H1 experiment are discussed with a special focus on subsystems relevant for this thesis.

In the age of fast, distributed computing, the simulation of scattering processes has become an essential tool of particle physics. It allows to develop and test measurement strategies, study the effects of various systematic errors on the results of a measurement and compare the results with theoretical models. The simulated event samples used for this analysis are presented in chapter 5.

The measurement of charged current processes from the selection of data periods to the calculation of cross sections is discussed in chapter 6.

The selected charged current event samples obtained in chapter 6 are then used to study charm production in charged current processes. An introduction to this subject is given in chapter 7. Different methods for the extraction of the charm fraction in charged current are then studied in the chapters 8 and 9.

Finally, the results of this thesis are summarized and discussed in chapter 10.

[1] In principle this is also true for atoms, where the vacuum polarization due to short-lived particle-antiparticle pairs has very small but detectable effects.

Chapter 2

Theory

2.1 Electron-Proton Scattering

2.1.1 Introduction to ep Scattering

Since the 1960s it is known that protons are not fundamental particles but rather complex constructs. The macroscopic properties of a proton are determined by its three *valence quarks*: Two up-quarks u and one down-quark d. The term valence quarks shows the analogy to atoms, where the macroscopic chemical properties are determined mainly by the valence electrons. These valence quarks in the proton interact permanently with each other via the exchange of *gluons*, the force carrier gauge bosons of the strong interaction. The gluons themselves can also interact among each other or produce short lived quark-antiquark pairs, the so called *sea quarks*. The strong force and the structure of the proton are described by the theory of *Quantum Chromodynamics* (see section 2.2.2), which still has many open questions. Therefore there is great interest in testing QCD by measuring the structure and dynamics inside the proton.

The reconstruction of a scattering process is much easier if the probing particle is pointlike and structureless. Furthermore for technical reasons the probing particles should be easy to produce in big amounts and have a long lifetime. Electrons fulfill all these criteria and are therefore ideal probes to study the proton structure.

Both quarks and electrons carry electromagnetic and weak charge, but unlike quarks, electrons do not carry strong charge. This means that while QCD is necessary to describe the structure of the scattering target, the ep scattering process itself is described by *electroweak theory* (see section 2.3). In the scattering process a virtual gauge boson is exchanged. In *neutral current (NC)* processes a photon γ or a Z boson is exchanged, in *charged current (CC)* processes a charged W^+ or W^- boson is exchanged. In NC reactions an electron is present in the final state (the scattered beam electron) while in CC reactions a neutrino appears in the final state. These basic scattering processes can be seen in fig. 2.1.

2.1.2 Kinematics in ep Scattering

In the following k and P denote the four-momenta of the electron and the proton in the initial state and $k^{'}$ and $P^{'}$ the four-momenta of the electron (or neutrino) and the proton (or proton remnant) in the final state. Schematically the ep scattering process can be written as

$$e(k) + p(P) \longrightarrow e(k^{'}) + X(P^{'}). \tag{2.1}$$

The *center of mass energy* $\sqrt{s}$ of the ep scattering process is related to the energies of the incoming electron and proton E_e and E_p with

$$s = (k + P)^2 \approx 4E_eE_p, \tag{2.2}$$

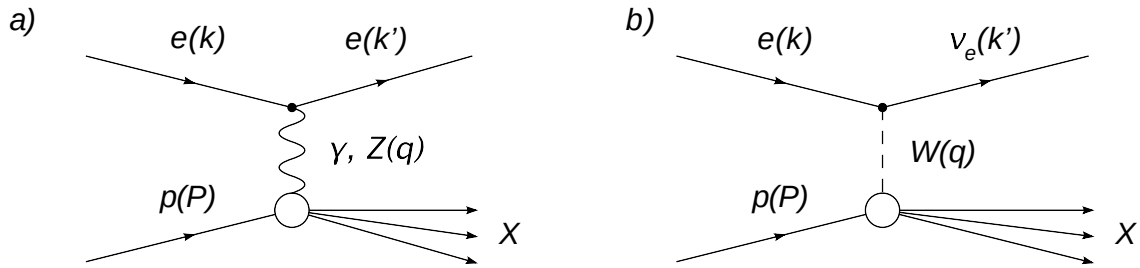

Figure 2.1: Lowest order graphs for ep scattering. a) Neutral current (NC) process with exchange of a photon or Z boson and the scattered electron in the final state. b) Charged current (CC) process with exchange of a W boson and a neutrino in the final state.

neglecting the particle masses. Therefore the center of mass energy is given by the accelerator and is fixed unless the beam energies are changed.

The four-momentum $q = k - k^{'}$ of the exchanged boson is equal to the four-momentum transfer at the electron vertex. Used for describing the scattering process is usually the Lorentz invariant and positive quantity

$$Q^2 = -q^2 = -(k - k^{'})^2, \tag{2.3}$$

which is called *virtuality* of the exchanged boson. Q^2 is an important characteristic of a scattering event. Because of their high mass in the propagator ($M_W \approx 80$ GeV/c^2 and $M_Z \approx 91$ GeV/c^2 [17]), W and Z exchange processes are suppressed with $Q^2/(Q^2 + M^2)$ relative to photon exchange [18]. This means that the contribution of W and Z boson exchange to the total ep scattering cross section depends on Q^2 and for $Q^2 \ll M^2$ ep scattering is mediated almost exclusively by photons. For $Q^2 \approx 0$ GeV^2 the exchanged photon is quasi-real. This regime is called *photoproduction*. For $Q^2 > 0$ GeV^2 the photon is virtual and the process belongs to the *Deep Inelastic Scattering* (DIS) regime. Furthermore Q^2 can be seen as a measure of the spatial resolution of the photon probing the proton: The wavelength λ of the virtual photon is proportional to $1/Q$ and the minimal size of the structures that can be resolved is of the order of λ.

The *inelasticity* y of the reaction is defined by

$$y = \frac{P \cdot q}{P \cdot k}. \tag{2.4}$$

In the proton rest frame the inelasticity is the fraction of the incoming electron energy carried by the exchange boson.

The *Bjørken scaling variable* x is defined as

$$x = \frac{Q^2}{2P \cdot q}. \tag{2.5}$$

Since the proton is not a fundamental particle, the exchange boson interacts with a constituent of the proton and not with the proton as a whole. In the Quark Parton Model (see section 2.2.1) the fraction of the proton momentum carried by this constituent is given by x.

A further quantity sometimes used for characterizing ep scattering processes is the *boson-proton center of mass energy* W (identical to the invariant mass of the hadronic final state), given by

$$W^2 = (q + P)^2. \tag{2.6}$$

All the discussed Lorentz invariant quantities can be used to characterize an event. They are however not independent and linked by the following relations (neglecting particle masses):

$$Q^2 = xys \tag{2.7}$$

$$W^2 = ys - Q^2. \tag{2.8}$$

Therefore for fixed center of mass energy $\sqrt{s}$ the event kinematics is fully determined by any combination of two of these quantities. In elastic scattering the additional condition $W = M$ (with M being the proton rest mass) applies and the event kinematics for the elastic case is even fully determined by any single quantity.

2.1.3 Elastic Scattering

In elastic scattering the particles in the initial and final state are the same, only their four-momentum (energy and momentum) change in the scattering process. The discussion of elastic scattering in this section follows [19]. The non-relativistic cross section for the scattering of electrons off atomic nuclei with charge Ze into the solid angle element $d\Omega$ is given by the *Rutherford cross section*

$$\left(\frac{d\sigma}{d\Omega}\right)_{Rutherford} = \frac{4Z^2\alpha^2(\hbar c)^2 E'^2}{|Qc|^4}. \tag{2.9}$$

Here E' denotes the energy of the scattered electron and Q^2 is the negative squared four-momentum transfer. The constants α, $\hbar$ and c are the coupling constant of the electromagnetic interaction, the Planck constant and the speed of light. The recoil of the nucleus has been neglected. For relativistic energies of the electron the spin effects have to be taken into account, resulting in the *Mott cross section* (for $v_e \approx c$)

$$\left(\frac{d\sigma}{d\Omega}\right)^*_{Mott} = \left(\frac{d\sigma}{d\Omega}\right)_{Rutherford} \cdot \cos^2\frac{\theta}{2}. \tag{2.10}$$

The asterisk indicates that the recoil of the nucleus has still been neglected and θ is the scattering angle. It has been found that experimental data is described by the Mott cross section only for $Q^2 \to 0$. For higher values of Q^2 the measured cross sections are systematically below the predictions. This can only be explained if the nucleus has a structure and is not pointlike. Q^2 is a measure of the spatial resolution (see section 2.1.2). For large values of Q^2 the probing photon does not see the whole charge of the nucleus anymore, but only a fraction. Therefore the cross section, which is proportional to the square of this charge, gets smaller for higher values of Q^2. This effect is parameterized in a *form factor* $F(Q^2)$, defined by

$$\left(\frac{d\sigma}{d\Omega}\right)_{exp.} = \left(\frac{d\sigma}{d\Omega}\right)^*_{Mott} \cdot \left|F\left(Q^2\right)\right|^2. \tag{2.11}$$

In the approximation of negligible recoil of the nucleus the form factor is simply the Fourier transform of the charge distribution $\rho\left(\overrightarrow{r}\right)$ of the nucleus:

$$F\left(Q^2\right) = \int e^{i\overrightarrow{q}\,\overrightarrow{r}/\hbar}\rho\left(\overrightarrow{r}\right)d\overrightarrow{r}. \tag{2.12}$$

Here $\overrightarrow{q}$ is the three-momentum transfer. The equations (2.11) and (2.12) have a very important implication: It is possible to get information on the structure of the target (or at least the distribution of the electromagnetic charge) by measuring the Q^2 dependence of the cross section in a scattering experiment.

For electron-proton or electron-neutron scattering (i.e. $Z = 1$) the recoil of the target cannot be neglected anymore. This introduces an additional factor E'/E in the cross section and it becomes

$$\left(\frac{d\sigma}{d\Omega}\right)_{Mott} = \left(\frac{d\sigma}{d\Omega}\right)^*_{Mott} \cdot \frac{E'}{E}. \tag{2.13}$$

Introducing also the spin of the nucleon (proton or neutron) and the interaction between the electron current and the magnetic moment of the nucleon, the cross section for electron-nucleon scattering is

given by the *Rosenbluth formula* [20]

$$\frac{d\sigma}{d\Omega} = \left(\frac{d\sigma}{d\Omega}\right)_{Mott} \cdot \left[\frac{G_E^2\left(Q^2\right) + \tau G_M^2\left(Q^2\right)}{1+\tau} + 2\tau G_M^2\left(Q^2\right)\tan^2\frac{\theta}{2}\right], \tag{2.14}$$

where $\tau = Q^2/4M^2$. $G_E^2\left(Q^2\right)$ and $G_M^2\left(Q^2\right)$ are the electric and magnetic form factors of the nucleon. In the limit $Q^2 \to 0$ the electric form factors must be equal to the electric charge of the respective nucleon (1 for protons, 0 for neutrons in units of the elementary charge e) and the magnetic form factors are equal to the magnetic moment of the nucleon (2.79 for protons, -1.91 for neutrons in units of the nuclear magneton μ_N). The shape of the form factors at higher values of Q^2 gives an interesting insight into the structure of the nucleons. Some experimental results from elastic scattering are discussed in section 3.2.

2.1.4 Deep Inelastic Scattering

Scattering processes in DIS are described by form factors as in elastic scattering, but in the inelastic case they are called *structure functions* F_1 and F_2. Unlike in elastic scattering the condition $W = M$ does not hold for DIS events. Therefore cross sections and structure functions depend on two parameters instead of one. Instead of the Rosenbluth formula (2.14) the differential cross section for the deep inelastic case becomes

$$\frac{d^2\sigma}{dxdQ^2} = \frac{2\pi\alpha^2}{xQ^4}\left[\left(1+(1-y)^2\right)F_2\left(x,Q^2\right) - y^2 F_L\left(x,Q^2\right)\right], \tag{2.15}$$

with the longitudinal structure function

$$F_L\left(x,Q^2\right) = F_2\left(x,Q^2\right) - 2xF_1\left(x,Q^2\right). \tag{2.16}$$

Again as in elastic scattering it is possible to determine the structure of the proton by measuring the ep scattering cross section. In the DIS case it is however more complicated since it is necessary to measure double differential cross sections instead of single differential ones and the structure functions depend on two parameters. The longitudinal structure function F_L is equal to zero in a simple Quark Parton Model (see section 2.2.1) and only appears at higher order in α_s, where gluon radiation takes place (see section 2.2.2). Therefore the contribution to the inclusive ep cross section from F_L is much smaller than from F_2 and is only relevant for $y \approx 1$. In most measurements of F_2 the contribution from F_L is neglected.

Some experimental results from DIS are discussed in section 3.3.

2.2 DIS in the Quark Parton Model and QCD

2.2.1 Quark Parton Model

By the end of the 1960s the framework of Quantum Electrodynamics (QED) was well established and the electromagnetic interactions between charged particles well known. But inelastic electron-proton scattering was still not understood because one question was still open: What is the probing electron actually scattering on? The proton is not fundamental and must have some structure. In the *Quark Parton Model* proposed by Feynman [21] in 1969 the proton consists of non-interacting pointlike constituents (*partons*). The partons have spin $\frac{1}{2}$ and carry a fraction x of the proton momentum. In this picture inelastic electron-proton scattering in fact can be seen as elastic electron-parton scattering as shown in fig. 2.2. Elastic scattering on a pointlike particle implies a constant structure function, i.e. $F_2\left(x,Q^2\right)$ should only depend on x, but not on Q^2 for high values of Q^2 (for low Q^2 this is not true since in this regime there is elastic scattering on the proton instead of the parton). This prediction is known as *Bjørken scaling* [22]. In [23] Bjørken and Paschos further refine the predictions and identify

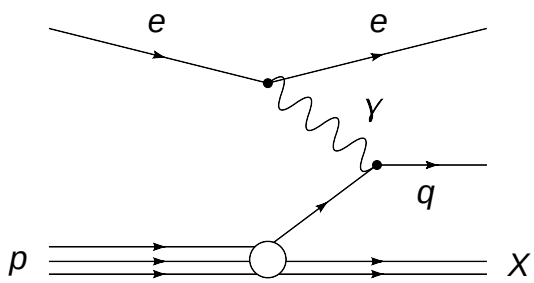

Figure 2.2: DIS Feynman graph according to the Quark Parton Model.

Feynman's partons with Gell-Mann's *quarks* [8]. The QPM gained credibility when Bjørken scaling was confirmed by experiments [9, 24].

The cross section for elastic scattering of an electron e and a quark q_i calculated in QED gives

$$\left(\frac{d^2\sigma}{dxdQ^2}\right)_{eq_i\to eq_i} = \frac{2\pi\alpha^2}{Q^4} e_i^2 \left(1+(1-y)^2\right)\delta(x-\xi), \tag{2.17}$$

where e_i is the charge of the quark and ξ is the fraction of the proton momentum carried by the struck quark. The δ-function shows the interpretation of x in the QPM as the proton momentum fraction taking part in the interaction. The *parton density functions* (PDF) $q_i(\xi)$ parameterize the probability to find a quark with type ("flavor") i and a proton momentum fraction ξ in the proton. Using these PDFs the inclusive cross section can be written as

$$\frac{d^2\sigma}{dxdQ^2} = \sum_i \int_0^1 d\xi q_i(\xi) \left(\frac{d^2\sigma}{dxdQ^2}\right)_{eq_i\to eq_i}. \tag{2.18}$$

Inserting (2.17) in (2.18) and comparing with (2.15) the structure functions in the QPM become

$$F_2\left(x,Q^2\right) = x\sum_i e_i^2 q_i(x) \tag{2.19}$$

$$F_L\left(x,Q^2\right) = 0. \tag{2.20}$$

These structure functions are independent of Q^2, Bjørken scaling is a direct consequence of the QPM. From (2.20) and (2.16) follows the *Callan-Gross relation* [25]

$$F_2(x) = 2xF_1(x). \tag{2.21}$$

The QPM has later been identified with the leading order (in α_s) approximation of Quantum Chromodynamics (see the next section).

2.2.2 Quantum Chromodynamics (QCD)

When experiments a few years later gained access to higher values of Q^2 and lower x, deviations from a perfect scaling behavior of the structure functions in DIS were observed [26]. These *scaling violations* could not be explained by the QPM. Furthermore it is not possible in the QPM to explain why there are never free quarks observed in the final state even though they appear quasi-free inside the proton in the scattering process itself. These problems are solved by the theory of *Quantum Chromodynamics* (QCD) [11]. In QCD a new fundamental force is introduced and described, the *strong force*, in addition to the already known gravitational, electromagnetic and weak forces. The strong force acts on a new kind of charge, the so called *color charge*, which can have six possible

values: Red, blue, green and their anticolors (sometimes denoted as cyan, magenta and yellow). The carriers of this charge are the quarks introduced already by Gell-Mann [8] and the QPM. A bound state of quarks as a whole is always colorless (i.e. rotationally invariant in color space SU(3)). As for the other fundamental forces there is also a force mediating boson for the strong force, the *gluon* (so called because it "glues together" the quarks in the nucleons).

The gluons themselves also carry color charge and can therefore interact with other gluons. For instance a gluon can split into a pair of gluons, a process not possible for photons in QED. This *gluon self-interaction* leads to a completely different behavior of the strong force compared to the electroweak interactions. While the electroweak coupling constant α increases with higher Q^2 (corresponding to short distances), the strong coupling constant α_s decreases. This is known as *asymptotic freedom* [27], [28] and explains why the quarks in the scattering process appear to be quasi-free. For low Q^2 and corresponding long distances α_s gets large, effectively binding quarks together. This is called *confinement* and also explains why no free quarks can be observed. The behavior of α_s as a function of Q^2 (called "running") can be written in leading order perturbation theory (pQCD) as

$$\alpha_s\left(Q^2\right) = \frac{12\pi}{(33 - 2N_f) \cdot \ln\left(Q^2/\Lambda_{QCD}^2\right)}. \tag{2.22}$$

Here N_f denotes the number of active quark flavors with mass $m_q^2 < Q^2$. The parameter Λ_{QCD} determines the scale at which α_s becomes large, so that perturbation theory is not applicable anymore. If α_s is measured at any scale Q^2 it can be determined at any other scale by using equation (2.22).

QCD also changed the picture of the proton. While in the QPM the three valence quarks are non-interacting, in QCD there is a permanent exchange of gluons between them. Besides the already mentioned self-interaction, gluons can also split into quark-antiquark pairs. These short-lived quarks and antiquarks are called *sea quarks*. The (simplified) picture of the proton in the QPM and in QCD is illustrated in fig. 2.3.

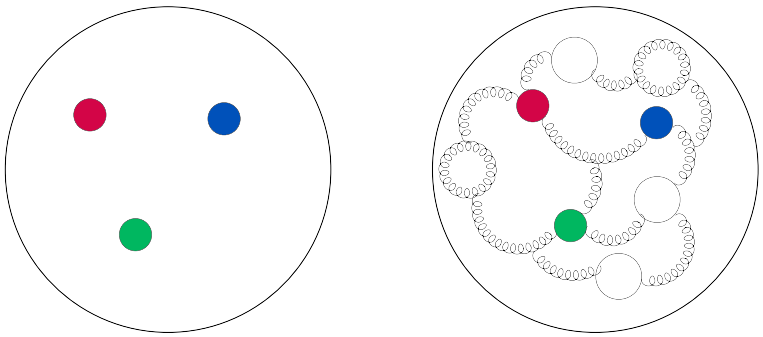

Figure 2.3: The proton structure in the QPM on the left side and in QCD on the right side. The colored balls are the valence quarks, the spiralling lines correspond to gluons and the solid lines to quarks and antiquarks in the sea.

2.3 Electroweak Processes: NC and CC Interactions

2.3.1 NC and CC Cross Sections

While QCD describes the dynamics inside the proton and therefore the target the electron is scattering on, the electron-proton scattering process itself proceeds via electroweak interactions described by QED. As already briefly explained in section 2.1.1, different types of interactions can occur. In the case of an electromagnetic process, the electron interacts with the quark via the exchange of a photon γ. Also possible are weak interactions with exchange of a neutral Z or a charged W boson. The properties of these different types of electroweak interactions are discussed in this section [18].

The exchange of a photon or a Z boson is called *neutral current* (NC). Its cross section is given by

$$\frac{d^2\sigma_{NC}^{e\pm p}}{dxdQ^2} = \frac{2\pi\alpha^2}{x}\left[\frac{1}{Q^2}\right]^2 \phi_{NC}^{e\pm p}, \tag{2.23}$$

with the reduced NC cross section

$$\phi_{NC}^{e\pm p} = Y_+ F_2^{\pm}\left(x,Q^2\right) - y^2 F_L^{\pm}\left(x,Q^2\right) \mp Y_- x F_3^{\pm}\left(x,Q^2\right). \tag{2.24}$$

The helicity dependence of the weak Z exchange is contained in $Y_\pm = 1 \pm (1-y)^2$. The longitudinal structure function F_L is only relevant at high y and low x and Q^2. In the kinematic range of this thesis, the contribution from F_L can therefore be neglected. The structure functions F_2 and F_3 contain terms from γ exchange, Z exchange and γZ interference. In the Quark Parton Model (see section 2.2.1) F_2 is given by

$$F_2 = \sum_i A_i^0\left(Q^2\right)\cdot\left(xq_i\left(x,Q^2\right) + x\bar{q}_i\left(x,Q^2\right)\right), \tag{2.25}$$

where for unpolarized lepton scattering

$$A_i^0\left(Q^2\right) = e_i^2 - 2e_i v_i v_e P_Z + \left(v_e^2 + a_e^2\right)\left(v_i^2 + a_i^2\right) P_Z^2. \tag{2.26}$$

Here v_i and a_i denote the NC electroweak vector and axial couplings of quark i and v_e and a_e the corresponding couplings of the electron, e_i is the quark charge. The first term in (2.26) contains the pure photon exchange and corresponds to equation (2.19). The term in P_Z contains the γZ interference and the term in P_Z^2 the pure Z exchange. Due to the large masses of the weak exchange bosons ($M_W \approx 80$ GeV and $M_Z \approx 91$ GeV [17]) compared to the massless photon, weak interactions are suppressed. The suppression of Z exchange relative to γ exchange is given by

$$P_Z^2 = \frac{Q^2}{Q^2 + M_Z^2}\frac{1}{\sin^2 2\theta_W}, \tag{2.27}$$

with the Weinberg angle θ_W. The structure function xF_3 is given by

$$xF_3 = \sum_i B_i^0\left(Q^2\right)\cdot\left(xq_i\left(x,Q^2\right) - x\bar{q}_i\left(x,Q^2\right)\right), \tag{2.28}$$

with

$$B_i^0\left(Q^2\right) = -2e_i a_i a_e P_Z + 4a_i v_i v_e a_e P_Z^2. \tag{2.29}$$

The structure function F_3, which does not contain pure photon exchange, violates parity. This feature of the weak interaction is explained in more detail below.

The exchange of a charged W boson is called *charged current* (CC). Since there is no charged exchange boson of the electromagnetic interaction, CC interactions are always weak processes. The CC cross section can be written in a similar way as the NC cross section with

$$\frac{d^2\sigma_{CC}^{e\pm p}}{dxdQ^2} = \frac{G_F^2}{2\pi x}\left[\frac{M_W^2}{Q^2 + M_W^2}\right]^2 \phi_{CC}^{e\pm p}, \tag{2.30}$$

where the reduced CC cross section is given by

$$\phi_{CC}^{e\pm p} = \frac{1}{2}\left[Y_+ W_2^{\pm}\left(x,Q^2\right) - y^2 W_L^{\pm}\left(x,Q^2\right) \mp Y_- x W_3^{\pm}\left(x,Q^2\right)\right]. \tag{2.31}$$

G_F is the Fermi coupling constant given by

$$G_F = \frac{\pi\alpha}{\sqrt{2}\sin^2\theta_W M_W^2}. \tag{2.32}$$

Since there are no contributions from electromagnetic interactions in CC, the structure functions are much simpler than in NC and can be written in the Quark Parton Model (where the longitudinal component W_L vanishes) as

$$W_2\left(x,Q^2\right) = \sum_i x\left(q_i(x,Q^2) + \bar{q}_i(x,Q^2)\right) \tag{2.33}$$

$$xW_3\left(x,Q^2\right) = \sum_i x\left(q_i(x,Q^2) - \bar{q}_i(x,Q^2)\right). \tag{2.34}$$

From (2.30) it can be seen that like Z exchange also W exchange is suppressed compared to γ exchange due to the W mass. Therefore electron-proton scattering is dominated by the electromagnetic γ exchange and the cross section for NC is much higher than for CC. Only for $Q^2 \gg M_Z^2 \approx M_W^2$, i.e. at high energies, the electromagnetic and weak interactions are of comparable strength. This *electroweak unification* at high energies can be seen in fig. 2.4.

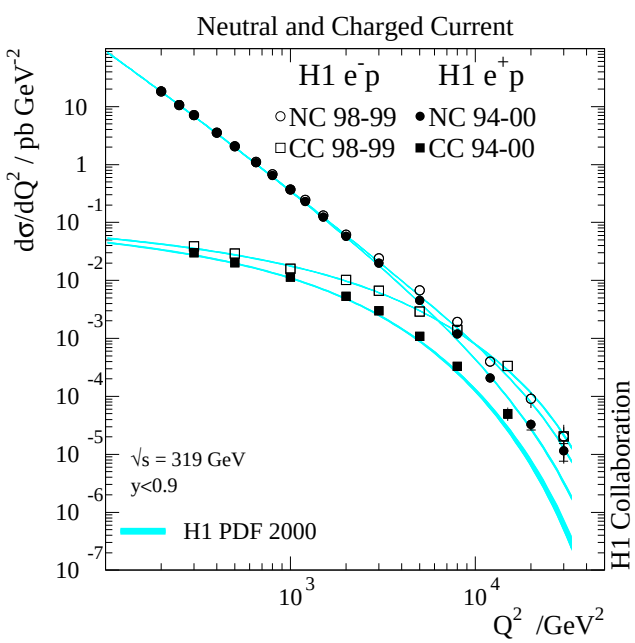

Figure 2.4: NC and CC cross sections in bins of Q^2 measured by the H1 Collaboration [29] in deep inelastic e^-p and e^+p scattering. At high values of Q^2 the NC and CC cross sections become comparable, demonstrating electroweak unification at high energies.

2.3.2 Parity Violation

An important feature of the weak interaction is the *violation of parity*, implied by the structure functions F_3 in equation (2.28) and W_3 in (2.34). Parity is often referred to as the mirror symmetry, transforming right-handed into left-handed states and vice versa, in analogy to a man standing in front of a mirror. Formulated in a more scientific way, the parity operation changes the *helicity* of a particle, given by

$$h = \frac{\vec{s} \cdot \vec{p}}{|\vec{s}| \cdot |\vec{p}|}. \tag{2.35}$$

Here $\vec{s}$ is the spin of a particle and $\vec{p}$ its momentum. Particles with $h = +1$ (spin parallel to momentum) are called right-handed and particles with $h = -1$ (spin antiparallel to momentum) left-handed. The electromagnetic and strong interactions conserve parity, i.e. they do not depend on the helicity of a particle. In 1957 Wu and collaborators discovered that the weak interaction behaves differently and indeed violates parity [30]. Massive particles always have a left-handed and a right-handed contribution, but massless particles such as the neutrino ν[1] can only be either fully left- or right-handed. Soon after the initial discovery of parity violation the famous Goldhaber experiment [32] showed that neutrinos are always left-handed. This result not only confirms maximal parity violation in weak interactions, it also indicates the $V - A$ type of the interaction (the vector contribution c_V and axial vector contribution c_A of the matrix element satisfy the relation $|c_V| = -|c_A|$). This means that the weak exchange bosons Z and W only couple to left-handed fermions and right-handed anti-fermions.

For DIS parity violation leads to a dependence of the cross sections on the *Polarization* P_e of the lepton beam, given by

$$P_e = \frac{N_R - N_L}{N_R + N_L}, \tag{2.36}$$

with N_R and N_L the number of right- and left-handed leptons in the beam. Since the weak exchange bosons only couple to left-handed electrons and right-handed positrons, the cross section will be higher for negatively polarized compared to positively polarized electron beams and for positively polarized compared to negatively polarized positron beams. This effect is much larger for CC than for NC, because NC is dominated by electromagnetic γ exchange while in CC there are only weak interactions. The polarization dependent cross section for CC contains an additional factor compared to (2.30) and becomes

$$\frac{d^2\sigma_{CC}^{e\pm p,polarized}}{dxdQ^2} = (1 \pm P_e)\frac{G_F^2}{2\pi x}\left[\frac{M_W^2}{Q^2 + M_W^2}\right]^2 \phi_{CC}^{e\pm p}. \tag{2.37}$$

This polarization dependence as a result of the parity violation in weak interactions can be seen in fig. 2.5.

[1] Neutrinos are massless in the Standard Model. In 2001 neutrino oscillations have been detected, indicating very small but not vanishing neutrino masses [31].

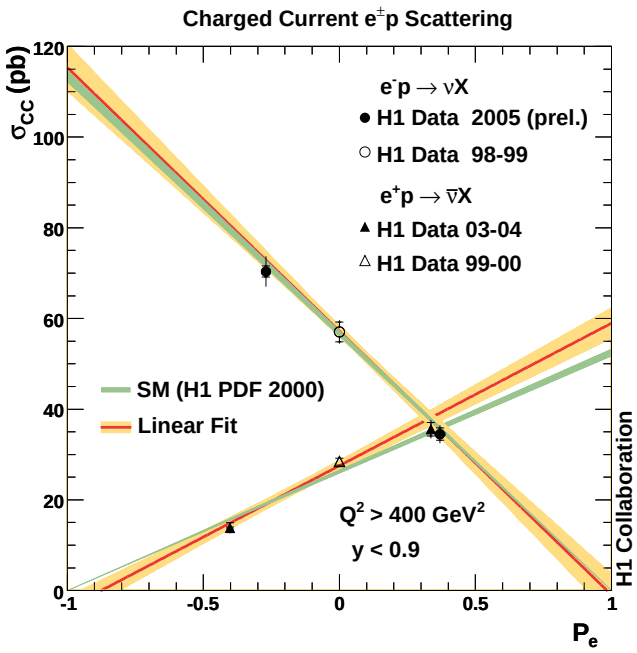

Figure 2.5: The polarization dependent CC cross sections measured by the H1 Collaboration [33]. The data is compared to the Standard Model prediction.

2.3.3 Electron-Proton vs. Positron-Proton Scattering

It is shown in fig. 2.5 that the total CC cross section for e^-p scattering is higher than for e^+p scattering at $P_e = 0$. The main reason for this is simple charge conservation: e^-p scattering is sensitive to the up valence quark density in the proton ($e^-u \to d\nu_e$ on parton level), while e^+p scattering is sensitive to the down valence quark density ($e^+d \to u\bar{\nu}_e$). Since the proton contains two up and only one down valence quark, this gives roughly a factor of two in the inclusive CC cross section. At high values of Q^2 the different x dependence of the up and down valence quark densities also leads to a different x dependence of the e^-p and e^+p CC cross sections.

Furthermore the angular dependence of the final state in the center-of-mass system is different in e^-p and e^+p scattering. As already mentioned above, the W boson only couples to left-handed fermions and right-handed anti-fermions. In the case of e^-p scattering, this means that the initial state consists of a left-handed electron and a left-handed quark, which results in an isotropic state with spin $J_z = 0$ in the center-of-mass (CM) system. The neutrino in the final state can be scattered in any direction with equal probability (the distribution of the polar angle θ of the neutrino is flat). In the case of e^+p scattering however, the initial state consists of a right-handed positron and a left-handed quark, which results in a $J_z = 1$ state in the CM system. Due to angular momentum conservation, the right-handed anti-neutrino in the final state cannot be back-scattered and a $(1 - \cos\theta)^2$ dependence on the polar angle is introduced. This is illustrated in fig. 2.6. This argument is reversed if a (right-handed) anti-quark in the proton sea takes part in the interaction instead of a (left-handed) quark. Since over a wide kinematical range the valence quarks are dominating CC interactions, the influence from anti-quarks is small.

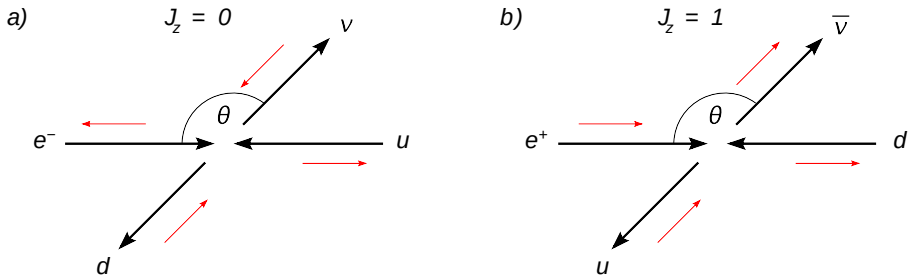

Figure 2.6: Angular momentum conservation in the center-of-mass system in CC interactions. The thin red lines correspond to the spin direction of the particles. The W boson only couples to left-handed fermions and right-handed anti-fermions. In a) a typical CC process for e^-p scattering is shown. The overall spin is zero. In b) a typical CC process for e^+p scattering is shown. The overall spin is one. The anti-neutrino cannot be back-scattered since this would violate angular momentum conservation. The anti-neutrino in this case has a $(1 - \cos\theta)^2$ dependence on the polar angle θ.

2.3.4 The CKM-Matrix

Unlike the electromagnetic and strong interactions, the weak interaction can transform one quark type (flavor) into another one. Due to charge conservation this is always the case for CC interactions. Flavor changing neutral currents (FCNC) with Z exchange have never been observed at tree level in the quark sector up to now. This changing of quark flavor under weak interactions can be explained when the weak eigenstates $d^{'}$, $s^{'}$ and $b^{'}$ are not equal to the mass eigenstates d, s and b, but rather mixings (rotations) of these states. This mixing is parameterized in the Cabibbo-Kobayashi-Maskawa (CKM) matrix. The elements of this matrix have to be measured experimentally and their current values are [17]

$$\begin{pmatrix} d^{'} \\ s^{'} \\ b^{'} \end{pmatrix} = \begin{pmatrix} V_{ud} & V_{us} & V_{ub} \\ V_{cd} & V_{cs} & V_{cb} \\ V_{td} & V_{ts} & V_{tb} \end{pmatrix} \begin{pmatrix} d \\ s \\ b \end{pmatrix} = \begin{pmatrix} 0.974 & 0.226 & 0.004 \\ 0.230 & 0.957 & 0.042 \\ \sim 0.007 & \sim 0.04 & \sim 1 \end{pmatrix} \begin{pmatrix} d \\ s \\ b \end{pmatrix} . \tag{2.38}$$

The probability for a transition of a quark with flavor i to a quark with flavor j in a weak interaction is proportional to the square of the corresponding matrix element $|V_{ij}|^2$. For example, a strange quark interacting with a W boson has a high probability of transforming into a charm quark ($V_{cs} = 0.957$), a much smaller probability of transforming into an up quark ($V_{us} = 0.226$) and will hardly ever transform into a top quark ($V_{ts} \approx 0.04$), even though this transformation also conserves charge.

The features of weak interactions play an important role in the subject of this thesis, the measurement of charm production in CC processes. The parity violating structure of the weak interaction mainly influences the inclusive CC cross sections by introducing a polarization dependence of the cross sections. This will be seen in chapter 6. The quark mixings parameterized in the CKM-matrix are important in understanding the production mechanisms of charm quarks in CC processes, as will be explained in chapter 7.

Chapter 3

The Strange Content of the Proton

3.1 Introduction

The valence quark content of all ordinary matter (matter built from atoms) is made up entirely of up and down quarks. So why are other quark flavors, such as strange quarks, important? As already explained in section 2.2.2, at high spatial resolutions (corresponding to high values of Q^2) the valence quarks of the nucleons (protons and neutrons) are not isolated anymore, but embedded in a sea of gluons and short-lived quark-antiquark pairs. In this sea all quark flavors are present, including strange quarks (heavy quarks are suppressed and only become important at high Q^2 and low x).

The interest in the strange sea was triggered with the *proton spin crisis* in 1988. The *European Muon Collaboration (EMC)* found that polarized proton-muon DIS data cannot be explained by the valence quark spin components alone and concluded, that *"the total quark spin constitutes a rather small fraction of the spin of the nucleon"* [34]. The interpretation of this experimental result started a fierce discussion among theorists. In this debate the EMC results were even taken as evidence against QCD and it was claimed that other theories such as Quark Geometrodynamics and Anisotropic Chromodynamics manage to describe the data better than QCD [35]. Reacting to these claims F. E. Close published a paper titled *"Polarized strange quarks in the proton and the validity of quantum chromodynamics"*, where he states that claims to overthrow QCD arise from an overestimation of the polarization of the strange sea [36].

Following this theoretical dispute about the EMC results and their interpretation, several experiments dedicated to the measurement of sea quarks, in particular strange quarks, in protons and neutrons have been done. In this chapter, the experimental results on the strange sea in the proton and the neutron are summarized.

3.2 Elastic Scattering

3.2.1 Formalism and Measured Quantities

In elastic scattering two types of quantities are usually measured: Form factors and helicity asymmetries of cross sections [37]. Form factors have already been introduced in section 2.1.3. Measured are the electric and magnetic form factors G_E and G_M as given in the Rosenbluth formula (2.14). The total form factors for the proton $G^p_{E,M}$ are composed of the different quark contributions in the proton with

$$G^{\gamma p}_{E,M} = \frac{2}{3}G^{p,u}_{E,M} - \frac{1}{3}G^{p,d}_{E,M} - \frac{1}{3}G^{p,s}_{E,M}. \tag{3.1}$$

An analogous relation is also valid for the neutron. Here it is assumed that contributions from heavier quarks can be neglected at the energies of elastic scattering experiments. The goal of these

measurements is to determine the strange quark form factors $G_{E,M}^{p,s}$. Usually charge symmetry between proton and neutron is assumed:

$$G_{E,M}^{p,u} = G_{E,M}^{n,d}; \qquad G_{E,M}^{p,d} = G_{E,M}^{n,u}; \qquad G_{E,M}^{p,s} = G_{E,M}^{n,s} = G_{E,M}^{s}. \tag{3.2}$$

Using these relations it is possible to gain information on the proton form factors by studying the neutron. But since there are no free neutron targets, information on neutrons has to be gained by scattering on deuterium or helium.

Even using the charge symmetry relations (3.2) it is not possible to disentangle the different contributions to the total proton and neutron structure functions without using additional information. This information is provided by the *parity violating asymmetry* A_{RL} of the cross sections for elastic electron-nucleon scattering, defined by

$$A_{RL} = \frac{\sigma_R - \sigma_L}{\sigma_R + \sigma_L}. \tag{3.3}$$

Here $\sigma_{R(L)}$ is the cross section for right- (left-) handed electrons. This asymmetry arises from the parity violating structure of the weak Z exchange (see section 2.3.2). Since the total elastic electron-nucleon scattering cross section is dominated by the helicity independent photon exchange, A_{RL} is very small (in the ppm range). Both γp and Zp scattering access the same flavor structure in the proton, but with different coupling constants. While the form factor for γp scattering is given by (3.1), for Zp scattering it can be written as

$$G_{E,M}^{Zp} = \left(\frac{1}{4} - \frac{2}{3}\sin^2\theta_W\right) G_{E,M}^{p,u} + \left(-\frac{1}{4} + \frac{1}{3}\sin^2\theta_W\right) \cdot \left[G_{E,M}^{p,d} + G_{E,M}^{s}\right], \tag{3.4}$$

where θ_W is the Weinberg angle. Using A_{RL} to determine the electromagnetic and weak contributions to elastic scattering, it is possible to measure individual quark contributions to the total proton form factor. For instance scattering off the ^{4}He nucleus is directly sensitive to G_E^s [37]. For this case, and neglecting radiative corrections, the asymmetry is given by

$$A_{RL}^{e\,^4\mathrm{He}} = A_0\tau\left(4\sin^2\theta_W + \frac{2G_E^s}{G_E^p + G_E^n}\right), \tag{3.5}$$

with $\tau = Q^2/4M_p$ and

$$A_0 = \frac{G_F M p^2}{\sqrt{2}\pi\alpha} = 316.7 \text{ ppm}. \tag{3.6}$$

3.2.2 HAPPEX

The HAPPEX experiments are located at the Thomas Jefferson National Accelerator Facility and are dedicated experiments to measure the strange contribution to the proton electric and magnetic form factors using elastic scattering of electrons on protons and ^{4}He. The first HAPPEX experiment took data in 1998 and 1999 at a scattering angle of 12.3° in the lab system and $Q^2 = 0.5$ GeV^2. The strange contribution was found to be $(G_E^s + 0.392G_M^s) = 0.025 \pm 0.020 \pm 0.014$, consistent with zero [38].

The second HAPPEX experiment (HAPPEX-II) took data in 2005 at a scattering angle of 6° in the lab system and $Q^2 \approx 0.1$ GeV^2. The results for the strange contributions to the proton were $G_E^s = 0.002 \pm 0.014 \pm 0.007$ and $(G_E^s + 0.09G_M^s) = 0.007 \pm 0.011 \pm 0.006$ [39], providing even stricter limits on the role of the strange quarks in the nucleon. This result is illustrated in fig. 3.1.

The next HAPPEX generation, denoted HAPPEX-III, is already approved and will take data in 2009 at $Q^2 = 0.62$ GeV^2.

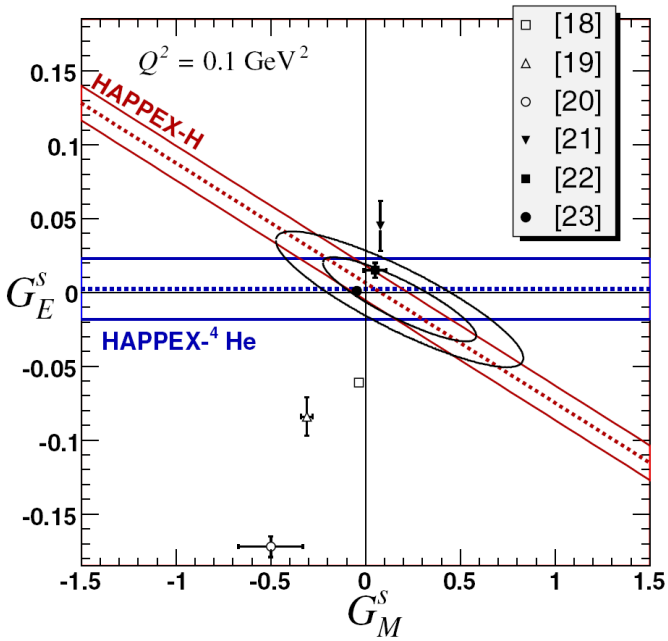

Figure 3.1: Measurement of the strange form factors by the HAPPEX collaboration [39]. The ellipses correspond to the 68 % and 95 % C.L. regions. For references to the individual measurements and predictions see the publication.

3.2.3 G0

Like the HAPPEX experiments, the G0 experiment is located at the Thomas Jefferson National Accelerator Facility and was taking data in 2004-2006. The main physics goal of the G0 experiment is to determine whether the strange form factors of nucleons are non-zero. Polarized electrons with an energy of 3 GeV were scattered on a 20 cm liquid hydrogen target. The recoiling elastic protons were also measured, allowing for simultaneous measurements in the range $0.12 < Q^2 < 1.0$ GeV^2. The G0 measurements indicate non-zero, Q^2 dependent G_E^s and G_M^s [40], as can be seen in fig. 3.2.

3.2.4 A4 and SAMPLE

The A4 experiment at MAMI (Mainzer Mikrotron) is taking data since the year 2000. A4 uses a polarized electron beam with energies from 315 MeV to 855 MeV and liquid hydrogen and deuterium targets. Measuring the strange form factors is one of the main physics goals. A measurement at $Q^2 = 0.1$ GeV^2 yields a parity violating asymmetry $A_{RL} = (-1.36 \pm 0.29 \pm 0.13) \cdot 10^{-6}$, corresponding to a positive strange contribution $G_E^s + 0.106 G_M^s$ at the 2σ significance level [41].

The SAMPLE experiment at the MIT-Bates Linear Accelerator Center took data in 1998 and 1999 and specifically focused on backward angle scattering at low energy, which isolates the magnetic structure of the nucleon. Therefore SAMPLE results mainly constrain G_M^s.

The constraints on the strange form factors from the A4 and SAMPLE experiments can be seen in fig. 3.3.

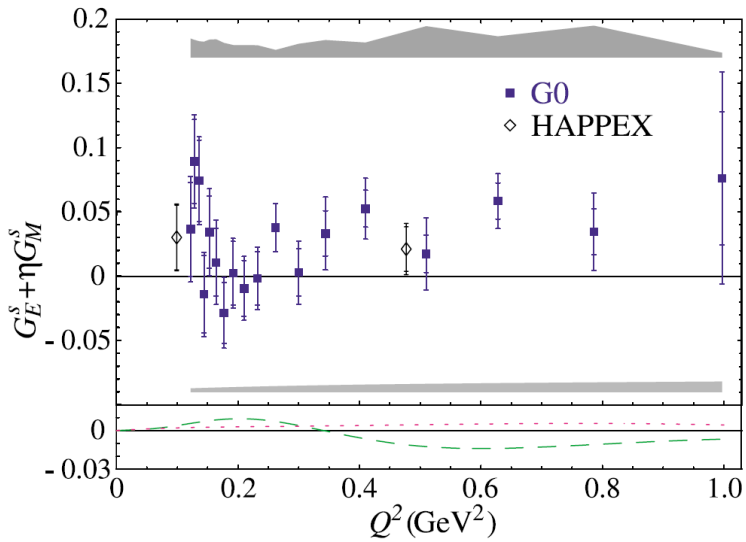

Figure 3.2: Measurement of the strange form factors by the G0 collaboration [40]. The grey bands indicate systematic uncertainties. The lines in the lower plot correspond to different models. For explanations of these models see the publication.

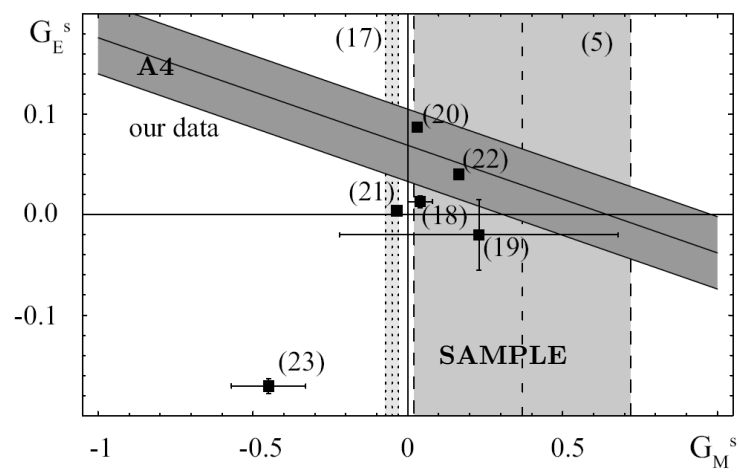

Figure 3.3: Measurement of the strange form factors by the A4 collaboration [41]. The solid lines correspond to the 1σ error band of A4, the dashed lines to the 1σ error band of SAMPLE. The dotted lines represent a lattice gauge theory calculation. The black squares represent different model predictions. For references see the publication.

3.3 Neutrino-Nucleon Deep Inelastic Scattering

3.3.1 Formalism

In neutrino-nucleon scattering the parameters κ and α are usually used to parameterize the strangeness contribution to the nucleon sea. The strangeness suppression factor κ is related to the overall strangeness content in the nucleon and is defined by

$$\kappa = \frac{\int_0^1 \left[xs\left(x, Q_0^2\right) + x\bar{s}\left(x, Q_0^2\right)\right] dx}{\int_0^1 \left[x\bar{u}\left(x, Q_0^2\right) + x\bar{d}\left(x, Q_0^2\right)\right] dx}. \tag{3.7}$$

Here $q\left(x, Q^2\right)$ (with $q = u, d, s$) are the PDFs introduced in section 2.2.1, x is the Bjørken scaling variable and Q_0 is a reference scale. The dependence of κ on the reference scale can be neglected within the kinematic range of a single experiment and is usually also neglected when comparing results from different neutrino DIS experiments. $\kappa = 0$ means a vanishing contribution of strange quarks to the nucleon sea, while $\kappa = 1$ implies a flavor symmetric sea with the same amount of up, down and strange quarks. The dependence of the strange sea on x is parameterized by α. It is defined relative to the shape of the non-strange sea by

$$xs\left(x, Q^2\right) = A_s(1-x)^\alpha \, \frac{x\bar{u}\left(x, Q^2\right) + x\bar{d}\left(x, Q^2\right)}{2}, \tag{3.8}$$

with $xs\left(x, Q^2\right) = x\bar{s}\left(x, Q^2\right)$. A value of $\alpha = 0$ implies that the strange and non-strange sea have the same x dependence. The normalization constant A_s can be computed numerically for given values of κ and α. A_s becomes identical to κ if $\alpha = 0$.

3.3.2 Dimuon Events

In neutrino DIS, strange quarks in the nucleon are usually accessed using *charm production in charged current*. In order to produce a charm quark in CC, a down or strange quark in the nucleon has to take part in the interaction. This is illustrated in fig. 3.4 for the case of a ν_μ beam, where a W^+ boson is exchanged. For a $\bar{\nu}_\mu$ beam a W^- boson is exchanged and a $\bar{c}$ quark produced. At high values of x, W^+ exchange processes are dominated by valence d quarks. At lower x there is a significant contribution from s quarks, since the CKM matrix element V_{cs} is about four times larger than V_{cd} (see equation (2.38) in section 2.3.4).

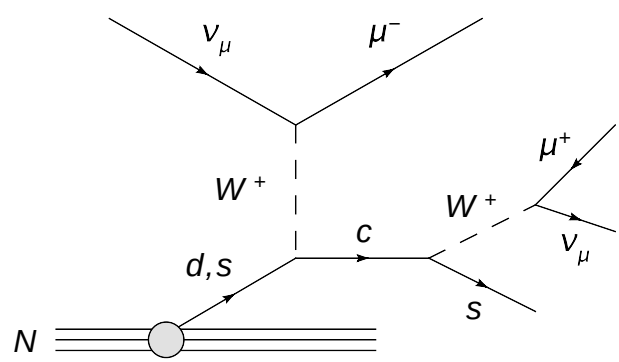

Figure 3.4: Feynman graph for charm production in charged current in neutrino DIS.

For the analysis of charm production in CC *dimuon events* are used, i.e. events where in addition to the primary muon produced directly in the CC process a second muon is produced from the decay of

the charmed particle. As can be seen in fig. 3.4, this muon and the primary muon must have opposite charge. This results in a very clear experimental signature which can be triggered and selected with high efficiency. A dimuon event in the CHARM II calorimeter can be seen in fig. 3.5.

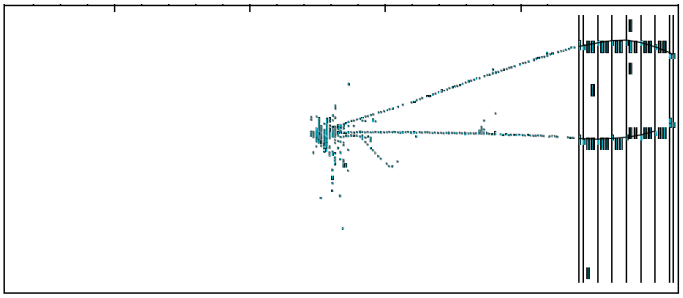

Figure 3.5: Dimuon event in the CHARM II calorimeter. Figure taken from [42].

3.3.3 CHARM II

The CHARM II experiment was located at CERN and used the wide band neutrino and antineutrino beams at the Super Proton Synchrotron (SPS). The CHARM II detector consisted of a massive, low-density target calorimeter followed by a toroidal iron muon spectrometer equipped with scintillator planes and drift chambers. The data was taken from 1986 to 1991.

4111 ν_μ and 871 $\bar{\nu}_\mu$ induced opposite sign dimuon events have been observed at $Q^2 > 5.5$ GeV^2. The strangeness suppression factor has been found to be $\kappa = 0.39 \pm 0.09$, indicating a significant contribution from strange quarks in the nucleon sea [42]. The quark mass m_c and the CKM matrix element $|V_{cd}|$ have also been constrained. The CHARM II results are summarized in table 3.1.

Table 3.1: CHARM II fit results of the free parameters for the dimuon cross section with statistical errors only [42]. m_c is the charm quark mass, B_μ denotes the branching ratio of charm hadrons into muons and ϵ is a free parameter describing the fragmentation of charm quarks using the Peterson fragmentation function [43].

$m_c\left(\mathrm{GeV}/c^2\right)$	κ	α	$B_\mu(\%)$	ϵ
$1.79^{+0.26}_{-0.28}$	$0.388^{+0.074}_{-0.061}$	$1.12^{+0.78}_{-0.72}$	$9.05^{+0.71}_{-0.69}$	$0.072^{+0.010}_{-0.009}$

3.3.4 NuTeV and CCFR

The NuTeV and CCFR experiments were located at Fermilab. CCFR took data from 1979 (then still called CCFRR) until 1988. The NuTeV collaboration used for their data taking in 1996 and 1997 to a large extent the same experimental setup for the detector, but a different neutrino beam line. The detector consisted of a 690 tons steel target calorimeter and an iron toroid muon spectrometer.

The collected samples of dimuon events contain 5102 ν_μ induced and 1458 $\bar{\nu}_\mu$ induced events for NuTeV and 5030 ν_μ induced and 1060 $\bar{\nu}_\mu$ induced events for CCFR. Parameters extracted from leading order (LO) fits to the data sets depend on the PDF set used in the fit [44]. In order to minimize model dependencies a fit to differential dimuon cross section tables has been performed for the NuTeV, CCFR and combined data sets. The results are summarized in table 3.2.

Table 3.2: Results of LO fits to dimuon cross section tables extracted from NuTeV, CCFR and combined data sets [44]. κ and α ($\bar{\kappa}$ and $\bar{\alpha}$) are the strangeness parameters obtained from ν_μ ($\bar{\nu}_\mu$) events.

Set	$m_c\left(\mathrm{GeV}/c^2\right)$	$B_\mu(\%)$	κ	$\bar{\kappa}$	α	$\bar{\alpha}$
NuTeV	1.30 ± 0.22	10.22 ± 1.11	0.38 ± 0.08	0.39 ± 0.06	-2.1 ± 1.0	-2.4 ± 0.5
CCFR	1.56 ± 0.24	12.08 ± 0.99	0.28 ± 0.05	0.33 ± 0.05	3.9 ± 1.2	3.3 ± 0.8
Combined	1.40 ± 0.16	11.00 ± 0.71	0.36 ± 0.05	0.38 ± 0.04	-1.1 ± 0.7	-2.1 ± 0.4

3.3.5 CHORUS and NOMAD

The CHORUS and NOMAD experiments were exposed to the CERN SPS wide band neutrino beam from 1994 to 1997 (NOMAD until 1998). The main physics motivation was to look for neutrino oscillations, but both experiments also published results on dimuon events. While NOMAD used an iron scintillator calorimeter as target for the dimuon study, CHORUS contained a nuclear emulsion target.

CHORUS has selected 8910 ν_μ and 430 $\bar{\nu}_\mu$ induced dimuon events. The strangeness parameters have been extracted using a four parameter maximum likelihood fit of the simulation to the data. The results are summarized in table 3.3. The parameter α has not been extracted.

The published NOMAD sample of dimuon events contains 2714 ν_μ and 115 $\bar{\nu}_\mu$ induced events. The results have been extracted using a χ^2 minimization procedure for each parameter. The NOMAD results are also listed in table 3.3.

Table 3.3: Results of fits of the simulation to the dimuon data obtained by the CHORUS and NOMAD collaborations [45, 46].

Set	$m_c\left(\mathrm{GeV}/c^2\right)$	$B_\mu(\%)$	κ
CHORUS	$1.26 \pm 0.16 \pm 0.09$	$9.6 \pm 0.4 \pm 0.8$	$0.33 \pm 0.05 \pm 0.05$
NOMAD	$1.3 \pm 0.3 \pm 0.3$	$9.5^{+0.7+1.4}_{-0.7-1.3}$	$0.48^{+0.09+0.17}_{-0.07-0.12}$

3.4 Measurements at HERA

Deep inelastic scattering of electrons off protons at high center of mass energies was only done at the accelerator HERA at DESY in Hamburg. For details on HERA see chapter 4. Here only the results obtained so far at HERA concerning the strange content of the proton will briefly be summarized.

3.4.1 HERMES

HERMES is a fixed target experiment where the electrons (or positrons) of the HERA lepton beam collide with a gas target. The data for the presented measurement was taken in the years $1996 - 2000$ (HERA I), therefore the experimental conditions will be discussed for this time period only. There were three main components of the HERMES experiment: The polarized lepton beam, the polarized gas target and the spectrometer. The polarization of the HERA lepton beam is described in more detail in chapter 4. The target used in $1996 - 1997$ contained polarized hydrogen and in $1998 - 2000$

polarized deuterium. The source of the polarized atoms was an atomic beam source based on the Stern-Gerlach effect. HERMES had a forward spectrometer with large acceptance which detected the scattered electron (positron) as well as hadrons in coincidence. The setup allowed a good tracking and particle identification. A schematic view of the spectrometer is shown in fig. 3.6. For more details on the HERMES experimental setup see [47].

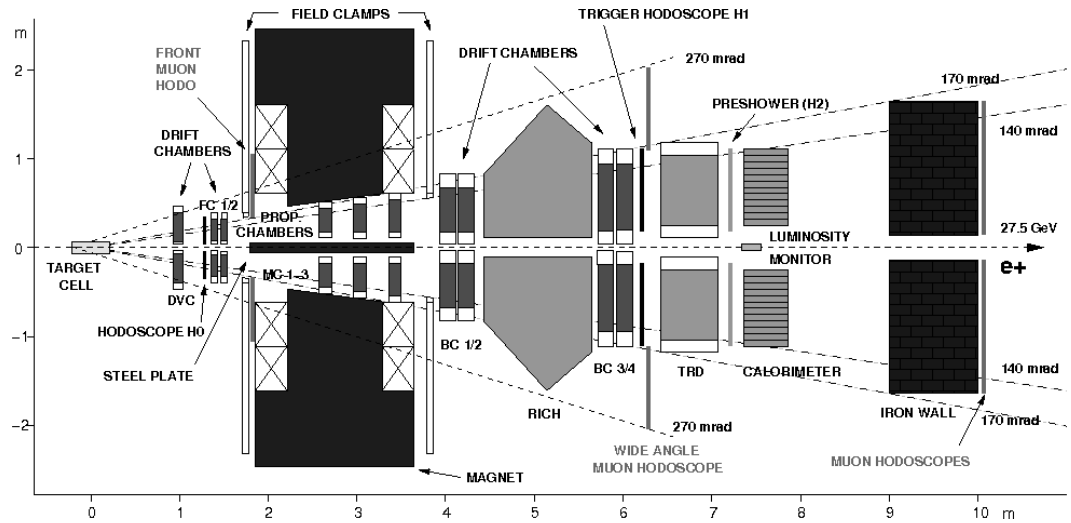

Figure 3.6: Schematic side view of the HERMES spectrometer in the configuration 1998 – 2000 [48].

HERMES measured helicity distributions $\Delta q(x, Q^2)$ separately for up, down and strange quarks in the nucleon [47]. The quark helicity distributions are defined by

$$\Delta q(x, Q^2) = q^+(x, Q^2) - q^-(x, Q^2), \tag{3.9}$$

where q^+ (q^-) are the number densities of quarks or antiquarks with their spins in the same (opposite) direction as the spin of the nucleon. For this analysis both information on the spin and the flavor of the struck quarks are needed. The helicity distribution can be accessed by measuring the polarization asymmetry of the cross section, defined by

$$A = \frac{\sigma_{1/2} - \sigma_{3/2}}{\sigma_{1/2} + \sigma_{3/2}}, \tag{3.10}$$

where $\sigma_{3/2\,(1/2)}$ is the cross section for photon spin (anti-) parallel to the nucleon spin. Information on the flavor of the struck quark can be gained by flavor tagging. In this method the leading particle (particle with highest momentum in the event) is identified and it is assumed that the struck quark is contained in this particle. For instance if the leading particle is a positively charged pion $\pi^+ = (u\bar{d})$, the struck quark was probably an u or $\bar{d}$ quark. In this case the struck quark will usually be a u quark, since the cross section is higher than for $\bar{d}$ quarks (charge) and it is more abundant in nucleons (valence quark). Struck u quarks result in leading π^+ in most cases, struck d quarks in leading π^- and struck s quarks in leading K^-. Therefore events with leading kaons give access to the strangeness content of the nucleon.

HERMES found the polarization of the up quark to be positive and of the down quark to be negative. All extracted sea quark polarizations are consistent with zero, including the strange quark polarization. The HERMES results on the quark helicity distributions can be seen in fig. 3.7. For more details see [47].

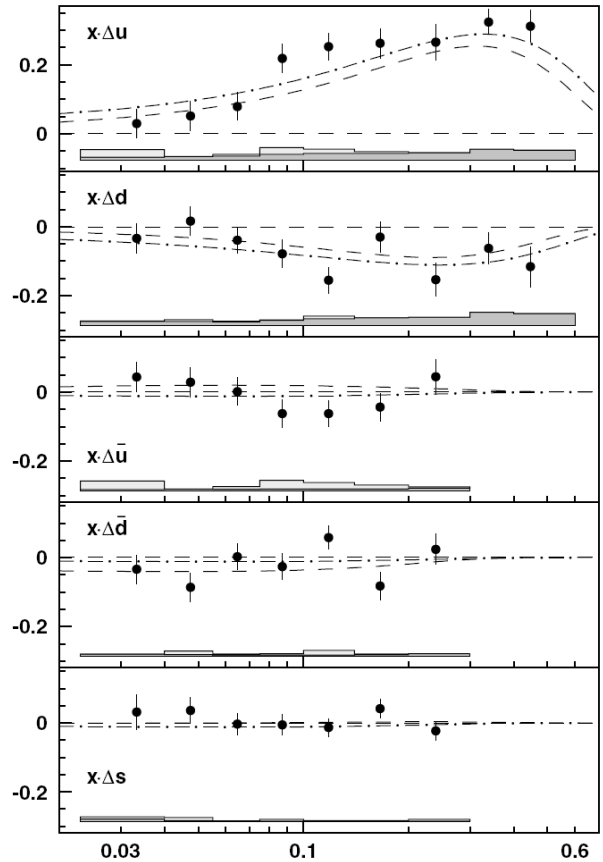

Figure 3.7: The quark helicity distributions $x\Delta q\left(x, Q_0^2\right)$ evaluated at $Q_0^2 = 2.5$ GeV^2 as a function of x, measured by the HERMES collaboration [47]. The error bars are statistical only. The grey bands show systematic uncertainties. The dashed and dash-dotted lines show different parameterizations. For details see the publication.

3.4.2 ZEUS

ZEUS is a multipurpose colliding beams experiment at the HERA accelerator facility. The data used for the measurement of the strange sea was taken in the years $1995-1997$ with a positron beam energy of 27.5 GeV and a proton beam energy of 820 GeV. The beams collided in the central region of the detector. This interaction point was surrounded by tracking detectors, the calorimeter and dedicated muon detectors. Due to the higher energy of the proton beam, the experimental setup is asymmetric in the direction of the beam. A schematic view of the ZEUS detector can be seen in fig. 3.8.

The ZEUS collaboration used $\phi(1020)$ mesons in order to access the strange sea in the proton [50]. The decay channel $\phi \to K^+K^-$ gives a clean signature in the detector and has therefore been used to reconstruct the ϕ mesons, which are almost pure $s\bar{s}$ states. The s or $\bar{s}$ quarks in the ϕ meson can originate from the strange sea, from boson-gluon fusion processes (BGF) or from hadronisation. It is possible to fit the shapes of the different contributions (taken from simulation) to measured differential cross sections in order to determine the relative contributions of these processes to the total cross section. This is shown in fig. 3.9. In particular it is in principle possible to extract the contribution of the strange sea using this method.

With the data sample considered in the publication, the sensitivity of this method to the strange sea contribution to the ϕ meson production cross section is not high enough to quantitatively measure

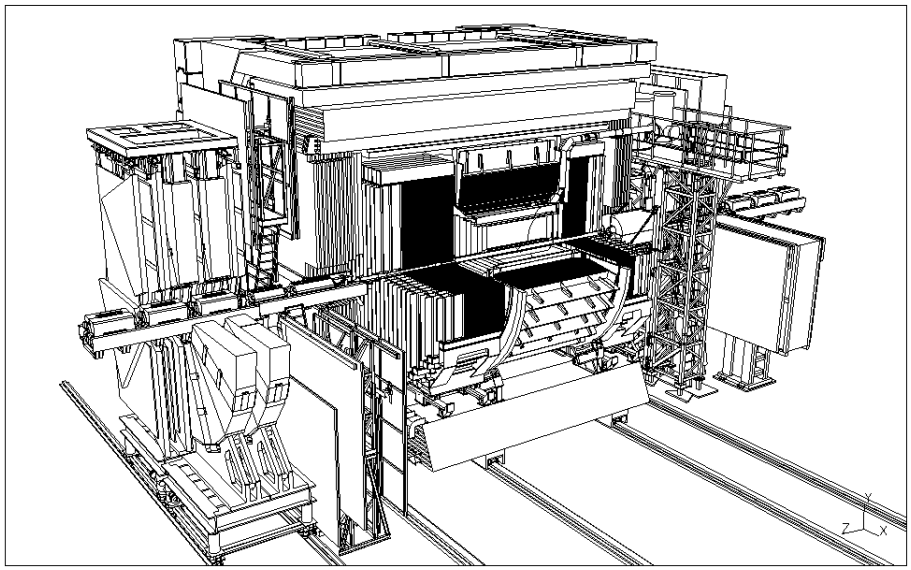

Figure 3.8: Schematic view of the ZEUS detector [49].

the strange content of the proton. The agreement of the measured ϕ meson production cross section with the simulation is however better with a contribution from processes involving the strange sea in the simulation. Therefore ZEUS claims this measurement to show the first direct evidence for the existence of the strange sea in the proton at low values of x.

3.4.3 H1

Like the ZEUS experiment, H1 is a large multipurpose colliding beams experiment using the beams of the HERA storage ring. The strange sea in the proton has not yet been measured with H1 data. In this thesis, the production of charm quarks in charged current processes using H1 data is studied. Similar to dimuon events in neutrino-nucleon DIS, this process allows to access the strange quarks in the proton.

3.5 Putting the Picture Together

The most stringent constraints of the strange sea in the proton are set by neutrino-nucleon DIS experiments. The results obtained by these experiments are summarized in table 3.4 [51]. The suppression factor κ, defined by equation (3.7), is well constrained to $0.3 \lesssim \kappa \lesssim 0.6$. This implies strangeness in the proton sea, but it is suppressed compared to the u and d sea. The parameter α, defined by equation (3.8) and describing the shape in x of the strange sea, is much less constrained. The only next-to-leading order (NLO) analysis performed gets a value of α consistent with zero, which implies that the strange sea has the same x dependence as the up and down sea.

Results from neutrino-nucleon and electron-nucleon DIS have been combined in [52]. A combined NLO analysis of various data sets has been performed and the PDFs of the proton have been extracted. The resulting PDFs can be seen in fig. 3.10. The strange PDF clearly is not zero, but smaller and less constrained by the fit than the up and down PDFs. The strange asymmetry $s\left(x, Q_0^2\right) - \bar{s}\left(x, Q_0^2\right)$ at $Q_0^2 = 20$ GeV^2 is found to be very small, consistent with zero. Concluding it is stated, that "the strange and antistrange densities are still the least known PDFs" [52].

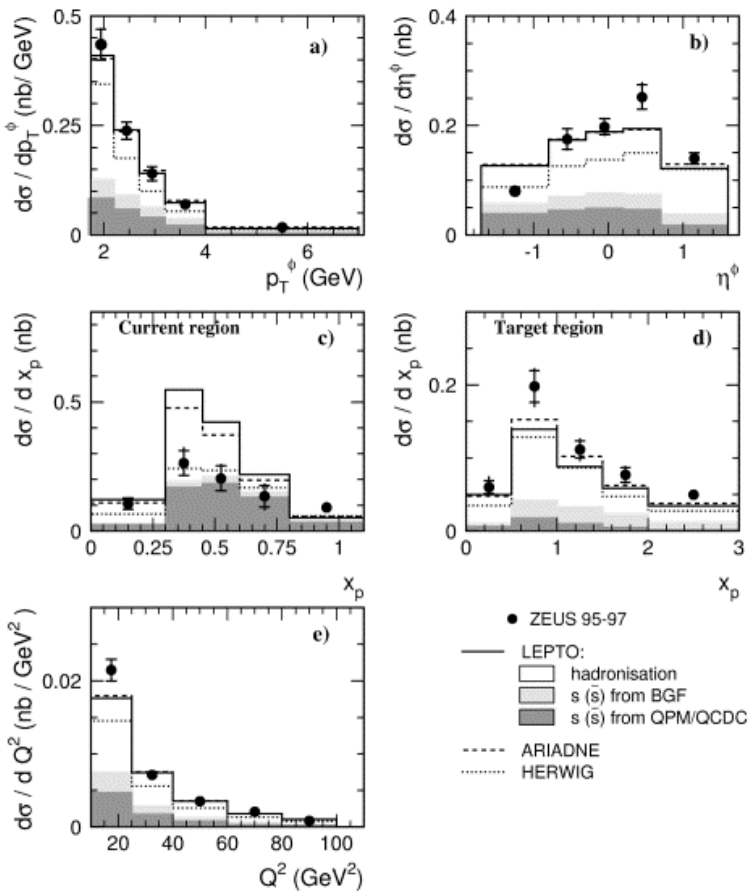

Figure 3.9: Differential ϕ meson cross sections measured by ZEUS [50] as a function of (a) p_T^ϕ, (b) η^ϕ, (c) and (d) x_p and (e) Q^2, compared to predictions by LEPTO, ARIADNE and HERWIG. The data is also compared to contributions in LEPTO from ϕ mesons produced with quarks from the strange sea (dark shaded area), from BGF (light shaded area) and from hadronisation only (unshaded area). For details see the publication.

Table 3.4: Summary of neutrino DIS results on the strange sea, taken from [51]. For references to the individual measurements see the publication.

Set	κ	α
LO CCFR	$0.373^{+0.048}_{-0.041} \pm 0.018$	$2.50^{+0.60\ +0.36}_{-0.55\ -0.25}$
NLO CCFR	$0.477^{+0.046\ 0.023}_{-0.044\ -0.024}$	$-0.02^{+0.60\ +0.28}_{-0.54\ -0.26}$
LO NuTeV	$0.32 \pm 0.06 \pm 0.04$	$-1.10 \pm 1.05 \pm 0.59$
LO NuTeV and CCFR	0.36 ± 0.05	-1.12 ± 0.73
LO CHORUS	$0.56 \pm 0.05 \pm 0.045$	
LO CDHS	$0.47 \pm 0.08 \pm 0.05$	
LO NOMAD	$0.48^{+0.09\ +0.17}_{-0.07\ -0.12}$	
LO CHARM II	$0.39^{+0.07}_{-0.06} \pm 0.07$	

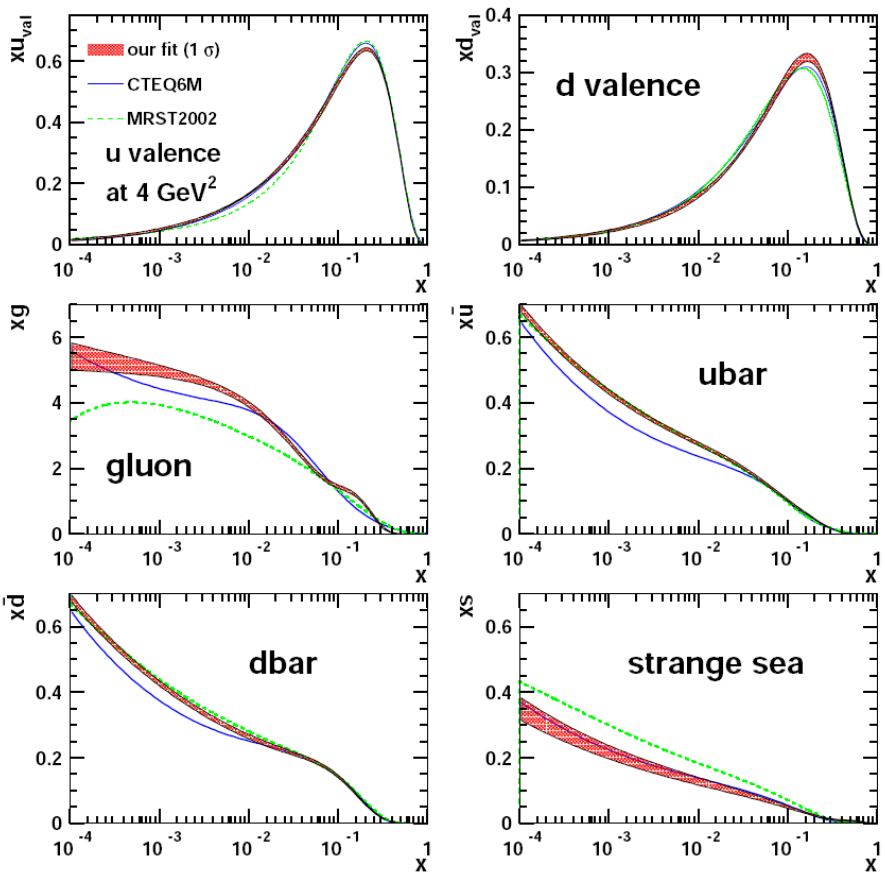

Figure 3.10: The proton parton distribution functions obtained in a combined analysis of various data sets [52]. The red shaded areas correspond to 1σ error bands of the fit, the solid and dashed lines are predictions. For details and references to the individual data sets see the publication.

Chapter 4

The H1 Experiment at HERA

4.1 The HERA Accelerator

The HERA (Hadron Elektron Ring Anlage [12]) collider at DESY in Hamburg was the only machine world-wide colliding electrons or positrons (in the following summarized as "leptons") with protons at high energies. First collisions were achieved in 1992 and operation stopped in 2007. Apart from several smaller preaccelerators, HERA contained two main accelerators in a common ring tunnel with 6.3 km circumference. The lepton machine stored and accelerated the leptons to energies of 27.6 GeV (27.5 GeV until the year 2000). Charged particles lose energy due to *synchrotron radiation* when they are forced on a circular path. The amount of energy lost ΔE by a relativistic particle with mass m and $v \approx c$ in a single revolution in the ring is given by

$$\Delta E = \frac{4\pi\alpha\hbar c}{3r}\gamma^4 = \frac{4\pi\alpha\hbar c}{3r}\left(\frac{E}{mc^2}\right)^4 . \tag{4.1}$$

Here r is the radius of the storage ring. The energy lost due to synchrotron radiation is proportional to the fourth power of the particle energy. Therefore the maximal achievable energy of the beam leptons for the given HERA ring radius was limited by synchrotron radiation and accelerating the beam particles to their final energy was the main technical challenge for the lepton machine. The other main accelerator, the proton machine, stored and accelerated protons to energies of 920 GeV[1]. Because of their higher mass, energy loss due to synchrotron radiation is not an issue for protons (the energy loss is proportional to $1/m^4$, see (4.1)). Instead the main technical challenge for the proton machine (and limiting the maximal achievable energy of the protons) was to keep the beam centered inside the accelerator ring. This was achieved using superconducting magnets. Because of the combined challenges of the lepton and proton machine, HERA was one of the most complex colliders ever built. A schematic view of HERA is shown in fig. 4.1.

The experiments were located in the center of the four straight sections of HERA. The counter-rotating beams were brought into collision at two places in the ring, called interaction points H1 and H2. The collision rate at the interaction points was 10.4 MHz, i.e. every 96 ns two particle bunches crossed each other. The interaction point H1 gave the name for one of the two big multi-purpose experiments [13, 14], while the other one, located at H2, is called ZEUS [15]. These two experiments have been designed to cover a similar and very broad spectrum of measurements. Therefore also their technical design is similar. Differences in the experimental setup are due to the fact that H1 has been optimized for the measurement of neutral current processes and ZEUS for charged current processes. The design of H1 will be discussed in more detail in the following sections. The other two straight sections of HERA were equipped with fixed target experiments, HERMES [16] and HERA-B [54]. In HERMES a polarized gas target was brought into the HERA lepton beam in order to study the spin

[1] Running periods with proton beam energies of 460, 575 and 820 GeV are not considered in this thesis.

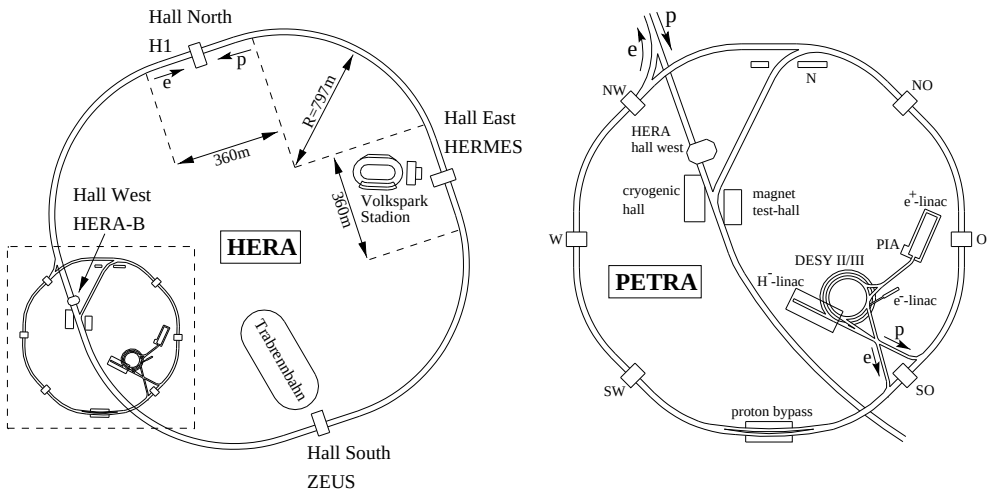

Figure 4.1: Schematic drawing of the HERA collider [53]. On the right hand side a more detailed view of the preaccelerators is shown.

structure of nucleons and measure various polarization asymmetries in inclusive and semi-inclusive DIS processes. Exclusive processes such as deeply virtual Compton scattering have also been measured. The HERA-B experiment used the HERA proton beam and up to eight fixed wire targets. Its main goal was to measure CP violation in the B system. HERA-B stopped operation in 2003.

While the performance of a collider depends on many parameters, for the physics program at a collider mainly two parameters are important (apart from the type of the beam particles): The center-of-mass energy $\sqrt{s}$ and the instantaneous luminosity $\mathcal{L}$. The center-of-mass energy is determined by the beam energies (see section 2.1.2) and was $\sqrt{s} = 319$ GeV at HERA. The instantaneous luminosity $\mathcal{L}$ is a measure for the number of reactions in a given time. For a collider experiment with equal beam sizes it is given by

$$\mathcal{L} = fn\frac{N_1 N_2}{4\pi\sigma_x\sigma_y}. \tag{4.2}$$

Here f is the frequency of revolution for particles in the ring, n is the number of (colliding) bunches, N_1 and N_2 are the number of particles per bunch for the two beams and σ_x and σ_y denote the beam size transverse to the beam direction. This machine parameter together with the cross section σ_p of a process P, which contains the physics model of the process, determines the expected rate of events (number N_P of events per time) for the process P with

$$\frac{dN_P}{dt} = \sigma_p\mathcal{L}. \tag{4.3}$$

Relevant for any physics analysis is the total number of events rather than the rate of events. Using the integrated luminosity $L = \int \mathcal{L}dt$, the total number of events N_P is given by

$$N_P = \sigma_p L. \tag{4.4}$$

In the years 2000 to 2002 the HERA accelerator and the experiments underwent a luminosity upgrade. Superconducting final focussing magnets were installed close to the interaction points within H1 and ZEUS. As can be seen from equation (4.2), smaller beam sizes result in higher instantaneous luminosity. As a consequence of the new final focussing magnets, the interaction region in the experiments had to be redesigned and the circular geometry of the beam pipe and the vertex detectors was replaced by an elliptical geometry. This extended shutdown was also used to do various upgrades on other subsystems of the experiments. The time period before the upgrade is referred to as HERA I,

while the operation after the upgrade is called HERA II. The total integrated luminosity collected by the H1 experiment can be seen in fig. 4.2. The luminosity upgrade reflects in the steeper slope of the integrated luminosity in HERA II.

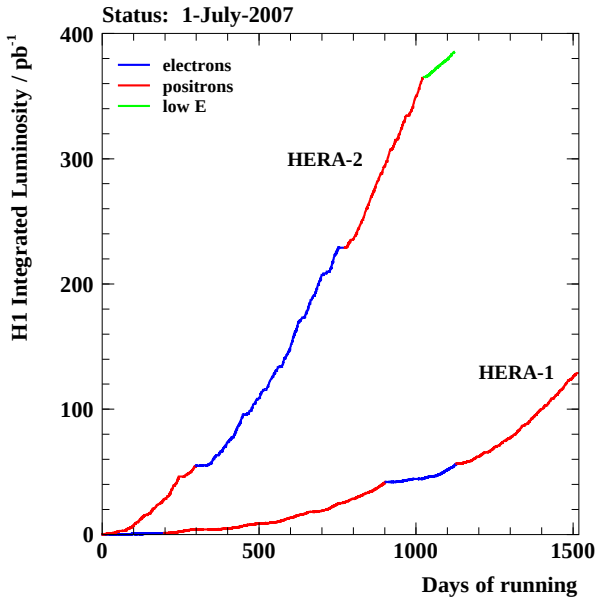

Figure 4.2: The total integrated luminosity L collected by the H1 experiment [53].

Particles in a storage ring become spin polarized in the direction transverse to the plane of the ring through emission of synchrotron radiation. This effect is known as *Sokolov-Ternov effect* [55]. Since electrons and positrons produce much more synchrotron radiation than protons, this polarization only becomes relevant for the lepton beam at HERA. The Sokolov-Ternov effect for a single revolution in the ring is small, but since the particles are stored in HERA for several hours a significant polarization P of the lepton beam can build up, with

$$P(t) = P_{max}\left(1 - e^{-t/\tau}\right). \tag{4.5}$$

The theoretical maximum for the polarization is $P_{max} \approx 0.93$ (not taking into account any depolarizing effects). The build-up time τ depends on the radius of the storage ring and the particle energy, at HERA $\tau \approx 40$ min. Due to depolarizing effects such as beam-beam interactions, the maximal achieved polarization at HERA is about 60 % with time constants of $\tau \approx 20$ - 24 min. The measured polarization in the course of two typical luminosity fills at HERA is shown in fig. 4.3.

The polarization of the lepton beam can be used to measure parity violation in weak processes (see section 2.3.2). For such measurements the polarization needs to be longitudinal (in the direction of the beam) rather than transverse. Therefore the spin of the leptons has to be rotated before the beam enters the experiments and rotated back after the experiments before entering the first bending magnets. This is illustrated in fig. 4.4. The rotation of the lepton spin is achieved with *spin rotators* [57], a complicated set of magnets. It is also possible to choose the helicity of the leptons (the direction in which the spin is rotated) by changing the configuration of the spin rotators. Around the HERMES experiment spin rotators were already installed for HERA I, around H1 and ZEUS only for HERA II.

The polarization of the lepton beam was measured by two independent devices: The longitudinal polarimeter LPOL [58] between the spin rotators close to the HERMES experiment and the transverse

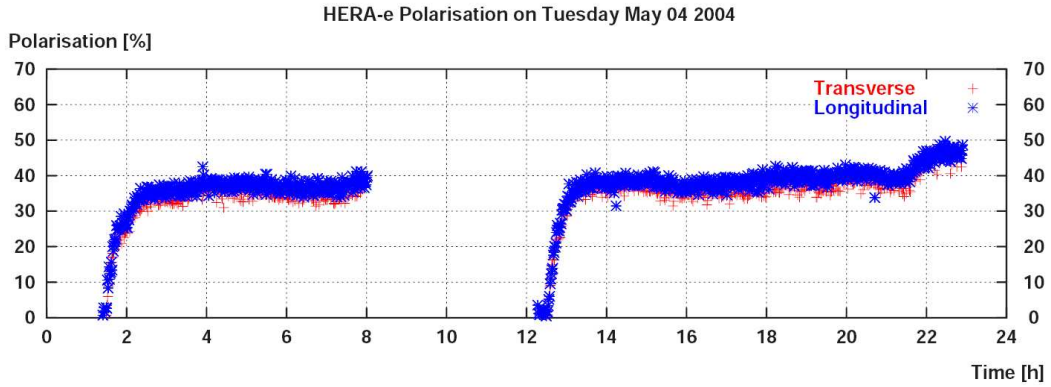

Figure 4.3: Polarization measured by the longitudinal (blue) and transverse (red) polarimeters in the course of two typical luminosity fills at HERA. Figure taken from [56].

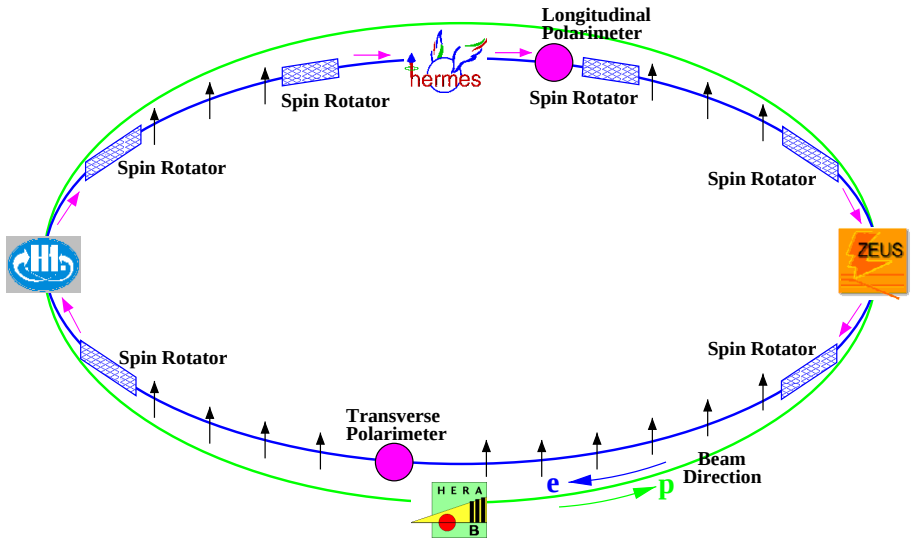

Figure 4.4: Schematic view of the lepton beam polarization at HERA [48].

polarimeter TPOL [59] close to the HERA-B experiment. Assuming fully efficient spin rotators, the values measured by the two polarimeters should be equal within errors. The LPOL measurements are based on the energy asymmetry of the Compton back-scattering cross section of a circularly polarized laser beam off the longitudinally polarized lepton beam. The LPOL operates in multi-photon mode, due to the intense laser beam there are always several photons scattered for every laser-lepton interaction and their total combined energy is measured in a calorimeter. The TPOL follows a similar strategy: Circularly polarized laser light is Compton back-scattered from the transverse polarized lepton beam and measured in a very sensitive calorimeter. The helicity of the laser is flipped with a frequency of 90 Hz. The measured up-down asymmetry relative to the accelerator plane is proportional to the lepton beam polarization. The TPOL operates in single-photon mode: The energy and position of each scattered photon is measured separately in the calorimeter.

4.2 Overview of the H1 Detector

The H1 experiment [13, 14] is in many respects a typical high energy physics multi-purpose collider experiment, with the exception of its asymmetric design along the beam axis due to the different beam energies at HERA. The H1 detector consists of many subdetectors with different tasks, arranged in several layers around the beam axis. The innermost layer contains the tracking system. These subdetectors allow a precise measurement of tracks, i.e. position and momentum of charged particles produced in the interaction. The next layer is constituted by calorimeters, which provide a precise energy measurement by absorbing most of the particles. Surrounding the calorimeters in the central region, the H1 solenoid magnet coil produces a strong magnetic field of 1.2 T in order to allow momentum and charge measurements in the tracking system. The outermost part of the detector is the iron return yoke of the magnet, which is also instrumented for the measurement of muons. A schematic view of the H1 detector with its main components can be seen in fig. 4.5. In the following the individual parts of the H1 detector are discussed in more detail with a special focus on parts relevant for this thesis.

The H1 coordinate system has the nominal interaction point as origin. The x axis points horizontally to the center of the HERA ring, the y axis upwards and the z axis along the proton beam direction. Usually a cylindrical system is used, where the x and y coordinates are replaced by the polar angle θ, defined as angle to the positive z axis, and the azimuthal angle ϕ, defined as angle to the positive x axis. Instead of θ also the pseudorapidity η can be used with $\eta = -\ln[\tan(\theta/2)]$.

4.3 Tracking System

The task of the tracking system is to provide precise measurements of particle tracks. Only charged particles leave tracks, neutral particles cannot be detected in the tracking system and have to be identified in the calorimeters. A precisely measured track allows to determine or at least constrain several important properties of the corresponding particle:

- Charged particles are deflected in the strong magnetic solenoid field in H1. It is possible to determine the *particle momentum* from the radius of the corresponding track curvature.
- From the direction of the deflection in the magnetic field the sign of the *particle charge* can be determined.
- By extrapolating the measured track back to the beam line the *point of origin* (production) of the corresponding particle can be constrained. It is for instance possible to determine whether the particle has been produced at the primary vertex or at a secondary vertex (if the distance from the primary vertex is large enough, see section 4.3.2).
- By extrapolating the track back to the assumed point of origin the *flight direction* of the corresponding particle at the production vertex is determined.
- From the signal amplitude in the tracking chambers the specific energy loss (energy loss per track length dE/dx) can be determined. This allows *particle identification* if the track momentum is not too high ($p \lesssim 1$ GeV).

Furthermore, the number of charged particles (track multiplicity) and their spatial distribution provide important information on the primary interaction.

Since the energy measurement in the calorimeters should not be influenced by the tracking system, the energy loss of particles traversing the tracking system should be as small as possible. In combination with the required high spatial resolution this poses a major challenge to the design and construction of tracking devices. Today mainly two types of devices are used: Gas chambers and silicon detectors. Both types were used in H1 and described in more detail in the following sections.

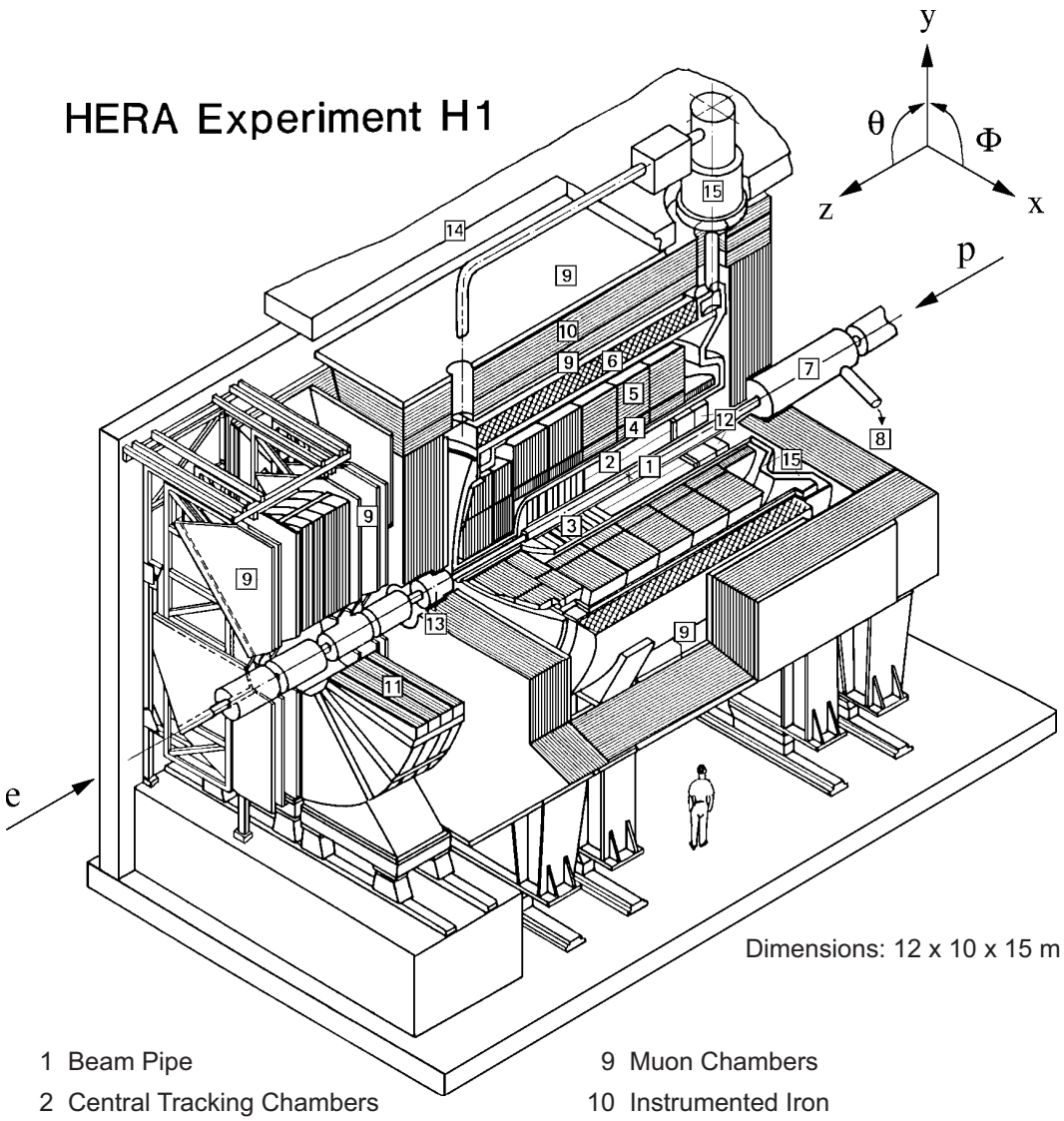

Figure 4.5: Schematic view of the H1 detector with its main components. The H1 reference frame is also shown.

4.3.1 Tracking Chambers

The central tracking system of H1 consisted of several subdetectors with different properties and tasks. A radial view of the setup is shown in fig. 4.6.

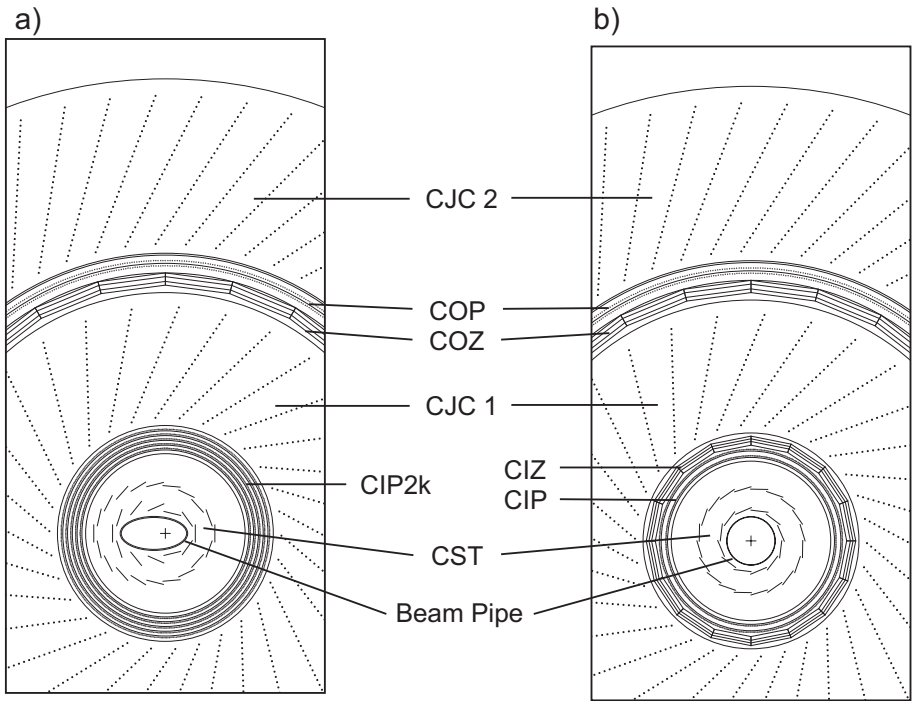

Figure 4.6: Schematic view of the H1 central tracking system in a) the HERA II and b) the HERA I configuration. The main differences between the setup for HERA I and HERA II are explained in the text.

The biggest and most important component of the central tracking system was the *Central Jet Chamber (CJC)* [60]. The CJC was a drift chamber filled with a gas mixture of about 49.6 % argon, 49.6 % ethane and 0.8 % ethanol. It consisted of two separate concentric devices, the inner CJC1 with 30 azimuthal cells and 24 signal wires per cell and the outer CJC2 with 60 azimuthal cells and 32 signal wires per cell. The signal wires registered the charge pulse caused by a traversing charged particle ionizing the gas. The cells were tilted by about 30° relative to radial direction. This ensured that high momentum tracks crossed the wire plane at least once per chamber, which allowed a robust measurement. Furthermore this geometry leads to the ionization electrons drifting perpendicular to high momentum tracks under the influence of the electric field in the chamber and the magnetic field produced by the H1 solenoid.

In the transverse plane the position of a track could be calculated from the drift time of the ionization electrons to the wires and the precise knowledge of the drift velocity, drift direction in the magnetic field and wire positions. The single hit resolution achieved in the transverse plane (coordinates r-ϕ) is 150 μm [61]. Since the wires were mounted parallel to the beam axis, the coordinate z along the beam axis could not be determined equally well. It had to be determined by using charge division and could be measured with an accuracy of a few centimeters.

The momentum of tracks could be measured using the curvature of the track in the magnetic field. The achieved resolution for the transverse momentum of tracks is [61]

$$\frac{\sigma_{p_T}}{p_T} = 0.005\,\frac{p_T}{\mathrm{GeV/c}} \oplus 0.015. \tag{4.6}$$

To improve the determination of the z coordinate of tracks, dedicated z chambers have been used. These z chambers had the wires strung perpendicular to the beam axis in a 24-fold polygon. The *Central Inner Z Chamber (CIZ)* located just inward of the CJC1 has only been present in HERA I, while the *Central Outer Z Chamber (COZ)* between the two chambers of the CJC has been used both in HERA I and HERA II. The single hit resolution of the CIZ and COZ in the z coordinate was about 400 μm [61].

The multi-wire proportional chamber *Central Inner Proportional Chamber (CIP)* provided fast tracking information, allowing a reconstruction of the position of the primary electron-proton interaction vertex along the beam line already on trigger level. Due to the precise time information for hits in the CIP an event T_0 could be calculated for event timing constraints on trigger level. During the HERA luminosity upgrade the CIP and the CIZ have been replaced by the CIP2k [62]. The CIP2k consisted of five layers with a 16-fold segmentation in ϕ. For a fast track reconstruction the pads were arranged in a projective geometry as can be seen in fig. 4.7.

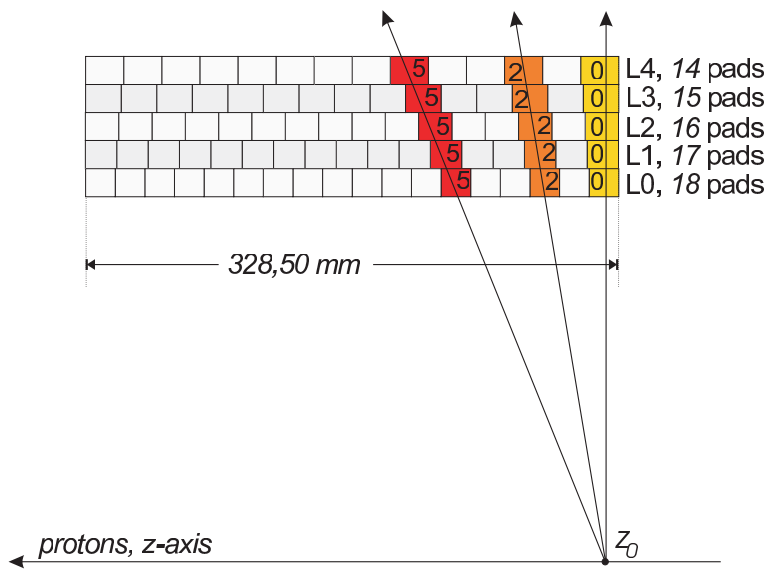

Figure 4.7: Standard block of the projective geometry of the CIP2k. All tracks originating from a common vertex on the beam axis produce the same track pattern in every layer of the CIP. Figure taken from [62].

The forward region at polar angles $5° < \theta < 25°$ was instrumented with the *Forward Tracking Detector (FTD)*. In order to cope with the high track multiplicities in the forward region the FTD consisted of several subsystems. For HERA I these subsystems included proportional chambers, radial and planar drift chambers and transition radiation detectors. During the luminosity upgrade the proportional chambers, radial chambers and transition radiation detectors have all been removed and replaced by new planar drift chambers ("Q chambers") in addition to the old planar drift chambers ("P chambers"). All the FTD components were installed in three supermodules perpendicular to the beam axis. A schematic drawing of the FTD is shown in fig. 4.8.

In the backward region the tracking system was completed by the *Backward Drift Chamber (BDC)*, which was replaced during the luminosity upgrade by the *Backward Proportional Chamber (BPC)*. These devices have not been used for this thesis.

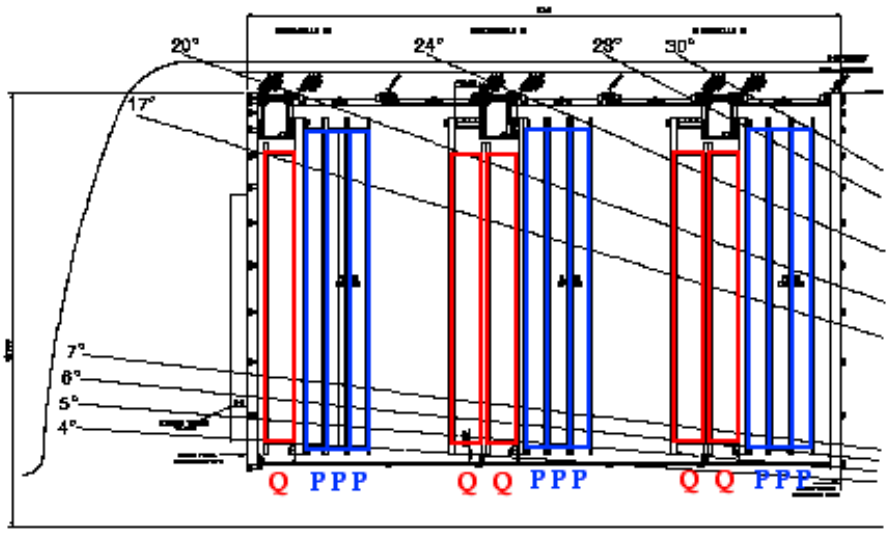

Figure 4.8: Technical drawing of the Forward Tracking Detector in the HERA II configuration. The old P chambers are colored in blue and the new Q chambers in red. Figure taken from [53].

4.3.2 Silicon Vertex Detectors

Many interesting physics processes involve short-lived particles such as heavy quarks. Since the lifetime of these particles is too short for entering the active detector volume, only their decay products are measured. The tracks of these daughter particles can be identified because in general they do not point to the primary electron-proton interaction vertex of the event. The spatial resolution of the tracking chambers is however not sufficient for this task. For this reason three silicon solid-state detectors were installed close to the beam pipe, the *Forward, Central* and *Backward Silicon Tracker* (FST, CST and BST). The FST was only installed for the HERA II running period. Since the FST and BST are not used in this thesis, only the CST will be explained in the following in more detail.

The CST [63] consisted of two layers of two-sided silicon strip detectors, arranged in 32 ladders. The strips on the p side were oriented parallel to the beam axis with a strip pitch of 50 μm, allowing a precise measurement of track points in the coordinates $r\phi$. For the measurement of the z coordinate the strips on the n side were oriented perpendicular to the beam axis with a pitch of 88 μm. A single hit resolution in $r\phi$ of 11 μm has been achieved [61]. Relevant for the identification of tracks originating from secondary decay vertices is the resolution of the distance of closest approach d_{ca} of the track to the primary electron-proton interaction vertex. The d_{ca} resolution is shown in fig. 4.9. It is not symmetric in ϕ because of the elliptical geometry of both the beam spot and the CST in HERA II.

4.3.3 Track Reconstruction

The track reconstruction software combines the individual hits in the different subsystems of the H1 tracking system to tracks with precisely determined parameters. It starts with identifying triplets of hits from adjacent wires in the CJC. From these track seeds a circle fit (because of the track curvature in the magnetic field) in the $r\phi$ plane is performed, first for CJC hits only. Then information from other subsystems is gradually added and the fit redone. In the rz plane a simple straight line fit is performed. This procedure ends with a set of non-vertex-fitted tracks.

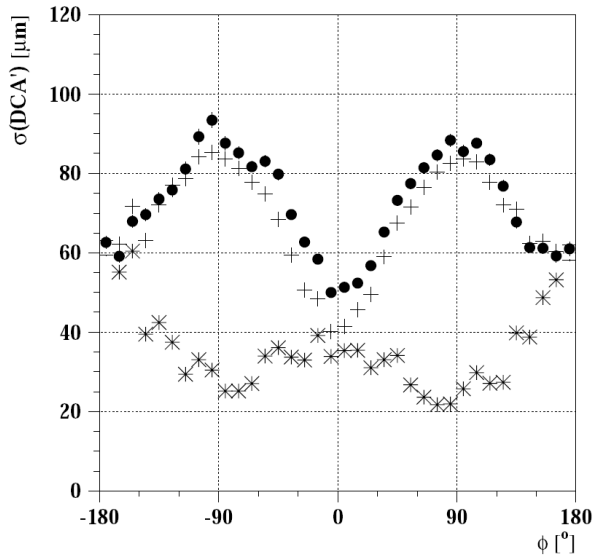

Figure 4.9: Resolution of the d_{ca} for tracks with transverse momentum $p_T > 6$ GeV in microns as a function of ϕ for the 2006 e^- data period. The dots represent the measured values, the stars the contribution from the CST intrinsic resolution and multiple scattering. The crosses include in addition the contribution from the expected beam size. Figure taken from [61].

Finally the assumption of a common interaction vertex of the tracks is used as an additional (and very powerful) constraint. The intersection of all tracks with the beam line is used to determine a starting value for the z coordinate of the interaction vertex z_{vtx}. The beam position at this z_{vtx} is then used as starting value for x_{vtx} and y_{vtx}. The tracks are now refitted in the $r\phi$ plane, using this vertex as an additional constraint. The new track parameters obtained from this fit are then used for a common fit in rz of the tracks, defining a new z_{vtx}. This procedure is repeated iteratively.

Further complicating the track reconstruction, particles also suffer energy loss traversing the beam pipe and the detector material and multiple scattering processes can occur, leading to kinks in particle trajectories.

4.4 Calorimeters

Particles traversing matter lose energy and interact with the medium. Secondary particles produced in these interactions can again make further interactions and an avalanche-like shower of particles is produced. Calorimeters measure energies and positions of particles by absorbing the complete shower produced by the initial particle. Therefore contrary to tracking devices, calorimeters must be built as massive as possible. While only charged particles can be detected in the tracking system, in calorimeters also neutral particles are measured. It is also possible to gain information on the type of the initial particles by measuring shower shapes. Since showers produced by electromagnetic particles such as electrons or photons have different characteristics from showers produced by hadrons, the main calorimeters are subdivided into dedicated electromagnetic and hadronic sections. The H1 experiment contained four calorimeters: The *Liquid Argon (LAr) calorimeter* covered the central and forward region of the H1 detector. In the very forward part it was complemented by the *PLUG calorimeter* and in the backward region by the *Spaghetti Calorimeter (SpaCal)*. The hadronic *Tail Catcher* measured the energy leaking out of the LAr calorimeter.

4.4.1 Liquid Argon Calorimeter

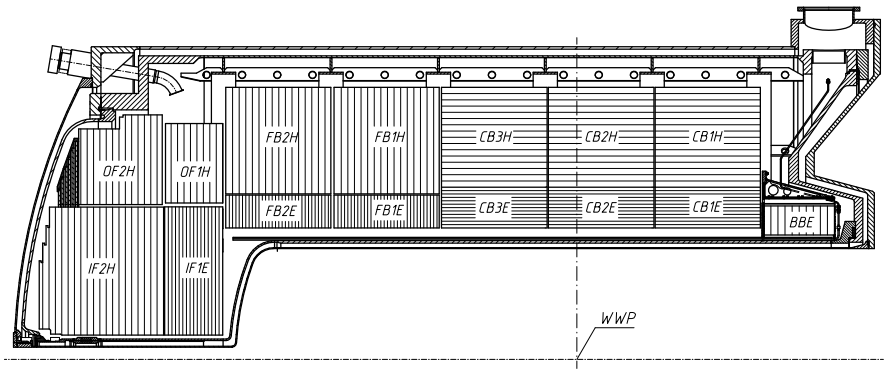

Figure 4.10: Longitudinal cross section of the upper half of the LAr calorimeter. The segmentation into eight wheels and into electromagnetic and hadronic parts can be seen. 'WWP' denotes the electron-proton interaction point. Figure taken from [64].

The LAr calorimeter [64] was the biggest and most important calorimeter in H1. It provided full azimuthal coverage and a polar angle coverage of $4° < \theta < 154°$. It was divided into eight wheels, most of which had an inner electromagnetic and an outer hadronic section. A longitudinal cross section of the LAr calorimeter is shown in fig. 4.10. The wheels were divided along the azimuthal angle into eight octants. The regions between the octants (wheels) were insensitive, referred to as ϕ-cracks (z-cracks).

The LAr calorimeter was a sampling calorimeter composed of alternating absorber layers and liquid argon filled gaps. The electromagnetic part contained lead absorber plates and had a depth of 20 to 30 radiation lengths. The hadronic part contained stainless steel absorber and had a depth of five to eight nuclear interaction lengths (including the electromagnetic section).

In test beam measurements with electrons [65] and pions [66], the energy resolution was found to be

$$\frac{\sigma^{em}(E)}{E} = \frac{11.5\,\%}{\sqrt{E/\mathrm{GeV}}} \oplus 1\,\% \tag{4.7}$$

for electromagnetic showers and

$$\frac{\sigma^{had}(E)}{E} = \frac{50\,\%}{\sqrt{E/\mathrm{GeV}}} \oplus 2\,\% \tag{4.8}$$

for hadronic showers.

After a noise suppression step neighboring cells with deposited energy were joined to clusters, which are formations of cells that are likely to contain the shower cascade of a single incident particle. The LAr calorimeter was a non-compensating calorimeter. This means that for hadronic showers a significant fraction of the energy was consumed in nuclear interactions, which cannot be detected. This effect needs to be corrected offline.

4.4.2 Spaghetti Calorimeter

The Spaghetti Calorimeter (SpaCal) [67] covered the backward region of the H1 detector, with a polar angle range of $153° < \theta < 177.5°$ for the HERA I running period and $153° < \theta < 174°$ for HERA II. The main task of the SpaCal was the detection of the scattered beam lepton. The presence or absence of a scattered beam lepton in the detector allows to differentiate between photoproduction and DIS processes and is also an important criterion for the rejection of NC DIS events in the CC

sample. A precise measurement of the energy and scattering angle of the scattered beam lepton is essential for NC DIS processes, since it allows the reconstruction of the event kinematics. The angular coverage of the SpaCal corresponds to measurements of the scattered lepton in the kinematic range $2 < Q^2 < 150$ GeV^2 for the HERA I period and $4 < Q^2 < 150$ GeV^2 for the HERA II period.

Like the LAr calorimeter, the SpaCal was a sampling calorimeter with an inner electromagnetic and an outer hadronic section. Both parts were made of long scintillating fibres (hence the name "Spaghetti Calorimeter") placed parallel to the beam axis and embedded in a lead matrix as absorber material. In test beam measurements [68] the energy resolution was found to be

$$\frac{\sigma^{em}(E)}{E} = \frac{7.1\,\%}{\sqrt{E/\mathrm{GeV}}} \oplus 1.0\,\%. \tag{4.9}$$

The SpaCal also provided a precise time-of-flight measurement with a time resolution of better than 1 ns. This permits the suppression of non-ep background, which is asynchronous to the nominal bunch crossings.

4.5 Muon System

Since the LAr calorimeter and the solenoid coil absorbed the vast majority of particles produced in electron-proton collisions, tracks of particles measured outside these detector components usually belong to muons. Therefore the instrumented iron return yoke of the solenoid is referred to as *Central Muon Detector* (CMD). It was complemented in the forward region by the *Forward Muon Detector* (FMD).

4.5.1 Central Muon Detector

The Central Muon Detector [69] was the outermost hermetic subsystem of H1 enclosing the inner subdetectors and the solenoid coil in the form of an octagonal barrel. In the forward and backward region the barrel was closed with endcaps. The barrel and endcaps together had an angular coverage of $5° < \theta < 175°$. The barrel was again divided into a forward and backward barrel. Each of the four parts of the CMD consisted of 16 modules. A schematic layout of the CMD can be seen in fig. 4.11.

The iron yoke was instrumented with gas filled limited streamer tubes inserted between iron sheets of 75 mm thickness. An additional three streamer tube layers ("muon boxes") were mounted inside and outside the total ten sheets of iron. The tubes had a cross section of 10 x 10 mm^2 and a single sense wire strung in the center. The tubes were oriented parallel to the z-axis in the barrel region and along the x-axis in the endcaps. The top sides of the layers were equipped with either strip or pad cathodes. The strip cathodes were mounted perpendicular to the sense wires in order to allow a two-dimensional position measurement. A spatial resolution of about 3 to 4 mm for the sense wires and 10 to 15 mm for the strip cathodes was achieved. The pad cathodes were used to resolve ambiguities and to measure hadronic energy leaking out of the LAr calorimeter. The single layer muon detection efficiency reached about 80 %.

4.5.2 Forward Muon Detector

The Forward Muon Detector [70] consisted of six double layers of drift chambers and a toroidal magnet between the third and fourth layer. The FMD covered the angular region $3° < \theta < 17°$. The toroidal field allowed a momentum measurement of muons in the range 5 GeV $< p < 200\ GeV$. The minimum of 5 GeV corresponds to the minimal energy of a muon to reach the fourth layer. Two layers had radially strung layers for the measurement of the ϕ coordinate of muon tracks, whereas the wires in the other four layers were circularly spanned in order to measure θ.

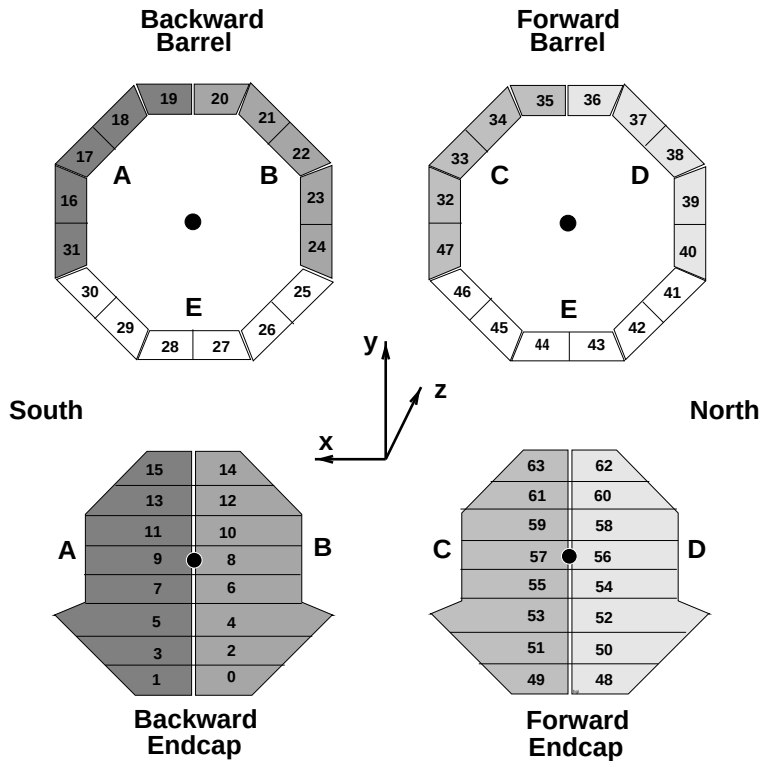

Figure 4.11: Schematic layout of the Central Muon Detector. The 64 modules and their assignment to hardware clusters A-E are shown. Figure taken from [69].

4.6 Luminosity Measurement

The instantaneous luminosity can be determined using equation (4.3) by counting the rate at which a specific process occurs, for which the theoretical cross section is well known. For the determination of the luminosity delivered by HERA the Bethe-Heitler process $ep \to ep\gamma$ [71] was used [72]. The cross section for this process is both large and precisely calculable in QED. The electron and photon were mostly scattered at small angles and left the H1 detector through the backward beam pipe. The photons were detected by a quartz-fiber calorimeter with tungsten absorber located in the HERA accelerator tunnel at a distance of about 100 m to the H1 interaction point. The scattered electrons were deflected in the magnetic fields of the H1 solenoid and the HERA beam magnets and did not reach the photon detector.

The luminosity can be determined from the counting rate of the photon detector. The transverse beam shape and the tilt of the beam determine the acceptance of the photon detector, which was usually around 95 %. The acceptance had to be corrected for and monitored permanently because it could change on short time scales of minutes. For physics analyses the luminosity for a specific range in z around the nominal interaction point (typically within $z = \pm 35$ cm) is relevant, the H1 luminosity system is however sensitive to interactions over a much broader range in z. This also needs to be corrected, taking into account the longitudinal shape of the beams.

The experimental precision of the luminosity measurement was 1.5 % in the HERA I period [29] and about 3 % in HERA II [73].

4.7 Trigger and Data Acquisition

The bunch crossing rate at HERA was 10.4 MHz, corresponding to one potential electron-proton collision every 96 ns. It was not possible to read out and store the complete information gathered by the H1 detector (approximately 500'000 channels) on this short time scale. In fact only about 10 to 50 events per second could be stored. Therefore the event rate had to be reduced online by a factor of one million. This was the task of the *trigger system*.

The majority of the bunch crossings did not produce any activity in the detector. The rate of events with activity seen by the H1 trigger system (input rate) was several 100 kHz depending on the beam quality. The input rate was dominated by non-ep background such as beam-gas or beam-wall collisions as well as detector noise. Therefore the primary task of the trigger system was to reject this background by means of constraints on the timing and the location of the event vertex. But even with a perfect rejection of all non-ep events (which is not possible), the remaining rate of about 1 kHz of actual ep collision events was still too high for storage. The reduction by another factor of about 100 was then done by selecting events according to predefined priorities, which had to be agreed upon by the H1 collaboration based on physics considerations. The complete event classification and rate reduction was performed by a four level filter system (denoted L1, L2, L3 and L4), as illustrated in fig. 4.12.

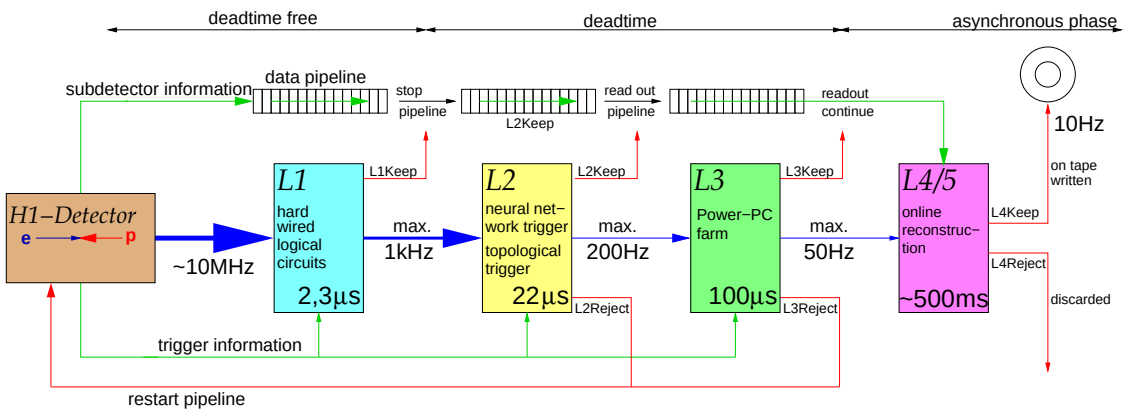

Figure 4.12: Schematic design of the H1 trigger system. Figure adapted from [74].

The first trigger level (L1) was implemented in hardware and reached a decision within 2.3 μs (24 bunch crossings). During this time all subsystems in H1 buffered their complete information on the events in circular pipelines, effectively keeping a history of at least the latest 24 events. Therefore data taking could continue during the L1 decision time and L1 operated dead-time free. Since it was not possible to read out and process the complete information of all subsystems at a rate of 10.4 MHz, L1 could access only a limited set of information. This information was coded in 256 trigger elements, which were then combined by the central trigger logic to 128 subtriggers resembling specific physics processes. If an event fulfilled all conditions of one of the subtriggers, it was accepted by L1 and passed on to L2. An additional complication arose from the fact that some subtriggers still had too high rates and had to be prescaled. A prescale of n of a subtrigger means that only every n-th event fulfilling the conditions of the corresponding subtrigger was passed on to L2.

The second trigger level (L2) had a decision time of 20 μs. The longer decision time compared to L1 allowed the use of more complex algorithms and the combination of information from different subdetectors. Since it was not possible to keep such a long history of events in the individual subsystems, data taking was stopped as soon as an event was accepted by L1, inducing dead-time. If the event was rejected by L2, the readout pipelines were restarted and data taking continued. If on the

other hand the event was accepted by L2, it was passed on to L3 and at the same time the readout of the complete H1 detector started.

The third trigger level (L3) was implemented in software, allowing very complex and highly selective algorithms with a decision time of about 100 μs. Before L3 was activated in mid-2006, all events accepted by L2 were passed on directly to L4. After a negative decision by L3 the already started detector readout was aborted and data taking restarted. If the event was accepted by L3, the readout was completed, taking about $1 - 2$ ms in total.

The fourth trigger level (L4) performed a full event reconstruction on a processor farm. The events reaching this level were classified according to the type of physics process involved. The rate of very frequent types of events involving soft physics processes at low p_T and low Q^2 was further reduced by downscaling. Events belonging to a class of downscaled events were assigned a weight, where an event weight of n means that $(n - 1)$ other similar events have been discarded.

After passing all four trigger levels the remaining events were written to tape. In a later offline analysis of the data sets, correction factors such as calibration[2] and alignment constants for the various subdetectors were derived. Using these correction factors the data sets can be reprocessed at a later time providing more accurate measurements for physics analyses.

[2]Some calibration factors could also be calculated and applied online.

Chapter 5

Simulation of Electron-Proton Collision Events

5.1 Simulation of Events

The number of events produced by a specific physics process depends on the luminosity of the machine and the cross section of the process (see section 4.1). If the luminosity is known and the cross section can be calculated in a theoretical framework, a prediction for the number of produced events can be made, based on the assumptions of the theoretical model used in the cross section calculation. Not all of these produced events will however be detected. The number of measured events is much more difficult to predict than the number of produced events, both for experimental and theoretical reasons. From the experimental side, the geometrical detector acceptance and the non-perfect efficiency and finite resolution of the detector need to be taken into account. Interactions of particles with the detector material, such as multiple scattering and energy loss, also influence measurements of particle properties. From the theoretical side, even if the hard electron-proton interaction itself can be calculated analytically for a specific process, the hadronisation processes producing the measured final state particles from the initially produced partons have to be phenomenologically modelled and cannot be calculated from first principles.

While some of the parameters of a simulated event can be estimated in a theoretical framework (depending on the physics process e.g. the cross section of the hard interaction), others are fixed by the experimental conditions (e.g. the detector geometry or dead channels) and again others need to be chosen randomly based on statistical distributions of these parameters using a Monte Carlo (MC) method[1] (e.g. the virtuality Q^2 of the event or the decay channel of a short-lived particle).

The simulation of events in the H1 experiment is done in three steps:

- An event generator program incorporates the physics model of the process under study. The four-momenta of the particles produced are generated randomly according to probabilities predicted by a theoretical framework. Parton showers, hadronisation processes and subsequent decays of short-lived particles are also performed. The four-momenta of all particles in the event are then stored together with information concerning their production and decay.
- The detector simulation contains a detailed detector description and simulates both the interactions of the particles in the detector material and the detector response to the particles. For the H1 experiment, these tasks are performed by the H1SIM software based on the GEANT program package [75]. The detector simulation takes into account effects such as geometrical acceptances, inefficiencies of the detector due to hardware problems and secondary particle productions due to interactions of particles in the detector material.

[1] The MC method is named after the city district of Monaco with the famous casino, because the Roulette game is an example of a simple random number generator.

- The event reconstruction software H1REC treats output of the detector simulation the same way as data events. In this step the detector information is processed into an output format suitable for physics analysis. This data format is the same for simulated and measured events, with the exception of links from the reconstructed objects such as tracks and calorimeter clusters to the generated particles, which are only available for simulated events.

The generation of events is explained in more detail in section 5.2.1 for the DJANGO event generator program.

5.2 Simulated Event Samples

5.2.1 Charged Current

Charged current processes have been simulated using the DJANGO [76] event generator (versions 1.2 and 1.4). DJANGO is a software package providing a common interface for different programs for the individual steps in the generation of lepton-proton scattering events. The lepton-proton scattering is based on the event generator LEPTO [77], where the leading order interaction matrix elements for CC interactions are implemented. Leading order QED corrections are included using the HERACLES [78] program. In higher order QCD, the partons produced in the lepton-proton interaction lose energy by radiating other partons. This parton showering is generated by ARIADNE [79] using the Colour Dipole Model (CDM) [80][2]. It is stopped when the energy of the partons is below ~ 1 GeV. At these energies the strong coupling constant α_s becomes too large for a further calculation of the parton showering processes in perturbative QCD. At this stage, the produced partons are "free". In the next step, hadronisation takes place and the colored partons are bound into colorless hadrons according to empirical models. The hadronisation process is simulated by JETSET [81] with the Lund String Fragmentation model [82] implemented. The MRSH parameterization [83] for the proton PDF is used, corrected to the H1 PDF 2000 fit [29] on analysis level.

A schematic view of the event generation and detector simulation steps is shown in fig. 5.1 for a neutral current DIS process.

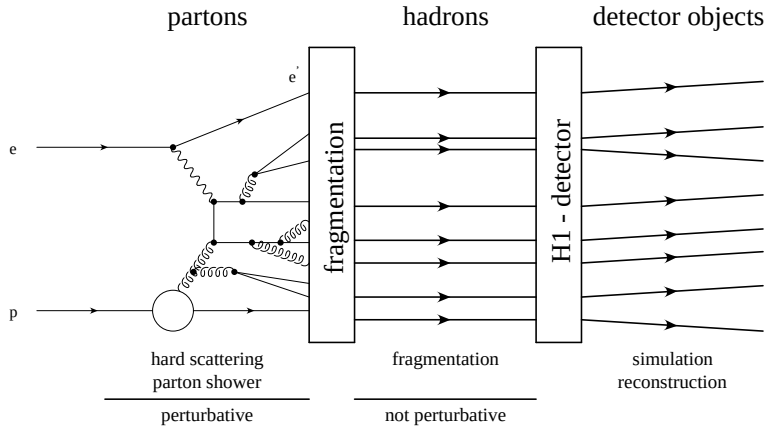

Figure 5.1: Schematic view of the event generation and detector simulation for a neutral current DIS event (figure taken from [84]).

The simulated CC samples used for this analysis are listed in table 5.1. The lowest order Feynman graph for CC processes is shown in fig. 5.2 b).

[2]DJANGO is also capable of using standard matrix element parton shower (MEPS) instead of CDM, for this thesis however only CDM has been used.

Table 5.1: Simulated charged current samples.

ID	Lepton	Year	Min. Q^2 $[\mathrm{GeV}^2]$	Luminosity $[\mathrm{pb}^{-1}]$	Events
845	e^+	99/00	100	2637.4	100k
4361	e^-	06	100	1421.2	100k
5040	e^+	06/07	10	6993.2	300k

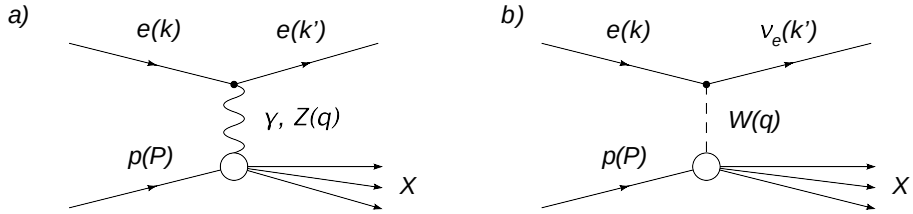

Figure 5.2: Feynman graphs for DIS processes. a) Neutral current (NC) process with exchange of a photon or Z boson and the scattered electron in the final state. b) Charged current (CC) process with exchange of a W boson and a neutrino in the final state.

5.2.2 Background Processes

The main signature of a CC event is missing transverse momentum due to the undetected neutrino. Several other ep scattering processes have the same signature or at least the potential to fake it. The contribution of these background events to the CC sample is studied in simulation. The simulated samples of background processes used for this thesis are listed in table 5.2. In different simulated samples of the same process different generator level cuts and event weights have been used, explaining the differences in event yields. For the flavor inclusive CC measurement, photoproduction processes are by far the most important background contribution, followed by NC DIS and the production of real W bosons (see table 6.6). For the extraction of the charm fraction using muons, the production of real W bosons and muon pair production events become important due the large content of muons in these samples (see table 9.4). In the following, the different sources of ep scattering background processes to the CC sample are explained.

Neutral Current DIS

A lowest order Feynman graph of neutral current DIS is shown in fig. 5.2 a). Instead of a W boson as in CC processes a photon or Z boson is exchanged. The transverse momentum of the hadronic final state is balanced by the scattered electron. If for some reason the scattered electron is not detected (e.g. because it hits a crack in the LAr calorimeter), missing transverse momentum can be faked.

Neutral current DIS processes have been simulated with the DJANGO event generator similar to the CC signal simulation.

Photoproduction

Processes with virtuality $Q^2 \approx 0$ are called photoproduction (γp) and proceed almost exclusively through photon exchange (due to the suppression of the heavy W and Z bosons at low Q^2, see section 2.1.2). In direct photoproduction the photon interacts directly with a quark in the proton or a quark generated by the dissociation of a gluon. In resolved photoproduction the photon dissociates into a quark-antiquark pair and one of these quarks interacts with a parton in the proton. As a consequence

a hadronic remnant of the photon is produced in addition to the proton remnant. Feynman graphs of photoproduction processes are shown in fig. 5.3.

For the modelling of photoproduction processes the PYTHIA generator [85] is used (versions 6.1 and 6.2) with the photon PDF GRV LO [86].

Table 5.2: Simulated background samples.

ID	Process	Generator	Luminosity $[\mathrm{pb}^{-1}]$	Events
4685	NC e^-	DJANGO 1.4	594.0	2.0M
4381	NC e^+	DJANGO 1.4	32.9	200k
4382	NC e^+	DJANGO 1.4	49.2	300k
4517	γp uds dir.	PYTHIA 6.1	30.7	866k
4541	γp uds dir.	PYTHIA 6.2	60.1	146k
4538	γp uds dir.	PYTHIA 6.2	60.0	261k
4524	γp uds res.	PYTHIA 6.1	30.1	5.2M
4539	γp uds res.	PYTHIA 6.2	59.8	1.4M
4540	γp uds res.	PYTHIA 6.2	60.0	1.3M
4512	γp charm dir.	PYTHIA 6.1	30.0	317k
4536	γp charm dir.	PYTHIA 6.2	60.0	95k
4511	γp charm res.	PYTHIA 6.1	29.4	13k
4537	γp charm res.	PYTHIA 6.2	60.4	26k
4494	Real W prod. in e^+p	EPVEC	100′068.7	44k
4968	Real W prod. in e^-p	EPVEC	1′000′000.0	410k
4489	e^+e^- prod.	GRAPE	30′000.0	152k
4491	$\mu^+\mu^-$ prod.	GRAPE	50′000.2	119k
4492	$\tau^+\tau^-$ prod.	GRAPE	100′000.0	112k

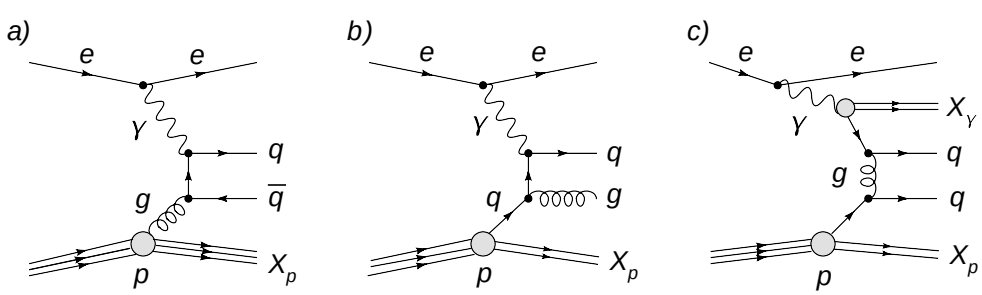

Figure 5.3: Photoproduction Feynman graphs. Graph a) shows a Boson-Gluon-Fusion (BGF) process, b) QCD Compton and c) a resolved process.

Real W Boson Production

The production of real W bosons at HERA has a small cross section of about 0.1 pb^{-1}. Since some of these processes cannot be distinguished from CC lepton-proton interactions, it is still a significant contribution to the background in the CC sample. This is illustrated in fig. 5.4, where two example processes for real W production are shown. In a) the final state contains a neutrino instead of the charged beam lepton. Even though a neutral current electron-proton interaction takes place, the final state is faking a charged current process. In b) the final state contains the scattered beam electron and it can therefore be distinguished from CC processes. These events can however still have a large missing transverse momentum if the W boson decays leptonically in the channel $W \to l\nu_l$ and the neutrino carries a large (undetected) momentum. If at the same time the scattered beam lepton is not identified such events can also fake CC events.

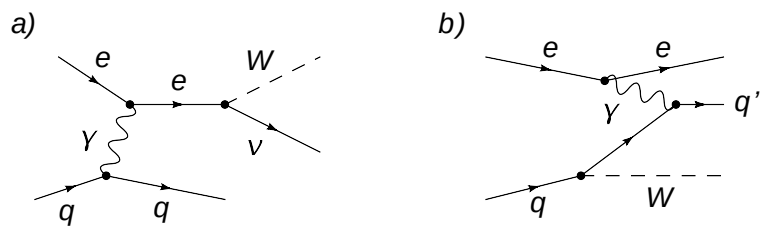

Figure 5.4: Example Feynman graphs for real W production. Process a) cannot be distinguished experimentally from a CC process.

The production of real W bosons is simulated using the EPVEC generator framework [87].

Lepton Pair Production

If high momentum μ or τ leptons are produced in the process $ep \to eXl^+l^-$, the energy carried by the leptons is not fully contained in the calorimeter. This can lead to a significant missing transverse momentum in the event, faking a CC event if at the same time the scattered beam lepton is not identified. The main production process for lepton pairs at HERA is shown in fig. 5.5.

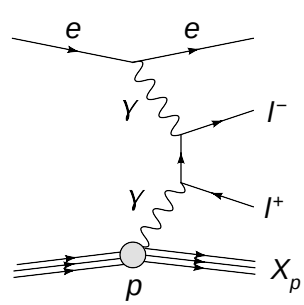

Figure 5.5: Leading order Feynman graph for lepton pair production.

Lepton pair events at HERA are generated by the GRAPE program [88].

5.3 Event Reweighting and Pseudo Charged Current

5.3.1 Reweighting of Simulated Events

The aim of the simulation of ep collisions is to describe the data as good as possible in all details. The simulation includes the physics of the simulated process (in some theoretical framework) and the detector properties such as its geometry and its response to specific types of particles. Even after taking into account all these effects, the simulated distributions for some variables do not describe the data. In such cases, weights are assigned on an event-by-event basis to the simulated events in order to change the shape of the simulated distributions and adjust them to the data distributions.

In the following, the event weights applied to simulated CC events will be explained.

Trigger Weight

The task of the H1 trigger system is the selection of the most interesting events for storage among the 10.4 million potential ep collisions per second (see section 4.7). Only triggered events can enter the offline analysis. As the trigger efficiency depends on the event properties (within the event selection range of the offline analysis), the distributions for these variables are altered by the shape of the trigger efficiency. The simulation of the LAr calorimeter trigger does not manage to describe these features correctly. Therefore the simulated events have to be reweighted according to the trigger efficiency for the corresponding events in data. The trigger efficiency for CC events is determined in a Pseudo CC sample (see section 5.3.2) and explained in more detail in section 6.1.

Vertex Weight

The primary ep interaction vertex position along the beam axis influences the reconstruction of the event kinematics and needs to be described by the simulation. In simulation, the z coordinate of the vertex is distributed according to a Gaussian distribution. This is not true in data, where both the mean vertex position and its distribution depend on the running conditions. This is taken into account by reweighting the simulated events depending on their simulated vertex position according to the vertex distribution measured in the data sample. The weighted and unweighted distributions of the z coordinate of the simulated vertices are compared to the measured data distribution in fig. 5.6 b) and c).

PDF and Polarization Weight

The simulated CC sample has been produced using the MRSH parameterization for the proton PDF. This has to be corrected to the data, which is described by the H1 PDF 2000 fit. Furthermore the effect of the lepton beam polarization is not simulated. Instead, random polarization values are assigned to the simulated events according to the polarization distribution measured in data. The cross section for a simulated event using the H1 PDF 2000 fit and taking into account also the polarization value assigned to this event is calculated. The ratio of this cross section to the generated cross section for the corresponding event is used for reweighting the event.

Luminosity Weight

The luminosity weight is a simple normalization constant taking into account the simulation and data luminosities.

Global Weight

The global weight is the product of all above mentioned weights, which are assumed to be independent, and is applied to the simulated CC events. The distribution of the global weight for HERA II e^+p CC simulation without the luminosity weight included is shown in fig. 5.6 a). Without the luminosity

normalization, the global weight for simulated events ranges from 0 to 2. No large weights significantly above two are observed. This is important, since large weights would lead to systematic uncertainties.

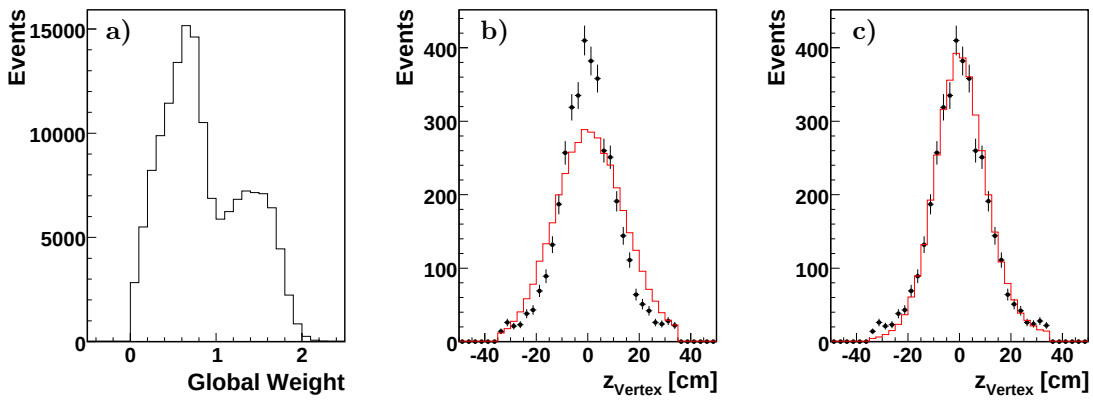

Figure 5.6: Global weight for HERA II e^+p CC simulation. In a) the distribution of the global weight without the luminosity normalization included, in b) the z coordinate of the primary vertex without and in c) with the global weight applied are shown. The histogram corresponds to the simulation and the dots with error bars in b) and c) denote the e^+p data.

5.3.2 Pseudo Charged Current

Some effects, such as the trigger efficiency for CC events, can only be studied in data and not in simulation. The statistics of the CC data sample is however small, leading to large statistical uncertainties in more detailed studies. For this purpose, pseudo charged current (PsCC) data samples are produced. PsCC events are NC events with all information on the scattered beam lepton removed on detector hit level. The altered events are then reconstructed again in the same way as CC events. An example for a NC event transformed into a PsCC event is shown in fig. 5.7. For this thesis, PsCC has only been used to determine the trigger weights for simulated events and is therefore not discussed in detail.

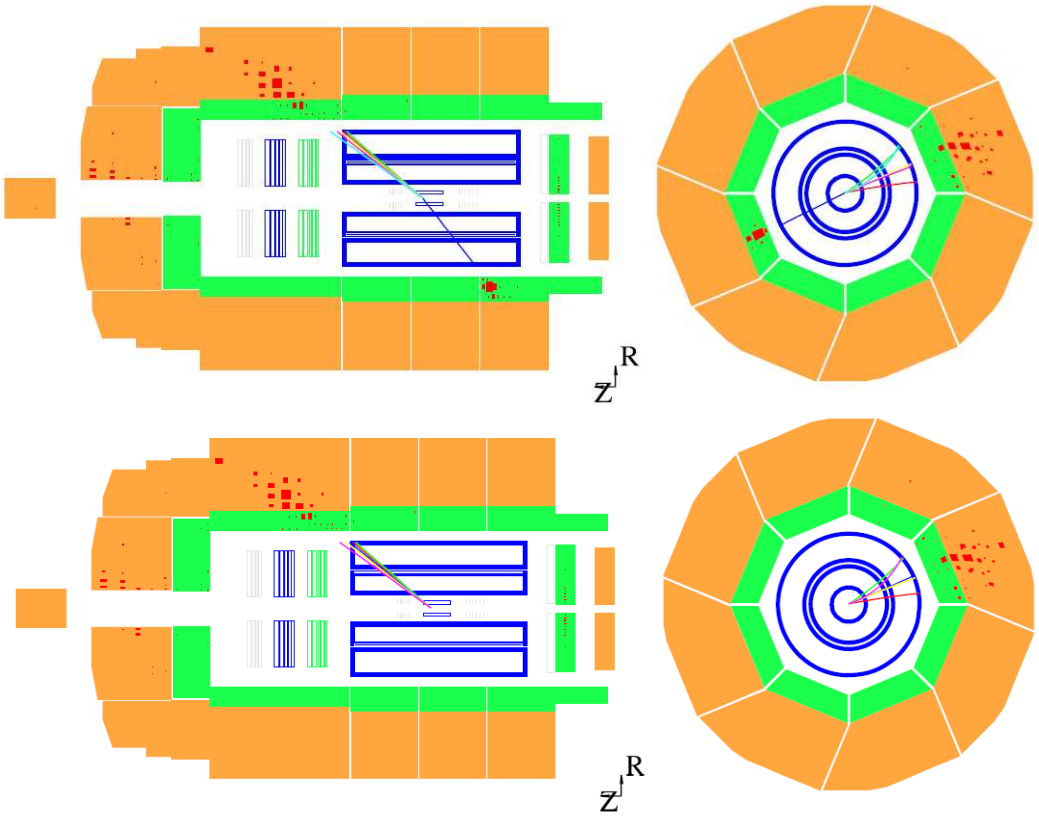

Figure 5.7: A NC event (top) transformed into a PsCC event (bottom) by removing the scattered beam lepton. Figure taken from [89].

Chapter 6

Charged Current Measurement

The measurement of charm production in CC actually consists of two measurements: The measurement of CC processes and the determination of the charm fraction in the selected CC events. In this chapter, the CC measurement is presented. The determination of the charm fraction in CC is discussed in the chapters 7, 8 and 9.

The CC measurement is presented following the steps of the analysis: First the triggering of CC events and the data selection are discussed. Then, the event selection and rejection of background is explained. The selected event samples are compared to the expectation from simulation. In a next step, the systematic uncertainties of the measurement are studied. Finally, the measured CC cross sections for e^+p and e^-p data dependent on the lepton beam polarization are presented.

6.1 Trigger

Of the 10.4 million potential ep collisions per second in the H1 detector only about 10 to 20 were stored. The selection of these events, done by the H1 trigger system, is therefore the first selection step in any data analysis. The H1 trigger system is explained in detail in section 4.7. In this section only the subtriggers used for the CC measurement are discussed.

6.1.1 CC Trigger Definitions

The subtriggers (ST) used for the selection of CC events are ST66, ST67 and ST77. In order to have a well defined sample of events with a known trigger efficiency, only events saved by these three ST are selected. The technical definitions (trigger elements) of the individual ST at the end of the HERA high energy data taking are listed in table 6.1. While the conditions defining the physics signature of the target events (physics conditions) were constant over all run periods considered in this thesis, the much more complicated conditions against non-ep background (timing and veto conditions) had to be adjusted to different running conditions.

ST66 is mainly sensitive to CC events. The main requirement is a large imbalance in the transverse plane of the energy deposits in the LAr calorimeter (trigger element `LAr_Etmiss>2`). A part of the energy needs to be deposited in the inner forward region of the LAr calorimeter (`LAr_IF>1`).

ST67 is designed for the triggering of high Q^2 NC events, where there is a high energetic compact shower in the electromagnetic part of the LAr calorimeter (`LAr_electron_1`) caused by the scattered beam electron. This ST can also be used for other physics processes with high energetic clusters in the electromagnetic LAr, including CC processes.

ST77 is used for both NC and CC processes. Like ST66, it also triggers on an imbalanced energy distribution in the LAr calorimeter (`LAr_Etmiss>1`), but with a lower threshold than ST66.

Not only electron-proton collisions produced activity in the H1 detector, but also other processes such as cosmic muons or collisions of beam particles with collimators or remaining gas atoms in the

Table 6.1: Technical definitions (trigger elements) of the CC subtriggers at the end of the HERA high energy data taking. The physics conditions have been constant over all run periods considered in this thesis, the timing and veto conditions have been adjusted for different running conditions.

ST	Physics conditions	Timing and veto conditions
66	`(LAr_IF>1)&&(LAr_Etmiss>2)`	`(!SPCLh_AToF_E_1)&&(!VETO_BG)&&((!(BToF_BG &&BToF_Gl&&(!BToF_IA)))&&(!SToF_BG))&&(CIP_T0 ||(LAr_T0&&(!CIP_T0_nextbc)))&&(FIT_IA ||(!FIT_BG))&&(!((CIP_mul>7)&&(CIP_sig==0)))`
67	`LAr_electron_1`	`((CIP_mul>0)||(!Mu_BIEC))&&(!VETO_BG)&& ((!(BToF_BG&&BToF_Gl&&(!BToF_IA)))&&(!SToF_BG)) &&(CIP_T0||(LAr_T0&&(!CIP_T0_nextbc)))&&(FIT_IA ||(!FIT_BG))&&(!((CIP_mul>7)&&(CIP_sig==0)))`
77	`LAr_Etmiss>1`	`((!(BToF_BG&&BToF_Gl&&(!BToF_IA)))&&(!SToF_BG)) &&(CIP_T0&&(CIP_sig>0))&&(FIT_IA||(!FIT_BG)) &&(!((CIP_mul>7)&&(CIP_sig==0)))`

beam pipe. Furthermore, activity in the detector could be faked by noise in the detector electronics. A ST with only the physics conditions described above would therefore mainly trigger noise or non-ep background. This problem is reduced by timing and veto conditions. The exact time when a signal occurs is measured by several subdetectors (in particular the CIP, CJC and LAr calorimeter). If the activity measured in the detector is originating from an ep collision, it must be in coincidence with a bunch crossing. Electronics noise and cosmic muons on the other hand are independent of bunch crossings. This fact is used by the timing conditions in the triggers to suppress non-ep background. Collisions of beam particles with collimators and gas atoms in the beam pipe usually produce many tracks originating from a point located far outside the ep interaction region. Events with such tracks are suppressed by the veto conditions. It is also possible to cut on the ratio of central to forward and backward tracks, resulting in a condition on a central interaction vertex. Such a condition (`CIP_sig>0`) has been used for ST77 since this ST has a weaker physics condition than ST66 and ST67.

With the timing and veto conditions included, typical trigger rates for ST66 were 0.4 Hz, for ST67 2 Hz and for ST77 1 Hz. These ST could always run with a prescale of 1, meaning every triggered event was passed on to L4 (neither of these ST had a L2 or L3 condition). Since L4 was transparent for high Q^2 events, all triggered CC events were also stored.

6.1.2 Trigger Efficiency

The efficiency of the CC triggers is determined in pseudo CC (PsCC, see section 5.3.2). Since the events in this sample are triggered by NC triggers and the missing transverse momentum is introduced artificially by removing the scattered beam lepton, the PsCC sample is well suited for cross checking efficiencies of triggers based on missing transverse energy.

The efficiency of the CC subtriggers (defined as the number of triggered and selected events divided by the number of selected events) in bins of missing transverse momentum and polar angle of the hadronic final state (HFS) is shown in fig. 6.1. The main subtrigger for CC events is ST77. For events with $p_{T,\,miss}$ larger than $\sim$ 25 GeV the CC trigger efficiency is above 95 %. At the CC event selection cut value of $p_{T,\,miss} = 12$ GeV the trigger efficiency is steeply rising. For this reason, the simulated CC events need to be reweighted according to the trigger efficiency (see section 5.3.1).

The steep rise of the efficiency of ST66 in forward direction of the HFS is due to the condition on the energy deposited in the inner forward part of the LAr calorimeter.

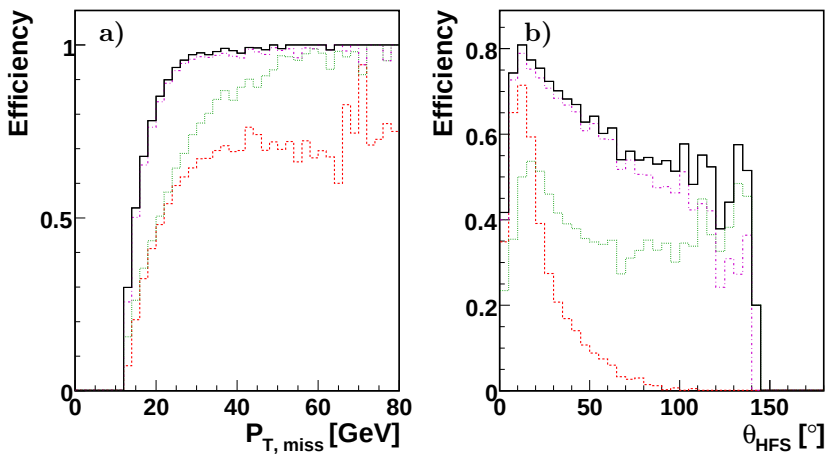

Figure 6.1: Efficiency of the CC subtriggers a) in bins of $p_{T,\,miss}$ and b) θ_{HFS}. ST77 is represented by the magenta, dash-dotted line, ST67 by the green, dotted line and ST66 by the red, dashed line. The black, solid line corresponds to the combination of all CC subtriggers.

6.2 Data Selection

The H1 data sets are divided into time periods with constant readout and trigger settings, the so called runs. Only runs fulfilling the following criteria have been used:

- The run has to be between the start of e^+p data taking in 1999 and the end of HERA high energy data taking.
- The run quality has to be good or medium. This quality flag depends on the subsystems which are operational during the run. Runs without the LAr calorimeter, the SpaCal or the luminosity system are qualified as poor. The same is true if none of the subsystems CJC1, CJC2 and CST are read out or if the duration of the run is less than 30 s. Furthermore a run can be degraded to poor quality if a technical problem in a major subsystem is found in offline analysis.
- The minimal integrated luminosity of the run has to be larger than 0.1 nb^{-1}. A lower luminosity collected in a run often is an indication of a technical problem.
- All of the following subsystems must be read out: CJC1, CJC2, LAr calorimeter, SpaCal, TOF, VETO, luminosity system, CIP and calorimeter trigger. These systems are needed either for the trigger or the analysis of CC events. It is also checked on an event-to-event basis if the high voltage of these systems is on.
- The subtriggers ST66, ST67 and ST77 must have a prescale factor of one. This was always the case if there was no major technical problem (in which case the run quality would be poor anyway), this explicit requirement allows to neglect prescale factors for the analysis of CC events.
- A valid polarization measurement by at least one of the polarimeters must be available.

Run ranges with technical problems specific to the analysis of CC events, which do not result automatically in a poor run quality, are excluded. This mainly concerns problems with the CIP trigger and high noise levels in the LAr calorimeter or the calorimeter trigger.

The luminosity is calculated for the logical "OR" of the CC subtriggers ST66, ST67 and ST77, which is equal to the total integrated luminosity, because the prescale factors of these triggers is one.

Only the luminosity for electron-proton collisions within ±35 cm around the nominal interaction point is considered.

In table 6.2 the integrated luminosity and mean polarization of the data samples used for the CC analysis are listed separately for different beam leptons and different lepton beam helicities. The HERA I e^- data sample has not been considered for this thesis due to the low statistics of only 10.6 pb^{-1} for this sample[1].

Table 6.2: Integrated luminosity and mean polarization of the data samples used for the CC analysis. For the errors on these quantities see the discussion of systematic uncertainties in section 6.7.

Period	Type	Helicity	L [pb^{-1}]	$\overline{P}$ [%]
HERA I	e^+	-	61.1	0
HERA II	e^+	RH	102.8	31.46
HERA II	e^+	LH	79.7	−36.21
HERA II	e^-	RH	53.0	33.45
HERA II	e^-	LH	101.9	−26.26

6.3 Rejection of Non-ep Background

The events triggered by the CC subtriggers ST66, ST67 and ST77 have large energy deposits in the LAr calorimeter, which are not balanced in the transverse plane (with the exception of events triggered by ST67, which does not have such a condition). This is the key signature of CC events, but of many non-ep background events as well. For instance, a collision of a beam proton with a collimator just outside the detector can result in such a signature. The same is true for halo muons or cosmic muons traversing the LAr calorimeter. The timing and veto conditions on the triggers avoid the triggering of most of these non-ep background events. Since they occur much more frequently than real CC events, the contribution from non-ep background to the samples of ST66, ST67 and ST77 triggered events is still dominating the real CC events. The ratio of ep to non-ep events in the triggered sample depends on the background situation and is therefore not constant in different data periods. For instance for the 2004-2006 e^- LH sample, the combined cuts against non-ep background (including vertex cut) reject 92.4 % of the events triggered by ST66, ST67 or ST77, while for the 2006 e^+ LH sample "only" 85.1 % of the triggered events are rejected.

Background from non-ep processes dominates in particular at high $p_{T,\,miss}$ and is therefore of special importance in CC measurements. This can be seen in fig. 6.2, where the $p_{T,\,miss}$ distribution of the event sample triggered by the CC subtriggers is shown with and without the non-ep rejection criteria applied. These criteria are explained in the following sections. Due to the dominance of non-ep background events at high $p_{T,\,miss}$, the contribution of these events to the selected CC event sample can still be significant, even after the non-ep background rejection criteria have been applied. The contribution from non-ep events to the selected event sample is problematic since it cannot be modelled and estimated in simulation.

How non-ep events can fake CC events with missing transverse energy in the LAr calorimeter is illustrated in fig. 6.3, where a CC event and a halo-muon event are shown. In xy view, the missing transverse energy in the LAr calorimeter is visible.

[1] The low sample statistics for HERA I e^- is also reflected in the low number of selected muons for this sample: Only one positively and one negatively charged muon have been selected in HERA I e^-.

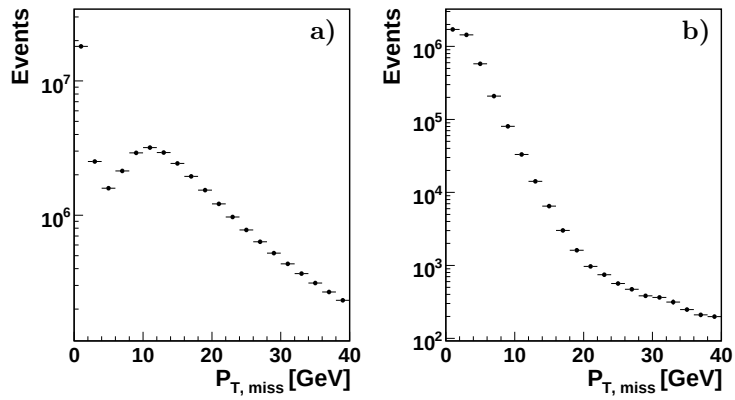

Figure 6.2: Missing transverse momentum $p_{T,\,miss}$ of the triggered data sample in HERA II e^+p running a) without and b) with the non-ep rejection criteria applied. The tail at high values of $p_{T,\,miss}$ is dominated by non-ep background events.

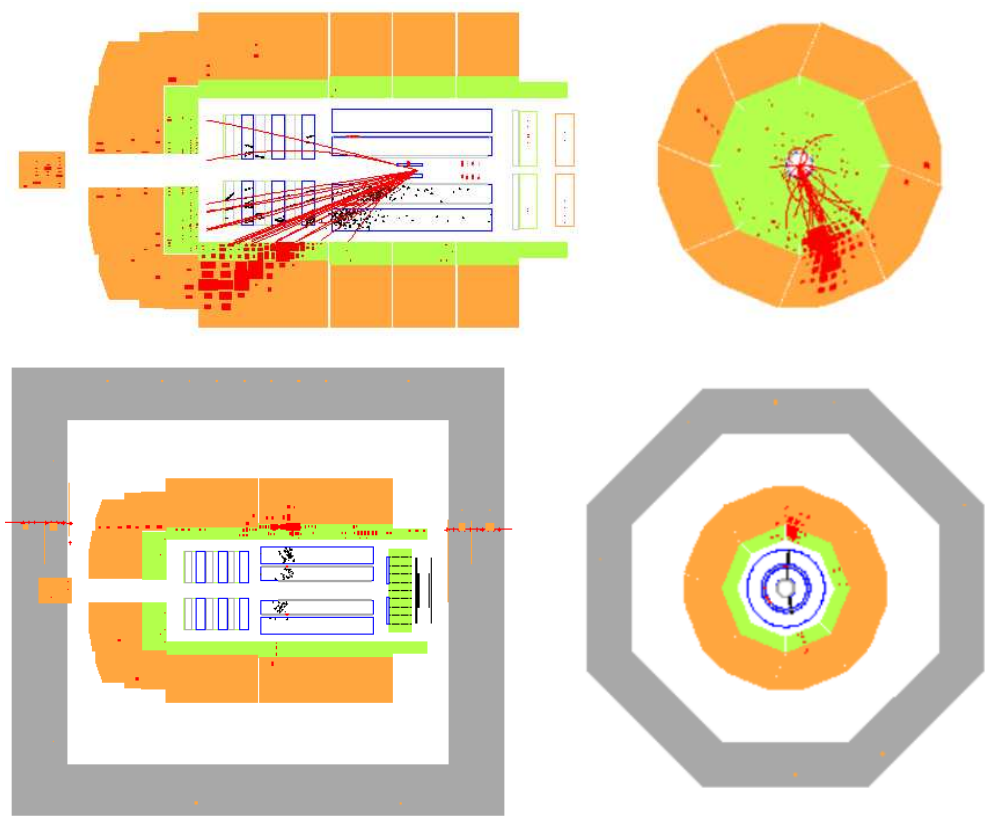

Figure 6.3: A CC event (top) and a halo muon event (bottom) in the H1 event display in rz (left) and xy (right) view.

6.3.1 Event Timing

The timing constraints are the most important cuts against non-ep background, rejecting about three quarters of the cosmic and halo muons traversing the H1 detector [90]. Electron-proton collisions can only occur at exactly known and discrete points in time, during the bunch crossings. Requirements on the event timing are already implemented in the triggers (see section 6.1.1). In addition to the trigger timing requirements, constraints on the event timing are made in the offline analysis using information from the CJC and the LAr calorimeter. The CJC timing $T_{0,CJC}$ is defined as the time when most charged particles cross the chamber and is measured relative to the nominal bunch crossing time in units of CJC ticks (500 CJC ticks = 96 ns). The CJC achieves an event time resolution of about 2 ns. The LAr calorimeter event timing $T_{0,LAr}$ is derived from the time structure of the energy depositions measured in units of bunch crossings (BC) and has a resolution of about 10 ns. The constraints on the event timing in the offline analysis are

$$410 \leq T_{0,CJC} \leq 510 \text{ ticks} \qquad \text{and} \qquad -0.54 \leq T_{0,LAr} \leq 0.54 \text{ BC}. \tag{6.1}$$

The CJC and LAr T_0 are shown in fig. 6.4 for a H1 data sample without any selection cuts applied in HERA II e^+ running. Since the triggers already include timing constraints, the selection cuts (6.1) do not result in a large reduction of the sample statistics. The periodic structure with 20 ticks period in $T_{0,CJC}$ seen in fig. 6.4 a) originates from events without reconstructed tracks in the CJC, where $T_{0,CJC}$ is deduced from the rising flank of the drift time spectrum with a granularity of 20 ticks. These events are rejected by the vertex cut described in section 6.3.3.

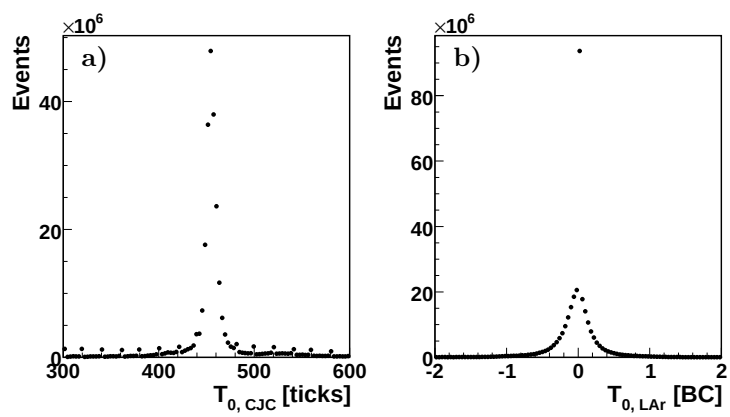

Figure 6.4: a) CJC and b) LAr T_0 for a H1 data sample without any selection cuts in HERA II e^+p running.

6.3.2 Background Finder

Most non-ep background events passing the timing requirements can be rejected based on the topology of the events. For this purpose, a set of topological background finding algorithms [90–92] is used. These algorithms use tracking, calorimeter and muon system information in order to identify patterns in the H1 detector specific to cosmic muons, halo muons and beam-gas events. For instance two matching tracks on exactly opposite sides in an otherwise empty detector are a clear sign for a cosmic muon. Likewise, a horizontally aligned set of clusters in the hadronic section of the LAr calorimeter with matching activity in the muon system endcaps is an indication of a halo muon traversing the detector (compare fig. 6.3). Beam-gas or beam-wall collisions usually result in a lot of tracks in the backward region of the tracking system pointing to a vertex outside of the H1 detector itself.

The individual background finder flags available in the H1 analysis software framework are listed in appendix A.

6.3.3 Vertex

A precisely measured primary electron-proton interaction vertex in the central region of the detector is important for the reconstruction of kinematic quantities such as the Q^2 of the event. The requirement of a primary vertex close to the nominal interaction point also rejects non-ep background events from beam-gas or beam-wall interactions outside this range. Halo and cosmic muons even result in events with no vertex at all, except if a cosmic muon passes exactly through the beam spot or the muon is overlayed over a real ep collision event. For these reasons, the position of the primary vertex along the beam line has been constrained to

$$-35 \text{ cm} < z_{vtx} < 35 \text{ cm}, \tag{6.2}$$

relative to the nominal electron-proton interaction point. The z_{vtx} distribution can be seen in fig. 5.6.

The position of the primary vertex is reconstructed by extrapolating tracks to the beam line (see section 4.3.3). Usually tracks measured in the CJC are used for this purpose, with additional information from other subsystems if available. If no CJC track is available, it is also possible to determine a primary vertex from tracks measured in the FTD alone. Because these FTD vertices are less precisely determined, a CJC vertex is required explicitly for the selection of CC events. This results in the rejection of events without any tracks in the CJC.

6.3.4 LAr Calorimeter Noise

The key signature of CC events, the large missing transverse energy, can be faked by noise in the LAr calorimeter. A dedicated algorithm is searching for indications of coherent noise in parts of the calorimeter caused by the detector electronics. Events with detected calorimeter noise are rejected.

6.4 CC Event Selection

6.4.1 Event Kinematics Criteria

The requirement on the missing transverse momentum $p_{T,\,miss}$[2] is the main cut in the selection of CC events, rejecting most photoproduction and NC DIS events. The cut value chosen is

$$p_{T,\,miss} > 12 \text{ GeV}. \tag{6.3}$$

Below this value the trigger efficiency is very low (see section 6.1.2 and fig. 6.1) and the contributions from other physics processes become dominant. As can be seen in fig. 6.5 a) and b), the reweighting of simulated CC events according to the trigger efficiency (see section 5.3.1) has a large influence on the $p_{T,\,miss}$ distributions in simulation. While a) corresponds to the physical distribution of all CC events, in b) the simulation describes the triggered sample after the trigger efficiency has been taken into account. About 30 % of the unweighted CC events in simulation have a $p_{T,\,miss}$ of less than 12 GeV. In data most of these low $p_{T,\,miss}$ events are already lost on trigger level. Of the triggered CC events, only ~ 5 % are lost by the offline analysis cut on $p_{T,\,miss}$. The distribution of all data events in the HERA II e^+p period triggered by ST66, ST67 or ST77 is shown in fig. 6.5 c) for comparison. It peaks at low values of $p_{T,\,miss}$, demonstrating the dominance of background in this region. The distribution shows two components: Events triggered by the $E_{T,\,miss}$ subtriggers ST66 and ST77 with

[2] $p_{T,\,miss}$ is defined by $\vec{p}_{T,\,miss} = -\vec{p}_{T,\,FS}$, where $\vec{p}_{T,\,FS}$ is the transverse component of the four-momentum sum of all final state particle candidates (including the scattered beam lepton, if present). Particle candidates include (calibrated) clusters in the calorimeter and tracks reconstructed in the tracking system, where matching track-cluster pairs only count as one particle candidate.

a correct $E_{T,\,miss}$ reconstruction in the LAr trigger are located at high values of $p_{T,\,miss}$ and contain the CC events as well as a dominant contribution from non-ep background events (see section 6.3). The steeply falling component at low $p_{T,\,miss}$ corresponds to events either triggered by the high Q^2 NC DIS subtrigger ST67 or events, where the offline reconstructed value of $E_{T,\,miss}$ differs from the $E_{T,\,miss}$ on trigger level.

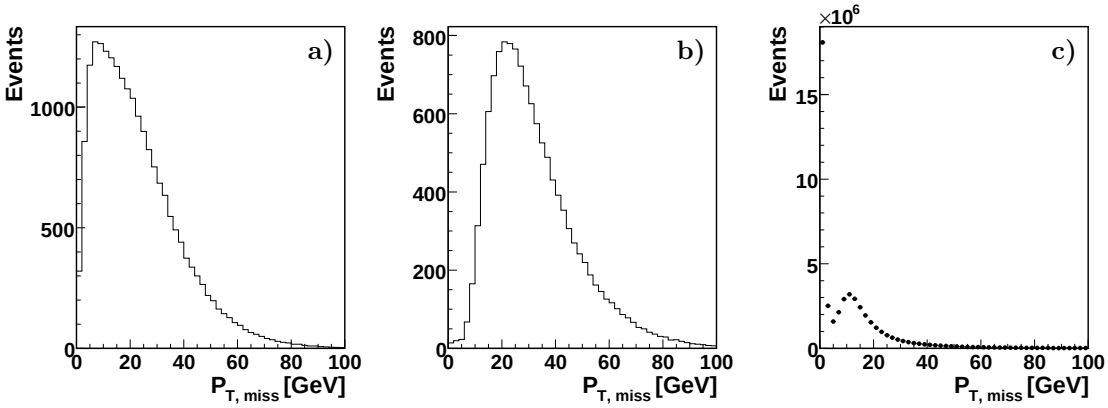

Figure 6.5: $p_{T,\,miss}$ of a) simulated CC events without reweighting, b) simulated CC events with trigger weight applied and c) all data events in the HERA II e^+p period triggered by the CC subtriggers. For explanations see the text.

At low values of the virtuality Q^2, photoproduction processes and NC DIS with photon exchange have a much higher cross section than CC and are therefore dominant. In order to suppress this background and to provide a well defined DIS phase space, the events must fulfill the following condition[3]:

$$Q^2 > 223 \text{ GeV}^2. \tag{6.4}$$

This condition alone has an efficiency of 89.8 % for CC events and 1.1 % for photoproduction events triggered by the CC subtriggers.

The inelasticity y of the event is correlated with the polar angle of the hadronic final state θ_{HFS}. It is constrained to the range

$$0.03 < y < 0.85. \tag{6.5}$$

For very low θ_{HFS} corresponding to low values of y, a part of the energy is lost in the beam pipe, resulting in a decrease of the trigger efficiency (compare fig. 6.1). For this reason, the lower bound of $y > 0.03$ is chosen. In the central part of the LAr calorimeter, the trigger efficiency again decreases for increasing θ_{HFS} and y. This is due to the high energy thresholds of the LAr triggers in the central region because of high pad capacities and corresponding high noise levels. Furthermore, the resolution of Q^2 decreases with increasing y. For these reasons, an upper limit of $y < 0.85$ has been set.

6.4.2 Rejection of Remaining Photoproduction Events

The main difference between CC and photoproduction (γp) events is the imbalance of the energy and momentum carried by particles in the plane transverse to the beam axis. This is already exploited by the $p_{T,\,miss}$ cut. Another way to make use of these event characteristics is a cut on the energy flow isotropy V_{ratio}. This quantity is defined as the ratio of the transverse energy flow antiparallel (V_{ap})

[3]The "strange" value of 223 GeV^2 has its origin in the logarithmic Q^2 binning of former CC analyses. It has been kept for compatibility.

and parallel (V_p) to the direction of the transverse momentum of the hadronic final state $\vec{p}_{T,h}$ (defined as the vector sum of the transverse momenta of all HFS particles)[4]:

$$V_{ratio} = \frac{V_{ap}}{V_p}, \tag{6.6}$$

with

$$V_{ap} = -\sum_{\substack{\text{HFS particles } i \\ \vec{p}_{T,i}\cdot\vec{p}_{T,h}<0}} \frac{\vec{p}_{T,i}\cdot\vec{p}_{T,h}}{p_{T,h}} \tag{6.7}$$

and

$$V_p = \sum_{\substack{\text{HFS particles } i \\ \vec{p}_{T,i}\cdot\vec{p}_{T,h}>0}} \frac{\vec{p}_{T,i}\cdot\vec{p}_{T,h}}{p_{T,h}}. \tag{6.8}$$

For CC events V_{ratio} is expected to be close to zero, while for γp events V_{ratio} is much larger. This is illustrated in fig. 6.6.

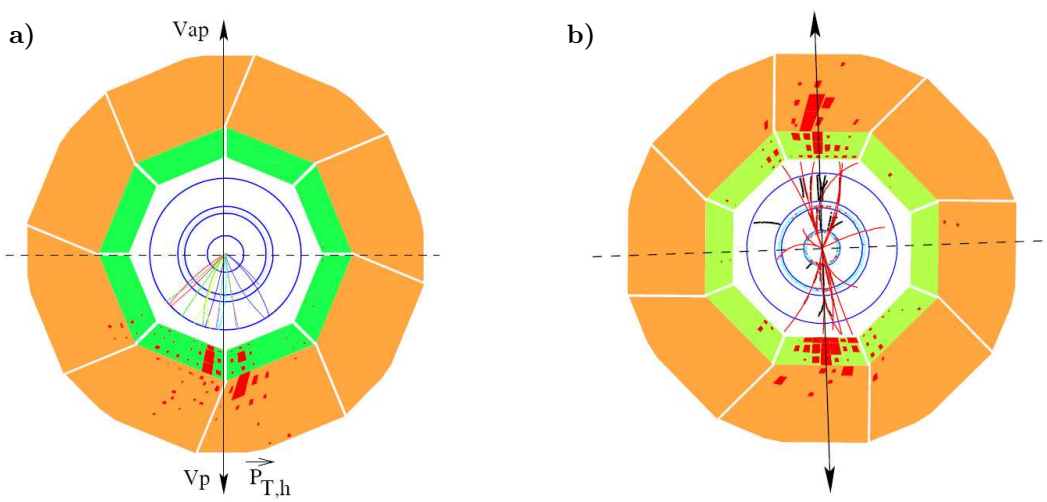

Figure 6.6: Energy flow isotropy in a) CC events with $V_{ratio} \approx 0$ and b) γp events with $V_{ratio} \approx 1$. Figure taken from [89].

For the separation of CC and γp events, a two-dimensional cut on V_{ratio} and $p_{T,h}$ is used:

$$V_{ratio} < \begin{cases} 0.15 & \text{if } p_{T,h} \leq 27 \text{ GeV}, \\ 0.25 & \text{if } p_{T,h} > 27 \text{ GeV}. \end{cases} \tag{6.9}$$

The background contribution from γp events is mainly distributed at low $p_{T,h}$ and high V_{ratio}. Therefore the V_{ratio} cut has to be stronger at lower values of $p_{T,h}$. The efficiency of this two-dimensional condition is 0.1 % for γp and more than 90 % for CC events triggered by the CC subtriggers (90.1 % in e^+p and 93.6 % in e^-p running). For events passing all other CC event selection criteria (including also the anti-NC criteria described below), the efficiency of the energy flow isotropy cut is 92 % for CC and 2.3 % for γp events. This condition allows therefore to strongly suppress remaining photoproduction background while maintaining a high selection efficiency for CC events. The two-dimensional distributions of CC and γp events in the variables V_{ratio} and $p_{T,h}$ are shown in fig. 6.7.

[4]In events without a scattered beam lepton (as in γp and CC events), the relation $\vec{p}_{T,h} = -\vec{p}_{T,miss}$ is valid. In a perfectly balanced event $\vec{p}_{T,h}$ is zero.

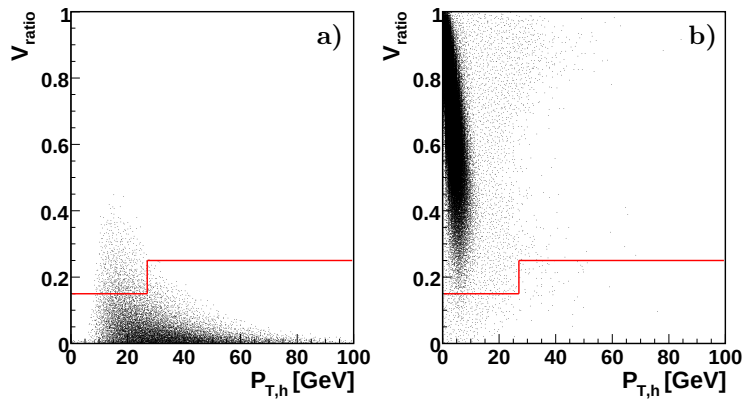

Figure 6.7: Two-dimensional distributions of a) simulated CC and b) simulated γp events in the variables V_{ratio} and $p_{T,h}$. The selection cut is indicated by the red line.

6.4.3 Rejection of Remaining Neutral Current DIS Events

The selection criteria concerning $p_{T,miss}$ and V_{ratio} reject most NC DIS events (see table 6.4). While in photoproduction the scattered beam lepton is not detected and the isotropic energy and momentum distribution is achieved by the hadronic final state alone, in NC events the transverse energy and momentum of the HFS are balanced by the scattered beam lepton. If for any reason the scattered beam lepton is not detected, the event shares the characteristics of a CC event and passes the $p_{T,miss}$ and V_{ratio} cuts (this fact is used for the production of Pseudo CC, see section 5.3.2). Therefore criteria for the rejection of NC DIS events need to safeguard against unidentified scattered beam leptons.

All isolated tracks in the event are considered potential candidates for the scattered beam lepton. A track is flagged as isolated, if its transverse momentum is larger than 1 GeV, its polar angle larger than 25° and the distance $d_{\eta\phi} = \sqrt{(\eta_1 - \eta_2)^2 + (\phi_1 - \phi_2)^2}$ to the closest other track in pseudorapidity η and azimuthal angle ϕ is more than 0.5.

If the scattered beam lepton is absorbed in an insensitive region of the LAr calorimeter, it might not be detected. These insensitive areas are located at the edges of the ϕ octants of the LAr calorimeter in periodic intervals in ϕ of 45°. An event is rejected if an isolated track in the event points to within $\pm 2°$ in ϕ of one of these calorimeter cracks.

Another indication of a possible misidentified scattered beam lepton is an isolated track opposite to the HFS. An event is rejected if an isolated track exists with $|\phi_{track} - \phi_{HFS}| > 160°$.

If at least one electron candidate was identified in the event, the electron candidate with the highest transverse momentum is taken to be the candidate for the scattered beam lepton. An event is rejected, if this scattered beam lepton candidate is opposite to the HFS with $|\phi_{elec} - \phi_{HFS}| > 160°$, even if it is not isolated.

In simulation, the combination of these anti-NC criteria alone has an efficiency of 99.4 % for CC DIS events and 4.9 % for NC DIS events. For events passing all other CC event selection cuts, the efficiency of the anti-NC criteria is 99.7 % for CC and 46.9 % for NC events. This means that the NC contribution to the selected event sample can be halved with rejecting only very few CC events.

6.4.4 Polarization

The CC cross section depends on the polarization of the lepton beam (see section 2.3.2). In the data selection a valid polarization measurement by at least one of the polarimeters is required (see section 6.2). In order to increase the polarization of the data samples, a minimal lepton beam polarization of 20 % at the time of a selected CC event is required. This increases the difference of the measured cross sections for left- and right-handed samples and allows to determine the polarization dependence of the CC cross section more precisely. Lepton beam polarizations of less than 20 % only occur at the beginning of luminosity fills, when the polarization is still rising (see fig. 4.3). For e^+ data, only 3.4 % of all otherwise selected events are rejected by this requirement, while for e^- data about 16.4 % of the otherwise selected events are rejected. The difference between e^+ and e^- data is due to the smaller polarization in the e^- LH running period because of technical problems. It is in general more difficult to achieve high polarizations in e^- running because of the larger depolarizing beam-beam effects due to the attraction of the oppositely charged electron and proton beams. This is also reflected in the polarization distribution of the data samples shown in fig. 6.8.

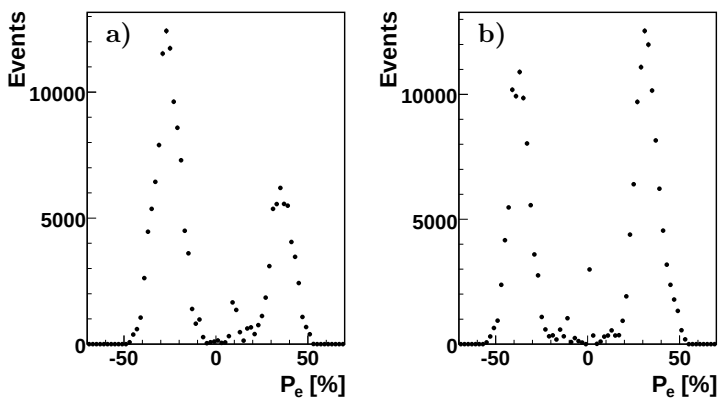

Figure 6.8: Polarization P_e distribution for the HERA II a) e^- and b) e^+ data samples.

The longitudinal lepton beam polarization was only available in the H1 region of HERA for the HERA II running period. For HERA I data, the longitudinal lepton beam polarization is zero and no event selection cut on the polarization is applied.

6.4.5 Visual Scanning

The selected events have been scanned by eye using the H1 event display. In total 78 events showing clear signs of a wrong reconstruction or non-ep background processes have been removed. The efficiency of this visual scanning is assumed to be 100 % for ep scattering events. Even though most non-ep background events are rejected by the selection criteria discussed in section 6.3, there is still a contribution from non-ep events remaining in the sample. In particular events with cosmic or halo muons overlaying a photoproduction event or events with a cosmic or halo muon interacting in the detector and thereby not showing the typical topological signatures of such events can pass the selection criteria. As an example, the event displayed in fig. 6.9 is likely to be a cosmic muon absorbed in the LAr calorimeter.

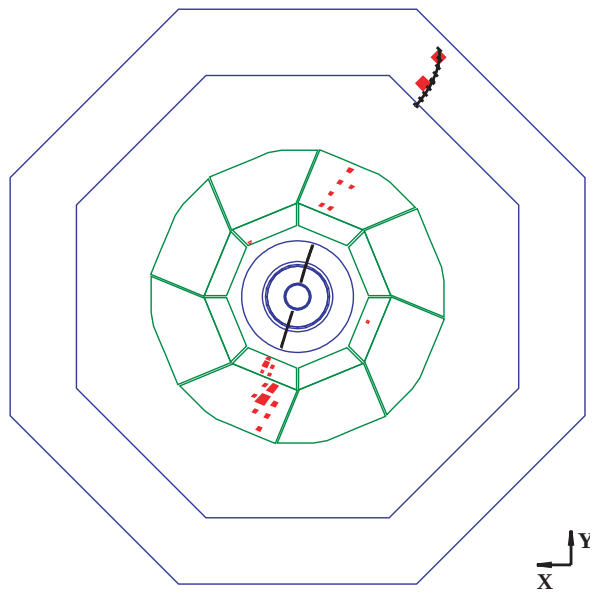

Figure 6.9: Event display of a suspected cosmic ray muon event passing the CC selection.

6.5 Summary of the CC Event Selection

All data selection and event selection cuts for the CC measurement are summarized in table 6.3. The efficiencies of the different sets of selection criteria in simulation are listed in table 6.4. The efficiencies given for the kinematical criteria are somewhat misleading due to generator level cuts on the minimal Q^2 of the events. The CC signal simulation has a generator level cut of $Q^2 > 10$ GeV^2 applied. Since CC events are located at high values of Q^2 due to the W boson mass, this generator level cut does not have a significant effect. On the NC DIS simulation however a generator level cut of $Q^2 > 100$ GeV^2 is applied, which has a large effect on the photon exchange component. The number given in table 6.4 for the efficiency of the kinematical cut set on NC DIS events therefore is restricted to events with $Q^2 > 100$ GeV^2 and would be much lower for all NC DIS events without this restriction. The photoproduction simulation has no generator level cut on Q^2 applied. The lepton beam polarization is not simulated. Instead, the polarization of simulated events is randomly chosen according to the polarization distributions of the data samples. Therefore the efficiency of the polarization cut is by definition the same for simulation and data. It is larger for e^+p than for e^-p data because of the polarization distribution in these samples (see section 6.4.4). This is also reflected in the higher overall selection efficiency for e^+p data.

Real W boson production, which is also a major contribution to the background in the selected event sample (see table 6.6), is not included in table 6.4. This is due to the fact that these events are indistinguishable from CC events if the W boson was emitted by the beam lepton in the final state (see section 5.2.2) and cannot be separated from CC events using event selection criteria. Therefore the efficiency of the selection criteria for real W boson production events is the same as for CC events.

In data, the event sample triggered by the CC subtriggers is dominated by non-ep background, in particular at high $p_{T,\,miss}$ (see section 6.3). For instance, more than 20 % of the events triggered by the CC subtriggers pass the kinematic criteria, but the non-ep background cuts remove 99.8 % of these events. Additional events are later removed by visual scanning, which is only done in data. Since background from non-ep processes is such an important contribution to the data samples and is not included in the simulations, the "efficiencies" of the event selection criteria in data cannot directly be compared to the efficiencies in simulation and are not included in table 6.4.

Table 6.3: Data selection and event selection criteria for the CC measurement.

Cut variable	Cut value
Data Selection	
Run period	Start of 99 e^+ until end of HERA high energy running
Run quality	Good or medium
Run luminosity	$L_{run} > 0.1$ nb^{-1}
Operational subsystems	CJC1, CJC2, LAr, SpaCal, TOF, VETO, CIP, luminosity system, calorimeter trigger
Trigger prescales	Prescale 1 for ST66, ST67 and ST77
Polarimeter	Valid measurement by at least one polarimeter
Technical problems	No technical problems in any of the relevant subsystems
Non-ep background rejection	
Event timing	$410 \leq T_{0,CJC} \leq 510$ ticks
	$-0.54 \leq T_{0,LAr} \leq 0.54$ BC
Event topology	No background finder flag set
Vertex position	-35 cm $< z_{vtx} < 35$ cm
LAr noise	No noise detected in the LAr calorimeter
CC event selection	
Missing transverse momentum	$p_{T,\,miss} > 12$ GeV
Virtuality	$Q^2 > 223$ GeV^2
Inelasticity	$0.03 < y < 0.85$
Energy flow isotropy	$V_{ratio} < 0.15$ if $p_{T,h} \leq 27$ GeV
	$V_{ratio} < 0.25$ if $p_{T,h} > 27$ GeV
Isolated tracks	No isolated track pointing to a LAr crack
	No isolated track with $\lvert\phi_{track} - \phi_{HFS}\rvert > 160°$
Electron acoplanarity	No electron candidate with $\lvert\phi_{elec} - \phi_{HFS}\rvert > 160°$
Polarization	$P > 20$ %
Visual scanning	No hint of a non-ep background event

6.6 Selected Event Samples

The number of selected CC events in the different samples are listed in table 6.5. For the extraction of the CC cross section, the selected event samples with the cut on the minimal lepton beam polarization of 20 % applied are used. This allows a better measurement of the polarization dependence of the CC cross section. For the extraction of the charm fraction discussed in chapters 7, 8 and 9, the selected event samples without this cut are used, since it is assumed that the charm fraction in CC events is independent of the lepton beam polarization. The data selection criterion of a valid polarization measurement is however still applied. The event yield for the different running periods is shown in fig. 6.10 in bins of 1 pb^{-1}. Very broad bins correspond to periods with no new data, as it is the case for general machine and detector shut downs, major technical problems or running with a different lepton type. Because of the polarization dependence of the CC cross section (see equation (2.37)), the event yields for the HERA II $e^{\pm}$ periods have been multiplied with a factor of 1/(1±polarization). This is not necessary for HERA I, since the lepton beam was not polarized during this period.

Table 6.4: Efficiencies of individual sets of selection criteria in simulation. The efficiencies in NC and photoproduction (γp) simulation do not depend on the lepton beam charge, except for the polarization distribution, where e^+p running has been assumed in this table. For explanations see the text.

Applied cut set	Efficiency in simulation [%]			
	CC e^+p	CC e^-p	NC	γp
Non-ep	88.0	87.2	94.5	83.6
Kinematics	87.2	88.9	0.9	0.1
Anti γp cuts	90.1	93.6	0.3	0.1
Anti NC cuts	99.4	99.5	4.9	91.4
Polarization	94.9	83.5	94.9	94.9
All cuts combined	67.6	61.8	0.004	0.001

Table 6.5: Number of selected CC events and mean polarization for the different samples, with and without the polarization cut ($P > 20$ %) applied.

Period	L [pb^{-1}]	$\overline{P}_{\text{no cut}}$ [%]	$\overline{P}_{\text{cut}}$ [%]	Without P cut	With P cut
HERA I e^+	61.1	0	0	1543	-
HERA II e^+ RH	102.8	31.46	33.00	2765	2690
HERA II e^+ LH	79.7	−36.21	−37.10	1152	1093
HERA II e^- RH	53.0	33.45	35.97	1428	1240
HERA II e^- LH	101.9	−26.26	−28.56	4825	3983

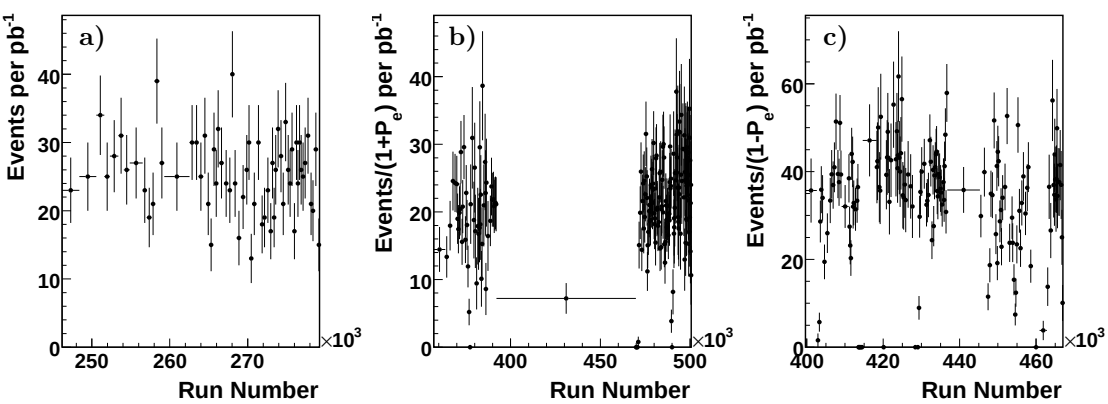

Figure 6.10: Yield of selected events in a) HERA I e^+, b) HERA II e^+ and c) HERA II e^- data. In b) and c) (event yield)/(1 ± polarization) is plotted because of the polarization dependence of the CC cross section (see equation (2.37)). One bin corresponds to an integrated luminosity of 1 pb^{-1}. Very broad bins correspond to shut downs, major technical problems or a running period with the other lepton type.

The remaining background contributions from ep scattering processes are determined from the simulation of these processes (see section 5.2.2). The expected background contributions are listed in table 6.6. Also listed are the number of expected CC events and the number of selected events in data. The relative amount of background in the selected event samples varies due to the dependence of the CC cross section on the beam lepton type and the polarization (the higher the signal cross section, the lower the relative contribution from background). Comparing the total number of expected events with the number of selected events in data, the number of selected data events tends to be lower than the number of expected events, except for the HERA I period. The largest difference between predicted and measured number of events is seen in the e^- LH data set. This leads to lower than expected cross sections, as will be seen in section 6.8.2. For the interpretation of this deviation from the prediction see the discussion of the measured cross sections in section 6.8.2.

Table 6.6: Expected background and signal contributions to the selected event samples. All numbers for HERA II are given with the polarization cut of $P > 20\,\%$ applied.

Process	HERA I e^+	e^+ LH	e^+ RH	e^- LH	e^- RH
γp uds resolved	62.8	85.7	115.8	90.9	51.5
γp uds direct	24.0	28.6	36.8	33.7	18.1
γp charm resolved	2.5	3.6	4.8	2.6	2.3
γp charm direct	10.9	14.3	12.0	7.6	6.1
Neutral current	5.7	4.3	10.3	10.8	3.1
Real W boson production	9.9	12.9	16.4	12.8	7.4
Dimuon production	4.0	5.2	6.5	5.5	3.1
Dielectron production	0.2	0.3	0.4	0.3	0.2
Ditau production	2.0	2.7	3.3	2.8	1.6
Total expected background	122.0	157.5	206.3	166.8	93.4
Expected charged current	1294.8	987.6	2698.2	4685.1	1269.3
Selected data events	1543	1093	2690	3983	1240

The agreement of different event properties between data and simulation for the two largest selected samples, the e^- LH and e^+ RH samples, is shown in fig. 6.11 and fig. 6.12. The lower than expected number of data events in the e^- LH sample compared to the prediction from simulation is clearly visible. Furthermore, a deficit of the data compared to simulation at low y and low polar angles of the hadronic final state is observed. This feature is present in all samples, but most prominent in the e^- samples[5].

[5]This effect is seen by all CC studies using H1 data.

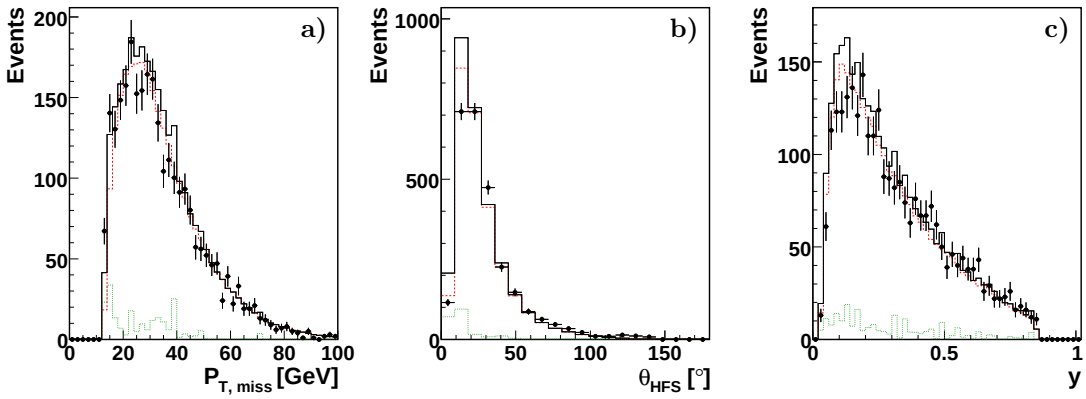

Figure 6.11: Comparison of data and simulation for the selected e^+ RH sample. In a) the missing transverse momentum $p_{T,miss}$, in b) the polar angle of the hadronic final state θ_{HFS} and in c) the inelasticity y are presented. The dots with error bars denote the data, the red, dashed line the CC simulation, the green, dotted line the combined background simulations and the black, solid line the sum of the signal and background simulations.

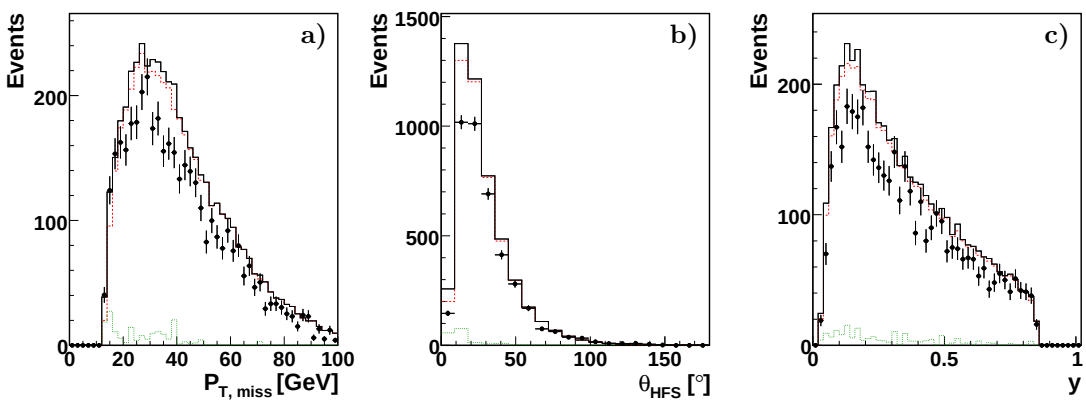

Figure 6.12: Comparison of data and simulation for the selected e^- LH sample. In a) the missing transverse momentum $p_{T,miss}$, in b) the polar angle of the hadronic final state θ_{HFS} and in c) the inelasticity y are presented. The dots with error bars denote the data, the red, dashed line the CC simulation, the green, dotted line the combined background simulations and the black, solid line the sum of the signal and background simulations.

6.7 Systematic Uncertainties

Two types of measurement errors have to be considered: Statistical errors caused by the finite data event samples[6] and systematic uncertainties related to the experimental method. Systematic uncertainties include for example uncertainties caused by the finite detector resolution and model dependencies of the simulation. The following sources of systematic errors have been considered[7]:

[6]Usually Gaussian statistics is assumed, where one standard deviation of a sample containing N events is $\sqrt{N}$.

[7]Where no other references are given, the systematic uncertainties considered for this thesis correspond to the recommendations of the H1 inclusive analysis group [93].

- The hadronic energy scale of the LAr calorimeter is assigned an uncertainty of 2 %. The energy scale is for instance needed for the determination of the missing transverse energy in the event.
- The polar angle θ of the hadronic final state is used for the reconstruction of the event kinematics. A systematic shift in θ changes the event selection efficiency due to the shift in the kinematical event selection criteria. To account for this effect, an uncertainty of ± 3 mrad is applied on θ.
- Energy deposits in the LAr calorimeter attributed to noise are not included in the reconstruction of the final state. An uncertainty of 10 % is assumed for this noise subtraction.
- The variable V_{ratio} used for the rejection of photoproduction events (see section 6.4.2) is varied by ± 0.02.
- The primary event vertex is needed for the calculation of the event kinematics and events without reconstructed vertex are rejected in the CC event selection. A y dependent uncertainty on the primary vertex reconstruction efficiency is applied: 15 % for $y < 0.06$, 7 % for $0.06 < y < 0.1$, 4 % for $0.1 < y < 0.2$ and 1 % for $y > 0.2$.
- The efficiency of the CC triggers ε_{trig} is estimated in PsCC (see section 6.1.2). The uncertainty on ε_{trig} is estimated by $15\,\%\,(1-\varepsilon_{trig}) \oplus \mathrm{Error}^{stat}_{PsCC}$ [94], where $\mathrm{Error}^{stat}_{PsCC}$ is the statistical error of the PsCC sample. This uncertainty is larger for e^+p than for e^-p running, since CC events in e^+p running tend to lower values of $p_{T,\,miss}$[8] with a consequently lower average ε_{trig} than in e^-p running.
- The efficiencies of the non-ep background finder algorithms for CC events are estimated in PsCC. For e^+p data, an uncertainty of 2 % for $y < 0.1$ and 1 % for $y > 0.1$ is assumed, for e^-p data the corresponding errors are 3 % for $y < 0.1$ and 2 % for $y > 0.1$.
- On the background subtraction an uncertainty corresponding to the statistical error of the number of events passing the CC event selection in the simulated sample is applied. Even though the statistics of the simulated background samples is large, only very few events in these samples pass the event selection. The statistical error of the number of selected events is therefore not negligible. For the subtraction of photoproduction events this error amounts to 30 %, for NC it is 10 %.
- QED radiative corrections can be estimated in the CC simulation, where also radiative processes with the exchange or emission of an additional boson are simulated. A systematic uncertainty on the CC cross section of 1 % arising from these corrections has been assumed [95].
- A 0.5 % uncertainty is caused by the choice of the PDF used in the simulation. The uncertainty was estimated by comparing the effect of different PDFs (MRSH, CTEQ4 and H1 PDF 2000) in the simulation [89].
- The luminosity measurement has an uncertainty of 1.5 % in HERA I [29] and 3 % in HERA II [73].
- The uncertainty on the polarization measurement does not have an effect on the cross section itself, but on the polarization at which the cross section was measured. This uncertainty is therefore not included in the systematic error on the cross section in the tables 6.7 and 6.9, but corresponds to the horizontal error bars in fig. 6.13. The uncertainty on a single measurement is 1.6 % for LPOL [58] and 3.5 % for TPOL [96] measurements. If available, always the polarization measurement of the LPOL has been taken. The resulting systematic error on the mean polarization of the sample is 0.8 % for the e^- RH sample, 0.6 % for e^- LH, 0.6 % for e^+ RH and 0.8 % for e^+ LH.

The effect of a systematic uncertainty on the cross section was determined in simulation and enters the cross section calculation via the varied efficiency ε (see section 6.8.1), with the exception of the uncertainties on the background subtraction, where the number of estimated background events is varied. The resulting systematic errors of the cross sections are listed in table 6.7. The contributions from the different sources of systematic errors are assumed to be uncorrelated and can therefore be added in quadrature.

[8] Differences in the production mechanisms of CC events in e^+p and e^-p data lead to different distributions of kinematical variables. This is discussed in detail in the sections 7.2 and 7.3.

Table 6.7: Systematic uncertainties on the total CC cross sections.

Systematic effect	Error on the cross section [%]				
	HERA I e^+	e^+ RH	e^+ LH	e^- RH	e^- LH
Had E scale	0.4	0.3	0.3	0.4	0.4
Polar angle	0.2	0.2	0.1	0.1	0.1
Hadronic noise	0.1	0.1	0.2	0.5	0.1
V_{ratio} cut	1.5	1.9	1.9	1.1	1.3
Vertex efficiency	0.8	1.0	1.0	0.8	0.8
CC trigger efficiency	3.4	4.6	4.6	2.2	2.2
BG finder	0.0	0.1	0.1	0.1	0.1
γp subtraction	1.3	1.4	2.6	1.3	0.7
NC subtraction	0.1	0.1	0.1	0.1	0.1
Radiative Corrections	1.0	1.0	1.0	1.0	1.0
PDF	0.5	0.5	0.5	0.5	0.5
Luminosity	1.5	3.0	3.0	3.0	3.0
Total systematic error	4.5	6.2	6.6	4.4	4.3

The main systematic error for the e^+p samples arises from the determination of the CC trigger efficiency in PsCC (see section 6.1.2). For the e^-p samples, the uncertainty on the luminosity measurement has the largest effect on the cross section.

6.8 Charged Current Cross Sections

6.8.1 Calculation of the Cross Section

The cross section σ_P for a process P was introduced in section 4.1. This cross section depends on the number of produced events N_P for the corresponding process and the integrated luminosity L with $N_P = \sigma_p L$.

However, not all of these N_P events are detected. The geometrical acceptance of the detector is not covering the complete solid angle around the interaction vertex and therefore in some events the final state particles will not enter the detector. Even if particles produced in the event enter the detector volume, the detection and reconstruction efficiency of these particles is not perfect. Finally, some of the detected and reconstructed events do not pass the offline selection criteria (in the case of this thesis the CC event selection criteria). Because of these problems, the selected number of events $N_{P,data}$ is smaller than the actual number of events N_P with $N_{P,data} = \varepsilon \cdot N_P$. The efficiency ε includes all of the effects discussed above and has to be determined in simulation.

Since the selected data events N_{data} contain contributions from other processes than the process under study P, this background contribution N_{BG} has to be subtracted with $N_{P,data} = N_{data} - N_{BG}$. The background events in the selected event samples have very similar properties to events of the process of interest, otherwise they would have been rejected by the selection criteria. Since it is not possible to separate these remaining background events from the signal events, their number has to be estimated using simulation (see section 6.6).

Taking into account the non-perfect efficiency and the background contribution in the selected sample, the cross section formula (4.4) becomes

$$\sigma = \frac{N_{data} - N_{BG}}{\varepsilon \cdot L}. \tag{6.10}$$

The event samples used for the calculation of the CC cross section are presented in section 6.6. The numbers used for the calculation of the cross section are listed in table 6.8. An additional complication arises from the polarization dependence of the CC cross section. The cross section is calculated separately for the different beam lepton helicity samples. Since the dependence of the CC cross section on the polarization is linear (see section 2.3.2), the cross section calculated from the number of events in a sample corresponds to the cross section evaluated at the mean polarization of the sample.

Table 6.8: Parameters used in the cross section calculation: The integrated luminosity L, number of selected data events N_{data}, number of estimated background events N_{BG} and efficiency (including acceptance) ε are listed for the different data samples.

Period	L [pb^{-1}]	N_{data}	N_{BG}	ε [%]
HERA I e^+	61.1	1543	122.0	72.7
HERA II e^+ RH	102.8	2690	206.3	67.7
HERA II e^+ LH	79.7	1093	157.5	67.6
HERA II e^- RH	53.0	1240	93.4	63.9
HERA II e^- LH	101.9	3983	166.8	61.1

6.8.2 Measured Charged Current Cross Sections

The measured CC cross sections for the different data samples are listed in table 6.9 and shown as a function of the lepton beam polarization P_e in fig. 6.13. The cross sections have been calculated using equation (6.10).

Table 6.9: Measured CC cross sections with statistical and systematic errors. The predictions from H1 PDF 2000 [29] are also listed with errors [97].

Period	$\overline{P}$ [%]	Cross Section [pb]	$\sigma_{stat.}$ [pb]	$\sigma_{syst.}$ [pb]	Theory [pb]
HERA I e^+	0	32.0	0.9	1.4	29.1 ± 0.4
HERA II e^+ RH	33.00	35.7	0.7	2.2	38.8 ± 0.5
HERA II e^+ LH	−37.10	17.4	0.6	1.2	18.3 ± 0.3
HERA II e^- RH	35.97	33.9	1.0	1.5	37.5 ± 0.4
HERA II e^- LH	−28.56	61.3	1.0	2.6	75.2 ± 0.8

The dependence of the cross section on the lepton beam polarization P_e has been fitted with linear functions separately for e^-p and e^+p data, using a least squares approach. The resulting fit functions are shown in fig. 6.13. The fitted polarization dependent cross sections are

$$\begin{aligned} \sigma_{CC} &= (28.9 \pm 1.4) + P_e \cdot (28.6 \pm 4.7)\ \text{pb} \qquad \text{for } e^+p \text{ and} \\ \sigma_{CC} &= (49.2 \pm 2.3) - P_e \cdot (42.5 \pm 6.8)\ \text{pb} \qquad \text{for } e^-p. \end{aligned} \tag{6.11}$$

The measured polarization dependent cross section for e^+ data shows an excellent agreement with the prediction and is almost exactly 0 at $P_e = -1$. The cross section for e^- data however is lower and has a weaker P_e dependence than predicted because of the measured cross section in the e^- LH sample, which is 18 % lower than predicted. This is partly due to a deficit of events in data

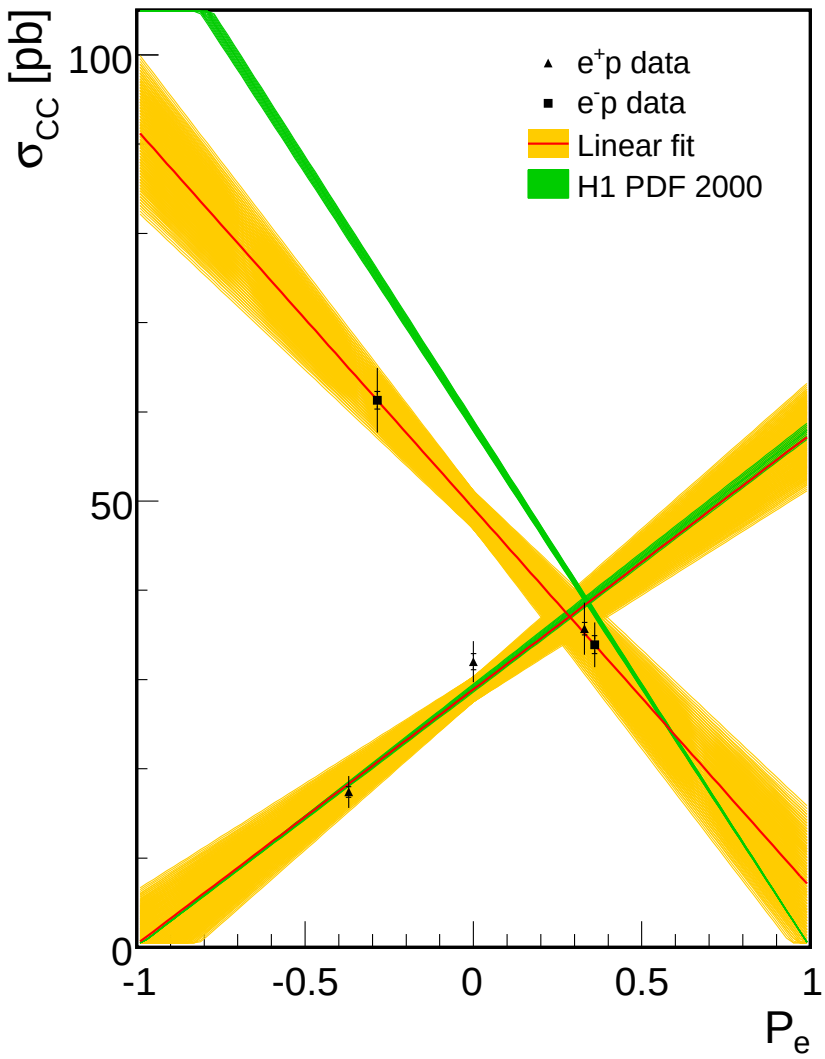

Figure 6.13: Measured CC cross sections as a function of the lepton beam polarization. The triangles represent the measured e^+p cross sections and the squares the e^-p cross sections. The inner error bars correspond to the statistical errors and the outer include also systematic uncertainties. The broad, orange bands correspond to the one standard deviation uncertainty band of the fit and the narrow, green bands to the H1 PDF 2000 prediction.

compared to the simulation at low y and low polar angles of the hadronic final state. This effect is seen in all data periods, but most prominent in e^-. For the e^- LH sample, this problem can however only explain a part of the observed difference between data and simulation. The comparison of the presented analysis with another ongoing CC study at H1[9] showed a good agreement of the number of selected data events, but different cross sections, in particular for the e^- LH sample. This indicates a well understood data event selection, but a problem in the description of the data event selection efficiency ε in the simulation.

[9]Due to several not understood features in different data periods, no results of CC analyses have been published by H1 up to now for data taken after the shut down in 2004, which constitutes 85 % of the total polarized ep scattering data.

The extraction of the charm fraction is not affected by the CC event selection efficiency in the simulation, since it has no effect on the selected data samples. It is assumed that the fraction of charm events in the selected samples is not changed by problems with the absolute normalization. For the calculation of the charm cross sections, the theory predictions for the flavor inclusive CC cross sections are used (see section 9.10.2).

Chapter 7

Charm in Charged Current and the Strange Content of the Proton

7.1 Measuring the Strange Sea in the Proton

Two main approaches for a measurement of the strange sea in the proton are possible: Strangeness production in neutral current and charm production in charged current.

In NC processes the flavor of the quark in the proton taking part in the hard interaction (in the following called "primary quark") is not changed in the process and the primary quark is still present in the final state of the event. Usually the final state particle containing the primary quark carries a significant amount of the transverse momentum of the final state (this can be used for flavor tagging, see section 3.4.1). Therefore NC events with a strange primary quark have high momentum strange hadrons in the final state. The strange quark in most strange hadrons produced in ep DIS however originates from hadronisation processes and not from the strange sea in the proton [50]. As an example, the production mechanisms of ϕ mesons ($s\bar{s}$ states) are shown in fig. 7.1. The contribution of the strange sea to the production of strange hadrons needs to be extracted by exploiting differences in distributions of kinematic variables between events with a strange primary quark and events with a strange quark from hadronisation. This method was used by the ZEUS collaboration for the measurement of ϕ mesons [50] (see section 3.4.2). The same method is also applicable to the production of other strange hadrons, such as K_s^0 mesons and Λ baryons.

In CC processes the flavor of the primary quark is changed according to the probabilities given by the CKM matrix (see section 2.3.4). Since $V_{cs} \approx 4V_{us}$ and $V_{ts} \approx 0$, most events with a strange primary quark in CC will have a charm quark in the final state. Charm production in CC has already been used by neutrino-nucleon DIS experiments for measurements of the strange sea in the nucleon (see section 3.3). Since the contribution from hadronisation processes is smaller than for strangeness production in NC, this method is less sensitive to the hadronisation models implemented in the simulation. The drawback of the charm in CC measurement is the much lower cross section compared to strangeness production in NC, resulting in larger statistical uncertainties of the measurement.

Charm production in CC is discussed in more detail in the following section.

7.2 Charm Production in Charged Current

Separating different production mechanisms for charm in CC in data is difficult and would need more statistics than is available. Therefore all studies of charm production processes presented in this chapter are using simulation. All numbers given are for inclusive CC processes without any phase space cuts applied.

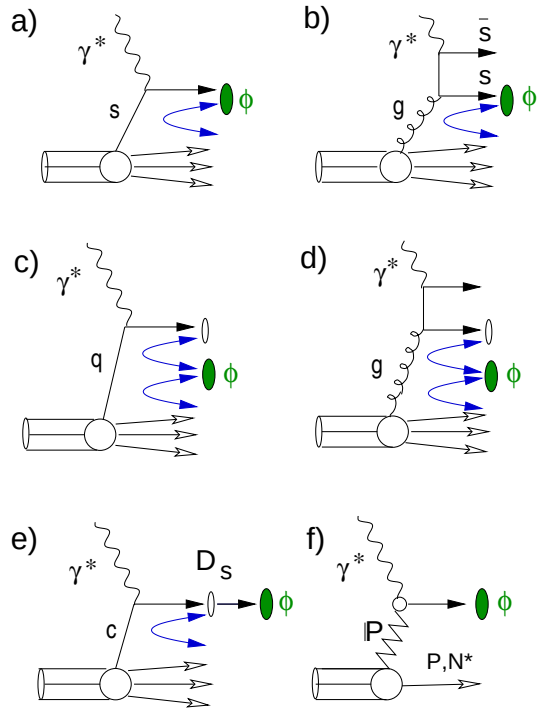

Figure 7.1: Schematic representation of different mechanisms for ϕ production in NC DIS: a) A ϕ meson is produced from a strange quark from the proton sea and a strange quark from the hadronisation process; b) A ϕ meson is produced from a strange quark emerging from a boson-gluon fusion process and a second strange quark from hadronisation; c)-d) A ϕ meson is produced solely by the hadronisation process; e) A ϕ meson is produced from a resonance decay (in this case a D_s meson decay) and f) a ϕ meson is produced by a diffractive process. Figure taken from [50].

7.2.1 Production Processes

The production mechanisms of charmed hadrons in CC are illustrated in fig. 7.2. In the quark initiated process a), the charm quark is produced directly in the interaction of the W boson with a primary quark in the proton. Due to charge conservation, the primary quark must be a down, strange or beauty quark. Interactions involving beauty quarks are suppressed because of their high mass and can be neglected. The relative contributions from down and strange primary quarks to quark initiated charm production depend on the beam lepton charge. For e^+p scattering, a W^+ boson is exchanged, which couples to down and strange quarks in the proton. Down quarks are more abundant in the proton than strange quarks because of the valence down quark content of the proton, which dominates at high values of x. Events with strange primary quarks are however more likely to produce charm than events with down primary quarks, since $V_{cs} \approx 4V_{cd}$ (in events with down primary quarks, usually up instead of charm quarks are produced, see section 2.3.4). Therefore the contribution of strange primary quarks to the quark initiated production of charm is about a factor 2.5 larger than the contribution from down primary quarks in e^+p scattering. In e^-p data, a W^- boson is exchanged, which couples to anti-strange and anti-down quarks in the proton. In this case, there is no valence quark involvement in the quark initiated process. The contribution of anti-strange primary quarks to the quark initiated production of anti-charm quarks in e^-p scattering is a factor of about eight larger than the contribution from anti-down primary quarks.

The production mechanism b) in fig. 7.2 proceeds via boson-gluon fusion (BGF). In e^+p scattering a charm quark and a anti-down or anti-strange quark are produced (usually an anti-strange quark

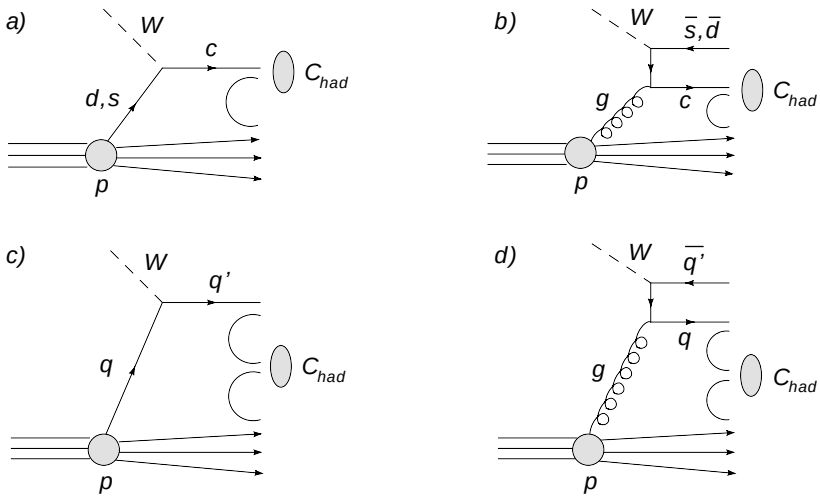

Figure 7.2: Schematic representation of different mechanisms for charmed hadron (denoted as C_{had}) production in CC: a) The charm quark is produced directly in the interaction of a W boson with a down or strange quark in the proton; b) The charm quark is produced in a boson-gluon fusion process and c)-d) the charm quark is produced during the hadronisation process.

because of the same arguments as above), while in e^-p scattering an anti-charm quark and a down or strange quark are produced.

Charm and anti-charm quarks can also be produced in hadronisation, as illustrated in fig. 7.2 c) and d). In this case, charm production is independent of the flavor of the quarks taking part in the hard interaction. While in quark initiated and BGF processes only one charm (or anti-charm) quark per event is produced, a $c\bar{c}$ pair emerges from hadronisation. Due to the charm quark mass, charm pair production is suppressed in hadronisation processes compared to light quarks.

The dominating mechanism for charm production in CC are BGF processes. In e^-p CC simulation, about 64 % of the charm quarks are produced in BGF processes, 28 % in quark initiated processes and 8 % in hadronisation. For e^+p the relative contributions are about 61 % from BGF, 35 % from quark initiated processes and 4 % from hadronisation. While for BGF the cross section is independent of the lepton beam charge, the cross section for quark initiated charm production is higher in e^+p scattering because of the valence down quark contribution. Charm production in hadronisation is completely independent of the interaction mechanism and is therefore proportional to the inclusive CC cross section. Since the inclusive unpolarized CC cross section in e^-p DIS is about twice as large as in e^+p DIS (see section 2.3.3), the cross section for charm production in hadronisation is also about twice as large in e^-p DIS compared to e^+p DIS.

An additional mechanism leads to charm quarks in the final state: Quark initiated processes with charm primary quarks. The primary quark itself is transformed into a strange or down quark in the CC process. Charm quarks in the proton exist however only as $c\bar{c}$ quark pairs in the proton sea and if one of the quarks in such a pair is taking part in the CC interaction, the other one is still present in the final state. This remaining charm quark is part of the proton remnant and has usually $p_z \gg p_T$. Since these charm quarks are leaving the detector through the beam pipe, events with this mechanism of "charm production" are not contributing to the measured charm fractions and are in the following not considered as charm events.

Charm quark production in beauty hadron decays can be neglected, because in CC almost no beauty is produced due to the structure of the CKM matrix ($V_{ub} \approx 0$, see section 2.3.4).

7.2.2 Theoretical Expectation for the Charm Fraction in Charged Current

The cross section for charm production in CC $\sigma_{CC,c}$ is of comparable size in e^-p and e^+p scattering. The prediction from the simulation is $\sigma_{CC,c} = 7.2$ pb in e^-p and $\sigma_{CC,c} = 8.3$ pb in e^+p data. As discussed in section 7.2.1, the cross section of the BGF process, which is the dominant contribution, is independent of the lepton beam charge. The effects of the lepton beam charge on the cross sections of the quark initiated and hadronisation charm production are in opposite directions and partly compensate each other.

The prediction for the inclusive, unpolarized CC cross section σ_{CC} is 70.4 pb in e^-p and 42.9 pb in e^+p scattering. This σ_{CC} is dominated by scattering on the valence quarks in the proton. In e^-p, 72 % of the CC interactions in simulation proceed via the quark initiated process with an up primary quark. In e^+p, the analogous process with a down primary quark only contributes to 35 %. This difference is explained by the valence quark content of the proton $p = (uud)$ and leads to the significantly larger inclusive CC cross section in e^-p compared to e^+p.

The almost constant $\sigma_{CC,c}$ and large difference in σ_{CC} lead to different fractions of events with charm in the CC event samples. The prediction of the simulation for the charm event fraction is 10.3 % in e^-p and 19.6 % in e^+p scattering.

All numbers are given for unpolarized lepton beams and the full phase space. The lepton beam polarization influences the CC cross section because of the parity violating structure of the weak interaction (see section 2.3.2). This difference only concerns the coupling of the W boson to the beam lepton, while the partons in the proton are not polarized. Therefore the lepton beam polarization changes the cross section of all CC subprocesses likewise and the charm event fraction is not affected by the polarization. Phase space cuts on the other hand can have an influence on the charm fraction in the CC event sample, if charm events have different kinematic properties than other events. This is investigated in section 7.3.

7.3 Properties of Charm Events in Charged Current

7.3.1 Kinematics of Charm and Uds Events

The kinematics of an ep scattering event depends on the parton in the proton taking part in the interaction. For instance, BGF processes access smaller average x values than quark initiated processes and primary valence quarks tend to have higher x values than primary quarks from the sea. In CC events, the kinematics of the quark initiated process also depends on the lepton beam charge, since valence up quarks tend to higher x values than valence down quarks and the valence quark contribution to quark initiated processes is higher for e^-p than for e^+p scattering. Therefore a difference in the kinematics of BGF and quark initiated processes is expected, as well as additional differences between e^-p and e^+p data. Since the contribution from BGF processes is higher for charm events than for non-charm events, these differences also propagate to the kinematics of charm and non-charm events. The distributions of x and the CC event selection variables $p_{T,miss}$, V_{ratio} and Q^2 (see section 6.4 for definitions) for BGF and quark initiated as well as for charm and non-charm events in e^-p and e^+p scattering are shown in fig. 7.3 - 7.6. The decay mode of the charmed hadron (semileptonic or hadronic) does not have a significant impact on the distributions of these variables for charm events.

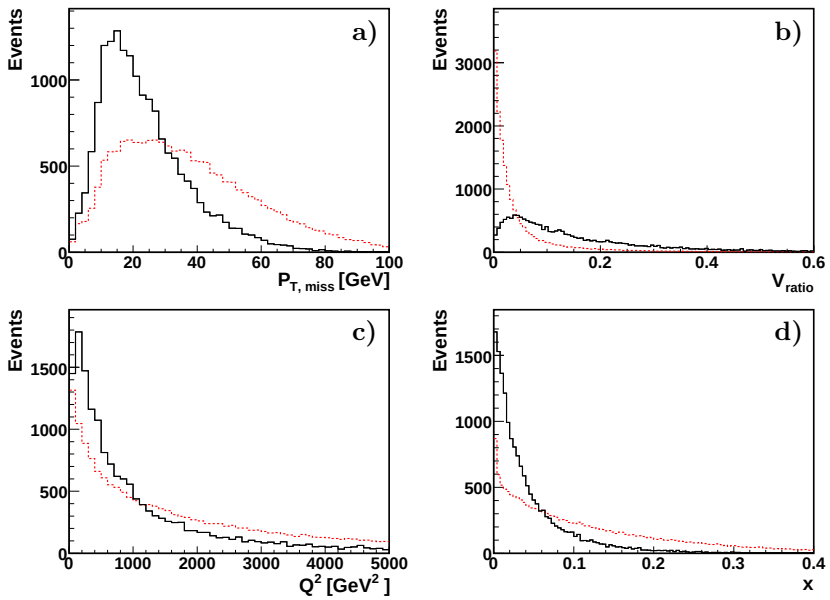

Figure 7.3: Kinematics of BGF (black, solid) and quark initiated (red, dashed) processes in e^-p scattering. The event quantities a) missing transverse momentum $p_{T,miss}$, b) energy flow isotropy V_{ratio}, c) four-momentum transfer squared Q^2 and d) Bjørken scaling variable x are shown. The histograms are scaled to the same number of entries.

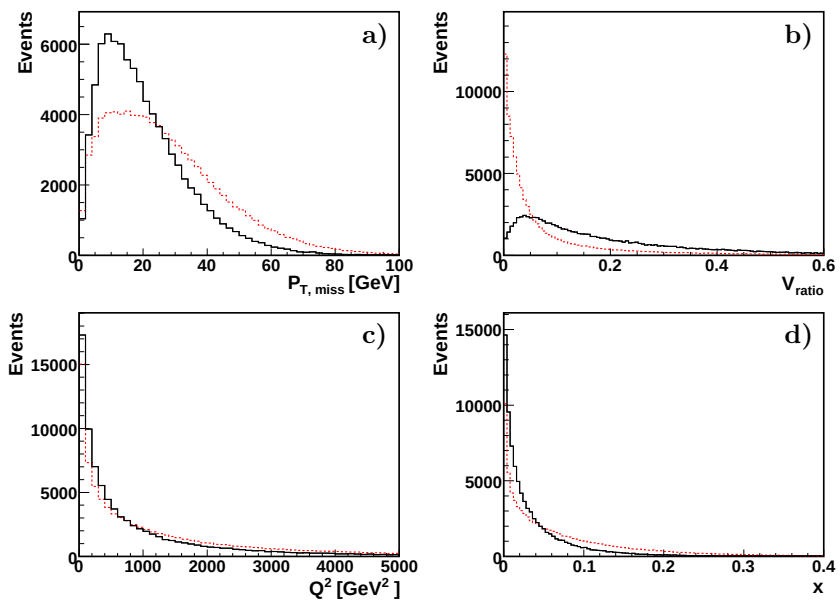

Figure 7.4: Kinematics of BGF (black, solid) and quark initiated (red, dashed) processes in e^+p scattering. The event quantities a) missing transverse momentum $p_{T,miss}$, b) energy flow isotropy V_{ratio}, c) four-momentum transfer squared Q^2 and d) Bjørken scaling variable x are shown. The histograms are scaled to the same number of entries.

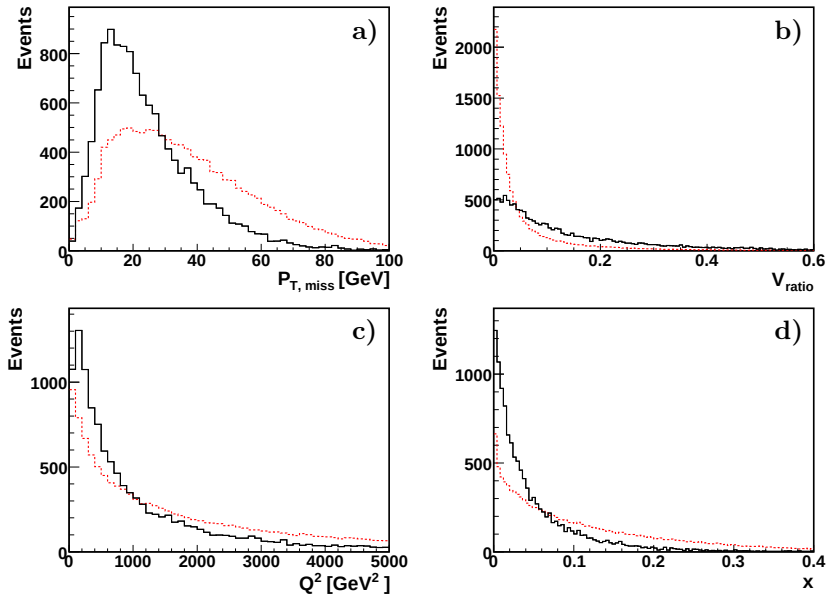

Figure 7.5: Kinematics of charm (black, solid) and non-charm (red, dashed) events in e^-p scattering. The event quantities a) missing transverse momentum $p_{T,miss}$, b) energy flow isotropy V_{ratio}, c) four-momentum transfer squared Q^2 and d) Bjørken scaling variable x are shown. The histograms are scaled to the same number of entries.

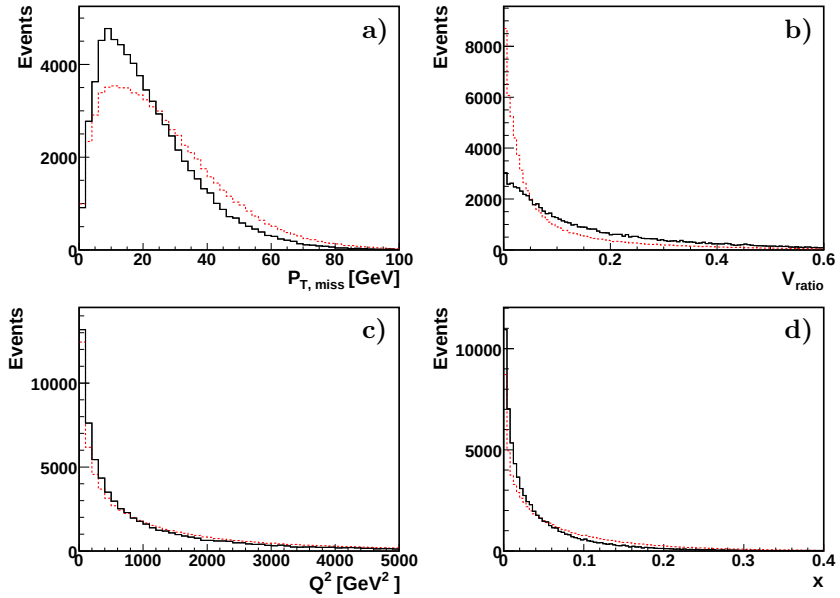

Figure 7.6: Kinematics of charm (black, solid) and non-charm (red, dashed) events in e^+p scattering. The event quantities a) missing transverse momentum $p_{T,miss}$, b) energy flow isotropy V_{ratio}, c) four-momentum transfer squared Q^2 and d) Bjørken scaling variable x are shown. The histograms are scaled to the same number of entries.

7.3.2 Selection Efficiency of Charm and Non-Charm Events

As a consequence of the differences in the event kinematics between quark initiated and BGF processes, the CC event selection efficiency for charm and non-charm events is different. In table 7.1 the efficiencies of the CC event selection determined from simulation for charm and non-charm CC events are listed. The charm events are further subdivided into events with hadronic and (semi-) leptonic decay modes of the charmed hadron. The selection efficiency for charm events is lower than for non-charm events, which is expected from the distributions of kinematic variables shown in section 7.3.1. The efficiencies for the e^+p sample are consistently higher than for e^-p because of the cut on the minimal lepton beam polarization of 20 %, which has a higher efficiency in the e^+p data sample (see section 6.4.4).

Table 7.1: Event selection efficiency for charm and non-charm CC events. The charm events are further subdivided into events with hadronic and (semi-) leptonic decay modes of the charmed hadron. The selection cuts applied correspond to the CC event selection summarized in section 6.5.

Event type	CC event selection efficiency [%]	
	e^-p	e^+p
Inclusive	61.8	67.6
Non-charm	62.4	68.8
Charm	56.8	63.3
Charm hadronic decay	57.5	63.7
Charm semileptonic decay	53.8	61.4

The differences in the CC event selection efficiency lead to different charm fractions in the selected CC event samples and unselected CC events. The charm fractions in unselected CC events can be calculated from the measured charm fractions in the selected CC event samples using the selection efficiencies given in table 7.1.

7.4 Methods for Charm Tagging

The lifetime of charmed hadrons is too short to enter the active detector volume. Therefore any measurement of charmed hadrons can only rely on their decay products. Different approaches have been used in the past for measurements of charm production processes:

- *Exclusive final states* such as decays of D^* mesons in the so called "golden channel" ($D^{*\pm} \to \pi^\pm D^0 \to \pi^\pm\pi^\pm K^\mp$) are often used for charm tagging [98–100]. If the fragmentation of charm into D^* mesons and the branching ratio of D^* mesons into the golden channel is known, the inclusive charm production cross section can be calculated from the number of tagged D^* mesons. Since the branching ratio of D^* mesons decaying in the golden channel is only about 2.6 % [17], this approach for charm measurements is only possible for event samples with high statistics. In an analysis of CC data, the event statistics are very limited. Nevertheless, this method has been used for a study of charm in CC [101]. Because of the limited statistics only an upper limit on the charm cross section in CC of $\sigma^{e^+p\to\bar{\nu}_e cX} < 109$ pb could be derived at 90 % confidence level in the kinematic range $Q^2 > 200$ GeV^2 and $y < 0.9$[1].

[1]The measurement presented in this thesis results in much better constraints on the charm cross section in CC, as will be seen in section 9.10.

- *Inclusive lifetime tagging* methods make use of the finite lifetime of charmed hadrons. This can lead to a displacement of the decay vertex from the primary event vertex of up to a few 100 μm. As a consequence, the tracks of charm decay particles in general do not point back to the primary vertex. This can be exploited either on the basis of statistical distributions of the distance between tracks and the primary vertex [102,103] or by explicitly reconstructing secondary vertices. Reconstructed secondary vertices have already been used for the measurement of charm in CC [104]. This approach is described in chapter 8.
- *Semileptonic decays into muons* of charmed hadrons are also used for charm production measurements [99], although this approach is more commonly used for the tagging of beauty hadrons. Muons provide a clean signature in the detector, which can be identified and selected with high efficiency. The charm fraction measurement using muons from semileptonic charmed hadron decays is described in chapter 9.

Chapter 8

Charm Fraction Extraction using Lifetime Information

8.1 Introduction

Hadrons containing a charm quark ("charmed hadrons") only have a finite lifetime and usually decay in the beam pipe before entering the active detector volume. The mean lifetime τ and flight distance $c\tau$ of some charmed hadrons in the hadron rest frame are listed in table 8.1.

Table 8.1: Lifetime τ in the hadron rest frame and flight distance $c\tau$ of some charmed hadrons [17].

Hadron	τ [fs]	cτ [μm]
$D^{\pm}$	1040 $\pm$ 7	311.8
D^{0}	410 $\pm$ 1.5	122.9
$D_s^{\pm}$	500 $\pm$ 7	149.9
Λ_c^{+}	200 $\pm$ 6	59.9
Ξ_c^{+}	442 $\pm$ 26	132

Charmed hadrons are produced close to the primary interaction vertex (in the following denoted PV)[1]. Typical decay lengths (distances between production and decay vertex) of charmed hadrons are up to a few 100 μm. A secondary vertex (SV) at a distance in this order of magnitude from the PV in a CC event is therefore an indication of a charmed hadron decay. The explicit reconstruction of a SV is discussed in section 8.3. If the efficiency of the SV reconstruction is known from simulation, the charm production cross section can be calculated from the number of reconstructed SVs. Tracks produced at a SV in general do not point to the PV position. This fact does not only help in identifying tracks originating from decays, it can also be used directly to separate charm from non-charm events on a statistical basis. This procedure is explained in section 8.4.

Analysis techniques based on lifetime information are well established for the measurement of charmed and beauty hadron decays in NC processes [102–104]. The event statistics of the CC sample is however much smaller. In addition to the problem of small CC statistics, charm decays are more difficult to reconstruct than beauty decays. This has several reasons: First, the lifetimes of beauty hadrons are larger than those of charmed hadrons due to the structure of the CKM matrix. This leads

[1] Charm production in beauty hadron decays can be neglected, because in CC almost no beauty is produced due to the structure of the CKM matrix ($V_{ub} \approx 0$).

to larger decay lengths and a clearer separation of primary and secondary vertex for beauty decays. Second, beauty hadrons are heavier than charmed hadrons, leading to larger transverse momenta of the decay particles relative to the beauty hadron flight direction. This facilitates the identification of decay tracks. Third, the decay multiplicities are higher for beauty decays than for charm decays. The decay multiplicity of charmed hadrons in simulation is shown in fig. 8.1. In average only 1.8 charged particles are produced in the decay of a charmed hadron. Taking into account the limited geometrical detector acceptance and track selection efficiency, only about a quarter of these decay particles can be used for the reconstruction of the SV (see section 8.2.3).

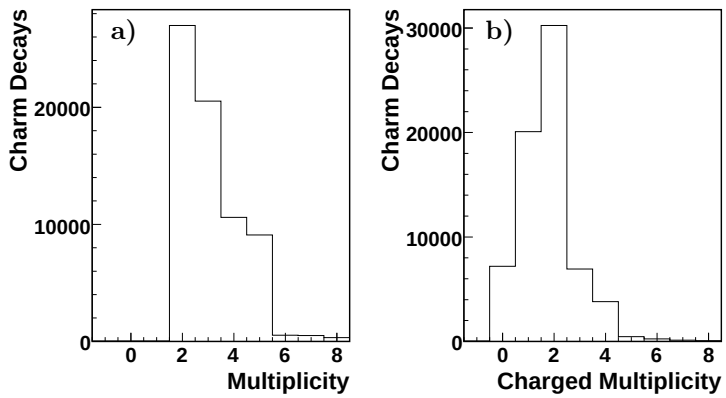

Figure 8.1: Multiplicity of charmed hadron decays a) in all particles and b) in charged particles.

In this chapter, the studies of charm in CC using analysis techniques based on lifetime information are documented. It is shown that the charm fraction in CC cannot be extracted with these techniques due to the low statistics of the CC event sample in combination with the low decay multiplicities of charmed hadron decays.

8.2 Tracks and Jets

All lifetime analysis techniques are based on the study of *tracks*. A track is the reconstructed trajectory of a charged particle traversing the tracking system of the H1 detector. For the lifetime studies only tracks measured in the Central Jet Chamber (CJC) are considered, since the resolution of the track parameters is not sufficient in the forward and backward region of the detector. In this section, the set of tracks used for the lifetime analysis is defined and explained.

8.2.1 Track Reconstruction Efficiency

The track reconstruction algorithm is briefly explained in section 4.3.3. The track reconstruction efficiency ε, defined as the ratio of reconstructed to simulated tracks, is shown in fig. 8.2 for tracks of charged pions in bins of transverse momentum p_T, polar angle θ and azimuthal angle ϕ of the simulated tracks. A steep rise of ε between track p_T values of 50 MeV and 100 MeV is observed. For $p_T \gtrsim 180$ MeV, ε is above 95 %. The shape of ε in θ is explained by the geometrical acceptance of the CJC. As expected, no dependence of ε on ϕ is observed.

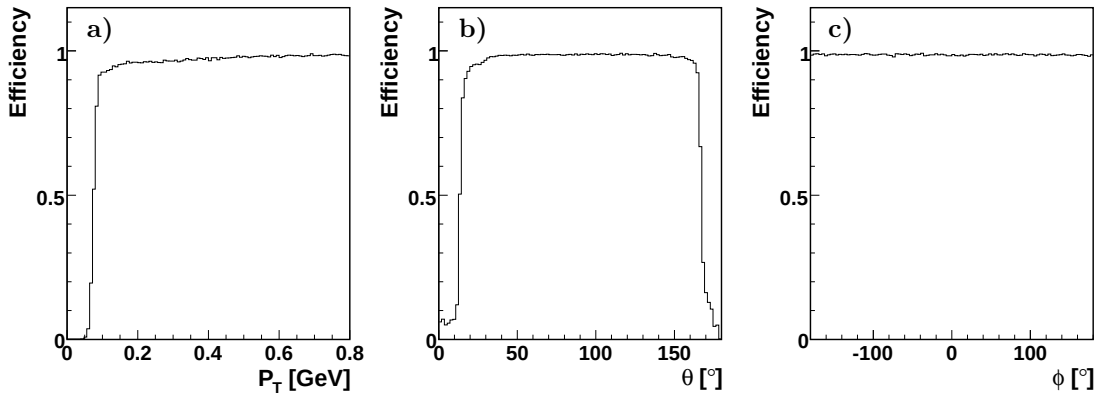

Figure 8.2: Track reconstruction efficiency for charged pions in simulation a) in bins of transverse momentum p_T for tracks with polar angle $40° < \theta < 140°$, b) in bins of θ for tracks with $p_T > 0.5$ GeV and c) in bins of azimuthal angle ϕ for tracks with $40° < \theta < 140°$ and $p_T > 0.5$ GeV.

8.2.2 CST Linking

Tracks originating from secondary vertices in general do not point back exactly to the primary event vertex. The distance of closest approach d_{ca} of a track is defined as the minimal distance of the extrapolated track to the reconstructed PV in the plane transverse to the beam axis. The expected decay lengths of charmed hadrons are in the range of a few 100 μm (see table 8.1). Therefore track d_{ca} resolutions below 100 μm are needed for lifetime measurements. The CJC only achieves a d_{ca} resolution of about 200 μm for tracks with $p_T > 1$ GeV [61]. The d_{ca} resolution is improved to about 50 to 90 μm for high p_T central tracks (depending on the azimuthal angle ϕ[2]) by adding information from the Central Silicon Tracker (CST, see section 4.3.2). The d_{ca} resolution with CST information included is shown in fig. 4.9. This improvement compared to CJC tracks is achieved by linking hits in the two CST layers to the CJC tracks extrapolated into the CST. The number of CST hits linked to the tracks and the probability distribution of the CST linking to CJC tracks are shown in fig. 8.3. Due to the two CST layers, tracks usually have zero, one or two hits linked. Overlaps of sensor elements can lead to three or four hits linked to one track. The acceptance of the outer CST layer is smaller than the CJC acceptance and limited to the polar angle range $30° < \theta < 150°$. Tracks outside this range only have one or no CST hit linked.

The CST was not operational in the years 2003 and 2004 and operated with reduced efficiency in 2005. Data from these years cannot (or in the case of 2005 only partly) be used for lifetime studies. This results in reduced CC event statistics for the lifetime analysis compared to the inclusive CC measurement. The charm fraction extraction using muons described in chapter 9 does not suffer from this problem, since the track parameter resolutions do not need to be as precise as for lifetime studies and CST information is therefore not needed.

8.2.3 Track Selection

Not all tracks found by the H1 reconstruction software are considered for the lifetime studies. The selection criteria applied on the tracks are listed in table 8.2.

As discussed in section 8.2.2, the resolution of the track d_{ca} is not sufficient for CJC tracks without CST information. For this reason, only tracks with at least two CST hits are selected. The probability

[2]The d_{ca} resolution depends on ϕ due to the elliptical shape of both the beam spot and the CST in the transverse plane.

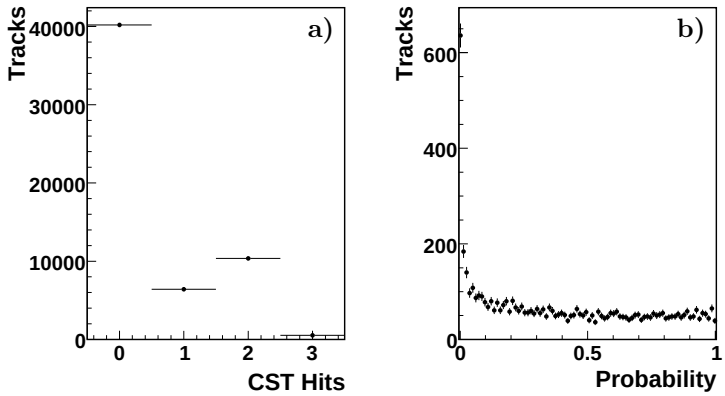

Figure 8.3: a) Number of CST hits linked to CJC tracks in 2006 data. The entries at zero hits are mainly due to the limited acceptance of the CST and very low momentum tracks where the track extrapolation is not reliable. b) Linking probability of CST hits to CJC tracks. The entries at very low probabilities are due to wrong combinations. The overall flat distribution indicates a correct treatment of the track and linking errors.

Table 8.2: Track selection criteria for the lifetime studies.

Cut variable	Cut value
Number of CST hits linked	$N_{\mathrm{CST}} \geq 2$
CST linking probability	$\mathrm{Prob}_{\mathrm{CST}} > 10\,\%$
Transverse momentum	$p_T > 300$ MeV
Radial length in CJC	$l > 15$ cm
Start radius	$r_{start} < 50$ cm
d_{ca} to the primary vertex	$d_{ca} < 2$ mm

of the CST hit linking to the CJC track needs to be above 10 % in order to suppress the linking of hits not caused by the track (detector noise or hits belonging to different tracks). At low track momenta, multiple scattering in the beam pipe or the detector material leads to large uncertainties on the track parameters. Therefore a minimal transverse momentum of the track of 300 MeV is required. The determination of the track parameters is also more precise for long tracks with many hits in the CJC. A minimal radial track length of 15 cm and a maximal start radius of 50 cm (meaning the first hit is still in the inner chamber CJC1) is necessary to pass the track selection.

Tracks originating from decays of charmed hadrons have a d_{ca} in the range of a few hundred μm at most. Tracks missing the primary vertex by several millimeters or more have their origin in decays of particles with longer lifetimes (mainly K_s^0 mesons), interactions of particles with matter or non-ep interactions such as beam-gas collisions. These tracks with large d_{ca} would dominate the reconstruction of secondary vertices and hide the charmed hadron signature in the event. Therefore tracks with a d_{ca} of more than two millimeters are rejected.

About 13 % of all CJC tracks found by the reconstruction software pass the track selection. For tracks originating from charmed hadron decays, the efficiency of the track selection is a factor of two higher at about 26 %. The inefficiency introduced by the track selection further aggravates the problem with low decay multiplicities of charmed hadrons (see section 8.1). The rejection of charm

decay tracks is mainly due to the cuts on the number of CST hits (imposing an indirect cut on the polar angle of about $30° < \theta < 150°$), transverse momentum and track length. These quantities are shown for charm decay tracks in simulation in fig. 8.4.

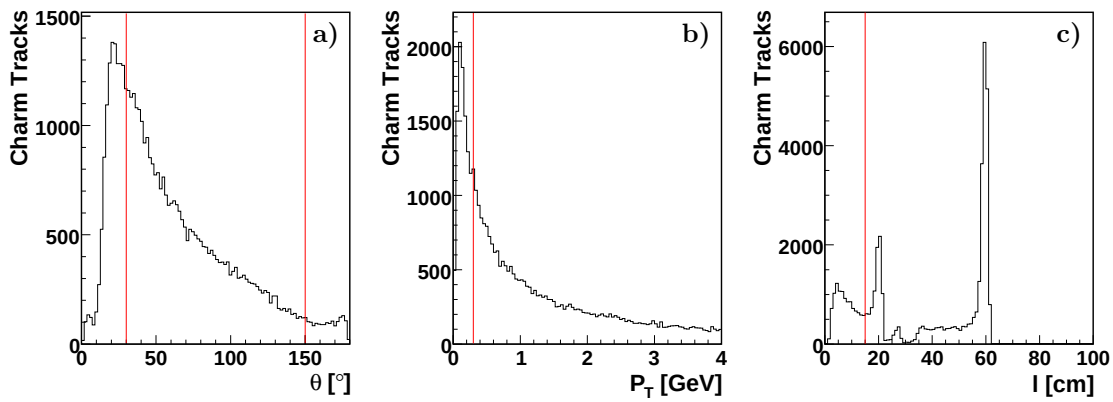

Figure 8.4: Properties of tracks originating from charm decays in simulation. In a) the polar angle θ, in b) the transverse momentum p_T and in c) the radial length l in the CJC of charm decay tracks are shown. The track selection conditions are indicated by the red lines.

8.2.4 Jets

In the hard ep interaction individual partons are produced. These outgoing partons produce parton showers and eventually recombine to hadrons. Since the transverse energies involved in the hadronisation process are typically much smaller than the hard scattering energies, the final state hadrons are collimated around the direction of the original parton. These bursts of particles in small angular regions of the detector are called *jets*. If the particles within a jet are reconstructed correctly and the assignment of particles to the jet is perfect, the direction and energy of the jet reflects the direction and energy of the original parton. In the case of charm production in CC, the charm quark produced in the hard interaction generates a jet along its original flight direction. The decay vertex of the charmed hadron is located within the jet, most likely close to the jet axis. Therefore the jets in an event give a starting point for the reconstruction of secondary vertices. This is illustrated in fig. 8.5, where the distance of the charm decay vertex to the jet axis $d_{\eta\phi} = \sqrt{(\eta_{vertex} - \eta_{jet})^2 + (\phi_{vertex} - \phi_{jet})^2}$ in pseudorapidity η and azimuthal angle ϕ is shown for the jet with highest and (if there is more than one jet) second highest p_T in the event. It can be seen that in most cases the charmed hadron is contained in the highest p_T jet in the event.

The jet objects are constructed from the measured tracks and energy deposits in the detector by first assigning particles to the jet (the jet finding) and then reconstructing the jet four-momentum from the four-momenta of the individual particles (the jet reconstruction). For the jets in this analysis the inclusive k_t-clustering algorithm [105, 106] with a p_T-weighted recombination scheme is used.

8.2.5 Assignment of Tracks to Jets

The jet finding algorithm mainly focusses on energy deposits and not on tracks. There is no minimal distance in space between two jets. If two jets are found close together, it is possible that individual particles are assigned to the wrong jet. In particular particles with high transverse momentum relative to the jet axis are affected. Due to the charmed hadron mass, tracks originating from charm decays

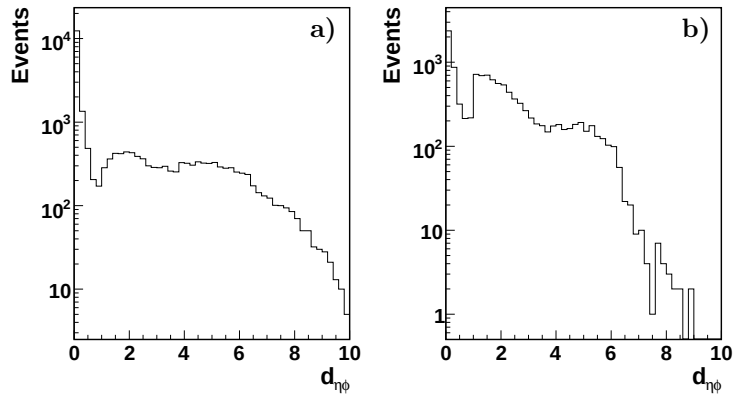

Figure 8.5: Distance in $\eta\phi$-space of the charm decay vertex to the jet axis for a) the highest p_T and b) the second highest p_T jet in simulated events. In most cases, the charmed hadron is contained in the highest p_T jet in the event and the jet axis reproduces the flight direction of the charmed hadron.

can have significant transverse momenta relative to the jet. Lifetime studies therefore do not rely on the association of tracks to jets performed by the jet finding algorithm. Instead, all tracks within a distance to the jet axis $d_{\eta\phi} < 1$ in pseudorapidity η and azimuthal angle ϕ are assigned to the jet. Only the jet axis is taken from the jet finding algorithm. This assignment of tracks to jets is not exclusive, a track can be associated to more than one jet.

For the reconstruction of secondary vertices from charm decays many possible combinations of tracks in an event have to be considered. By limiting the potential combinations to tracks in the same jet, the amount of possible track combinations is reduced substantially. In the following, the sets of tracks assigned to different jets are studied independently from each other.

8.2.6 Identification of Tracks Originating from Charm Decays

The reconstruction of secondary vertices from decays of charmed hadrons (in the following abbreviated with "charm decay vertices") would be much easier, if tracks originating from decays of charmed hadrons (in the following called "charm decay tracks") could be identified among the tracks associated to a jet. As potential discrimination variables for charm decay tracks the p_T and the d_{ca} significance $S_{dca} = d_{ca}/\sigma_{dca}$ of the tracks have been studied. In fig. 8.6 the p_T and S_{dca} rank of charm decay tracks are shown for the highest momentum jet in simulated events with exactly two charged charm decay tracks. The p_T rank of a track (and similarly the S_{dca} rank) denotes the position of the track in the p_T ordered list of tracks in the jet. A p_T rank of n indicates that the corresponding track has the $(n+1)$th highest p_T in the jet. If the charm decay tracks would always be the highest momentum tracks in a jet, the p_T rank of the tracks would always be one or two (since the events considered here contain charm decays with two charged tracks). This is not the case, as can be seen in fig. 8.6 a). Another reasonable assumption would be that charm decay tracks usually have a large d_{ca} and therefore a low S_{dca} rank in the jet. In fig. 8.6 b) it can be seen that this is not the case neither. Since it is not possible to reliably identify charm decay tracks within a jet by their high p_T and S_{dca}, charm decay tracks cannot be identified a priori and all tracks assigned to a jet have to be considered for the reconstruction of charmed hadron decays.

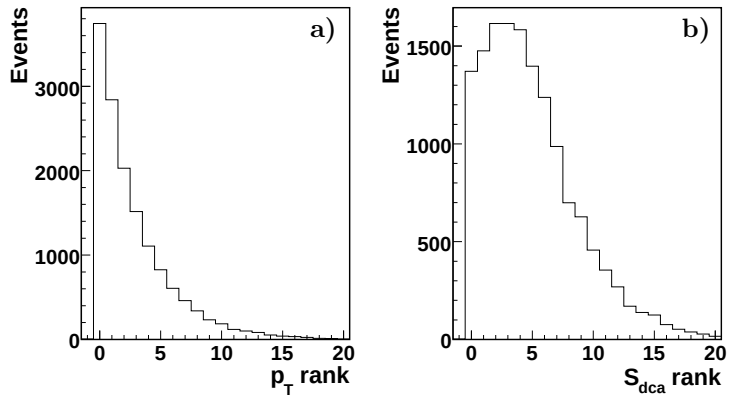

Figure 8.6: a) Transverse momentum p_T rank and b) significance of the distance of closest approach $S_{dca} = d_{ca}/\sigma_{dca}$ rank of charm decay tracks within the highest momentum jet in simulated e^+p events. Only events with charmed hadron decays into two charged tracks are shown. A p_T (S_{dca}) rank of n indicates that the corresponding track has the $(n+1)$th highest p_T (S_{dca}) in the jet.

8.3 Secondary Vertex Reconstruction

One way of charm tagging with lifetime information is the explicit reconstruction of decay vertices. The algorithm used for the secondary vertex finding and its performance are discussed in this section.

8.3.1 Deterministic Annealing Algorithm

For the reconstruction of exclusive final states, such as the decay $D^{*\pm} \to \pi^\pm D^0 \to \pi^\pm\pi^\pm K^\mp$, the decay multiplicity is fixed by the decay mode under study. The decay vertex can then be reconstructed by fitting every possible combination of a fixed number of tracks corresponding to the decay multiplicity and taking into account any additional constraints, e.g. the charge of the tracks. The fitted vertex with the best fit probability is then accepted as decay vertex candidate. In this scheme, the assignment of tracks to vertices is fixed.

In inclusive lifetime studies, the multiplicity of the decay is not known a priori. This can be taken into account by a more flexible assignment of tracks to vertices and a simultaneous fit of several vertices. The number of vertex candidates is not limited for the method presented here, however for this study only two vertex candidates have been implemented: A primary event vertex candidate (PV) and a secondary decay vertex candidate (SV). Each track in the jet is assigned a weight in the range from 0 to 1 to each vertex candidate. The weight w_{ij} of the track i to the vertex candidate j is given by

$$w_{ij}(T) = \frac{e^{-\frac{d_{ij}^2}{2T}}}{\sum\limits_{\text{vertices } k} e^{-\frac{d_{ik}^2}{2T}} + e^{-\frac{\mu^2}{2T}}}, \tag{8.1}$$

where $d_{ij} = d/\sigma_d$ with d the minimal distance of track i to vertex j is called the impact parameter significance of track i with respect to vertex j [107]. The parameter μ is a cut off for the rejection of outliers with $d_{ij} > \mu$. For this analysis μ is fixed with $\mu = 2$ cm. Because equation (8.1) appears similar to thermodynamic formulas, the parameter T is called "temperature".

The PV and SV candidates are found by an iterative procedure using deterministic annealing [108]. This method reliably converges to the global minimum of the minimization function by subsequently lowering T with each iteration. The two vertices and the assignment of tracks to vertices are deter-

mined simultaneously. The PV is constrained by the beam spot, while the SV has to stay outside the beam envelope. The input for the deterministic annealing process are two lists of tracks: A list of tracks in the jet, used for both the PV and SV determination, and a list of other tracks in the event, used only for the PV fit. The algorithm then proceeds as follows:

1. Choose two vertex prototypes. For the PV prototype, the PV position found by the H1 reconstruction software is set as initial position. For the SV prototype, the initial position is determined from the jet axis and the jet energy.
2. Set $T = T_{\text{start}}$.
3. Calculate all track-vertex weights according to equation (8.1). Tracks not belonging to the jet get a weight of 0 to the SV.
4. Refit both vertices individually taking into account the weights calculated in point 3.
5. Replace the vertices by the new vertices obtained in point 4.
6. Reduce T and go to point 3 if $T > T_{min}$, otherwise terminate.

The output of this algorithm are the positions of the PV and SV candidates and the track-vertex weights. The procedure is illustrated in fig. 8.7.

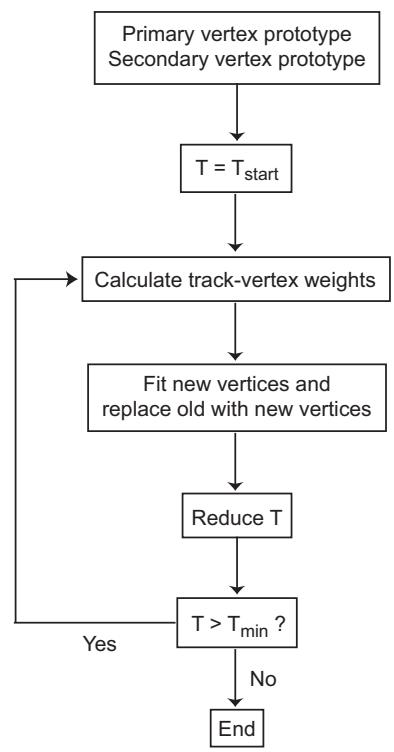

Figure 8.7: Schematic drawing of the deterministic annealing algorithm.

In every jet a SV candidate is constructed. Most jets however do not contain a charmed hadron and usually not even any decay vertex. Most of the obtained SV candidates are therefore fakes. Among the real decay vertices only a part originate from charmed hadron decays. The discrimination power between charm decay vertices and other vertices (including fakes) of different vertex properties has been studied. The most important quantities, the vertex multiplicity and the vertex decay length, are discussed in the following sections.

8.3.2 Track Weights and Vertex Multiplicity

The multiplicity of a vertex is defined as the number of tracks with a weight larger than 0.8 to this vertex. The weights of tracks in the highest p_T jet in the event to the primary and secondary vertex are shown in fig. 8.8 a) and b). A weight of 0 implies that this track-vertex combination has $d_{ij} > \mu$ and is not considered in the vertex fit. A large weight is achieved if the track is perfectly compatible with the vertex. The sum of the PV and the SV weight of a track does not rise above ~ 0.9 because of the outlier rejection term in equation (8.1). A weight of ~ 0.45 indicates an agreement of the track with both vertices. The large amount of tracks compatible with both vertices is an artefact of the method used for the vertex finding. In every jet a SV is constructed, even if in reality there is none. In such cases, all the tracks in the jet originate from the PV and the fitted SV will be located by construction at the center of the jet, where it is best compatible with most of the jet tracks. As a consequence, the tracks will be compatible with both the PV and the SV. The agreement of the data and the simulation is good but not perfect. In particular the fraction of tracks with a large weight $w \gtrsim 0.85$ to the SV is lower in simulation than in data. This is also reflected in a somewhat higher SV multiplicity for data as shown in fig. 8.8 d).

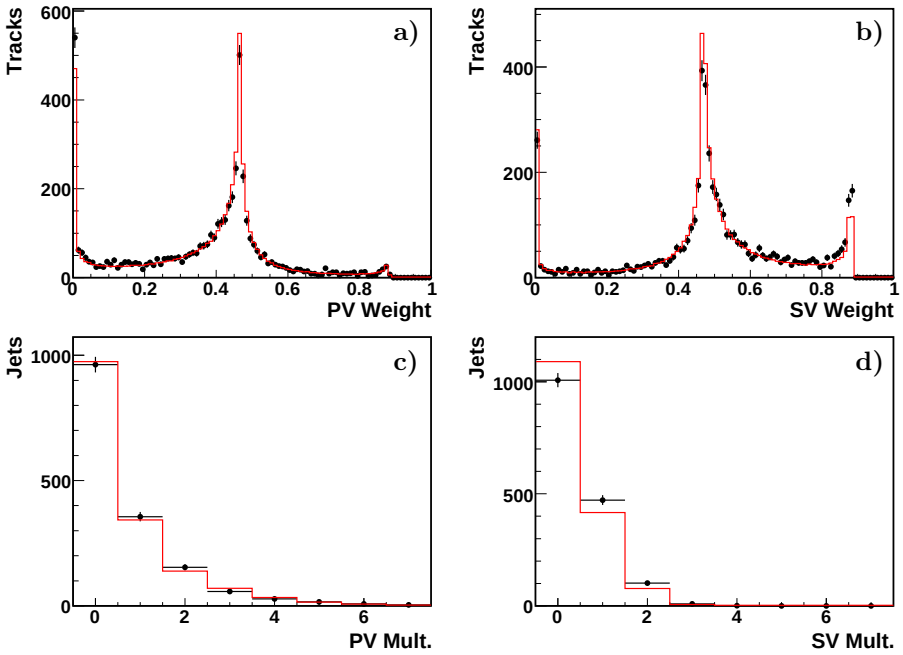

Figure 8.8: Track-vertex weights and vertex multiplicity in data (dots) and simulation (histogram). In a) the weight to the PV and in b) the weight to the SV of tracks assigned to the highest p_T jet in the event are shown. In c) the multiplicity of the PV and in d) of the SV are shown.

The contribution from fake SVs can be reduced by requiring a SV multiplicity of at least two, since a multiplicity of one could still be due to one single track in the jet with large d_{ca} to the primary vertex. More important than the discrimination between true and fake vertices is however the discrimination power of the multiplicity for jets containing a charmed hadron (in the following called "charm jets"). The multiplicities of the PV and the SV for charm and non-charm jets are shown in fig. 8.9 together with the number of tracks in the jet. To allow a better comparison of the distributions, the charm jet distributions are shown with and without scaling to the number of non-charm jets. It can be seen that the vertex multiplicity is higher for charm jets than for non-charm jets. This difference is however

small and not sufficient for the separation of the two contributions. This can be explained by the low charm decay multiplicity into charged tracks (see section 8.1), implying low vertex multiplicities for charm decay vertices. Not only the SV multiplicity, but also the PV multiplicity displayed in fig. 8.9 a) is higher for charm jets. The higher vertex multiplicities in charm jets are consistent with the higher number of selected tracks in charm jets compared to non-charm jets, which is shown in fig. 8.9 c).

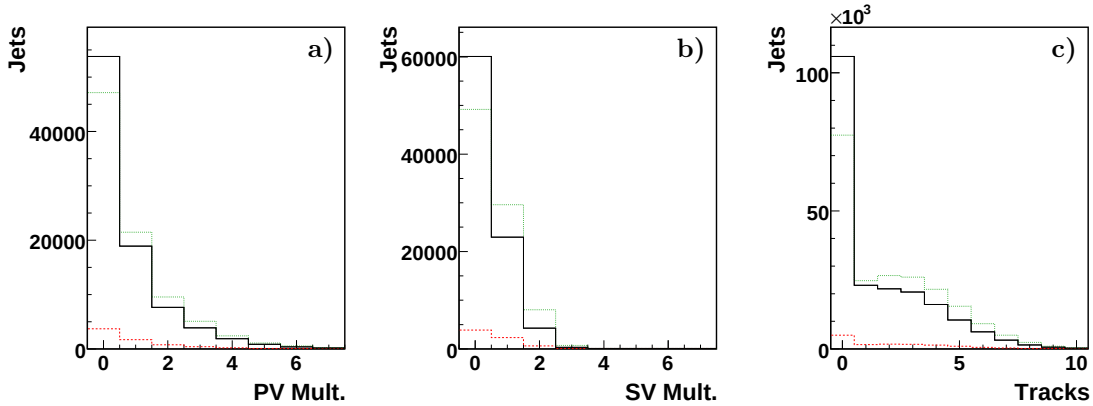

Figure 8.9: a) Primary and b) secondary vertex multiplicity for non-charm (solid, black) and charm jets in simulation. In c), the number of selected tracks in the jets is displayed. The charm jet histogram is shown with (green, dotted) and without (red, dashed) scaling to the number of entries in the non-charm histogram.

8.3.3 Decay Length

The decay length l of SV candidates, defined as the distance of the fitted primary and secondary vertices in the $r\phi$-plane projected on the jet axis, and its significance $S_l = l/\sigma_l$ are shown in fig. 8.10. The sign of the decay length is positive if $|\phi_{jet} - \phi_{vertex}| \leq 90°$ (modulo 2π) and negative otherwise. For these quantities the simulation shows a good agreement with the data.

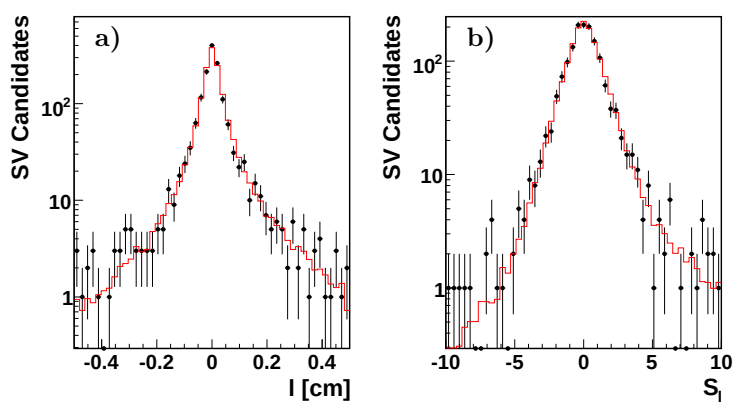

Figure 8.10: a) Decay length l and b) decay length significance $S_l = l/\sigma_l$ for all secondary vertex candidates in data (dots) and simulation (histogram).

The decay lengths for charmed hadron decays are in the range of a few hundred μm, for high momentum particles up to a few mm. For other vertices, l is expected to be either lower in the case of fake vertices or higher in the case of decays of strange particles such as the K_s^0. The l and S_l distributions for charm and non-charm jets are shown in fig. 8.11 a) and b). The distributions for charm jets are asymmetric towards positive decay lengths. This is due to correctly reconstructed charm decay vertices. Even at large positive l, the distributions are however still dominated by non-charm jets. The difference in the decay length of vertices in charm and non-charm jets is not large enough for a separation of the two contributions.

The contribution from fake SVs can be reduced by selecting only vertices with a multiplicity of at least two. The decay length significance for these SVs is shown in fig. 8.11 c). As expected, the asymmetry in S_l is larger for vertices with higher multiplicity due to the suppression of fake vertices. The statistics of the sample of jets with SVs with high multiplicity is however very small. The simulation shown in fig. 8.11 contains a factor of 30 more events than the selected CC sample in data. Therefore the statistics of the data sample is not sufficient to make use of the differences in S_l for charm and non-charm jets with a SV multiplicity of at least two.

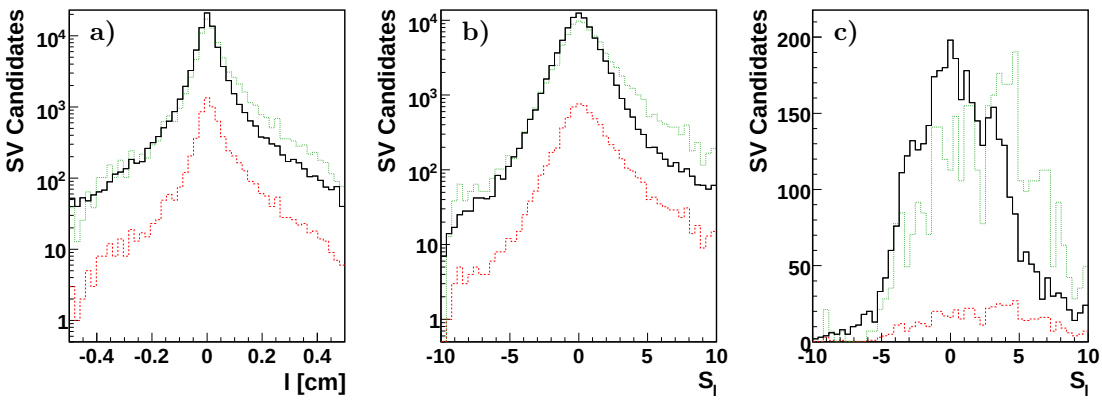

Figure 8.11: a) Decay length l and b) decay length significance $S_l = l/\sigma_l$ for all secondary vertex candidates in non-charm (black, solid) and charm jets in simulation. In c) S_l is shown for secondary vertices with a multiplicity of at least two. The charm jet histogram is shown with (green, dotted) and without (red, dashed) scaling to the number of entries in the non-charm jet histogram.

8.3.4 Performance of the Secondary Vertex Finding in Simulation

For correctly reconstructed charm decay vertices the decay length should always be positive. The negative contribution to the l and S_l distributions can partly be explained by resolution effects. Another explanation for negative l values in charm jets is a wrong reconstruction of SVs with PV tracks getting high weights to the SV. The origin of tracks with high weights to the SV and the performance of the algorithm in reconstructing the position of the SV have been studied.

The origin of tracks with weight $w > 0.8$ to the SV has been studied in simulation. In principle, tracks originating from the PV should always be compatible with the fitted PV and therefore get a weight to the SV of 0.5 in maximum. Therefore tracks with $w > 0.8$ to the SV should never originate

from the PV. This is however not true, as can be seen in table 8.3, where the origins of the tracks assigned to SVs are listed. For 78 % of all SVs with a multiplicity of at least one, all tracks (usually just one) with $w > 0.8$ originate from the PV. For 10 % of all SVs all tracks really originate from the same SV, which is however not a charm decay vertex. In 8 % of all cases all the high weight tracks originate from a charm decay vertex. For the remaining 4 % the tracks come from different vertices. The different contributions are listed in more detail in table 8.3.

Table 8.3: Origin of tracks with weight > 0.8 to the secondary vertex for secondary vertices with multiplicity > 0 in simulation.

Origin of tracks with $w > 0.8$	Contribution [%]
All from PV	78.0
All from the same non-charm SV when multiplicity = 1	9.6
All from the same non-charm SV when multiplicity > 1	0.5
All from the same charm SV when multiplicity = 1	6.4
All from the same charm SV when multiplicity > 1	1.3
One from a non-charm SV and the rest from the PV	2.3
One from a charm SV and the rest from the PV	1.2
Tracks from more than one SV	0.5

In simulation, the fitted SV position and its decay length can be compared to the "true" simulated values[3] in jets containing a charmed hadron. In fig. 8.12, the distance in the $r\phi$-plane between the fitted and the simulated position of the charm decay vertex is shown for all jets containing charm decay tracks. The mean distance between fitted and true vertex position is about 0.9 mm and has large tails. This means that in many cases the fitted position of the SV is off by several millimeters, even in jets containing tracks from charm decays. Also shown is the fitted against the simulated decay length of the charm vertex in these jets. As expected, the true decay length is almost always positive. The few cases of negative decay lengths originate from decays where the difference in ϕ of the charmed hadron flight direction and at least one of the decay tracks is large. The jet containing this track can then point to another direction than the charm decay vertex and the decay length can be negative. The fitted decay length on the other hand is almost symmetric around zero. The correlation of fitted and true decay length is poor, as can be seen in fig. 8.12 b).

The comparison of true and fitted vertex quantities explains the poor separation power of this vertex reconstruction method for charm and non-charm jets. The two most important discrimination variables both suffer from problems: The SV multiplicity (see section 8.3.2) contains a large contribution from PV tracks and the fitted decay length (see section 8.3.3) is only weakly correlated with the true decay length. Because of these problems, and taking into account the limited statistics of the CC sample, the charm fraction extraction with this method is not possible.

[3] In this case the position of the charm decay vertex and its distance to the primary event vertex after the generator and detector simulation step (see section 5.1).

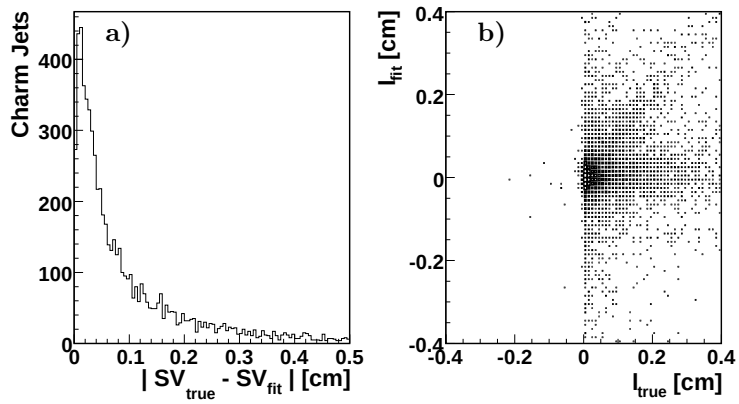

Figure 8.12: Comparison of simulated and fitted secondary vertex positions and decay lengths. In a) the distance in $r\phi$ between the simulated and the fitted secondary vertex position and in b) the simulated against the fitted decay length l is shown for jets containing charm decay tracks. There are only very few entries for negative simulated l since the "true" l in simulated jets is always positive (exceptions are due to a wrong assignment of tracks to jets). The vertical (horizontal) band of entries is due to jets with very small simulated (fitted) l. The diagonal structure in the upper right quadrant represents jets with correctly reconstructed l.

8.4 Statistical Analysis of Track Impact Parameters

8.4.1 Analysis Method

Lifetime information can also be used by means of a statistical analysis of track impact parameters without an explicit reconstruction of secondary vertices [102, 103]. Here the impact parameter δ of a track is defined as the minimal distance of the extrapolated track to the primary event vertex, with a positive sign if $|\phi_{\text{track}} - \phi_{\text{PV}}| \leq 90°$ (modulo 2π) and a negative sign otherwise[4]. The impact parameter significance S_δ is then defined by $S_\delta = \delta/\sigma_\delta$.

The following quantities are defined for jets:

- S_1 is the S_δ of the track with the highest S_δ in the jet.
- S_2 is the S_δ of the track with the second highest S_δ in the jet. A jet only enters the S_2 distribution if at least two selected tracks are linked to the jet and S_2 has the same sign as S_1.
- S_3 is the S_δ of the track with the third highest S_δ in the jet. A jet only enters the S_3 distribution if at least three selected tracks are linked to the jet and S_3 has the same sign as S_1 and S_2.

The distributions of these variables are determined in simulation for jets containing no heavy quarks (the so called uds jets), jets containing charmed hadrons and jets containing beauty hadrons (in the case of NC samples, in CC the beauty contribution can be neglected). These templates are then fitted to the data distributions using a Barlow fit [109] in order to extract the relative contributions from uds, charm and beauty jets to the total data sample.

The distributions of all variables derived from the impact parameter of tracks are asymmetric towards positive sign. This is due to tracks originating from decays of particles in the jet, which always have positive δ except for resolution effects. The contribution from decay tracks can be enlarged and resolution effects suppressed by a bin wise subtraction of the negative from the positive side of the distributions. The higher decay multiplicity of beauty hadron decays compared to charm decays is

[4]The impact parameter δ and distance of closest approach d_{ca} of a track are identical. Because the technique discussed here is known as "impact parameter method" [102], this quantity is called "impact parameter" in this section. In other sections the term d_{ca} is used.

exploited in NC samples by the S_2 and S_3 distributions. The uds contribution can be constrained in addition by using the overall normalization of the data compared to the simulation, i.e. the inclusive number of selected events.

8.4.2 Performance of the Impact Parameter Analysis in CC Simulation

The S1, S2 and S3 distributions for e^+p data and simulation are shown in fig. 8.13. Also shown are the subtracted distributions, where the negative side has been subtracted bin wise from the positive side of the distributions. The shapes of the S1, S2 and S3 distributions are well described by simulation. The separation power between the charm and uds contributions mainly arises from the subtracted distributions. The statistics of the CC data samples is however clearly not sufficient in order to use the data distributions in a fit. The impact parameter method is therefore not applicable for the small data sets studied in this thesis.

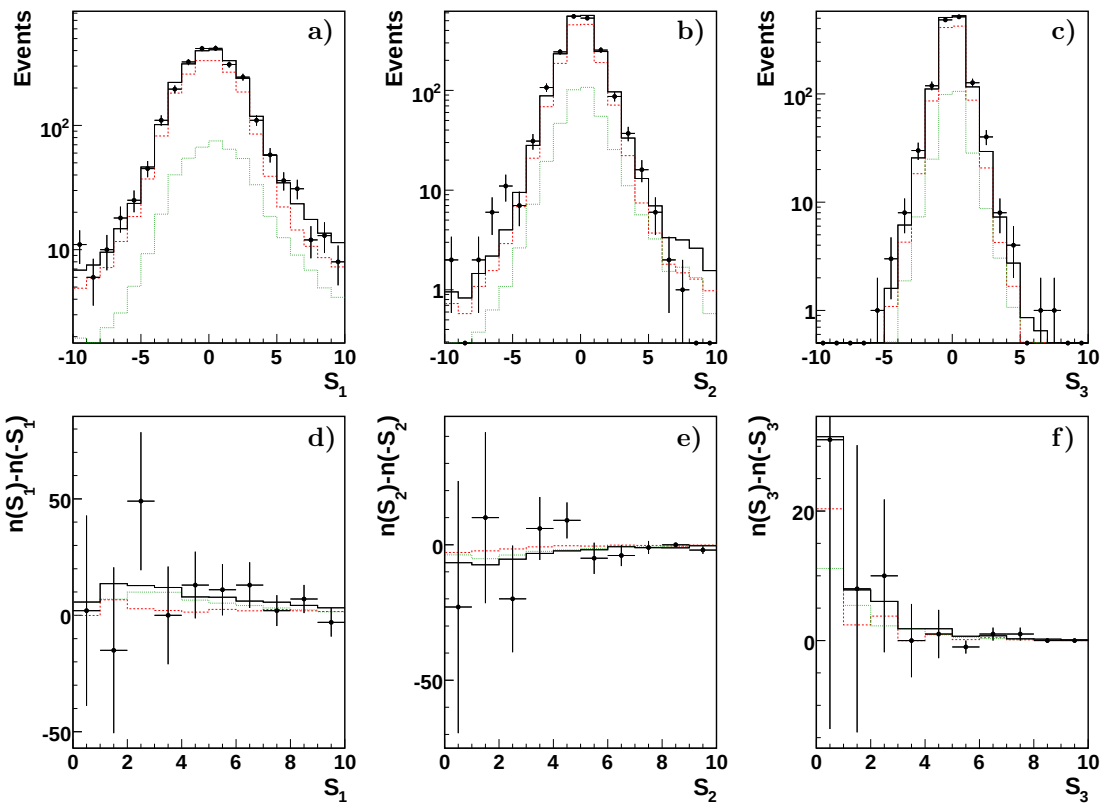

Figure 8.13: a) S1, b) S2, c) S3 and d)-f) corresponding subtracted distributions for the combined HERA I and HERA II positron CC data sample and simulation. The dots represent the data, the black, solid line the total simulation, the red, dashed line the uds contribution and the green, dotted line the charm contribution.

Chapter 9

Charm Fraction Extraction using Muons

9.1 Introduction

Using semileptonic decays of charmed hadrons is a well established method for charm measurements. The main advantage of this approach is the clear signature provided by the decay muon. The drawback is however the loss in statistics due to the branching ratio of charmed hadrons into decays containing muons, which is about 10 % [17]. This branching ratio reduces the already limited statistics of the charged current sample even more.

As a consequence of charge conservation at each vertex, muons produced in the decay of a charmed meson in CC events must have the same charge as the beam lepton (i.e. positive for positron running and negative for electron running). This is illustrated in fig. 9.1, using a typical process for charm in CC as an example. Muons originating from other processes are expected to have a smaller charge asymmetry. Therefore it is possible to extract the charm content of the CC sample by measuring the charge asymmetry of muons.

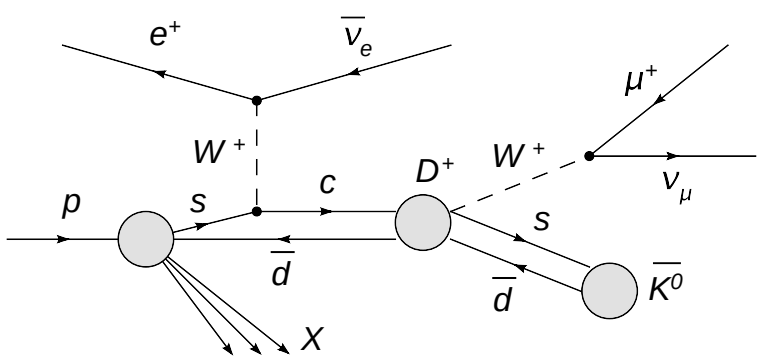

Figure 9.1: Example process for charm in charged current for e^+p scattering. The muon produced in the charmed meson decay must always have the same charge as the beam lepton.

The decay ratio of charmed hadrons into leptons and the charge distributions of these decay leptons in the simulation on generator level are shown in fig. 9.2. As a consequence of lepton number conservation, always pairs of a neutrino and a charged lepton (and therefore even numbers of leptons) are produced. Of these lepton pairs, only the charged lepton is measured while the neutrino escapes undetected. As can be seen in fig. 9.2 a), in 18 % of the charm decays one and in 0.2 % two charged

leptons are produced. These charged leptons are split about evenly between electrons and muons, with a very small contribution from taus[1]. In fig. 9.2 b) and c), the charged charm decay leptons are represented by their PDG code [17], where 11 stands for e^-, 13 for μ^-, 15 for τ^- and corresponding negative numbers for their anti-particles. The charge of the charm decay leptons is almost completely asymmetric as expected from the argument above. The contribution from leptons with "wrong" charge arises from events with a $c\bar{c}$ pair produced in fragmentation and consequently more than one charmed hadron in the event. The fraction of $c\bar{c}$ pairs from fragmentation in CC is independent of the beam lepton charge, while the fraction of single c quarks produced directly in the hard interaction in CC events is about twice as large in e^+p as it is in e^-p scattering (see section 7.2.2). Therefore the fraction of charmed hadrons produced in fragmentation is higher in e^-p, which reflects in the larger contribution from leptons with "wrong" charge in fig. 9.2 c).

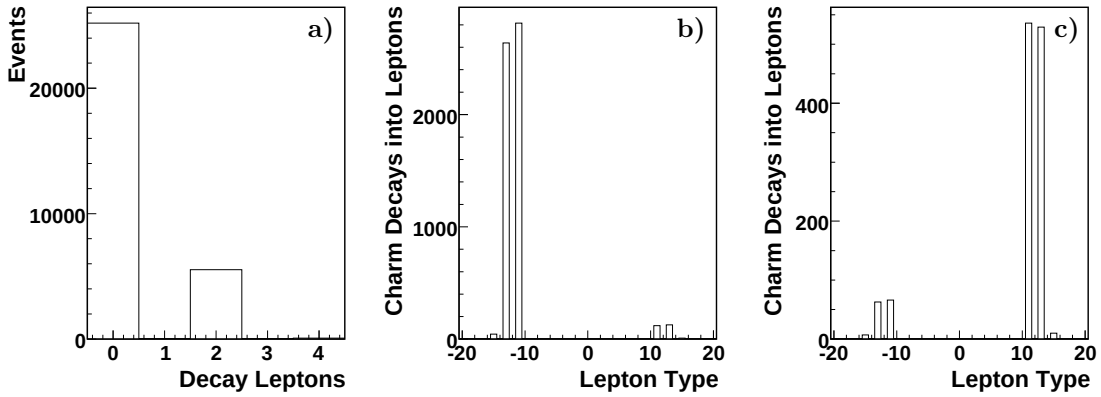

Figure 9.2: Properties of leptons from charm decays on generator level. a) Number of leptons (including neutrinos) from charm decays. b), c) Type of the charged lepton from charm decays, here $11 = e^-$, $13 = \mu^-$, $15 = \tau^-$ and corresponding negative numbers for their anti-particles. In b) e^+p and in c) e^-p simulation is shown.

9.2 Muon Selection

Muons are detected in most of the subsystems of H1, including the tracking system, LAr calorimeter and the dedicated muon system (see chapter 4 for technical details on the different subsystems). The main indication for a muon is however the presence of a track in the muon system, since most other types of particles would not be able to penetrate the massive calorimeters located between the muon chambers and the interaction point. In the following, the muon selection will be described in detail.

The choice of the cut variables for the muon selection is natural and to a large extent given by the hardware setup of H1. The optimal choice for the individual cut values is however not always obvious. While a harder cut in many cases leads to an improved purity of the muon candidate sample, it also results in a loss of statistics and corresponding higher statistical errors. An iterative procedure for the determination of the cut values has been used: The optimal value for a cut was defined as the value resulting in maximal expected significance of the charm fraction measurement (defined in simulation as the predicted result of the measurement divided by its predicted statistical error) with all other cuts kept fixed. Once this value was found, the corresponding cut was fixed and the next cut studied. This was iterated several times for all cuts involved in the muon selection.

[1] Tau leptons are much heavier than electrons and muons, with a mass of $m_\tau = 1.78$ GeV [17]. Since the masses of most charmed mesons are only marginally larger, the phase space for decays into taus is small.

9.2.1 Preselection of Muon Candidates

As a starting point for the muon selection the muon candidates found by the H1 reconstruction software H1REC have been used. In H1REC first the track finding algorithms are run for each subdetector separately. If a track was found in the muon system (referred to as outer track), all potential muon tracks in the tracking system (inner tracks) are identified. This is done by matching azimuthal and polar angles and selecting only tracks with a transverse momentum p_T larger than 1 GeV (for the cut on p_T see also section 9.2.3). The selected tracks are extrapolated to the muon system taking into account multiple scattering and energy loss due to ionization (assuming a muon). For each possible inner-outer track combination, a χ^2 value according to the equation

$$\chi^2 = \left(\overrightarrow{X}_{inner} - \overrightarrow{X}_{outer}\right)^T V^{-1} \left(\overrightarrow{X}_{inner} - \overrightarrow{X}_{outer}\right) \tag{9.1}$$

is calculated, where $\overrightarrow{X}_{inner}$ contains the track parameters of the extrapolated inner track and $\overrightarrow{X}_{outer}$ those of the muon system track. Used as track parameters are the z coordinate and the azimuthal angle of the innermost hit in the muon system and the azimuthal angle of the track in the muon system. V is the joint covariance matrix. If the probability derived from the calculated χ^2 is larger than 10^{-4}, the linking hypothesis is accepted. The cuts applied on tracks in the muon system and on the linking of inner and outer track in the barrel region are summarized in table 9.1. Similar sets of cuts also exist for the muon system endcaps.

Table 9.1: Muon preselection cuts in the CMD barrel. ρ_0 and z_0 are the cylinder coordinates of the extrapolated muon system track with respect to the event vertex at the point of closest approach.

Quantity	Cut
ρ_0	< 100 cm
z_0	< 100 cm
number of hit layers	> 2
first layer hit	≤ 5
last layer hit	≥ 2
link probability	$> 10^{-4}$

The preselected muon candidate sample also contains muon candidates found by a muon identification algorithm with looser cuts on the muon system track and the linking. Furthermore there are muon candidates identified in the LAr calorimeter without outer track. Therefore the preselected muon candidate sample contains muon candidates not fulfilling the cuts in table 9.1. All these additional muon candidates will however be removed by the selection cut on the linking discussed in section 9.2.4.

The efficiency of the muon identification in the muon system depends on the momentum of the muon and the polar angle. For muons with transverse momentum $p_T > 2$ GeV the efficiency of the muon preselection is between 60 % and 80 % for most regions in polar angle θ, except for the transition region from barrel to endcap. The efficiency in this region is lower, because the tracks pass both the edge of the endcap and the barrel, resulting in two very short tracks (there is no common track reconstruction in barrel and endcap). In fig. 9.3 the efficiency of the muon preselection in bins of θ and p_T is shown. A detailed study of the muon reconstruction efficiency can be found in [110]. A significant fraction of the muons originating from charm decays in CC events are produced at very low polar angles and low momenta and do not reach the muon system (see sections 9.2.2 and 9.2.3). These charm decay muons cannot be reconstructed and identified. Therefore the total efficiency of the preselection (including the reconstruction efficiency) for all produced charm decay muons in simulation is lower than the discussed identification efficiencies and is only about 36 %.

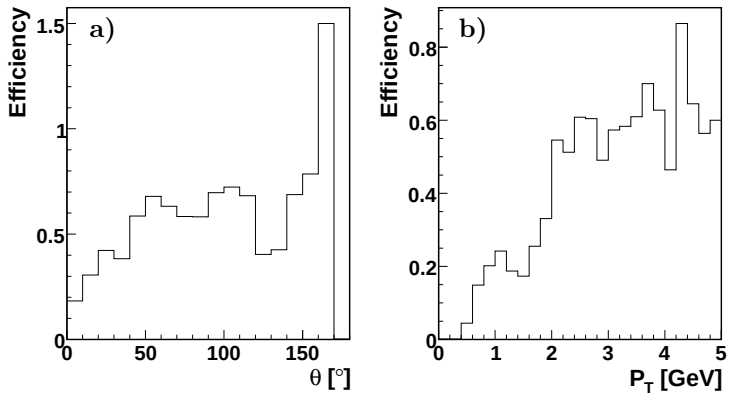

Figure 9.3: Efficiency of the muon preselection a) in bins of polar angle θ for muons with $p_T > 2.5$ GeV and b) in bins of p_T for central muons with $40° < \theta < 110°$.

The purity of the preselected muon candidate sample has been studied using simulation. In a simulated CC sample for e^+p running, the actual muons constitute only about 12 % of the preselected muon candidates. For muon candidates with an inner track originating from a charmed hadron decay (in the following called charm decay particles) this fraction is 72 %, meaning most of the charm decay particles identified as muons are real muons. Among other muon candidates (non-charm particles) only 9 % are actual muons. Instead, the majority of the non-charm muon candidates are charged pions. The constitution of the muon candidates in a simulated CC sample can be seen in fig. 9.4. The muon selection will enrich the charm content of the muon candidate sample, which in the preselected sample is only about 5 %, by rejecting background from fake muons.

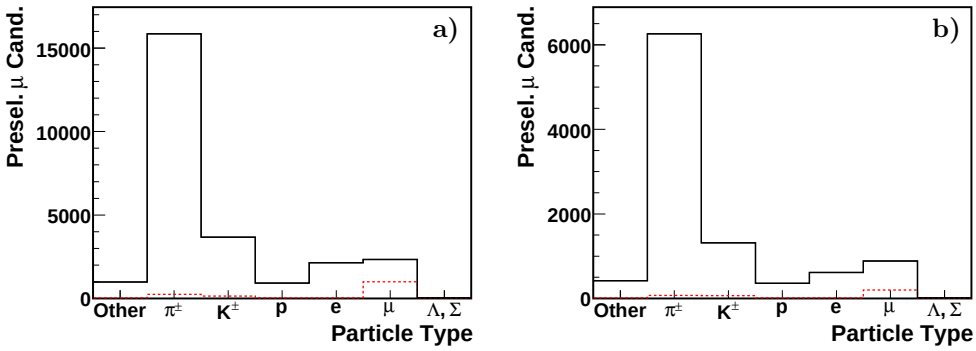

Figure 9.4: Particle type of preselected muon candidates in a) e^+p and b) e^-p CC simulation. The contributions from charged pions, charged kaons, (anti-) protons, electrons and positrons, muons and strange baryons are separately listed. All other particles are contained in the first bin. The black line represents particles not originating from charm decays while the dashed red line indicates charm decay particles.

9.2.2 Polar Angle

The cuts on the polar angle θ are motivated by the detector geometry and cannot be loosened without a significant increase of non-muon background in the sample. In the very forward region, the proton remnant produces many high momentum tracks faking muons. Furthermore tracking is very difficult because of high track densities and the inner/outer track link is therefore unreliable. For these reasons a cut on the polar angle of $\theta > 15°$ has been applied. In the backward region, the calorimeters contain much less material than in the forward and central region. Therefore particles lose less energy in the calorimeters and can penetrate into the muon system, producing a high rate of fake muons. To avoid these problems, the outer track of the muon candidate has to be either in the forward endcap or the barrel of the instrumented iron. Together with the cuts on the outer track length this poses an indirect cut on θ of about $\theta < 130°$.

In simulation, most charm quarks are produced in forward direction. This is shown in fig. 9.5 a). The CC event selection suppresses however events with charm quarks produced at a polar angle below 20°, mainly due to the vertex requirement. The vertex is reconstructed using tracks measured by the CJC. Very forward events without tracks in the angular acceptance of the CJC are rejected. Not suppressed are events containing a $c\bar{c}$ pair produced in fragmentation, where one of the charm quarks is in the very forward and one in the central region. The same is true for multiple jet events with a very forward jet containing the charm quark and at least one other jet in the acceptance of the CJC. These events are not affected by the vertex condition in the CC selection and lead to a steep rise of the polar angle distribution of the charm quark at $\theta < 5°$, as can be seen in fig. 9.5 b).

The polar angle distribution of muons produced in decays of charmed hadrons closely follows the distribution of the charm quarks and is shown in fig. 9.5 c). The muon selection requirement in the forward direction of $\theta > 15°$ leads to a significant loss in statistics for charm decay muons. Most of these very forward muons have however already been rejected by the vertex requirement in the CC event selection as explained above and, even more important, the inefficiency of the muon preselection in the forward region (see fig. 9.3). For this reason, the cut on the polar angle still has an efficiency of 88 % for preselected charm decay muons. The muon selection requirement in the backward region does not lead to a significant reduction in signal statistics. The charm content of the preselected sample is increased slightly to 6 % by the application of the polar angle cut in e^+p simulation.

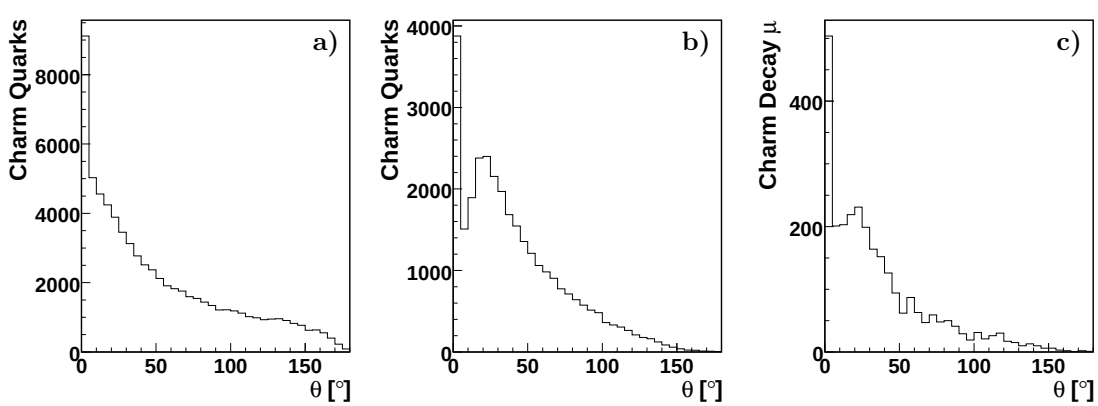

Figure 9.5: Polar angle θ on generator level in a simulated CC sample of a) the charm quarks without CC event selection, b) the charm quarks in selected events and c) the charm decay muons in selected events.

9.2.3 Momentum

Muons are minimal ionizing particles (MIPs) and do not produce showers in the calorimeters. A MIP deposits on average about 10 MeV energy per traversed centimeter in lead. In order to penetrate the calorimeter and reach the muon system, the muon energy has to be larger than 1.5 GeV (in the central region, the minimal energy varies depending on θ). In the muon system muons lose about 90 MeV per layer. Since a muon track needs to traverse several layers in order to be identified, the muon energy has to be above 2 GeV in order to be detected with an efficiency larger than 50 %. Therefore for muon candidates identified in the barrel of the muon system a cut on the transverse momentum of $p_T > 2$ GeV and in the forward endcap a cut on the momentum of $p > 2$ GeV has been applied.

As can be seen in fig. 9.6, this cut results in a significant loss of statistics for charm decay muons. Since a momentum cut has already implicitly been applied in the preselection, the additional effect of this cut on the preselected sample is small. The efficiency of the momentum cut is 80 % for preselected charm decay muons and the charm content of the preselected sample is increased to 9 % by the application of the momentum cut in e^+p simulation.

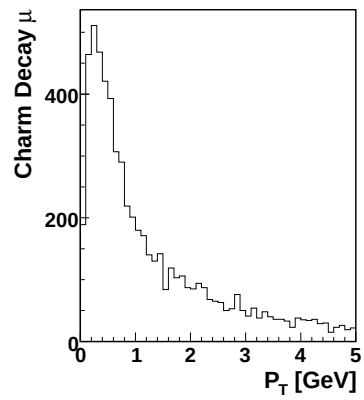

Figure 9.6: Transverse momentum of charm decay muons in simulation.

9.2.4 Linking

The cuts on the polar angle and the (transverse) momentum ensure that the muon candidate could potentially reach the muon system (in case the candidate really is a muon) and should leave a track both in the tracking chambers and the muon system. The cut on the linking of inner and outer track now explicitly requires the muon candidate to be detected by the muon system. It is only passed by muon candidates, if both tracks exist and their linking probability calculated from the χ^2 of equation (9.1) is above 5 %. The linking probability distribution can be seen in fig. 9.7. The entries at very low probabilities are due to wrong inner/outer track combinations, while the overall flat probability indicates a correct fit and good description of track errors.

The presence of a track in the muon system is the main criterion for the identification of muons. The cut on the linking probability rejects muon candidates with wrong inner/outer track link or no such link at all. This results in a drastic reduction of non-muon background: The fraction of muons in the muon candidate sample in e^+p simulation with the linking cut applied is 36.6 % compared to only 12 % in the preselected sample. Since the contribution from muons to the muon candidate sample is higher for charm than for uds, also the charm content of the sample is increased significantly to 21 % compared to 5 % in the preselected sample. The efficiency of the cut on the linking probability for preselected charm decay muons is 68 %.

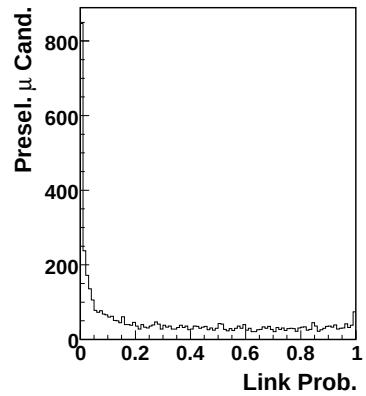

Figure 9.7: Probability of inner/outer track linking for all preselected muon candidates.

9.2.5 Track Length

In order to have well measured tracks, cuts are applied on the track length both for the inner and outer tracks. For tracks measured in the CJC a radial track length of at least 22 cm is required, ensuring the track was detected both in the inner CJC1 and the outer CJC2. For tracks in the FTD a cut on the track length along the beam axis of at least 40 cm is applied. These tracks are detected in at least two of the three FTD supermodules. Tracks in the muon system need hits in at least three layers in order to be accepted. Furthermore the first and last layer hit by a track need to be at least five layers apart. The relevant quantities of preselected muon candidates are plotted in fig. 9.8.

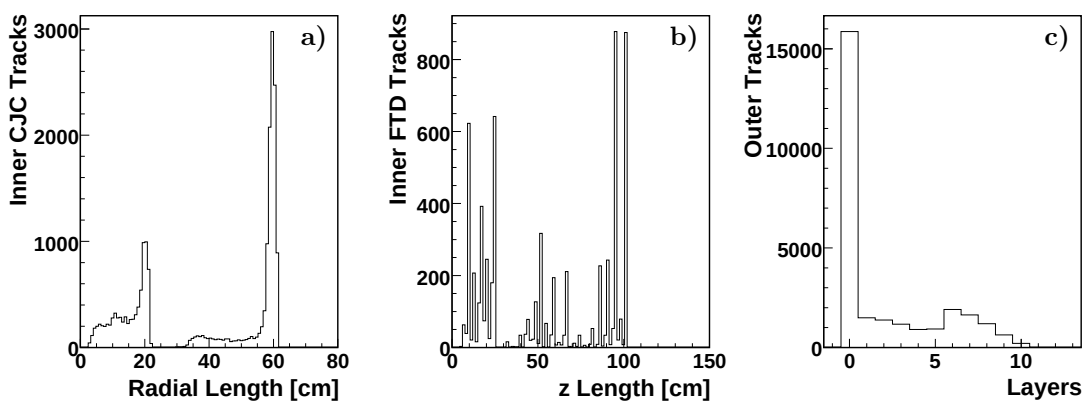

Figure 9.8: Track length quantities for preselected muon candidates. a) Radial track length of inner tracks in the CJC; b) Track length along the beam axis for inner tracks in the FTD; c) Number of layers hit by the outer track in the muon system.

The cuts on track length parameters implicitly cut also on the polar angle (due to limited acceptance, mainly of the tracking system), the momentum (long tracks in the muon system require high momentum) and the presence of an outer track. Furthermore fake tracks composed of noise hits are suppressed. Therefore the efficiency for preselected charm decay muons of 50 % is low compared to other muon selection cuts. The charm content of the preselected muon candidate sample in e^+p simulation is increased to 17 % by the application of the cuts on track length variables.

9.2.6 Complete Muon Selection

All cuts of the muon selection discussed in detail in the previous sections are summarized in table 9.2.

Table 9.2: Muon selection cuts.

Cut variable	Cut value
Polar angle	$15° < \theta \lesssim 130°$
	(track not in backward endcap)
Momentum	$p_T > 2$ GeV in barrel
	$p > 2$ GeV in forward endcap
Linking probability	Prob > 5 %
Inner track length	$l_r > 22$ cm in the CJC
	$l_z > 40$ cm in the FTD
Outer track length	$N_{\text{layer}} > 2$
	(first layer − last layer) > 4

The individual cuts have a big overlap. For instance the cut on the linking probability of inner and outer track indirectly cuts on the polar angle (polar angle dependent efficiency of the muon identification), the momentum (existence of an outer track) and the track length (identification of the tracks in the individual subsystems and quality of the fit). Therefore the efficiencies of the individual cuts cannot be simply multiplied. The efficiency of the total muon selection determined from simulation for preselected charm decay muons is 35.5 %.

Fig. 9.9 shows the contributions from different particles to the selected muon candidate sample in simulation. Compared to the preselected sample shown in fig. 9.4, the muon selection has both increased the fraction of real muons and the fraction of charm decay particles in the selected muon candidate sample. In e^+p simulation, charm decay particles contribute 43.3 % to the selected muon sample. As expected, the charm content of 26.2 % is smaller in e^-p due to the smaller charm fraction in the inclusive CC event sample. The smaller charm content also leads to a smaller fraction of real muons in the selected muon candidate sample. Particles from charm decays consist almost exclusively of muons (97 % for e^+p simulation). Particles not originating from charm decays only consist to 30 % of muons, the majority of these particles are charged pions and kaons faking muons. These remaining fake muons are discussed in section 9.4. The charm and muon contributions to the muon candidate samples with the individual cuts applied and all cuts combined are summarized in table 9.3 for e^-p and e^+p simulation.

9.3 Studies of Other Potential Muon Selection Quantities

The low statistics of the selected muon sample due to the low CC cross section, the charm fraction in the CC sample, the branching ratio into muons and the muon selection efficiency is the main problem of this analysis. The efficiency of the muon selection discussed in the previous section cannot be improved, since the polar angle and momentum cuts are mainly dictated by the geometry of the experiment while the cuts on the linking and the track length are necessary to suppress background from fake muons and achieve an acceptable purity of the sample. Any other cuts can only be applied in addition to the muon selection presented in section 9.2. Therefore the selected muon candidate sample with all cuts described in section 9.2 applied has been used for the study of other potential selection quantities. In order not to reduce the statistics even more, any additional cuts must suppress background while maintaining a high efficiency for charm decay muons.

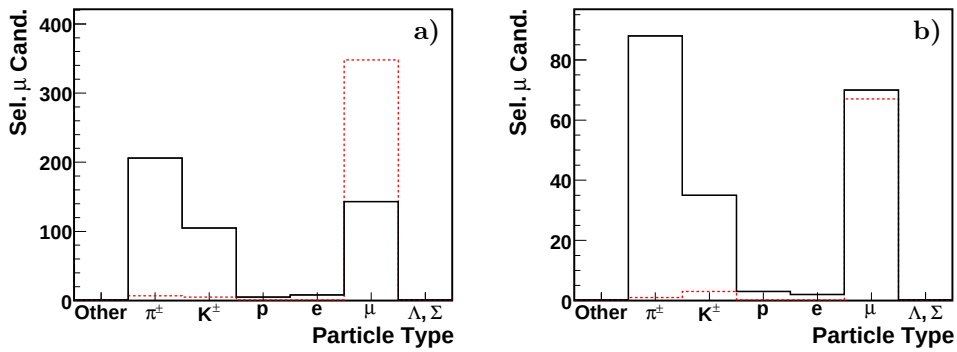

Figure 9.9: Particle type of selected muon candidates in a) e^+p and b) e^-p CC simulation. The contributions from charged pions, charged kaons, (anti-) protons, electrons and positrons, muons and strange baryons are separately listed. All other particles are contained in the first bin. The black line represents particles not originating from charm decays while the dashed red line indicates charm decay particles.

Table 9.3: Effect of individual cuts applied separately on the preselected muon candidate sample on the charm and muon content of the sample. The fraction of muon candidates passing the cut, the charm content and the muon content of the samples are given for e^-p and e^+p simulation. The effect of all cuts combined (complete muon selection) is also listed.

Cut	Sample size [%]		Charm fraction [%]		Muon fraction [%]	
	e^+	e^-	e^+	e^-	e^+	e^-
Preselection	100.0	100.0	5.1	3.4	12.2	10.7
Polar Angle	73.1	74.9	6.0	3.9	12.0	10.3
Momentum	40.7	40.8	8.9	5.6	16.4	13.3
Linking	12.5	10.4	21.2	14.3	36.6	34.6
Track Length	10.4	9.9	17.4	10.0	32.8	27.4
All combined	3.1	2.7	43.3	26.2	59.2	50.9

No such cuts have been found, any further background reduction would have resulted in an unacceptable loss of signal statistics. Some of the studied potential cut quantities are discussed in the following sections.

9.3.1 Isolation Criteria

Most fake muons are charged pions and kaons with high transverse momentum and are usually associated to a jet. Therefore a cut on the minimal distance of the muon candidate to the nearest jet or the nearest track in the tracking system would suppress most background. This is a very successfull approach for measurements of particle decays outside jets and with a significant branching ratio into $\mu\nu$, such as decays of real W bosons. The signature of these decays is a single, isolated muon (the neutrino is not measured). For charmed hadrons however the branching ratio for purely leptonic decays is very small (e.g. the fraction for the decay $D^+ \to \mu^+\nu_\mu$ is at the 10^{-4} level [17]) and other hadrons are produced along with the charmed hadron in the fragmentation process. Muons from charm decays are therefore produced inside jets. Once produced, charm decay muons also stay close to the jet since

their transverse momentum relative to the jet axis $p_{T,\,rel}$ is small. This $p_{T,\,rel}$ can be used in decays of heavy particles such as beauty hadrons to separate the decay muons from background. The masses of charmed hadrons are however too low in order to produce a significant $p_{T,\,rel}$ of decay muons.

Since both the charm decay muons and fake muons usually are close to the jet axis, isolation criteria cannot be used for the suppression of background. This can be seen in fig. 9.10, where the distance $d_{\eta\phi} = \sqrt{\left(\eta_{\mu\,cand.} - \eta_{jet\,(track)}\right)^2 + \left(\phi_{\mu\,cand.} - \phi_{jet\,(track)}\right)^2}$ in pseudorapidity η and azimuthal angle ϕ is shown.

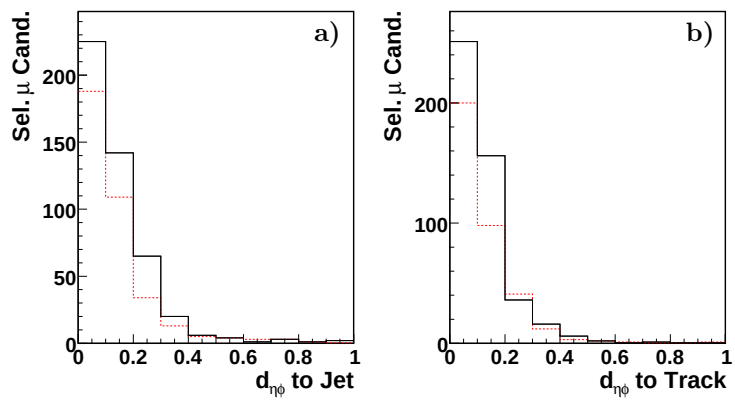

Figure 9.10: Distance $d_{\eta\phi}$ of the selected muon candidates a) to the nearest jet and b) to the nearest track in simulation. The black line represents particles not originating from charm decays while the dashed red line indicates charm decay particles.

9.3.2 Calorimeter Information

As already discussed in previous sections, muons deposit less energy per unit length in the calorimeters than other particles and do not produce electromagnetic showers. This information is exploited by the KALEP algorithm [111] implemented in the H1 reconstruction software H1REC. KALEP assigns potential muons a quality ranging from 0 (no muon) to 3 (good quality) based on the following discrimination variables:

- The sum of the cell energies in the electromagnetic part of the calorimeter within $R_a = 15$ cm around the extrapolated track helix,
- the sum of all cell energies in the calorimeter within $R_b = 30$ cm,
- the length of the extrapolated track from its entry into the calorimeter to the last assigned cell within $R_a = 15$ cm and
- the sum of all track lengths from the entry point into the calorimeter to all cells in the hadronic part of the calorimeter which are assigned to the track within $R_a = 15$ cm.

The KALEP quality assigned to the selected muon candidates can be seen in fig. 9.11. Most muons are not identified by KALEP. This is due to the fact, that the use of calorimeter information suffers from the same problem as the isolation criteria discussed in the previous section: Charm decay muons are usually part of a jet. The showers produced in the calorimeter by the jet particles overlap and it is not possible to separate the jet particles from one another (except for very low p_T jets). Energy deposits of other jet particles will be assigned to the muon by the KALEP algorithm, hiding the signature of the minimal ionizing muon. Therefore the identification of muons inside jets using calorimeter information is not reliable.

Another muon identification algorithm [112] makes use of calorimeter information in combination with energy deposits in the tail-catcher. A similar set of discriminators as in the KALEP algorithm is used. Energy deposits in an inner cone with radius 25 cm (50 cm in the hadronic part) and an outer cone with radius 35 cm (75 cm in the hadronic part) around the extrapolated muon candidate track are considered. The ratio of the energies deposited in these cones is shown in fig. 9.11. As for the KALEP quality, this muon identification algorithm works best for isolated muons and has poor separation power for muons in jets.

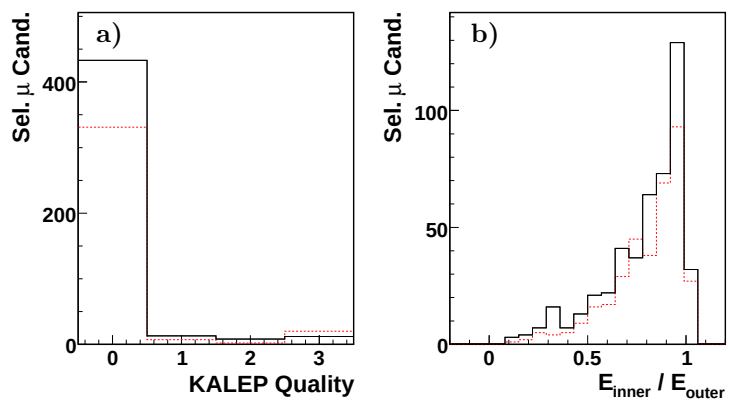

Figure 9.11: Calorimeter quantities for muon identification from simulation. a) The KALEP quality for selected muon candidates. b) Ratio of the deposited energy in inner and outer cone around the extrapolated track. The black line represents particles not originating from charm decays while the dashed red line indicates charm decay particles.

9.3.3 Distance of the Muon Track to the Event Vertex

The finite lifetime of the charmed hadron leads to a spatial separation of its decay vertex from the primary event vertex. A muon produced in the decay of a charmed hadron gets a transverse momentum relative to the flight direction of its mother particle and the muon track will therefore in general not point back exactly to the primary event vertex. The distance of closest approach $d_{ca}^{'}$ of the muon candidate tracks to the primary event vertex in the plane transverse to the beam axis has been studied. The sign of the $d_{ca}^{'}$ is positive, if the difference in the azimuthal angle ϕ of the point of closest approach and the track at this point is equal to $\pi/2$ and negative if it is $-\pi/2$ (modulo 2π). This is sketched in fig. 9.12. Because the position of the primary vertex is best constrained by high momentum tracks, the muon candidate track itself can spoil the primary vertex if it takes part in the fit of the primary vertex position. Therefore the primary vertex fit has been redone excluding the muon candidate track from the fitting procedure. The $d_{ca}^{'}$ of the muon candidate track to both the primary vertex determined with and without the track taking part in the fit is shown in fig. 9.13. The $d_{ca}^{'}$ distributions of charm decay particles tend to smaller absolute values than for other particles, but a significant reduction of the background cannot be achieved without a loss in signal efficiency. Therefore the $d_{ca}^{'}$ of the muon candidate has not been used in the muon selection.

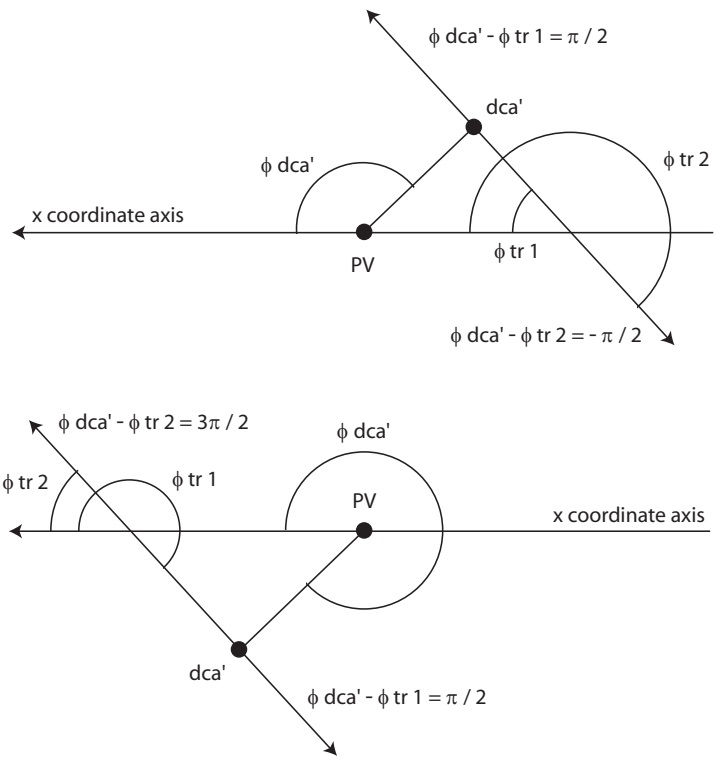

Figure 9.12: Definition of the sign of the $d_{ca}^{'}$ of a track. PV stands for the primary event vertex position and $dca^{'}$ for the position of the point of closest approach of the track to the PV.

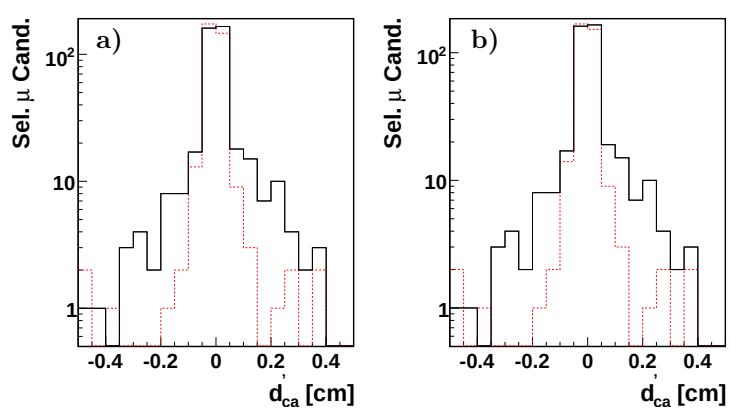

Figure 9.13: $d_{ca}^{'}$ of selected muon candidates with respect to a) the normal primary event vertex and b) the primary event vertex with the muon candidate track excluded from the vertex fit. The black line represents particles not originating from charm decays while the dashed red line indicates charm decay particles.

9.4 Remaining Background from Charged Pions and Kaons

As discussed in section 9.2.6, the remaining selected muon candidates not originating from the decay of a charmed hadron consist to about 30 % of muons and to 70 % of charged pions and kaons. The muon selection cannot distinguish between muons from different sources and enriches the charm contribution mainly by suppressing fake muons. A higher charm fraction in the selected muon sample could therefore be achieved by rejecting the remaining pion and kaon contributions in the selected muon candidate sample. In the following it is explained why this is not possible.

In ep-collisions, charged pions and kaons are produced in much larger numbers than muons. In CC simulation, high momentum particles with $p_T > 2$ GeV contain 160 times more charged pions and 30 times more charged kaons than muons. Unlike muons, most of these particles are however not able to penetrate the calorimeters and reach the muon system (punch-through). A second possibility to reach the muon system besides a punch-through is the in-flight decay of a charged pion or kaon into a muon. These particles would still be listed as pions (kaons) in fig. 9.9, since their inner track belongs to a pion (kaon). This inner track of the mother particle would then be linked to the outer track of the daughter muon. In simulation the pion contribution in the selected muon candidate sample originates to 69 % from punch-through and to 31 % from in-flight decays into muons. For the kaon contribution punch-through amounts to 85 % and in-flight decay to 15 %. Even though the probabilities for pions and kaons to either penetrate the calorimeter or decay into a muon before interacting in the calorimeter are small, the contribution of these processes to the selected muon candidate sample is still significant because of the high initial abundance of pions and kaons compared to muons.

A punch-through of a charged pion or kaon could be detected by using calorimeter information. The strongly interacting pions and kaons should deposit much more energy in the calorimeters than the minimal ionizing muons. Within a jet it is however not possible to separate energy deposits from different particles due to the overlap of their showers (see section 9.3.2). Therefore calorimeter information cannot be used to identify punch-throughs of pions and kaons.

Charged pions decay into muons with a branching ratio of almost 100 %. The reason why there are not more muons originating from pion decays detected is the long lifetime of charged pions. With an average flight distance $c\tau = 7.8$ m from production to decay vertex, pions are usually absorbed by the calorimeter before having a chance to decay. Similarly charged kaons have a branching ratio into muons of 63 % and $c\tau = 3.7$ m (all numbers taken from [17]). About 0.1 % of the pions and 1 % of the kaons with momentum $p = 2$ GeV decay into muons before entering the LAr calorimeter [113] and even less for higher momenta. In the case of in-flight decays, the particle traversing the calorimeter and leaving a track in the muon system is a real muon, which cannot be distinguished from muons from other production sources. A decay of a charged pion or kaon inside the tracking system results in a small kink of the measured track. For decays of high p_T pions and kaons this kink is not detected by the track reconstruction and might only result in a worse resolution of the track parameters and a larger χ^2 of the track fit. The effect on the track χ^2 is however too small to be exploited for the detection of in-flight decays. A different approach is using differences in the inner and outer tracks of the muon candidate. In the decay, the muon only gets a part of the mother particles momentum and energy, while the rest is carried away undetected by a neutrino. Therefore the outer track should have less energy and momentum than the inner track. The energy and momentum resolution of the muon system is however not good enough to measure these differences. Furthermore the inner and outer track should not be perfectly aligned, but have a small angle relative to each other. The difference in the azimuthal angles of the tracks and the χ^2 of the inner/outer track fit (defined by equation (9.1)) have been studied and no effect has been found. The extrapolation of the inner track across the calorimeter to the muon system introduces uncertainties which are too large in order to detect such small differences in track angles.

The charm fraction extraction with muon charge asymmetry (see section 9.7) relies on a correct description of the charge asymmetries of charm decay and background muon candidates (including fake muons) and on a correct description of the selection efficiency for charm decay muons. As long

as the charge distributions in the simulation describe the data, the result of the measurement does however not rely on a correct prediction of the absolute number of background muon candidates in the selected sample, since this number can be calculated using the charge distributions of signal and background muon candidates. Therefore the absolute number of fake muons in the data sample does not need to be known a priori and the muon misidentification probability ("fake rate") does not need to be determined. A detailed discussion of fake muons can be found in [113, 114].

9.5 Background Muons from Non-CC Events

The purpose of the muon selection presented in section 9.2 is the selection of muons and rejection of other particles, mainly pions and kaons. This selection is however not sensitive to the origin of muons. In a pure CC event sample this is not a problem, since charmed hadron decays are the dominant source of muons and a selection of muons corresponds to a selection of charm events. The selected CC event sample is however not background free (see section 6.6). The contribution from muons originating in non-CC processes is discussed in this section. Since this background source to the selected muon sample consists of real muons, the muon selection discussed above cannot reject this contribution.

9.5.1 Expectation for Muons from Non-CC Events

The expected number of selected muon candidates from non-CC background processes are listed in table 9.4. The main contributions originate from real W boson production and di-muon events. Even though the number of events in the selected CC event sample is small for these background sources, their contribution to the muon candidate sample is significant. This is due to the high fraction of events containing muons in these processes. Di-muon events always contain two muons by definition. The decay $W \to \mu\nu$ has a branching ratio of $\sim$ 10.6 % [17]. In photoproduction and di-lepton events, the selected muon candidates are expected to be independent of the lepton beam charge. The contribution from real W boson production however shows the same charge asymmetry as muons from charm decays in CC. This is due to charge conservation in the process represented in fig. 9.14 a), which is furthermore not separable experimentally from a CC event.

Table 9.4: Expected background contributions to the selected muon candidate sample from non-CC processes. The number of expected background events in the selected flavor inclusive CC event sample and the number of expected positively and negatively charged selected muon candidates are listed for the different sources of non-CC background and the different data periods.

Source	HERA I e^+			HERA II e^+			HERA II e^-		
	Events	μ^-	μ^+	Events	μ^-	μ^+	Events	μ^-	μ^+
γp uds res.	62.8	0	0	208.8	0	0	164.9	0	0
γp uds dir.	24.0	0	0	66.4	0	0	57.7	0	0
γp c res.	2.5	0	0	8.4	0	0	6.3	0	0
γp c dir.	10.9	0.6	0	32.9	0.4	0	26.3	0.8	0
Real W production	9.9	0.5	1.2	30.8	1.5	3.6	25.3	3.0	1.2
NC DIS	5.7	0	0	15.9	0	0	16.0	0	0
Di-electron prod.	0.2	0	0	0.7	0	0	0.6	0	0
Di-muon prod.	4.0	0.6	0.5	12.3	1.8	1.5	10.5	1.5	1.2
Di-tau prod.	2.0	0.2	0.2	6.3	0.6	0.6	5.2	0.5	0.5
Total	122.0	1.9	1.9	382.5	4.3	5.7	312.8	5.8	2.9

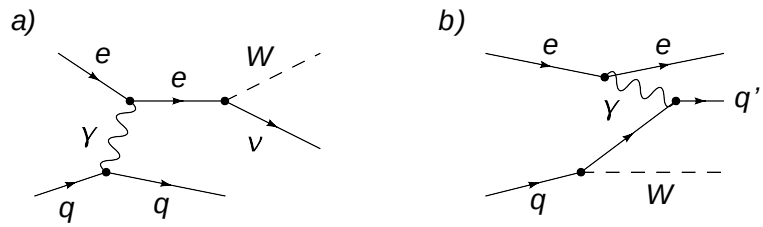

Figure 9.14: Example Feynman graphs for real W boson production. Process a) cannot be distinguished experimentally from a CC process and produces charge asymmetric decay muons.

9.5.2 Rejection of Muons from Non-CC Events

The main background contributions, real W boson production and di-muon events, have a distinguishing signature: The muons are not bound to a jet and therefore usually isolated. This is not the case for muons originating from charm decays in CC, which are contained in jets (see section 9.3.1). Therefore a distance of the muon candidate to the nearest jet of $d_{\eta\phi} < 1$ is required. This anti-isolation criterion effectively suppresses muons from real W boson production and di-muon events, as can be seen in table 9.5. Muon candidates from charm decays in photoproduction processes are not rejected by the anti-isolation condition, since these muons are contained in jets similarly as for charm decays in CC events. The remaining contribution from non-CC background events is subtracted from the selected muon candidate sample for the extraction of charm fractions (see section 9.7).

For otherwise selected muon candidates in CC events, the efficiency of the anti-isolation condition in simulation is 98 %. Therefore all isolated muon candidates are considered to be non-CC background.

Table 9.5: Expected background contributions to the selected muon candidate sample from non-CC processes with anti-isolation condition applied. The number of expected background events in the selected flavor inclusive CC event sample and the number of expected positively and negatively charged selected muon candidates are listed for the different sources of non-CC background and the different data periods.

Source	HERA I e^+			HERA II e^+			HERA II e^-		
	Events	μ^-	μ^+	Events	μ^-	μ^+	Events	μ^-	μ^+
γp uds res.	62.8	0	0	208.8	0	0	164.9	0	0
γp uds dir.	24.0	0	0	66.4	0	0	57.7	0	0
γp c res.	2.5	0	0	8.4	0	0	6.3	0	0
γp c dir.	10.9	0.6	0	32.9	0.4	0	26.3	0.8	0
Real W production	9.9	0.1	0.2	30.8	0.2	0.5	25.3	0.2	0.4
NC DIS	5.7	0	0	15.9	0	0	16.0	0	0
Di-electron prod.	0.2	0	0	0.7	0	0	0.6	0	0
Di-muon prod.	4.0	0	0	12.3	0.1	0.1	10.5	0.1	0.1
Di-tau prod.	2.0	0	0	6.3	0	0	5.2	0	0
Total	122.0	0.7	0.2	382.5	0.7	0.6	312.8	1.1	0.5

9.6 Selected Muon Data Samples

The muon selection has been applied to the selected charged current samples described in chapter 6, without the cut on the absolute value of the polarization. This cut has been omitted since the absolute value of the polarization is not relevant for the determination of the charm fraction in the sample. For the same reason the right- and left-handed samples with the same beam charge have been combined. A valid polarization measurement (independent of its value) is however still required in order to determine the cross section for charm production in CC. The different data samples and the number of selected muon candidates are summarized in table 9.6. The number of selected muon candidates is given both with and without the anti-isolation cut described in section 9.5.2 applied. In the following, the anti-isolation condition is always applied if not explicitly stated otherwise. For details on the data and CC event selection see chapter 6.

Table 9.6: Selected muon samples. The running period, beam lepton charge, integrated luminosity, mean polarization, number of selected flavor inclusive CC events and number of selected muons are given for the individual data samples. The number of selected muons is listed with and without the anti-isolation condition applied.

Period	L $[\mathrm{pb}^{-1}]$	$\overline{\mathrm{P}}$ [%]	Events	No anti-isolation cut		With anti-isolation cut	
				μ^+	μ^-	μ^+	μ^-
HERA I e^+	61.09	0	1543	7	2	5	2
HERA II e^+	182.51	+1.9	3917	11	8	9	5
HERA II e^-	154.83	−5.8	6253	10	16	9	12

The number of isolated muon candidates is compatible with the expectation for isolated muons from non-CC background, even though the number of isolated muons in data tends to be somewhat lower than expected. The number of muon candidates expected from the simulation of CC events can be compared to the number of selected non-isolated muon candidates (see table 9.6) with the expectation for remaining background from non-CC events (see table 9.5) subtracted. These numbers are listed in table 9.7. While the measured muon candidates with opposite charge than the beam lepton ("wrong charge") agree with the prediction, less muons with the same charge as the beam lepton ("right charge") have been found in the HERA II data samples compared to the simulation. A possible interpretation would be a good overall description of the data by the simulation for the almost charge symmetric non-charm muon candidates, indicated by the good agreement of the number of wrong charge muon candidates, while the highly charge asymmetric charm content is larger in simulation than in data, indicated by the difference for right charge muons. Due to the low number of selected muons and corresponding large statistical errors, no definite interpretations are however possible.

The isolated muon candidates tend to higher momenta then those contained in a jet. Among all selected muon candidates with $p_T > 20$ GeV, five are isolated and only one is close to a jet. This is expected, since in di-muon events the muons are produced directly in the hard interaction and in the decay of a W boson the muon obtains a high momentum from the W boson mass.

Apart from the muon charge distribution and the absolute number of selected muon candidates, the selected muon candidate sample after the removal of isolated muons is in good agreement with the CC signal simulation. The $P_{T,\,miss}$ distribution of all events containing a selected muon candidate is shown in fig. 9.15 a). No evidence for a dependence of the charge asymmetry of the selected muon candidates on $P_{T,\,miss}$ has been found.

Table 9.7: Expected and measured muon candidates. The number of measured CC muon candidates corresponds to the number of selected non-isolated muon candidates with the expectation for remaining non-CC background subtracted.

Period	Isolated Expected		Isolated Measured		CC Expected		CC Measured	
	μ^+	μ^-	μ^+	μ^-	μ^+	μ^-	μ^+	μ^-
HERA I e^+	1.7	1.2	2	0	4.4	1.5	4.8	1.3
HERA II e^+	5.1	3.6	2	3	13.2	4.4	8.4	4.3
HERA II e^-	2.4	4.7	1	4	10.7	16.9	8.5	10.9

The charge determination of a track is less reliable at high transverse momenta p_T of the track, which can lead to an underestimation of the charge asymmetry and consequently the charm fraction at high values of p_T (see section 9.9.1). The p_T distribution of all selected muon candidates is shown in fig. 9.15 b). No dependence of the charge asymmetry of the selected muon candidates on p_T has been found.

The muon reconstruction and selection efficiency depends on the polar angle θ. The θ distribution of the selected muon candidates is in agreement with the prediction from simulation, as can be seen in fig. 9.15 c).

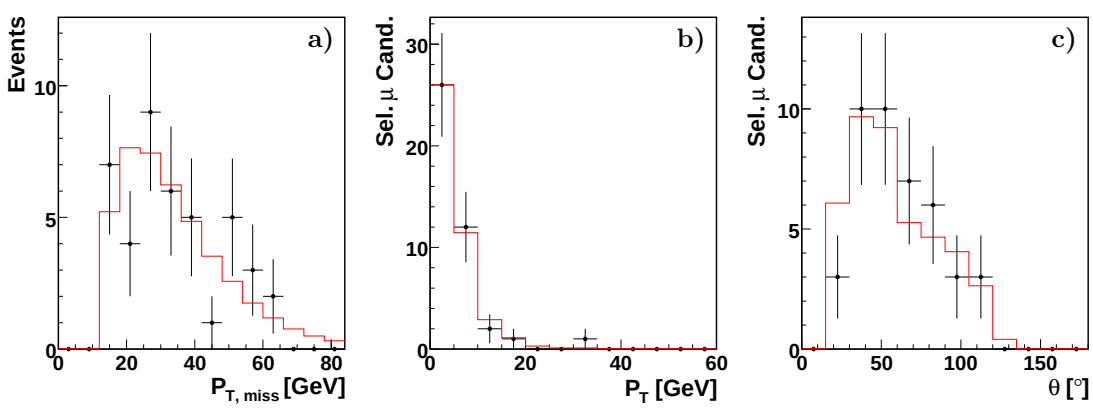

Figure 9.15: Properties of the selected muon candidate sample: a) $P_{T,\,miss}$ of events containing selected muon candidates, b) p_T and c) polar angle of selected muon candidates. The black dots with error bars represent the data while the red line is the prediction from the CC simulation.

Tables with more details on the events containing selected muon candidates, including also those with isolated muons, can be found in appendix B.

9.7 Charm Fraction Extraction using the Muon Charge Asymmetry

As can be seen in table 9.5, the selected muon candidate sample still contains a small contribution from non-CC background muons after the anti-isolation cut has been applied. For the extraction of the charm fraction in CC, this remaining background contribution is subtracted on a statistical basis from the number of selected muon candidates. After this subtraction, the sample is considered to consist only of muon candidates from CC processes and the CC signal simulation is used for the prediction of muon charge asymmetries and the calculation of the charm fraction in the selected CC event sample.

The charm decay muon must always have the same charge as the beam lepton (see section 9.1). The charge of the beam lepton will in the following be referred to as "right charge". Muon candidates with opposite charge ("wrong charge") are almost exclusively background (in the following denoted by "uds" for up, down and strange quarks) and can be used to control the amount of uds background with right charge. The ratio of right/wrong charge selected muon candidates for charm and uds is taken from simulation. In fig. 9.16 the charge distributions of the selected charm and uds muon candidates in e^-p and e^+p simulation are shown. The charge distributions of the selected charm decay muon candidates are as expected almost completely asymmetric. The remaining wrong charge charm decay particles are either muons from charm decays in events with a $c\bar{c}$ pair from fragmentation or muons with an incorrect charge reconstruction. The differences in the charge distributions of the selected uds muon candidates between e^-p and e^+p simulation are due to the different quark flavors produced in the hard interaction, which lead to different particle spectra at high momenta[2]. The charm fraction in the CC sample is smaller for e^-p than for e^+p running, which is also reflected in the smaller charm fraction in the selected muon sample in e^-p simulation.

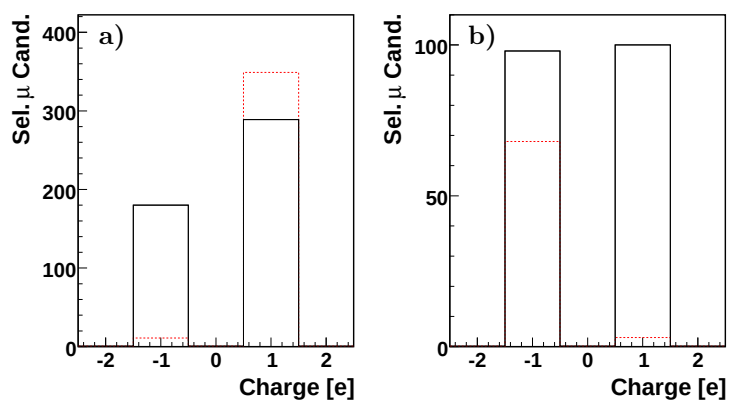

Figure 9.16: Charge of the selected muon candidates in a) e^+p and b) e^-p simulation. The black line represents particles not originating from charm decays while the dashed red line indicates charm decay particles.

[2]The highest momentum particles in the event often contain the quark produced in the hard interaction. This is for instance also used by the flavor tagging method described in section 3.4.1.

In a first step, the number of selected charm decay muon candidates with right charge is determined. Three methods can be used:

1. Use only the right charge bin and take the amount of uds background in this bin directly from simulation. The number of selected right charge charm muon candidates c_R can be calculated from the number of measured selected right charge muon candidates N_R with

$$\mathrm{c}_{R,\,measured} = N_R - \mathrm{uds}_{R,\,MC}, \tag{9.2}$$

where the number of selected right charge non-charm muon candidates uds_R is taken from simulation. Assuming Poisson statistics and neglecting statistical errors of the simulation, the statistical error becomes

$$\Delta\mathrm{c}_{R,\,measured} = \sqrt{N_R}. \tag{9.3}$$

2. Use the wrong charge bin to determine the amount of uds background in the right charge bin, neglecting the contribution of charm in the wrong charge bin. Unlike method 1, no predictions of the absolute number of background events are needed. Instead, only the ratio of right/wrong charge background is taken from simulation. With this method, the number of selected right charge charm muon candidates is

$$\mathrm{c}_{R,\,measured} = N_R - N_W \left(\frac{\mathrm{uds}_R}{\mathrm{uds}_W}\right)_{MC}, \tag{9.4}$$

with a statistical error, assuming Poisson statistics and neglecting statistical errors of the simulation,

$$\Delta\mathrm{c}_{R,\,measured} = \sqrt{N_R + N_W \left(\frac{\mathrm{uds}_R}{\mathrm{uds}_W}\right)^2_{MC}}. \tag{9.5}$$

3. Use the wrong charge bin to determine the amount of uds background in the right charge bin and do not neglect the contribution of charm in the wrong charge bin. From the measurement of N_R, N_W and the ratios $(\mathrm{uds}_W/\mathrm{uds}_R)_{MC}$ and $(\mathrm{c}_W/\mathrm{c}_R)_{MC}$ taken from simulation, there are four conditions for the four unknowns c_R, c_W, uds_R and uds_W:

$$\begin{aligned} N_R &= \mathrm{c}_R + \mathrm{uds}_R \\ N_W &= \mathrm{c}_W + \mathrm{uds}_W \\ \left(\frac{\mathrm{uds}_W}{\mathrm{uds}_R}\right)_{MC} &= \frac{\mathrm{uds}_W}{\mathrm{uds}_R} \\ \left(\frac{\mathrm{c}_W}{\mathrm{c}_R}\right)_{MC} &= \frac{\mathrm{c}_W}{\mathrm{c}_R}. \end{aligned} \tag{9.6}$$

This set of equations can be solved analytically and c_R becomes

$$\mathrm{c}_{R,\,measured} = \frac{N_W - N_R \left(\frac{\mathrm{uds}_W}{\mathrm{uds}_R}\right)_{MC}}{\left(\frac{\mathrm{c}_W}{\mathrm{c}_R}\right)_{MC} - \left(\frac{\mathrm{uds}_W}{\mathrm{uds}_R}\right)_{MC}}, \tag{9.7}$$

with a statistical error, assuming Poisson statistics and neglecting statistical errors of the simulation,

$$\Delta\mathrm{c}_{R,\,measured} = \frac{\sqrt{N_W + N_R \left(\frac{\mathrm{uds}_W}{\mathrm{uds}_R}\right)^2_{MC}}}{\left(\frac{\mathrm{uds}_W}{\mathrm{uds}_R}\right)_{MC} - \left(\frac{\mathrm{c}_W}{\mathrm{c}_R}\right)_{MC}}. \tag{9.8}$$

All three methods have been tested. For method 1, a prediction on the absolute number of background events (fake muon rate) would be needed. For the methods 2 and 3, only the charge distribution needs to be described correctly by the simulation, but not the absolute number of fake muons. The right charge background can be calculated from the wrong charge bin. As a consequence it has been decided not to use method 1. Since the contribution from charm in the wrong charge bin is small, the methods 2 and 3 give comparable results. All the results presented in this thesis on the charm fraction in CC have been obtained by method 3.

In a next step, the charm fraction in the selected CC sample can be computed using the fraction of charm events containing right sign charm decay muons (in the following called "branching") and the selection efficiency for these muons. These two factors are taken from simulation. In a last step, the cross section of charm in CC is calculated from the charm fraction, the mean measured polarization of the sample and the flavor inclusive CC cross section. A schematic diagram of the charm in CC measurement is shown in fig. 9.17.

The values of the input variables from simulation for the charm in CC cross section determination are listed in table 9.8 for the individual data periods.

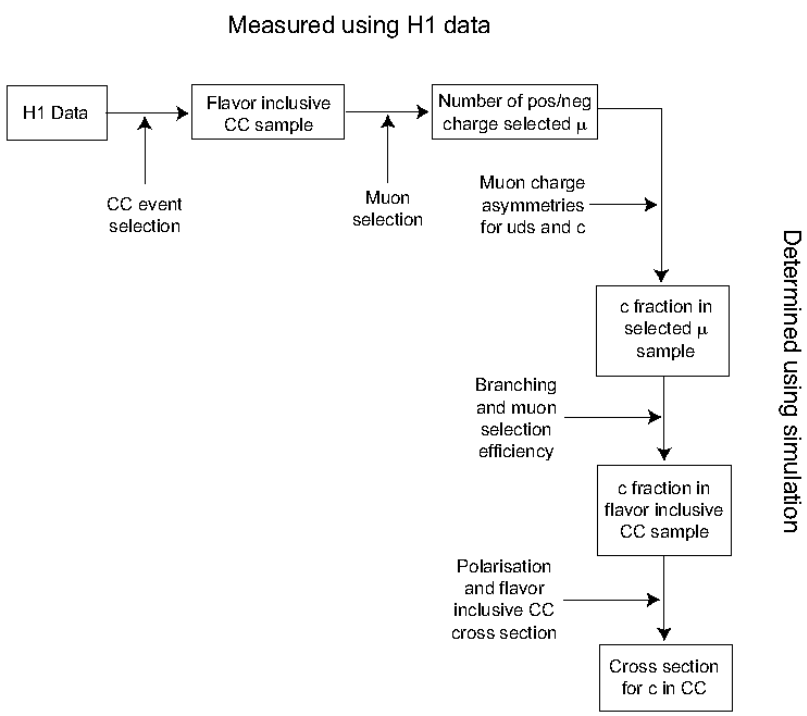

Figure 9.17: Schematic diagram of the charm fraction extraction.

Table 9.8: Parameters from simulation for the charm in CC cross section calculation.

Period	uds_R/uds_W	c_R/c_W	Branching [%]	Muon sel. eff. [%]
HERA I e^+	1.59	23.5	8.8	10.0
HERA II e^+	1.41	28.0	8.4	12.9
HERA II e^-	0.96	28.2	8.6	12.3

9.7.1 Combined Positron Sample

During the luminosity upgrade between HERA I and HERA II the main detector components used for muon identification, the Central Jet Chamber, the LAr calorimeter and the Central Muon Detector, have not been changed. The HERA I and HERA II positron samples can therefore easily be combined. The combined positron sample can be analyzed in the same way as the individual samples. For the calculation of the cross sections the parameters from the HERA II e^+ simulation in table 9.8 are used due to the larger statistics (and therefore smaller errors) of this sample. In fig. 9.18 it is demonstrated that the simulations for HERA I and HERA II e^+ data agree well for the relevant quantities of the muon selection.

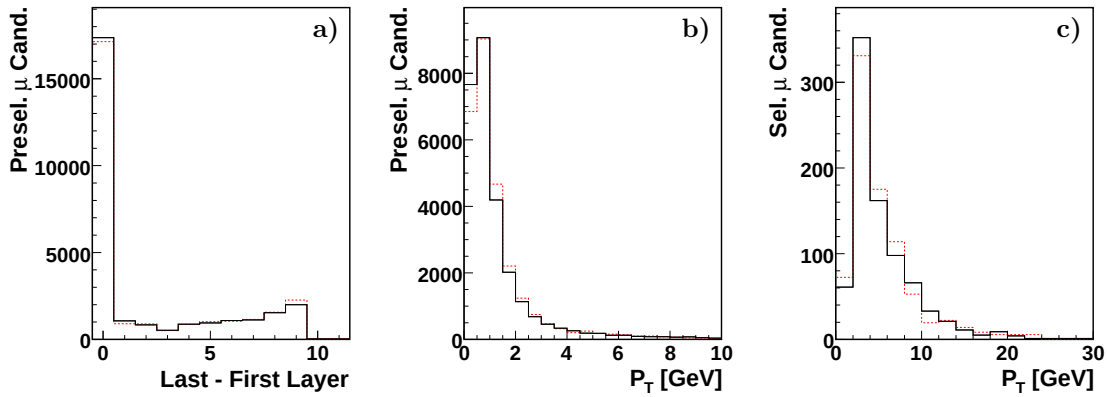

Figure 9.18: Comparison of muon quantities in HERA I (red, dashed) and HERA II (solid, black) positron simulation: a) Length of the track in the muon system (last minus first layer) and b) transverse momentum for all preselected muon candidates, c) transverse momentum of selected muon candidates.

9.7.2 Combined Electron/Positron Sample

In order to reduce the statistical error of the charm fractions, the e^+p and e^-p data sets have been combined. Due to the different charm fraction and the different uds charge asymmetry in e^+p and e^-p data, it is not possible to just combine the samples and use the methods described above for the charm fraction extraction of the combined e^+p and e^-p sample. Instead, charm fractions in the e^-p and the combined HERA I / HERA II e^+p sample are measured independently and then combined using the ratio of the predicted charm fractions in e^+p and e^-p data as an input parameter. In the following discussion, this parameter has been set to two, corresponding to the expected 20 % charm in e^+p and 10 % in e^-p CC processes.

With the ratio of the charm fractions in the e^+p and e^-p samples fixed, the measured e^+p and e^-p charm fractions F_+ and F_- can be seen as two measurements of the same quantity. The combined charm fractions can then be calculated with

$$\begin{aligned} F_{-,\,comb} &= \frac{1}{3}\left(F_- + F_+\right) \qquad \text{and} \\ F_{+,\,comb} &= \frac{2}{3}\left(F_- + F_+\right). \end{aligned} \tag{9.9}$$

Here the assumption $F_+ = 2F_-$ and $F_{+,\,comb} = 2F_{-,\,comb}$ has been used. The errors of the combined

charm fractions are then given by

$$\begin{aligned} \Delta F_{-,\,comb} &= \frac{1}{3}\sqrt{(\Delta F_-)^2 + (\Delta F_+)^2} \qquad \text{and} \\ \Delta F_{+,\,comb} &= \frac{2}{3}\sqrt{(\Delta F_-)^2 + (\Delta F_+)^2}. \end{aligned} \tag{9.10}$$

This simple combination procedure does not take into account the errors of the individual measurements for the calculation of the combined fraction. Therefore it will only produce sensible results if the errors of the charm fractions in e^+p and e^-p are comparable.

A more sophisticated method taking into account also the errors of the individual charm fraction measurements is using Lagrange multipliers [115] with the ratio of the charm fractions in e^+p and e^-p data as a constraint. The ansatz for this method is

$$\Phi = \left(\frac{F_+ - F_{+,\,comb}}{\Delta F_+}\right)^2 + \left(\frac{F_- - F_{-,\,comb}}{\Delta F_-}\right)^2 + 2\lambda\left(F_{+,\,comb} - 2F_{-,\,comb}\right). \tag{9.11}$$

The parameter λ is called Lagrange multiplier. The solutions for the combined charm fractions $F_{+,\,comb}$ and $F_{-,\,comb}$ are now extrema of the function Φ and can be calculated from the system of equations

$$\frac{\partial\,\Phi}{\partial\,F_{+,\,comb}} = 0; \qquad \frac{\partial\,\Phi}{\partial\,F_{-,\,comb}} = 0; \qquad \frac{\partial\,\Phi}{\partial\,\lambda} = 0. \tag{9.12}$$

The analytical solutions for the charm fractions from this set of equations are

$$\begin{aligned} F_{+,\,comb} &= F_+ - (\Delta F_+)^2 \cdot \frac{F_+ - 2F_-}{(\Delta F_+)^2 + 4(\Delta F_-)^2} \qquad \text{and} \\ F_{-,\,comb} &= F_- + 2(\Delta F_-)^2 \cdot \frac{F_+ - 2F_-}{(\Delta F_+)^2 + 4(\Delta F_-)^2}. \end{aligned} \tag{9.13}$$

Both methods have been tested and the results are compatible within errors. The results presented for the combined e^+p and e^-p measurement have been calculated with the Lagrange multiplier method. The errors on the individual charm fractions directly enter the calculated combined charm fractions and are not used in a normal error propagation. Therefore no errors will be given on the combined e^+p and e^-p results.

9.8 Charm Fraction Extraction using a Charge-p_T Likelihood

As an alternative to the charm fraction measurement using charge asymmetries only, the use of a two dimensional likelihood for the charge and the p_T of the selected muon candidates has been studied. For this purpose the TFractionFitter interface of the RooT analysis package [116] to the MINUIT minimization program [117] has been used. In addition to the charge asymmetries already discussed in section 9.7, also the shapes of the p_T distributions of selected charm decay and uds muon candidates have been taken from simulation. These templates for selected charm decay and uds muon candidates have been fitted to the data distribution using a Barlow fit [109]. In this fit procedure, a maximum likelihood technique with Poisson statistics is used. Uncertainties induced by the finite statistics of the simulation templates are also taken into account.

The fit does not converge to a stable result. The effect of higher statistics of the templates has been simulated by scaling and smoothing the template distributions. This procedure did not result in an improvement of the fit performance. This indicates that even with better template precision the data statistics is not sufficient for a likelihood fit approach in order to separate the charm and uds contributions to the selected muon candidate sample. The p_T distributions of the templates and the combined positron data sample are shown in fig. 9.19.

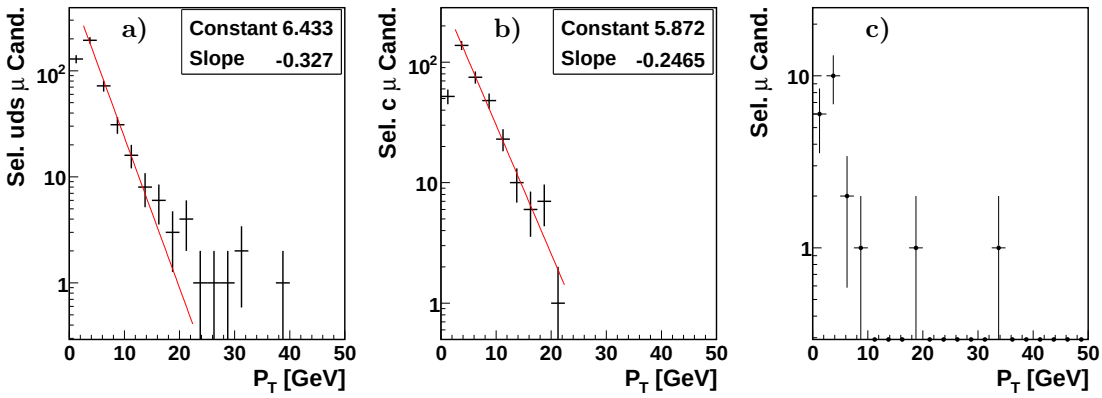

Figure 9.19: Selected muon p_T templates and data distribution for the p_T likelihood fit. a) Uds and b) charm templates from simulation with fitted exponential function (red line) and c) p_T of the selected muons in the combined positron data sample.

9.9 Systematic Errors of the Charm Fraction Extraction

In this section the individual sources of systematic uncertainties of the charm fraction extraction are discussed. The effect of these uncertainties on the charm fractions are summarized in section 9.9.5. Due to the large statistical errors of this analysis, systematic uncertainties can be estimated in a conservative way without the need for optimization and reduction of systematic effects. The uncertainty on the charge reconstruction affects the measured muon candidates in data, while the other uncertainties discussed in the following concern predictions from simulation.

9.9.1 Muon Charge Reconstruction

The measurement of the muon candidate charge is essential in the determination of the charm fraction. It is determined using the curvature of the inner track in the magnetic field of the H1 solenoid. Since the curvature of the track decreases with increasing particle momentum, the charge determination of very high momentum particles is not reliable any more. The track charge misidentification probability in bins of p_T for central tracks with radial length larger than 22 cm is shown in fig. 9.20. In the lowest p_T bin the charge misidentification probability is high due to poorly reconstructed tracks. This does not affect this analysis since the inner track of the muon candidate is required to have a minimal p_T of 2 GeV. Tracks with negative charge have a higher ionization potential in the tracking chambers than tracks with positive charge and their reconstruction is therefore more reliable. Since the highest momentum tracks in CC events have predominantly the same charge as the beam lepton, the charge misidentification probability is slightly higher for e^+p than for e^-p running. This effect is however only important at high values of p_T.

Due to the charge asymmetry, more muon candidates with right charge will be assigned wrong charge than vice versa. Therefore the charge misidentification leads to an underestimation of the charge asymmetry and consequently the charm fraction.

This effect is however small, as can be seen in fig. 9.20. Since all but one selected muon candidates have a p_T of less than 20 GeV, a charge misidentification probability for selected muon candidates of 4 % is assumed. Due to the low statistics of the selected muon sample in data (e.g. 5 positive and 2 negative muons in HERA I e^+), and since the charge of a muon can only be either correctly or wrongly reconstructed and not be 96 % correct, the effect of the uncertainty of the charge reconstruction on the charm fraction is neglected.

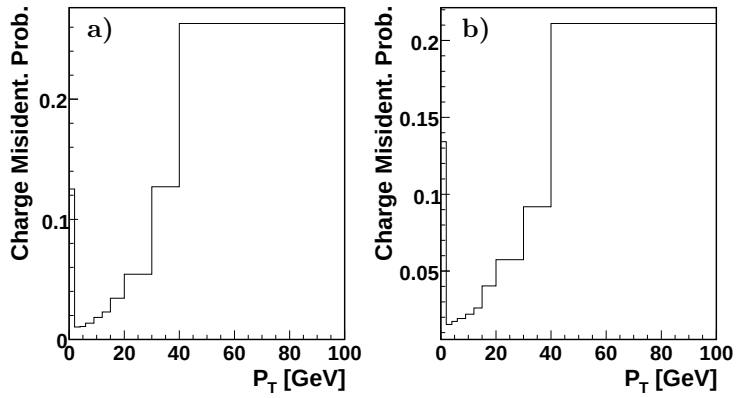

Figure 9.20: Charge misidentification probability for central tracks with radial length $l > 22$ cm in a) e^+p and b) e^-p simulation in bins of transverse momentum p_T.

9.9.2 Muon Selection Efficiency and Branching Ratio

The charm fraction in the selected CC sample is calculated from the charm fraction in the selected muon sample using the ratio of charm events containing a right sign muon ("branching") and the selection efficiency for charm decay muon candidates (including also the muon track reconstruction, see fig. 9.17). The value of this branching is assumed to be comparable for the different data periods. As an estimate of the systematic uncertainty the difference in the branching deduced from the different simulated CC samples has been used (see table 9.8), which is well covered by an assumed uncertainty of 5 % of the branching.

Unlike the branching, the muon selection efficiency can depend on the data period, due to different kinematics (see chapter 7). Since selected muon candidates originating from charm decays consist almost exclusively of muons (see fig. 9.9), the selection efficiency for charm decay muon candidates corresponds to the selection efficiency for real muons. The systematic uncertainty of the muon identification and selection efficiency is estimated to be 5 % [118][3].

Much more uncertain is the selection efficiency for non-muons (fake muons). This is however not relevant for the charm fraction extraction, since only the charge distribution (see section 9.9.3) and not the absolute number of fake muons is used.

9.9.3 Charge Asymmetries in the Simulation

The calculation of the charm fraction depends on the charge asymmetries for uds and charm selected muon candidates taken from simulation. The charge asymmetries obtained for the different periods are listed in table 9.8. The asymmetry of selected charm decay muon candidates is expected to be well known, since these muon candidates consist to 97 % of muons. The charge asymmetry of the charm decay muon candidates is therefore caused by the production processes of the muon candidates and the performance of the charge reconstruction (compare section 9.9.1). If the produced muons are fully asymmetric (all have right charge), a contribution of about 4 % wrong charge muons is

[3]In a more recent analysis a lower uncertainty on the muon reconstruction and selection efficiency of 3.6 % is assumed [119]. For this thesis however the more conservative 5 % is chosen.

expected due to the charge misreconstruction. This corresponds to a charge asymmetry factor for charm muons c_R/c_W of 24, in good agreement with the value found in the HERA I simulation. The asymmetries in the HERA II simulations are even higher at ~ 28, indicating that the 4 % charge reconstruction uncertainty is a safe estimate and in good agreement with fully charge asymmetric muons at production. An uncertainty of 10 % of the charge asymmetry for charm decay muon candidates is assumed, which is a very conservative estimate since the charge distribution of charm decay muons is well understood. This uncertainty also covers the limited statistics of the simulation. Due to the large charge asymmetry for charm muons, an uncertainty of 10 % has only a minor effect on the charge fractions, as can be seen in table 9.9.

Only about 30 % of the selected muon candidates not originating from charm decays ("uds muon candidates") are real muons (see fig. 9.9). Therefore the charge asymmetry of these muon candidates is dominated by the charge distribution of fake muons. The contribution from in-flight decays of pions and kaons is not problematic, since the charge distribution of the muons produced through in-flight decays mirrors the charge distribution of the original pions and kaons (apart from the small charge misreconstruction probability discussed above). This is assumed to be well described by the simulation. The fake muon contribution from punch throughs is however more uncertain, since the interaction of negatively and positively charged particles in matter are slightly different, which introduces a different punch through probability for positive and negative particles. This effect is however also accounted for in the simulation. In a study performed with the ZEUS detector, the charge distribution of fake muons is claimed to have an uncertainty of only 3 % [120]. Since a similar study has not been done using the H1 detector, a much more cautious uncertainty of 20 % has been assumed for this thesis, covering also the statistical errors of the simulation. The resulting systematic errors on the charm fractions are still significantly smaller than the statistical errors.

9.9.4 Background Subtraction of Muons from Non-CC Events

Most muon candidates from non-CC events are rejected by the anti-isolation criterion (see section 9.5). The remaining contribution is estimated from the simulation of the background processes and is subtracted from the number of selected muon candidates for the charm fraction calculation. The systematic uncertainty on this background subtraction corresponds to the statistical error of the respective simulations, which is 30 % for the photoproduction processes (the same as for the systematic uncertainties in the flavor inclusive CC measurement, see section 6.7). The statistical errors of the simulation of real W boson and di-muon production processes are negligible.

9.9.5 Total Systematic Errors on the Charm Fractions

The effects of the systematic uncertainties on the charm fractions are listed in table 9.9. The branching and charm decay muon selection efficiency enter the charm fraction calculation linearly, resulting in identical relative errors for all data samples. The relative uncertainties from the charge asymmetries and the background subtraction depend on the data sample and have been obtained by varying the respective numbers used in the charm fraction calculation. The dominant source of systematic uncertainties is the charge distribution of fake muons, which is a very conservative estimate and might be reduced by dedicated studies. The errors on all charm fractions are however dominated by the limited statistics of the data samples, therefore it has not been tried to reduce the systematic uncertainties.

Table 9.9: Resulting systematic uncertainties in percent of the measured charm fractions.

Systematic effect	Error on the charm fraction [%]			
	HERA I e^+	HERA II e^+	HERA II e^-	e^+ combined
Charge reconstruction	-	-	-	-
Selection efficiency	5.0	5.0	5.0	5.0
Branching	5.0	5.0	5.0	5.0
Charm charge asymmetry	0.9	1.7	1.1	1.0
Uds charge asymmetry	13.5	51.7	59.1	29.5
Background subtraction	10.3	6.9	9.1	8.4
Total systematic error	18.4	52.7	60.2	31.5

9.10 Results

For the extraction of the charm fractions in the selected charged current samples and the calculation of the corresponding cross sections, method 3 described in section 9.7 has been used. In the following the results obtained by this method for the individual and combined data samples are presented. Due to the large errors of the measured charm fractions, the strange content of the proton has not been extracted.

9.10.1 Charm Fractions

The measured charm fractions in the selected CC samples are summarized in table 9.10.

Table 9.10: Measured charm fractions in the individual and combined CC samples. The number of positive and negative muons correspond to the number of selected muons with the expected number of non-CC background muons subtracted. The first error given for the charm fractions is the statistical error, the second corresponds to systematic uncertainties. The number of selected flavor inclusive CC events in the samples is also given.

Sample	Events	μ^+	μ^-	Charm fraction [%]
HERA I e^+	1543	4.8	1.3	$22.3 \pm 23.2 \pm 4.1$
HERA II e^+	3917	8.4	4.3	$5.8 \pm 10.3 \pm 3.1$
HERA II e^-	6253	8.5	10.9	$4.4 \pm 6.9 \pm 2.6$
Comb. e^+	5460	13.2	5.6	$9.5 \pm 8.9 \pm 3.0$
Comb. e^+ and e^-	11713	21.7	16.5	9.3 (e^+), 4.7 (e^-)

All extracted charm fractions are consistent within errors both with a vanishing charm fraction and the theory prediction of 10 % for e^- and 20 % for e^+ running. All obtained charm fractions are however consistently lower than the predictions, except for the HERA I sample, which is the smallest sample with correspondingly large statistical errors. The lower charm fractions are consistent with the smaller than expected muon charge asymmetry (see section 9.6).

9.10.2 Cross Sections

The cross sections for charm in CC are calculated from the charm fractions in table 9.10 using the flavor inclusive CC theory cross sections for the mean polarizations of the corresponding samples. The results are listed in table 9.11.

Table 9.11: Measured charm cross sections in the individual and combined CC samples. The first error given for the charm cross sections is the statistical error, the second corresponds to systematic uncertainties.

Sample	$\overline{\mathrm{P}}$ [%]	$\sigma_{th}\left(\overline{\mathrm{P}}\right)\left[\mathrm{pb}^{-1}\right]$	Cross section $\left[\mathrm{pb}^{-1}\right]$
HERA I e^+	0	29.1	$6.5 \pm 6.8 \pm 1.2$
HERA II e^+	+1.9	29.7	$1.7 \pm 3.1 \pm 0.9$
HERA II e^-	−5.8	61.9	$2.7 \pm 4.3 \pm 1.6$
Comb. e^+	1.4	29.6	$2.8 \pm 2.6 \pm 0.9$
Comb. e^+ and e^-	1.4	29.6	2.8 (e^+)
Comb. e^+ and e^-	−5.8	61.9	2.8 (e^-)

As for the charm fractions, the cross sections for charm in CC are consistent with each other and compatible both with zero and the theory prediction. As a consequence of the low charm fractions, also the cross sections tend to be low compared to the predictions. Taking into account the large errors of the measurement, this deviations from the predictions are however not significant.

Chapter 10

Conclusions

10.1 Summary of the Results

The strange quark density in the proton is still the least known parton density. Currently, the most precise constraints come from measurements of neutrino-nucleon deep inelastic scattering (DIS). In electron-proton DIS at HERA, two main approaches for a measurement of the strange sea in the proton are possible: Strangeness production in neutral current (NC) and charm production in charged current (CC) processes. In this thesis, charm production in CC interactions has been studied.

The main difference between the measurement of NC and CC processes is the presence of the scattered beam lepton in NC, allowing a precise reconstruction of the event kinematics, while the final state neutrino in CC processes is not detected. There are also many other differences between the measurement of CC and NC processes: First, differences between e^-p and e^+p data sets are more pronounced for CC than for NC samples. This is due to different partons in the proton participating in the hard interaction in e^-p than in e^+p and consequently different event kinematics and cross sections. Second, the cross sections for CC processes depend on the lepton beam polarization due to the parity violating structure of weak interactions. The study of CC processes allows the test of these particularities of weak interactions in ep scattering. Third, the background from non-ep processes is much more important than in NC measurements. This is due to the main feature of CC events used for the triggering and the selection of these events: The missing transverse momentum. This signature can be faked by many non-ep background interactions.

For this thesis, the 1999/2000 HERA I e^+p data from the H1 detector with an integrated luminosity of 61 pb^{-1} and the complete HERA II data with 183 pb^{-1} of e^+p and 155 pb^{-1} of e^-p data has been used. The CC event selection criteria have been passed by 1543 events in the HERA I e^+p data set, 3917 events (3783 with an absolute value of the polarization above 20 %) in the HERA II e^+p data set and 6253 (5223) events in the HERA II e^-p data set. The polarization dependent cross sections

$$\sigma_{CC} = (28.9 \pm 1.4) + P_e \cdot (28.6 \pm 4.7)\ \text{pb} \qquad \text{for } e^+p \text{ and}$$
$$\sigma_{CC} = (49.2 \pm 2.3) - P_e \cdot (42.5 \pm 6.8)\ \text{pb} \qquad \text{for } e^-p$$

have been determined for the kinematic range $Q^2 > 223$ GeV^2 and $0.03 < y < 0.85$. While the cross section for e^+p data is in excellent agreement with the theoretical prediction, the fitted slope of the cross section for e^-p is lower than the prediction. This discrepancy is due to the measured cross section for the e^-p LH data sample, which is 18 % below the predicted value. The main reason for the disagreement of data and simulation for the e^-p LH period is assumed to be a wrong description of the data event selection efficiency in the simulation.

The charm fraction in the selected CC event sample has been studied using two different approaches: An inclusive measurement using lifetime information and muons from semileptonic charmed hadron decays.

It has been found that the extraction of the charm fraction using inclusive lifetime methods is not possible. This is due to the low charmed hadron decay multiplicities in combination with the limited statistics of the selected CC event samples.

The second approach, semileptonic decays into muons, has been more successful. Muons produced in the decay of a charmed hadron in CC events always have the same charge as the beam lepton (referred to as "right charge"). The background from muon candidates originating from other production processes (mostly pions and kaons faking muons) can be controlled using the number of "wrong charge" muon candidates. Background muons from remaining non-CC events in the selected sample can be suppressed by an anti-isolation condition. It has been shown that the measurement of the charm fraction in CC processes using the charge asymmetry of charm decay muons is possible, albeit with large statistical errors due to the limited data statistics. The following charm fractions in the selected CC event sample have been extracted:

$$\mathrm{F}_c = 9.5 \pm 8.9 \pm 3.0\ \% \qquad \text{for } e^+p \text{ and}$$
$$\mathrm{F}_c = 4.4 \pm 6.9 \pm 2.6\ \% \qquad \text{for } e^-p.$$

The first error corresponds to the statistical and the second to the systematic uncertainty. Due to the large statistical errors, the measured charm fractions are consistent both with a vanishing charm fraction and the prediction of about 10 % for e^-p and 20 % for e^+p. Normalized to the flavor inclusive CC theoretical cross sections, the measured values for charm in CC processes in the kinematic range $Q^2 > 223$ GeV and $0.03 < y < 0.85$ are

$$\sigma_{c\,in\,CC} = 2.8 \pm 2.6 \pm 0.9 \text{ pb} \qquad \text{for } e^+p \text{ and}$$
$$\sigma_{c\,in\,CC} = 2.7 \pm 4.3 \pm 1.6 \text{ pb} \qquad \text{for } e^-p.$$

In earlier studies of charm in CC processes at H1 with HERA I data, an excess of the charm fraction over the expectation in events with high missing transverse momentum $P_{T,\,miss} > 40$ GeV was observed [104]. This excess could not be confirmed. It is suspected that the observed excess was either a statistical fluctuation or due to remaining W boson production events in the selected event sample.

Due to the large statistical errors of the measured charm fractions, the strange density in the proton has not been extracted.

10.2 Outlook

In order to improve on the results obtained in this thesis, significantly larger data samples would be needed. However, HERA stopped operation in mid 2007. The results of the charm measurement in CC processes might be improved by adding information from semileptonic charmed hadron decays into electrons or by combining lifetime and lepton information using multivariate methods. Without more data statistics, it is however doubtful whether these extensions of the presented analysis would lead to a significant reduction in the experimental errors.

Since the cross sections for NC processes are much larger than for CC, the measurement of the strange content in the proton using strangeness production in NC is less statistically limited. The systematic uncertainties for this approach would however be large. Therefore no precise measurement of the strange quark density in the proton can be expected from this method.

At the Large Hadron Collider (LHC) [121–123] at CERN in Geneva it will be difficult to contribute to the understanding of the strange quarks in the proton. While the leptons colliding with protons at HERA represent pointlike probes and are thus providing a clear picture of the proton structure,

at the LHC protons will collide with other protons. The resulting events are very complex[1] and a reliable reconstruction of the primary partons in the protons taking part in the interaction is therefore very challenging. Furthermore, proton-proton collisions at the LHC will be dominated by interactions between gluons.

Since HERA has stopped operation and it is doubtful whether the LHC will provide precise measurements of individual quark densities in the proton, the study of the strange content of nucleons will stay a domain of neutrino-nucleon DIS experiments in the foreseeable future.

[1] At the nominal instantaneous luminosity of the LHC, not just one but even several (~ 20) collisions will take place during the same bunch crossing, further complicating the reconstruction of the events.

Appendix A

Non-ep Background Finder Flags

In this appendix, the individual non-ep background finder flags are listed. It is also stated whether they were used for this analysis. A more detailed description can be found in [90–92].

Table A.1: Non-ep background finder flags coded in the ibg array. Finders with names starting with HA are mainly used against halo muons, while names starting with COS indicate their use against cosmic muons.

Bit	Used	Finder	Description
0	Yes	HALAR	Longitudinal energy pattern in the LAr calorimeter
1	Yes	HAMULAR	Longitudinal energy pattern in the LAr calorimeter with energy deposited in the muon system backward endcap
2	Yes	HAMUMU	Horizontal muon track in the forward detector region and energy deposited in the muon system backward endcap
3	Yes	HASPALAR	Cluster in the inner forward (IF) LAr and matching energy deposit in the SpaCal
4	Yes	HAMUIF	Cluster in the inner forward (IF) LAr and matching energy deposit in the muon system backward endcap
5	Yes	COSMUMU	Two matching muon tracks on opposite sides of the CMD
6	Yes	COSMULAR	More than 90 % of the LAr energy aligned with a CMD muon track
7	Yes	COSTALAR	Two tail catcher clusters on opposite sides of the detector with more than 85 % of the LAr energy aligned between them
8	Yes	COSTRACK	Two matching CJC tracks on exactly opposite sides of the detector
9	Yes	COSLAR	Isolated LAr cluster with longitudinal shape and a small electromagnetic contribution

Table A.2: Non-ep background finder flags coded in the ibgam array.

Bit	Used	Finder	Description
0	Yes	BEAMGAS	Many CJC tracks in the backward detector region
1	Yes	COSLARSHAPE	Cosmic muon not crossing the CJC
2	Yes		Cosmic muon crossing the CJC with energy deposits on both sides of the LAr
3	No		Cosmic muon crossing the CJC with energy deposits in the LAr on one side and matching CMD track on the opposite side of the detector
4	No	COSLARTRACK	High energetic cluster in the LAr without matching track
5	Yes	HALARTRACK	High energetic horizontally oriented cluster in the LAr without matching track
6	Yes	HASPA	Uniform energy distribution in the SpaCal

Table A.3: Non-ep background finder flags coded in the ibgfm array. These bits code for one- and two-dimensional cuts on estimators used by the finders in ibg and ibgam. For details on their definitions see [90–92].

Bit	Used	Cut
0	Yes	N3PHI > 14
1	Yes	DMUBW < 50
2	Yes	DMUMU < 200
3	Yes	DIFSP < 30
4	Yes	SPMUMU > 0.8
5	No	EFOUTH < 0.05
6	No	EFOUTC < 0.02
7	Yes	EFMU > 0.8
8	No	DISPRH < 2
9	Yes	TDCAMU > 40
10	Yes	DTCLU > 0.2 and EFEMC < 0.1
11	Yes	DTCLU > 0.5 and EFMU > 0.05
12	Yes	DISPRC < 5 and EFTC > 0.25
13	Yes	DISPRC < 5 and EFMU > 0.05
14	Yes	DISPRC < 4 and EFOUTC > 0.05
15	Yes	THCLUM > 20 and ETTRA/ETCAL < 0.015

Appendix B

Selected Muon Events

In this appendix, the properties of events containing selected muon candidates and the properties of these muon candidates are listed. The ID in the event properties tables corresponds to the ID in the muon candidate properties tables. The muon selection and the selected muon samples are described in chapter 9.

Table B.1: Properties of events containing selected muons in HERA I e^+.

ID	Run	Event	Q^2 $[\mathrm{GeV}^2]$	$P_{T,\,miss}$ [GeV/c]	θ_{HFS} [°]	y
1	263213	93590	386	16.3	6.2	0.31
2	263337	17795	4960	49.9	35.0	0.50
3	265127	114277	337	15.0	64.1	0.33
4	265277	37935	373	18.1	7.8	0.12
5	266336	4126	6683	65.0	16.7	0.39
6	270097	9927	407	18.8	11.8	0.16
7	270219	95237	2229	31.4	78.4	0.56
8	276579	7806	6333	56.3	20.7	0.50
9	279139	12574	1055	26.8	31.1	0.32

Table B.2: Properties of selected muon candidates in HERA I e^+.

ID	Charge	p_T [GeV/c]	θ [°]	$d_{ca}^{'}$ [μm]	$d_{\eta\phi}$ to closest jet
1	-	2.9	40.9	-148	0.38
2	+	9.1	55.6	181	0.02
3	+	2.3	111.6	56	0.30
4	+	4.7	35.5	16	0.17
5	+	19.7	67.3	10	1.23
6	+	2.5	82	-25	3.07
7	+	3.6	93.4	-13	0.15
8	+	33.1	44.5	-16	0.03
9	-	4.6	64.4	211	0.06

Table B.3: Properties of events containing selected muons in HERA II e^+.

ID	Run	Event	Q^2 [GeV^2]	$P_{T,\,miss}$ [GeV/c]	θ_{HFS} [°]	y
10	363075	49014	1900	31.0	25.5	0.49
11	367292	23544	911	21.9	78.5	0.47
12	471176	113900	5710	36.6	29.4	0.78
13	473929	107593	3905	40.9	12.1	0.57
14	474629	54292	708	24.1	15.1	0.18
15	476014	4642	1117	28.9	29.0	0.25
16	477322	302536	3665	48.9	18.3	0.35
17	477669	48924	768	23.0	52.8	0.31
18	481552	287581	768	26.0	22.1	0.12
19	482861	119165	1987	40.1	17.4	0.19
20	483748	17449	365	16.4	5.1	0.27
21	484802	42454	2644	29.5	29.2	0.67
22	488817	294489	514	18.7	21.0	0.32
23	490746	40211	357	15.6	17.4	0.31
24	492443	94505	348	16.8	11.2	0.29
25	492696	8468	2027	25.6	58.1	0.68
26	492710	121870	8003	64.9	32.9	0.47
27	494115	121996	7858	35.8	22.6	0.84
28	499297	162210	4302	39.4	23.2	0.65

Table B.4: Properties of selected muon candidates in HERA II e^+. Muon 18 has been selected because it was detected in the forward endcap, where a cut on the momentum p instead of p_T is applied.

ID	Charge	p_T [GeV/c]	θ [°]	d'_{ca} [μm]	$d_{\eta\phi}$ to closest jet
10	-	3.3	79.0	29	0.23
11	-	2.4	110.1	3050	0.20
12	+	5.8	97.1	25	0.08
13	-	53.5	31.4	-10	3.69
14	+	4.3	58.6	-22	0.03
15	+	2.0	44.3	279	0.18
16	+	3.5	66.1	68	0.10
17	+	6.3	76.7	22	0.09
18	+	1.4	29.5	118	0.16
19	+	3.7	28.3	-52	0.05
20	-	28.0	46.7	2	4.18
21	-	4.3	97.1	-93	4.48
22	+	3.8	30.0	-8	2.31
23	+	3.0	33.6	-4	0.06
24	-	2.2	85.9	-955	0.16
25	+	2.6	106.8	44	0.19
26	-	17.9	44.9	-11	0.06
27	+	22.6	61.5	-74	2.19
28	-	2.1	95.7	198	0.63

Table B.5: Properties of events containing selected muons in HERA II e^-.

ID	Run	Event	Q^2 [GeV^2]	$P_{T,\,miss}$ [GeV/c]	θ_{HFS} [°]	y
29	403161	9761	1901	33.1	53.3	0.42
30	403290	66027	4940	48.9	43.3	0.52
31	403503	16430	2756	36.1	11.2	0.53
32	405979	9621	1242	20.3	30.2	0.67
33	408588	31212	1816	33.8	16.6	0.37
34	410819	58372	740	25.1	25.1	0.15
35	411019	59656	2028	32.0	59.5	0.49
36	411948	104641	266	15.0	27.0	0.16
37	421875	43326	1199	32.4	18.2	0.12
38	422012	4221	403	16.9	13.9	0.29
39	422168	47303	3402	49.7	23.0	0.34
40	425903	37016	479	17.2	29.9	0.38
41	432437	47430	1770	29.5	57.6	0.45
42	433167	81189	6907	59.4	39.6	0.49
43	433888	24625	23605	64.0	51.8	0.83
44	434278	60847	6619	59.5	31.4	0.47
45	450174	55768	1124	27.4	21.6	0.33
46	450980	65241	2414	40.0	26.1	0.34
47	451436	54741	4114	51.2	34.5	0.36
48	451464	73174	2233	40.9	14.6	0.12
49	453900	43188	1295	25.9	15.4	0.48
50	454505	28913	569	22.0	18.9	0.15
51	455790	77787	501	17.8	6.7	0.25
52	465429	60376	6727	44.9	38.5	0.70
53	465670	83634	4062	50.4	22.3	0.37
54	466445	11232	4654	45.2	49.6	0.56

Table B.6: Properties of selected muon candidates in HERA II e^-. A distance to the closest jet of 99 for muon candidate 48 indicates that there was no jet reconstructed in the corresponding event. With its large p_T, small polar angle and large $d_{ca}^{'}$, this muon candidate might be a halo muon, although it passes the non-ep background finder cuts in the CC event selection. A visual inspection in the event display gives no clear indication for this suspicion.

ID	Charge	p_T [GeV/c]	θ [°]	$d_{ca}^{'}$ [μm]	$d_{\eta\phi}$ to closest jet
29	+	3.1	71.0	-254	0.14
30	-	8.2	57.0	-132	0.11
31	+	6.7	59.9	1902	0.03
32	-	2.1	109.8	-6	3.82
33	-	3.8	44.3	-34	0.04
34	-	6.9	37.9	-97	0.06
35	-	3.2	74.1	-1514	0.08
36	-	5.4	57.7	10	0.07
37	+	2.0	17.4	5170	0.38
38	-	3.3	119.5	-27	3.68
39	-	8.6	48.8	-493	0.04
40	-	2.3	82.5	-95	0.28
41	+	5.0	78.5	149	0.08
42	+	5.3	53.2	91	0.10
43	+	5.7	72.1	-19	0.14
44	-	4.5	45.6	-8622	0.05
45	-	7.3	62.4	-4	0.08
46	+	2.1	43.8	366	0.04
47	-	2.4	45.6	-63	0.10
48	-	44.4	16.5	-13180	99.00
49	+	4.1	77.8	0	0.17
50	-	2.9	36.5	-40	0.09
51	+	10.4	46.5	-411	0.68
52	+	4.1	87.0	51	6.08
53	-	37.5	40.6	2	1.38
54	-	11.9	71.5	-193	0.10

List of Figures

2.1 ep scattering graph . . . 12
2.2 DIS Feynman graph according to the Quark Parton Model. . . . 15
2.3 Proton structure in QPM and QCD . . . 16
2.4 NC and CC cross sections in bins of Q^2 . . . 18
2.5 Polarization dependent CC cross section . . . 20
2.6 Angular momentum conservation in CC interactions . . . 21

3.1 Happex results . . . 25
3.2 G0 results . . . 26
3.3 A4 results . . . 26
3.4 Charm in CC Feynman graph for neutrino DIS . . . 27
3.5 Dimuon event in the CHARM II calorimeter . . . 28
3.6 Schematic view of the HERMES spectrometer . . . 30
3.7 Quark helicity distributions measured by HERMES . . . 31
3.8 Schematic view of the ZEUS detector . . . 32
3.9 Differential ϕ cross sections measured by ZEUS . . . 33
3.10 Proton PDFs with various data sets combined . . . 34

4.1 The HERA accelerator . . . 36
4.2 The total integrated luminosity collected by H1 . . . 37
4.3 Measured polarization in the course of a luminosity fill . . . 38
4.4 Schematic view of the lepton beam polarization at HERA . . . 38
4.5 Schematic view of the H1 detector . . . 40
4.6 Schematic view of the H1 central tracking system . . . 41
4.7 CIP2k projective geometry . . . 42
4.8 Technical drawing of the FTD . . . 43
4.9 CST d_{ca} resolution . . . 44
4.10 Longitudinal cross section of the LAr calorimeter . . . 45
4.11 Schematic layout of the Central Muon Detector . . . 47
4.12 Schematic design of the H1 trigger system . . . 48

5.1 Schematic view of the event generation and detector simulation . . . 52
5.2 NC and CC graph . . . 53
5.3 Photoproduction Feynman graphs . . . 54
5.4 Feynman graphs for real W production . . . 55
5.5 Feynman graph for lepton pair production . . . 55
5.6 Global weight for HERA II e^+p CC simulation . . . 57
5.7 NC event transformed into PsCC event . . . 58

6.1 CC trigger efficiency . . . 61
6.2 $p_{T,\,miss}$ of the triggered data sample with and without non-ep rejection cuts . . . 63

6.3 CC and halo muon event displays . . . 63
6.4 CJC and LAr T_0 . . . 64
6.5 $p_{T,\,miss}$ of simulated CC events and of triggered data events . . . 66
6.6 Energy flow isotropy in CC and γp events . . . 67
6.7 Two-dimensional distributions of CC and γp events in the variables V_{ratio} and $p_{T,h}$ . . . 68
6.8 Polarization distribution for the HERA II e^- and e^+ data samples . . . 69
6.9 Suspected cosmic ray muon event . . . 70
6.10 Yield of selected events . . . 72
6.11 Comparison of data and simulation for the selected e^+ RH sample . . . 74
6.12 Comparison of data and simulation for the selected e^- LH sample . . . 74
6.13 Measured CC cross sections as a function of the polarization . . . 78

7.1 Production processes of ϕ mesons in NC . . . 82
7.2 Production processes of charmed hadrons in CC . . . 83
7.3 Kinematics of BGF and quark initiated processes in e^-p scattering . . . 85
7.4 Kinematics of BGF and quark initiated processes in e^+p scattering . . . 85
7.5 Kinematics of charm and non-charm events in e^-p scattering . . . 86
7.6 Kinematics of charm and non-charm events in e^+p scattering . . . 86

8.1 Multiplicity of charmed hadron decays . . . 90
8.2 Track reconstruction efficiency for charged pions . . . 91
8.3 Number of CST hits linked and CST-CJC linking probability . . . 92
8.4 Properties of charm decay tracks . . . 93
8.5 Distance in $\eta\phi$-space of the charm decay vertex to the jet axis . . . 94
8.6 p_T and S_{dca} rank of charm decay tracks within a jet . . . 95
8.7 Schematic drawing of the deterministic annealing algorithm . . . 96
8.8 Track-vertex weights and vertex multiplicity in data and simulation . . . 97
8.9 Vertex multiplicity and number of jet tracks for charm and non-charm jets . . . 98
8.10 Decay length of secondary vertex candidates in data and simulation . . . 98
8.11 Decay length of charm and non-charm secondary vertex candidates . . . 99
8.12 Comparison of simulated and fitted secondary vertex positions and decay lengths . . . 101
8.13 S1, S2, S3 and subtracted distributions for positron data and simulation. . . . 102

9.1 Example process for charm in charged current . . . 103
9.2 Properties of leptons from charm decays on generator level . . . 104
9.3 Efficiency of the muon preselection . . . 106
9.4 Particle type of preselected muon candidates . . . 106
9.5 Polar angle of the charm quark and the charm decay muon . . . 107
9.6 Transverse momentum of charm decay muons . . . 108
9.7 Linking probability of preselected muon candidates . . . 109
9.8 Track length quantities for preselected muon candidates . . . 109
9.9 Particle type of selected muon candidates . . . 111
9.10 Distance of selected muon candidates to the nearest jet and to the nearest track . . . 112
9.11 Calorimeter quantities for muon identification . . . 113
9.12 Definition of the sign of the $d_{ca}^{'}$ of a track . . . 114
9.13 $d_{ca}^{'}$ of selected muon candidates . . . 114
9.14 Feynman graphs for real W production . . . 117
9.15 Properties of the selected muon candidate sample . . . 119
9.16 Charge of the selected muon candidates in simulation . . . 120
9.17 Schematic diagram of the charm fraction extraction . . . 122
9.18 Comparison of muon quantities in HERA I and HERA II positron simulation . . . 123
9.19 Selected muon p_T templates and data distribution for the p_T likelihood fit . . . 125

9.20 Charge misidentification probability 126

List of Tables

3.1 CHARM II results . . . 28
3.2 NuTeV and CCFR results . . . 29
3.3 CHORUS and NOMAD results . . . 29
3.4 Summary of neutrino DIS results on the strange sea . . . 34

5.1 Simulated charged current samples . . . 53
5.2 Simulated background samples . . . 54

6.1 Technical definitions of the CC subtriggers . . . 60
6.2 Data samples used for the CC analysis . . . 62
6.3 Data selection and event selection criteria . . . 71
6.4 Efficiencies of individual sets of selection criteria in simulation . . . 72
6.5 Number of selected CC events . . . 72
6.6 Expected background and signal contributions to the selected event samples . . . 73
6.7 Systematic uncertainties on the total CC cross sections . . . 76
6.8 Parameters used in the cross section calculation . . . 77
6.9 Measured and predicted CC cross sections . . . 77

7.1 Event selection efficiency for charm and non-charm CC events . . . 87

8.1 Lifetime and flight distance of some charmed hadrons . . . 89
8.2 Track selection criteria . . . 92
8.3 Origin of tracks with weight > 0.8 to the secondary vertex . . . 100

9.1 Muon preselection cuts in the CMD barrel . . . 105
9.2 Muon selection cuts . . . 110
9.3 Charm and muon content of the muon candidate samples . . . 111
9.4 Background contributions to the selected muon candidate sample from non-CC processes 116
9.5 Background contributions to the selected muon candidate sample from non-CC processes with anti-isolation cut applied . . . 117
9.6 Selected muon samples . . . 118
9.7 Expected and measured number of muon candidates . . . 119
9.8 Parameters from simulation for the charm in CC cross section calculation . . . 122
9.9 Systematic uncertainties on the charm fractions . . . 128
9.10 Measured charm fractions in the individual and combined CC samples . . . 128
9.11 Measured charm cross sections in the individual and combined CC samples . . . 129

A.1 Non-ep background finder flags coded in the ibg array . . . 135
A.2 Non-ep background finder flags coded in the ibgam array . . . 136
A.3 Non-ep background finder flags coded in the ibgfm array . . . 136

B.1 Properties of events containing selected muons in HERA I e^+ 137
B.2 Properties of selected muon candidates in HERA I e^+ 138
B.3 Properties of events containing selected muons in HERA II e^+ 138
B.4 Properties of selected muon candidates in HERA II e^+ 139
B.5 Properties of events containing selected muons in HERA II e^- 140
B.6 Properties of selected muon candidates in HERA II e^- 141

Bibliography

[1] Sylvia Berryman, Democritus, In Edward N. Zalta, editor, *The Stanford Encyclopedia of Philosophy*. Fall 2004.

[2] John Dalton, *A New System of Chemical Philosophy*, volume I - III. Manchester, 1808.

[3] Encyclopædia Britannica, Law of multiple proportions, Online, 18 March 2008.

[4] E. Rutherford, *"The scattering of α and β particles by matter and the structure of the atom"*, Phil. Mag., **21** 669–688, 1911.

[5] J. Chadwick, *"Possible Existence of a Neutron"*, Nature, **129** 312, 1932.

[6] Albert Einstein, *"Concerning an heuristic point of view toward the emission and transformation of light"*, Annalen Phys., **17** 132–148, 1905.

[7] Paul A. M. Dirac, *"The fundamental equations of quantum mechanics"*, Proc. Roy. Soc. Lond., **A109** 642–653, 1925.

[8] Murray Gell-Mann, *"A Schematic Model of Baryons and Mesons"*, Phys. Lett., **8** 214–215, 1964.

[9] Martin Breidenbach et al., *"Observed Behavior of Highly Inelastic electron-Proton Scattering"*, Phys. Rev. Lett., **23** 935–939, 1969.

[10] F. W. Busser et al., *"Observation of pi0 mesons with large transverse momentum in high-energy proton proton collisions"*, Phys. Lett., **B46** 471–476, 1973.

[11] F. Halzen and Alan D. Martin, *"Quarks and Leptons: An introductory course in modern particle physics"*, New York, Usa: Wiley (1984) 396p.

[12] G. A. Voss and B. H. Wiik, *"The Electron proton collider HERA"*, Ann. Rev. Nucl. Part. Sci., **44** 413–452, 1994.

[13] I. Abt et al., [H1], *"The H1 detector at HERA"*, Nucl. Instrum. Meth., **A386** 310–347, 1997.

[14] I. Abt et al., [H1], *"The Tracking, calorimeter and muon detectors of the H1 experiment at HERA "*, Nucl. Instrum. Meth., **A386** 348–396, 1997.

[15] U. Holm (ed.), [ZEUS], *"The ZEUS detector: Status report (unpublished), DESY"*, 1993, available on http://www-zeus.desy.de/bluebook/bluebook.html.

[16] HERMES Collaboration, [HERMES], *"HERMES technical design report"*, 1993, DESY-PRC-93-06.

[17] W. M. Yao et al., [Particle Data Group], *"Review of particle physics"*, J. Phys., **G33** 1–1232, 2006.

[18] R. Devenish and A. Cooper-Sarkar, *"Deep inelastic scattering"*, Oxford, UK: Univ. Pr. (2004) 403 p.

[19] B. Povh, C. Scholz, K. Rith and F. Zetsche, *"Particles and nuclei: An introduction to the physical conceptions. (In German)"*, Berlin, Germany: Springer (1993) 316 p.

[20] M. N. Rosenbluth, *"High Energy Elastic Scattering of Electrons on Protons"*, Phys. Rev., **79** 615–619, 1950.

[21] Richard P. Feynman, *"Very high-energy collisions of hadrons"*, Phys. Rev. Lett., **23** 1415–1417, 1969.

[22] J. D. Bjorken, *"Asymptotic Sum Rules at Infinite Momentum"*, Phys. Rev., **179** 1547–1553, 1969.

[23] J. D. Bjorken and Emmanuel A. Paschos, *"Inelastic Electron Proton and gamma Proton Scattering, and the Structure of the Nucleon"*, Phys. Rev., **185** 1975–1982, 1969.

[24] Elliott D. Bloom et al., *"High-Energy Inelastic e p Scattering at 6-Degrees and 10- Degrees"*, Phys. Rev. Lett., **23** 930–934, 1969.

[25] Jr. Callan, Curtis G. and David J. Gross, *"High-energy electroproduction and the constitution of the electric current"*, Phys. Rev. Lett., **22** 156–159, 1969.

[26] D. J. Fox et al., *"Test of Scale Invariance in High-Energy Muon Scattering"*, Phys. Rev. Lett., **33** 1504, 1974.

[27] H. David Politzer, *"Reliable perturbative results for strong interactions?"*, Phys. Rev. Lett., **30** 1346–1349, 1973.

[28] D. J. Gross and Frank Wilczek, *"Ultraviolet behavior of non-abelian gauge theories"*, Phys. Rev. Lett., **30** 1343–1346, 1973.

[29] C. Adloff et al., [H1], *"Measurement and QCD analysis of neutral and charged current cross sections at HERA"*, Eur. Phys. J., **C30** 1–32, 2003.

[30] C. S. Wu, E. Ambler, R. W. Hayward, D. D. Hoppes and R. P. Hudson, *"Experimental test of parity conservation in beta decay"*, Phys. Rev., **105** 1413–1414, 1957.

[31] Q. R. Ahmad et al., [SNO], *"Measurement of the charged current interactions produced by B-8 solar neutrinos at the Sudbury Neutrino Observatory"*, Phys. Rev. Lett., **87** 071301, 2001.

[32] M. Goldhaber, L. Grodzins and A. W. Sunyar, *"Helicity of neutrinos"*, Phys. Rev., **109** 1015–1017, 1958.

[33] B. Antunovic, [H1], *"Charged current interactions in electron proton collisions at HERA II"*, Prepared for 14th International Workshop on Deep Inelastic Scattering (DIS 2006), Tsukuba, Japan, 20-24 Apr 2006.

[34] J. Ashman et al., [European Muon], *"A measurement of the spin asymmetry and determination of the structure function g(1) in deep inelastic muon proton scattering"*, Phys. Lett., **B206** 364, 1988.

[35] Giuliano Preparata and Jacques Soffer, *"Evidence Against Perturbative QCD from Polarized Deep Inelastic Scattering"*, Phys. Rev. Lett., **61** 1167, 1988.

[36] F. E. Close, *"Polarized strange quarks in the proton and the validity of quantum chromodynamics"*, Phys. Rev. Lett., **64** 361–363, 1990.

[37] Robert Michaels, *"HAPPEX: Strange quarks in the proton and He-4"*, AIP Conf. Proc., **915** 719–724, 2007.

[38] K. A. Aniol et al., [HAPPEX], *"New measurement of parity violation in elastic electron proton scattering and implications for strange form factors"*, Phys. Lett., **B509** 211–216, 2001.

[39] A. Acha et al., [HAPPEX], *"Precision Measurements of the Nucleon Strange Form Factors at Q**2 0.1-GeV**2"*, Phys. Rev. Lett., **98** 032301, 2007.

[40] D. S. Armstrong et al., [G0], *"Strange quark contributions to parity-violating asymmetries in the forward G0 electron proton scattering experiment"*, Phys. Rev. Lett., **95** 092001, 2005.

[41] F. E. Maas et al., *"Evidence for strange quark contributions to the nucleon's form factors at Q**2 = 0.108-(GeV/c)**2"*, Phys. Rev. Lett., **94** 152001, 2005.

[42] P. Vilain et al., [CHARM II], *"Leading-order QCD analysis of neutrino induced dimuon events"*, Eur. Phys. J., **C11** 19–34, 1999.

[43] C. Peterson, D. Schlatter, I. Schmitt and Peter M. Zerwas, *"Scaling Violations in Inclusive e+ e- Annihilation Spectra"*, Phys. Rev., **D27** 105, 1983.

[44] M. Goncharov et al., [NuTeV], *"Precise measurement of dimuon production cross-sections in nu/mu Fe and anti-nu/mu Fe deep inelastic scattering at the Tevatron"*, Phys. Rev., **D64** 112006, 2001.

[45] A. Kayis-Topaksu et al., [CHORUS], *"Leading order analysis of neutrino induced dimuon events in the CHORUS experiment"*, Nucl. Phys., **B798** 1–16, 2008.

[46] P. Astier et al., [NOMAD], *"Neutrino production of opposite sign dimuons in the NOMAD experiment"*, Phys. Lett., **B486** 35–48, 2000.

[47] A. Airapetian et al., [HERMES], *"Quark helicity distributions in the nucleon for up, down, and strange quarks from semi-inclusive deep-inelastic scattering"*, Phys. Rev., **D71** 012003, 2005.

[48] HERMES Collaboration, http://www-hermes.desy.de/, Online, 20 May 2008.

[49] ZEUS Collaboration, http://www-zeus.desy.de, Online, 22 May 2008.

[50] S. Chekanov et al., [ZEUS], *"Observation of the strange sea in the proton via inclusive Phi-meson production in neutral current deep inelastic scattering at HERA"*, Phys. Lett., **B553** 141–158, 2003.

[51] Giovanni De Lellis, Pasquale Migliozzi and Pietro Santorelli, *"Charm physics with neutrinos"*, Phys. Rept., **399** 227–320, 2004.

[52] V. Barone, C. Pascaud, B. Portheault and F. Zomer, *"Parton distribution functions in a fit of DIS and related data"*, JHEP, **01** 006, 2006.

[53] H1 Collaboration, http://www-h1.desy.de, Online, 26 May 2008.

[54] E. Hartouni et al., *"HERA-B: An experiment to study CP violation in the B system using an internal target at the HERA proton ring. Design report"*, DESY-PRC-95-01.

[55] A. A. Sokolov and I. M. Ternov, *"On Polarization and spin effects in the theory of synchrotron radiation"*, Sov. Phys. Dokl., **8** 1203–1205, 1964.

[56] A. Nikiforov, *"Measurements of the Neutral Current e±p Cross Sections Using Longitudinally Polarised Lepton Beams at HERA II"*, PhD thesis Ludwig-Maximilian-University Munich, 2007.

[57] G. Z. M. Berglund, *"Spin-orbit maps and electron spin dynamics for the luminosity upgrade project at HERA"*, DESY-THESIS-2001-044.

[58] M. Beckmann et al., *"The longitudinal polarimeter at HERA"*, Nucl. Instrum. Meth., **A479** 334–348, 2002.

[59] J. Bohme, *"Precision measurement with the transverse polarimeter at HERA II"*, Eur. Phys. J., **C33** s1067–s1069, 2004.

[60] J. Burger et al., *"The Central jet chamber of the H1 experiment"*, Nucl. Instrum. Meth., **A279** 217–222, 1989.

[61] C. Kleinwort, [H1], *"H1 alignment experience"*, Prepared for 1st LHC Detection Alignment Workshop, Geneva, Switzerland, 4-6 Sep 2006.

[62] Max Christoph Urban, *"The new CIP2k z-vertex trigger for the H1 experiment at HERA"*, DESY-THESIS-2004-044.

[63] D. Pitzl et al., *"The H1 silicon vertex detector"*, Nucl. Instrum. Meth., **A454** 334–349, 2000.

[64] B. Andrieu et al., [H1 Calorimeter Group], *"The H1 liquid argon calorimeter system"*, Nucl. Instrum. Meth., **A336** 460–498, 1993.

[65] B. Andrieu et al., [H1 Calorimeter Group], *"Beam tests and calibration of the H1 liquid argon calorimeter with electrons"*, Nucl. Instrum. Meth., **A350** 57–72, 1994.

[66] B. Andrieu et al., [H1 Calorimeter Group], *"Results from pion calibration runs for the H1 liquid argon calorimeter and comparisons with simulations"*, Nucl. Instrum. Meth., **A336** 499–509, 1993.

[67] R. D. Appuhn et al., [H1 SPACAL Group], *"The H1 lead/scintillating-fibre calorimeter"*, Nucl. Instrum. Meth., **A386** 397–408, 1997.

[68] T. Nicholls et al., [H1 SPACAL Group], *"Performance of an electromagnetic lead / scintillating fiber calorimeter for the H1 detector"*, Nucl. Instrum. Meth., **A374** 149–156, 1996.

[69] H. Itterbeck, *"Techniques and Physics of the Central-Myon-Trigger System of the H1-Detector at HERA"*, Dissertation RWTH Aachen, PITHA 97/38.

[70] P. Biddulph et al., *"The H1 forward muon spectrometer"*, Nucl. Instrum. Meth., **A340** 304–308, 1994.

[71] H. Bethe and W. Heitler, *"On the Stopping of fast particles and on the creation of positive electrons"*, Proc. Roy. Soc. Lond., **A146** 83–112, 1934.

[72] H1 Collaboration, *"Luminosity Measurement in the H1 Experiment at HERA"*, Submitted to the 28th International Conference of High Energy Physics, Warsaw 1996.

[73] F. D. Aaron et al., [H1], *"Multi-Lepton Production at High Transverse Momenta in ep Collisions at HERA"*, 2008.

[74] A. W. Jung, *"Inbetriebnahme der dritten Stufe des schnellen Spurtriggers fuer das H1-Experiment"*, Univ. Dortmund diploma thesis 09/04, 2004.

[75] CERN Program Library Long Writeup W5013, *"GEANT - Detector Description and Simulation Tool"*.

[76] G. A. Schuler and H. Spiesberger, *"DJANGO: The Interface for the event generators HERACLES and LEPTO"*, In *Hamburg 1991, Proceedings, Physics at HERA, vol. 3* 1419-1432. (see HIGH ENERGY PHYSICS INDEX 30 (1992) No. 12988).

[77] G. Ingelman, A. Edin and J. Rathsman, *"LEPTO 6.5 - A Monte Carlo Generator for Deep Inelastic Lepton-Nucleon Scattering"*, Comput. Phys. Commun., **101** 108–134, 1997.

[78] A. Kwiatkowski, H. Spiesberger and H. J. Mohring, *"HERACLES: An event generator for e p interactions at HERA energies including radiative processes: Version 1.0"*, Comp. Phys. Commun., **69** 155–172, 1992.

[79] Leif Lonnblad, *"ARIADNE version 4: A Program for simulation of QCD cascades implementing the color dipole model"*, Comput. Phys. Commun., **71** 15–31, 1992.

[80] G. Gustafson, *"Dual Description of a Confined Color Field"*, Phys. Lett., **B175** 453, 1986.

[81] Torbjorn Sjostrand and Mats Bengtsson, *"The Lund Monte Carlo for Jet Fragmentation and e+ e- Physics. Jetset Version 6.3: An Update"*, Comput. Phys. Commun., **43** 367, 1987.

[82] Bo Andersson, G. Gustafson, G. Ingelman and T. Sjostrand, *"Parton Fragmentation and String Dynamics"*, Phys. Rept., **97** 31–145, 1983.

[83] Alan D. Martin, W. James Stirling and R. G. Roberts, *"Parton distributions updated"*, Phys. Lett., **B306** 145–150, 1993.

[84] S. Caron, *"Jets in Photoproduction at HERA"*, PhD thesis RWTH Aachen, DESY-THESIS-2002-035.

[85] Torbjorn Sjostrand et al., *"High-energy-physics event generation with PYTHIA 6.1"*, Comput. Phys. Commun., **135** 238–259, 2001.

[86] M. Gluck, E. Reya and A. Vogt, *"Photonic parton distributions"*, Phys. Rev., **D46** 1973–1979, 1992.

[87] U. Baur, J. A. M. Vermaseren and D. Zeppenfeld, *"Electroweak vector boson production in high-energy e p collisions"*, Nucl. Phys., **B375** 3–44, 1992.

[88] Tetsuo Abe, *"GRAPE-Dilepton (Version 1.1): A generator for dilepton production in e p collisions"*, Comput. Phys. Commun., **136** 126–147, 2001.

[89] B. Antunovic, *"A First Measurement of the Charged Current DIS Cross Sections with the Longitudinally Polarised Electrons in the H1 Experiment at HERA"*, PhD thesis Ludwig-Maximilians-University Munich, 2007.

[90] I. Negri, *"A Minimal Comprehensive Set of Muon Background Topological Finders for High P_T Physics Analysis"*, H1 internal note H1-IN-498(10/1996).

[91] E. Chabert, *"QBGFMAR: An Updated Phan Package for Cosmic and Halo Muon Topological Rejection in High P_T Physics Analysis"*, H1 internal note H1-IN-556(11/1998).

[92] Ch. Veelken, *"H1NonepBgFinder - Rejection of Cosmic Muon and Beam-Halo Events in the H1OO Framework"*, H1 internal note H1-IN-603(09/2002).

[93] H1 inclusive measurements and fits group, *"Systematic errors for ICHEP 2008 preliminary requests"*, Private communication.

[94] B. Heinemann, *"Measurement of Charged Current and Neutral Current Cross Sections in Positron-Proton Collisions at sqrt(s)=300 GeV"*, PhD thesis University of Hamburg.

[95] Z. Portheault, B. and Zhang, *"Radiative Corrections for Charged Current Process at HERA Revisited"*, H1 internal note H1-IN-614(11/2004).

[96] F. et al Corriveau, *"A Calibration of the HERA Transverse Polarimeter for the 2003/2004 Data"*, available at http://www.desy.de/ pol2000/documents/documents.html.

[97] B. Reisert and R. Placakyte, Private communication.

[98] A. Aktas et al., [H1], *"Production of D*+- mesons with dijets in deep-inelastic scattering at HERA"*, Eur. Phys. J., **C51** 271–287, 2007.

[99] A. Aktas et al., [H1], *"Measurement of charm and beauty photoproduction at HERA using D* mu correlations"*, Phys. Lett., **B621** 56–71, 2005.

[100] C. Adloff et al., [H1], *"Measurement of D*+- meson production and F2(c) in deep inelastic scattering at HERA"*, Phys. Lett., **B528** 199–214, 2002.

[101] Meng Wang, *"Charm production in charged current deep inelastic e+ p scattering at HERA"*, PhD thesis, BONN-IR-2006-02.

[102] A. Aktas et al., [H1], *"Measurement of F2(c anti-c) and F2(b anti-b) at high Q**2 using the H1 vertex detector at HERA"*, Eur. Phys. J., **C40** 349–359, 2005.

[103] A. Aktas et al., [H1], *"Measurement of charm and beauty dijet cross sections in photoproduction at HERA using the H1 vertex detector"*, Eur. Phys. J., **C47** 597–610, 2006.

[104] S. Mangano, *"Charm Production in Charged Current and Charm & Beauty Production in Neutral Current Interactions at High Q2"*, ETH Zurich, PhD thesis, ETHZ-IPP Internal Report 2005-02.

[105] S. Catani, Yuri L. Dokshitzer, M. H. Seymour and B. R. Webber, *"Longitudinally invariant K(t) clustering algorithms for hadron hadron collisions"*, Nucl. Phys., **B406** 187–224, 1993.

[106] Stephen D. Ellis and Davison E. Soper, *"Successive combination jet algorithm for hadron collisions"*, Phys. Rev., **D48** 3160–3166, 1993.

[107] R. Fruhwirth, W. Waltenberger, K. Prokofiev, T. Speer and P. Vanlaer, *"New developments in vertex reconstruction for CMS"*, Nucl. Instrum. Meth., **A502** 699–701, 2003.

[108] R. Frühwirth and A. Strandlie, *"Track fitting with ambiguities and noise: a study of elastic tracking and nonlinear filters"*, Computer Physics Communications, **120** 197–214, August 1999.

[109] Roger J. Barlow and Christine Beeston, *"Fitting using finite Monte Carlo samples"*, Comput. Phys. Commun., **77** 219–228, 1993.

[110] M. Goettlich, *"Study of Charm and Beauty Production at HERA/H1 using Dilepton Events"*, PhD thesis Univ. Hamburg, DESY-THESIS-2007-012.

[111] G. Schmidt, *"Nachweis von Myonen im H1-Kalorimeter"*, Univ. Hamburg diploma thesis 1/94, H1-IN-341, 1994.

[112] C. Veelken, *"Search for Events with Isolated Leptons and Large Missing Transverse Momentum in ep Collisions at HERA"*, Univ. of Liverpool PhD thesis 01/05, 2005.

[113] U. Langenegger, *"A Measurement of the Beauty and Charm Production Cross Sections at the ep Collider HERA"*, ETH Zurich PhD thesis no. 12676, 1998.

[114] C. Adloff et al., [H1], *"Measurement of open beauty production at HERA"*, Phys. Lett., **B467** 156–164, 1999.

[115] C. Blatter, *"Analysis 2"*, Berlin, Germany: Springer (1992), 3. Auflage.

[116] R. Brun and F. Rademakers, *"ROOT: An object oriented data analysis framework"*, Nucl. Instrum. Meth., **A389** 81–86, 1997.

[117] F. James and M. Roos, *"Minuit: A System for Function Minimization and Analysis of the Parameter Errors and Correlations"*, Comput. Phys. Commun., **10** 343–367, 1975.

[118] A. Aktas et al., [H1], *"Measurement of beauty production at HERA using events with muons and jets"*, Eur. Phys. J., **C41** 453–467, 2005.

[119] V. Michels, *"Measurement of Beauty Production in Deep Inelastic Scattering at HERA"*, PhD thesis University of Hamburg, 2008.

[120] I. Bloch, *"Measurement of beauty production from dimuon events at HERA / ZEUS"*, PhD thesis, University of Hamburg 2005.

[121] (Ed.) Bruning, O. et al., *"LHC design report. Vol. I: The LHC main ring"*, CERN-2004-003-V-1.

[122] (Ed.) Buning, O. et al., *"LHC Design Report. 2. The LHC infrastructure and general services"*, CERN-2004-003-V-2.

[123] (Ed.) Benedikt, M., (Ed.) Collier, P., (Ed.) Mertens, V., (Ed.) Poole, J. and (Ed.) Schindl, K., *"LHC Design Report. 3. The LHC injector chain"*, CERN-2004-003-V-3.

Danksagung

In der Öffentlichkeit herrscht oft noch das Bild des eigenbrötlerischen Wissenschaftlers vor, der alleine oder mit Hilfe eines Technikers oder Doktoranden in seinem eigenen, kleinen Labor Experimente plant, baut, durchführt und auswertet. Diese Zeiten sind jedoch, zumindest in der Hochenergiephysik, schon lange vorbei. Das H1-Experiment wurde von einer Kollaboration aus etwa 400 Physikern und Technikern betrieben. Eine Doktorarbeit in einem solchen Umfeld ist denn auch nur durch die Mithilfe von zahlreichen Kollegen möglich, angefangen von den Hardware-Experten, ohne die gar keine Daten genommen werden könnten, bis hin zu Bürokollegen, die bei alltäglichen Fragen und Problemen mit Rat und Tat zur Seite stehen. Einigen dieser Kollegen möchte ich nun im Folgenden besonders danken.

Ermöglicht wurde diese Doktorarbeit überhaupt erst durch meinen Doktorvater Ralph Eichler. Er hat mir immer viel Vertrauen entgegengebracht und mir bei der Ausgestaltung meiner Doktorarbeit viel Freiheit gelassen. In schwierigen Phasen der Arbeit hat er stets gute, pragmatische Denkanstösse gegeben.

Die Begutachtung dieser Arbeit und der Doktorprüfung wurde spontan und unkompliziert von Urs Langenegger übernommen.

Wohl am meisten Zeit verbracht, sowohl innerhalb wie auch ausserhalb des Büros, habe ich mit Guillaume Leibenguth. Wir haben (fast) gleichzeitig in Hamburg begonnen, zusammen den H1-Detektor und besonders "unseren" Subdetektor CST kennen, lieben und manchmal (besonders bei nächtlichen Anrufen von verzweifelten Schichtbesatzungen) auch hassen gelernt, zusammen die in dieser Doktorarbeit präsentierte Analyse entwickelt und implementiert und schliesslich (fast) gleichzeitig H1 und die ETH wieder verlassen. Guillaume hat auch diese Arbeit als Erster gelesen und viele Anregungen dazu gegeben.

Ein erstes Mal in Kontakt mit H1 kam ich durch Christoph Grab, bei dem ich einige Vorlesungen gehört hatte. Seine hilfsbereite und begeisterungsfähige Art hatte einen wesentlichen Anteil an meiner Entscheidung, eine Diplom- und später Doktorarbeit bei H1 zu machen. Während der Doktorarbeit konnte ich von seiner grossen Erfahrung profitieren. Hilfreich waren auch Christophs Kommentare zu den ersten Versionen dieser Arbeit.

Vieles, was ich heute über Teilchenphysik im Allgemeinen und H1 im Speziellen weiss, habe ich von Benno List gelernt. Während zahllosen Diskussionen und improvisierten Vorlesungen hat er mich und meine Kollegen mit viel Fachwissen, Geduld und didaktischem Geschick in die Wunder der Teilchenphysik, der Statistik, des CST und des objektorientierten Programmierens eingeführt.

Wenn ein unerwartetes Problem auftauchte oder ein Plot nicht aussah wie erwartet, haben Diskussionen mit André Schöning stets weitergeholfen. Mit seiner Erfahrung konnte er Lösungsansätze aufzeigen und die richtigen Prioritäten für das weitere Vorgehen setzen.

Nun sind aber die meisten Probleme, die bei einer Doktorarbeit auftauchen, nicht von grundsätzlicher, sondern eher von alltäglicher Natur. Wenn das Programm aus einem unerfindlichen Grund nicht kompilieren wollte oder die Schriftgrösse im Plot viel zu klein war, konnte ich jederzeit meine Doktoranden- und Diplomandenkollegen um Rat fragen. Insbesondere Nik, Ronnie, Michel, Marc, Lea und Roger haben mir bei unzähligen solchen kleineren und grösseren Ärgernissen geholfen. Besonders dankbar bin ich ihnen auch für die gute Zeit, die wir ausserhalb des Büros verbracht haben, von Filmabenden mit Cuba Libre über Pokerrunden bis hin zu den legendären Datscha-Partys.

Auch viele Mitglieder der H1-Kollaboration ausserhalb der ETH-Gruppe haben entscheidend zu einer gelungenen Doktorarbeit und einer guten Zeit in Hamburg beigetragen. Bei fachlichen Fragen zur Messung von Ereignissen des geladenen Stromes konnte ich stets auf die schnelle und kompetente Hilfe von Ringaile zählen. Auch Volker, der sowohl tagsüber wie auch abends so viel Zeit mit uns "ETHlern" verbracht hat, dass er quasi ein ETH-Ehrengruppenmitglied war, war bei Problemen und Fragen immer zur Stelle. Unsere zahlreichen gemeinsamen Unternehmungen haben uns sogar bis nach San Francisco geführt. Ebenfalls viel zu verdanken habe ich Mira, von unterhaltsamen Schichten bis zu neuen Hosen. Nicht zu vergessen sind auch die Dortmunder und Heidelberger Gruppen in H1, die immer einen Grund zum Feiern gefunden haben. Wenn es darum ging, enorme Mengen an Kuchen zu vertilgen oder frischgebackene Doktoren mit Wasserballons zu bewerfen, waren wir Schweizer oft auch eingeladen und gerne mit dabei.

Nicht nur in Hamburg, auch in Zürich herrschte immer eine angenehme Arbeitsatmosphäre. Mit Giovanna, Alex, Lukas, Andrea und Florian wurden die Kaffeepausen und das Mittagessen nie langweilig.

Bedingt durch den Arbeitsort Hamburg musste ich mich während der Doktorarbeit durch unzählige Reiseanträge und Reisespesenabrechnungen kämpfen. Dank unseren Institutssekretärinnen Marta und Rosa hat jedoch immer alles schnell und unkompliziert funktioniert. Durch ihre kompetente Unterstützung in allen administrativen Belangen haben sie mir das Leben erheblich vereinfacht.

Curriculum Vitae

Tobias Zimmermann

Born July 17 1979
in Zürich, Switzerland

Citizen of Zürich (ZH)
and Ebikon (LU)

Education

2004 – 2008	Doctoral studies at ETH Zürich, research at the H1 experiment at DESY, Hamburg
2004	Diploma in Physics at ETH Zürich, diploma thesis *"Measurement of Resonance Decays* $X \to K_s^0 K_s^0$ *at HERA"* in the group of Prof. Ralph Eichler
1999 – 2004	Studies of physics at ETH Zürich
1999	Compulsory military service in the Swiss army
1999	Eidgenössische Matura Typus E
1994 – 1999	Gymnasium in Winterthur
1986 – 1994	Primary and Secondary School in Spreitenbach and Winterthur